Titanium and Zirconium Permethylpentalene Chemistry: Ethylene Polymerisation and Small Molecule Activation

by

Duncan A. Fraser



This thesis is submitted in partial fulfilment of the requirement for the degree of Doctor of Philosophy at the University of Oxford

Balliol College

January 2018

The work described in this thesis was carried out in the Chemistry Research Laboratory, Mansfield Road, Oxford between October 2014 and January 2018 under the supervision of Professor Dermot O'Hare. All of the work is my own unless state to the contrary, and has not previously been submitted for any degree at this or any other university.

Duncan A. Fraser
Balliol College
January 2018

Abstract

Titanium and Zirconium Permethylpentalene Chemistry: Ethylene Polymerisation and Small Molecule Activation

Duncan Fraser **D.Phil Thesis**
Balliol College **Michaelmas Term 2017/18**

Chapter One provides an introduction to the chemistry of pentalene and its derivatives encompassing ligand synthesis, organometallic chemistry, and in particular ethylene polymerisation. In the second half, cationic polymerisation is introduced encompassing both main-group and transition-metal initiated polymerisations. The limitations of cationic ethylene polymerisation are highlighted.

Chapter Two describes the synthesis of a series of related complexes based on the Pn*MCp^{R}(X) motif for application as ethylene polymerisation catalysts. The products are characterised by NMR spectroscopy, single crystal X-ray diffraction, elemental analysis and, where relevant, EPR spectroscopy.

Chapter Three details the application of aforementioned Pn*MCp^{R}(X) complexes as ethylene polymerisation catalysts, tested in solution co-catalysed by methylaluminoxane, and in the slurry phase, immobilised on a variety of inorganic supports. Very high activities are observed for the zirconium congeners of this non-classic polymerisation motif, with the Cp ligand observed to affect activity more dramatically than the "X" ligand.

Chapter Four gives an account of mechanistic investigations examining the activity of the Pn*MCp^{R}(X) catalysts. Pre-catalyst activation studies implicate the formation of cationic derivatives, which are rationally synthesised. The unexpected activity of [Pn*ZrCp]$^{+}$ towards ethylene polymerisation is investigated by *in-situ* gas uptake measurements and small molecule activation studies, which do not readily accommodate a coordination-insertion mechanism. An alternative cationic initiation mechanism is proposed and explored.

Chapter Five describes the synthesis of titanium and zirconium hydride and deuteride complexes. Using either $LiAlH_4/D_4$ or H_2/D_2 as the hydrogen source, trimetallic hydride clusters are synthesised. Preliminary investigations into their reactivity with small molecules is presented.

Chapter Six details the synthesis of reduced permethylpentalene titanium complexes. Chlorine atom abstraction, scrambling of the Pn* ligand, and dinitrogen activation was observed depending on the nature of the reducing agent and the stoichiometry employed.

Chapter Seven provides experimental details and characterising data for the complexes presented in the preceding five chapters.

Acknowledgements

Firstly, I would like to thank Professor Dermot O'Hare for giving me the opportunity to pursue a D.Phil in his group. You've provided the freedom to explore new ideas, which has made the last year, in particular, hugely enjoyable. Thanks also for supporting my travel to conferences and SCG Chemicals – they have been fantastic experiences that I didn't think I would see during a D.Phil!

Secondly, thanks to JC, who has the unenviable task of hearing complaints in both ears from Oxford and Thailand alike! You've helped to create a warm and welcoming atmosphere in the group, and provided valuable advice, especially during Dermot's sabbatical. Of course, our trip to Thailand wouldn't have been possible if it wasn't for your hard work, so thanks for making such a highlight possible. I also owe a huge debt of gratitude to Zoë, not only for your crystallography skills, but also for the countless conversations and suggestions regarding the mechanism. Though I'm sure your patience was sometimes strained (sorry!), these discussions were a highlight!

I must also thank Dr. Nick Rees for the many solid-state NMRs, Zoë and Professor Jenny Green for running DFT calculations, Dr Will Myers for all his help with EPR, Sandy for introducing me to SQUID and electrochemistry, and for the adventure to attempt ReactIR, Golf and Jess for the awesome SEM images, Dana for guiding me through the GC-MS, Kate for running DSC/TGA, Norner AS for the collection of GPC data and SCG Chemicals for the large-scale catalyst testing.

I am hugely indebted to everyone who has proof-read this thesis: Chris, Sandy, Zoë and JC, your suggestions have been invaluable; it would have amounted to a time-consuming paperweight if it wasn't for your time and input! You'll be thanked with many of the Uni Club's finest, although maybe "finest" is a little generous for their stock. Still, beers all round!

Thanks to the many O'Hare group members who have made this such a great place to work. Yue; our trips to diamond were a filthy twix fest. Sorry I never made the FLP-MOF. Chris; for an ace trip to Aus. Because you haven't lived until you've nearly missed a flight. Tom R; if you managed the Pn* prep you can manage a child. Sandy, your Britney Spears will be infamous for years to come. Jess; we will never eat as well as we did this summer. Tom W; your height upsets me. Golf; I'm not sure I'll ever see such a clean fume-hood again. Kate; all those late night treats were a god-send. Maureen, Maureen, Maureen, Maureeen. And of course Katarina for you next-level baked goods – I'll make the long journey down the corridor when I smell them, I'm sure.

To friends of Farm Lane, and friends of the Megaron – you're the real deal. Whether depriving me of sleep, or letting loose in a field, it's all time well-spent with friends like these.

Finally, to Mum, Simon, Stuart, Ali, Nick, Caitlin and Stephane, I couldn’t wish for a more supporting, loving family around me. I could not have arrived to this point if it wasn’t for you all; I love you all so much. Simon’s ambiguous intentions notwithstanding, I look forward to many more wonderful years with you all.

Abbreviations List

°C	degrees Celcius
Å	Ångström, 10^{-10} m
ADF	Amsterdam Density Functional
acac	acetylacetonate, $CH_3COCHCOCH_3$
AMO-LDH	aqueous miscible organic solvent treated layered double hydroxide
^{n}Bu	*n*-butyl, $CH_2CH_2CH_2CH_3$
^{t}Bu	*tert*-butyl, CMe_3
ca.	*circa*, about
cent	centroid
χ	magnetic susceptibility
COD	cycloocta–1,4–diene
COSY	2D correlation spectroscopy
COT	cyclooctatetraene
Cp	cyclopentadienyl, $[C_5H_5]^-$
Cp*	pentamethylcyclopentadienyl $[C_5Me_5]^-$
CPMAS	cross polarisation magic angle spinning
CCDC	Cambridge crystallographic data centre
δ	chemical shift
$\Delta\nu_{1/2}$	peak width at half-height
d	doublet
DFT	density functional theory
DPMAS	direct polarisation magic angle spinning
DSC	differential scanning calorimetry
DtBP	2,6-di-tertbutylpyridine
η	hapticity
EPR	electron paramagnetic resonance
ESD	estimated standard deviation
Et	ethyl, CH_2CH_3
Et_2O	diethyl ether, $CH_3CH_2OCH_2CH_3$
FTIR	Fourier transform infrared
FVP	flash vacuum pyrolysis

GC-MS	gas chromatography mass spectrometry
GPC	gel permeation chromatography
h	hour
HDPE	high density polyethylene
HMBC	heteronuclear multiple bond correlation
HOMO	highest occupied molecular orbital
HSQC	heteronuclear single-quantum correlation spectroscopy
Hz	Hertz
$\{^1H\}$	proton decoupled
K	Kelvin
LDH	layered double hydroxide
LDH-MAO	methyaluminoxane impregnated layered double hydroxide
LUMO	lowest unoccupied molecular orbital
μ	bridging
m	multiplet
MAO	methylaluminoxane
Me	methyl, CH_3
MHz	megahertz
min	minutes
mmol	millimole
M_n	number-average molecular weight
MO	molecular orbital
M_w	weight-average molecular weight
μM	micromole
μ_{eff}	effective magnetic moment
μ_B	Bohr magneton
NMR	nuclear magnetic resonance
PDI	polydispersity index
PE	polyethylene
Ph	phenyl, C_6H_5
Pn	pentalene, C_8H_6
Pn†	1,4–bis(triisopropylsilyl)pentalene, 1,4–$C_8H_4(Si^iPr_3)_2$
Pn*	permethylpentalene, C_8Me_6

ppm	parts per million
^{i}Pr	*iso*-propyl, $CHMe_2$
Py	pyridine
q	quartet
quint	quintet
s	singlet, seconds
SEM	scanning electron microscopy
sMAO	polymethylaluminoxane
SOC	spin-orbit coupling
SOMO	singularly occupied molecular orbital
SSMAO	silica-supported methylaluminoxane
ssNMR	solid-state nuclear magnetic resonance
SQUID	superconducting quantum interference device
T	temperature
T_m	melting temperature
t	triplet, time
TEA	triethylaluminium
THF	tetrahydrofuran
TiBA	triisobutylaluminium
TMA	trimethylaluminium
TMEDA	*N,N,N',N'*-tetramethyl-ethane-1,2-diamine
vs.	*versus*
XRD	X-ray diffraction

Contents

Chapter 1: Introduction 1

1.1 Outline 1

1.2 Nomenclature 1

1.3 Synthesis of pentalene 2

1.4 Coordination chemistry of pentalene 4

1.5 Bonding in η^8–Pn* complexes 7

1.6 Small-molecule activation and catalysis with pentalene complexes 8

1.7 Ethylene polymerisation mechanism 13

1.8 Cationic polymerisation 15

1.9 Transition-metal catalysed cationic polymerisation 19

1.10 Cycloproponium Cations 21

1.11 Cationic ethylene polymerisation 25

1.12 Scope of Thesis 26

1.13 References 26

Chapter 2: Synthesis and Characterisation of Pn*MCp^R(X) Complexes 34

2.1 Introduction 34

2.2 Synthesis of Pn*MCp^R(Cl) (M = Ti, Zr) 34

2.3 Solid state structural analysis 36

2.4 NMR spectroscopic characterisation 41

2.5 Density Function Theory calculations 42

2.6 Synthesis and characterisation of Pn*MCp^R(Me) (M = Ti, Zr) 43

2.7 Synthesis and characterisation of Pn*MCp(H) (M = Ti, Zr) 44

2.8 Synthesis and characterisation of Pn*MCp(R) (M = Ti, Zr, R = Et, ^{n}Bu) 46

2.9 Synthesis and characterisation of Pn*ZrCp(CH_2Ph) 48

2.10 Synthesis and characterisation of Pn*MCp(C_3H_5) (M = Ti, Zr) 49

2.11 Spectroscopic studies of Pn*MCp(C_3H_5) 50

2.12 Solid state structural analysis of Pn*MCp(X) complexes 58

2.13 Conclusion 60

2.14 References 60

Chapter 3: Ethylene Polymerisation with Pn*MCp^R(X) Catalysts 63

3.1 Introduction 63

3.2 Solution phase ethylene polymerisation studies 64
3.3 Synthesis and characterisation of solid-supported zirconium complexes, and preliminary slurry-phase ethylene polymerisation studies 66
3.4 Pre-catalyst screening of polymethylaluminoxane complexes 70
3.5 Slurry-phase ethylene polymerisation studies with polymethylaluminoxane supported zirconium pre-catalysts 73
3.6 Polymer Characterisation 81
3.7 High-throughput catalyst testing with polymethylaluminoxane supported zirconium complexes 84
3.8 Large-scale polymerisation of polymethylaluminoxane-supported zirconium catalysts. 89
3.9 References 94
Chapter 4: Mechanism of Ethylene Polymerisation with Pn*MCp^{R}(X) Complexes ..97
4.1 Introduction 97
4.2 Ethylene polymerisation with permethylpentalene zirconium complexes 98
4.3 Identifying the products of activation 99
4.4 Attempted synthesis of cationic complexes by halide abstraction 103
4.5 Synthesis of cationic complexes by hydride/alkyl abstraction 107
4.6 Probing the mechanism of polymerisation 112
4.7 Synthesis and characterisation of Pn*(H)ZrCpCl$_2$ 120
4.8 Cationic initiation by [Pn*ZrCp]$^+$ 124
4.10 Reactivity with 2-butyne 129
4.11 Attempted synthesis of stable metal-carbocation complexes 134
4.12 Catalytic cationic initiation 136
4.13 Chain-transfer to aluminium: reactivity of Pn*MCp(Me) and AlMe$_3$ 137
4.14 Reactivity of Pn*ZrCp(R) (R = Et, ^{n}Bu) and AlMe$_3$ 138
4.15 Conclusions 145
4.16 References 146
Chapter 5: Synthesis of Metal-Hydride Complexes 151
5.1 Introduction 151
5.2 Synthesis of Pn*$_2$Ti$_2$(μ_2–H)$_5$Li.THF$_x$ 151
5.3 Reactivity of Pn*$_2$Ti$_2$(μ_2–H)$_5$Li.THF$_x$ 156
5.4 Synthesis of Pn*$_2$Zr$_2$(μ_2–H)$_5$Li.THF$_x$ 159

5.5 Comparison of solid-state structures, $Pn^*_2Ti_2(\mu_2–H)_5Li.THF_2$ and $[Pn^*_2Zr_2(\mu_2–H)_4(\mu_3–H)Li.THF]_2$ 163
5.6 Synthesis and characterisation of $Pn^*_3Ti_3(\mu_2–H)_3(\mu_3–H)$ 165
5.7 Reactivity of $Pn^*_3Ti_3(\mu_2–H)_3(\mu_3–H)$ 169
5.8 Density Functional Theory analysis of $Pn^*_3Ti_3(\mu_2–H)_3(\mu_3–H)$ 174
5.9 Attempted synthesis of titanium hydrides *via* β–hydride elimination 176
5.10 Conclusion 180
5.11 References 182
Chapter 6: Synthesis of Reduced Titanium Permethylpentalene Complexes 185
6.1 Introduction 185
6.2 Synthesis and Characterisation of $(Pn^*Ti)_2(\mu–Cl)_3$ 186
6.3 Synthesis and characterisation of $(\eta^8–Pn^*)Ti(\mu–\eta^5;\eta^5–Pn^*)Ti(\eta^8–Pn^*)$ 189
6.4 Synthesis and Characterisation of $Pn^*Ti(\mu–N_2)TiPn^*.MgCl_2.3THF$ 195
6.5 Synthesis of $Pn^*_2Ti_2HK.THF$ 200
6.6 Conclusions 201
6.7 References 201
Chapter 7: Experimental 204
7.1 General Methods 204
7.2 Experimental Details for Chapter 2. 206
7.2.1 $Pn^*TiCp^{Me}(Cl)$ 206
7.2.2 $Pn^*TiCp^{tBu}(Cl)$ 206
7.2.3 Pn*TiInd(Cl) 207
7.2.4 $Pn^*ZrCp^{Me}(Cl)$ 207
7.2.5 $Pn^*ZrCp^{tBu}(Cl)$ 208
7.2.6 $Pn^*ZrCp^{nBu}(Cl)$ 209
7.2.7 $Pn^*ZrCp^{1,2,3–Me}(Cl)$ 209
7.2.8 Pn*ZrInd(Cl) 210
7.2.9 Pn*TiCp(Me) 210
7.2.10 Pn*ZrCp(Me) 211
7.2.11 $Pn^*ZrCp^{Me}(Me)$ 211
7.2.12 Pn*TiCp(H) 212
7.2.13 Pn*ZrCp(H) 213
7.2.14 Pn*ZrCp(Et) 213

7.2.15 Pn*ZrCp(^{n}Bu) 214
7.2.16 Pn*ZrCp(CH_2Ph) 214
7.2.17 Pn*TiCp(C_3H_5) 215
7.2.18 Pn*ZrCp(C_3H_5) 216
7.2.19 Pn*TiCp 217
7.3 Experimental Details for Chapter 3 218
7.3.1 General procedure for immobilising catalysts on solid support. 218
7.3.2 General procedure for solution-phase polymerisation of ethylene. 218
7.3.3 General procedure for slurry-phase polymerisation of ethylene. 218
7.3.4 ZrPn*Cp$(Cl)_{sMAO}$ 218
7.3.6 ZrPn*Cp$^{Me}(Cl)_{sMAO}$ 219
7.3.7 ZrPn*Cp$^{tBu}(Cl)_{sMAO}$ 219
7.3.8 ZrPn*Cp$^{nBu}(Cl)_{sMAO}$ 219
7.3.9 ZrPn*Cp$^{1,2,3\text{-}Me3}(Cl)_{sMAO}$ 219
7.3.10 ZrPn*Ind$(Cl)_{sMAO}$ 219
7.3.11 ZrPn*Cp$^{Me}(Me)_{sMAO}$ 220
7.3.12 ZrPn*Cp$(Me)_{sMAO}$ 220
7.3.13 ZrPn*Cp$(C_3H_5)_{sMAO}$ 220
7.3.14 ZrPn*Cp$(^{n}Bu)_{sMAO}$ 220
7.4 Experimental Details for Chapter 4 221
7.4.1 Pn*TiCp(μ−Cl)$AlMe_3$ 221
7.4.2 Pn*ZrCp(μ−Cl)$AlMe_3$ 221
7.4.3 $[(Pn*TiCp)_2(\mu–Cl)][(B(3,5–C_6H_3(CF_3)_2)_4]$ 222
7.4.4 $[Pn*TiCp][(B(3,5–C_6H_3(CF_3)_2)_4]$ 222
7.4.5 $[Pn*ZrCp][(B(3,5–C_6H_3(CF_3)_2)_4]$ 223
7.4.6 $[Pn*ZrCp][(B(C_6F_5)_4]$ 223
7.4.7 $[(PnZrCp)_2(\mu–Cl)][B(C_6F_5)_4]$ 224
7.4.8 $[Pn*ZrCp(Py)][(B(3,5–C_6H_3(CF_3)_2)_4]$ 224
7.4.9 $[(PnZrCp)_2(\mu–Me)][B(3,5–C_6H_3(CF_3)_2)_4]$ 225
7.4.10 $[Pn*ZrCp(CO)][(B(3,5–C_6H_3(CF_3)_2)_4]$ 226
7.4.11 Pn*(H)$ZrCpCl_2$ 226
7.4.12 Pn*ZrCp$(OC(CF_3)_3)$ 227
7.4.13 $ClMg[(CH_2)_3CHPh_2]$ 227

7.4.14 Pn*ZrCp[$(CH_2)_3CHPh_2$] 228
7.4.15 Pn*ZrCp(μ–Me)$AlMe_2$R (R = Et, ^{n}Bu) 228
7.4.16 Pn*ZrCp(μ–Me)$AlMe_2$Et 229
7.4.17 Pn*ZrCp(μ–Me)$AlMe_2{}^n$Bu 229
7.4.18 Pn*(H)ZrCpCl_2 dry mixture sMAO 229
7.4.19 Pn*(H)ZrCp$Cl_{2\ sMAO}$ 230
7.4.20 Reactivity of [Pn*ZrCp][$B(C_6F_5)_4$] and 2-butyne 230
7.4.21 Pn*Ti(C_4H_8) 231
7.4.22 Hydrolysis of polymerisation mixture with H_2O and isolation of cyclopentadiene 232
7.4.23 Carbocation Tagging with $(CF_3)_3OH$ 233
7.5 Experimental Details for Chapter 5 234
7.5.1 Pn*$_2$Ti$_2$(μ$_2$–H)$_5$Li.THF$_x$ 234
7.5.2 Pn*$_2$Ti$_2$(μ$_2$–D)$_5$Li.THF$_x$ 235
7.5.3 [Pn*$_2$Zr$_2$(μ$_2$–H)$_4$(μ$_3$–H)Li.THF$_x$]$_2$ 235
7.5.4 [Pn*$_2$Zr$_2$(μ$_2$–D)$_4$(μ$_3$–D)Li.THF$_x$]$_2$ 236
7.5.5 Pn*$_3$Ti$_3$(μ$_2$–H)$_3$(μ$_3$–H) 237
7.5.6 Pn*$_3$Ti$_3$(μ$_2$–D)$_3$(μ$_3$–D) 237
7.5.7 Reactivity of Pn*$_2$Ti$_2$(μ$_2$–H)$_5$Li.THF$_x$ and CO_2 238
7.6 Experimental Details for Chapter 6 239
7.6.1 (Pn*Ti)$_2$(μ–Cl$_3$) 239
7.6.2 (η^8–Pn*)Ti(μ–η^5;η^5–Pn*)Ti(η^8–Pn*) 239
7.6.3 Pn*Ti(μ–N$_2$)TiPn*.MgCl$_2$.THF$_3$ 239
7.6.4 Pn*$_2$Ti$_2$HK.THF 240
Appendix A 241

Chapter 1: Introduction

1.1 Outline

The pentalene molecule has been a source of chemical intrigue for nearly a century: its once ambiguous structure is now known and synthetic strategies developed to overcome its inherent instabilities have cleared a path to its modern applications in molecular electronics and coordination chemistry. The history of pentalene and its rich organometallic chemistry has previously been reviewed in detail elsewhere.[1–4] This chapter therefore provides a brief introduction to the ligand: its nomenclature, synthesis and coordination chemistry is discussed with a primary focus on the η^8–coordination mode. Finally, ethylene polymerisation and other small molecule activations are considered, with a particular emphasis on cationic polymerisation.

1.2 Nomenclature

In this thesis, "Pentalene" may be used to refer to pentalenic derivatives, neutral and charged, encompassing dihydropentalene [C_8H_8], pentalene [C_8H_6] and the pentadienyl anion [C_8H_6]$^{2-}$. The numbering system for the carbocyclic framework is shown in Figure 1.1, which can be further divided into non-wingtip (1,3,5,7) and wingtip positions (2,6).

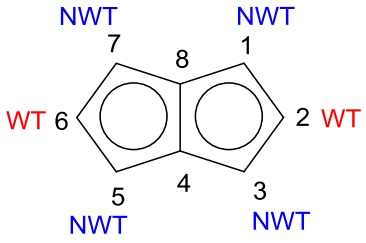


Figure 1.1. *Illustration of pentalene numbering system and nomenclature. WT = wingtip, NWT = non-wingtip.*

In the discussions of carbocations the nomenclature of Olah is adopted.[5,6] The suffix -enium denotes a classical, three-coordinate carbocation, while -onium describes non-classical species of higher valency. For example $C_2H_5^+$ is described as ethonium, while *iso*-$C_3H_7^+$ is propenium; carbocation is a generic term encompassing both non-classical and classical formulations (Figure 1.2).

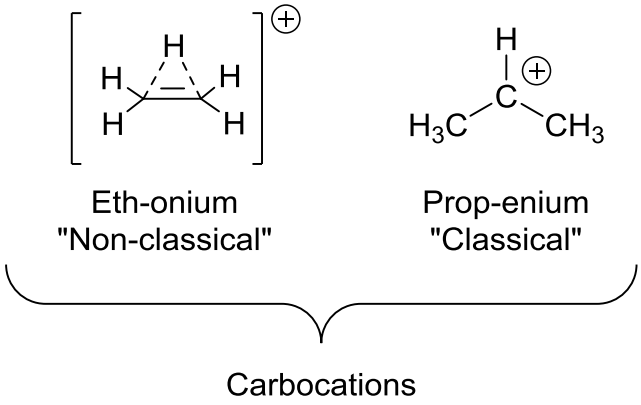
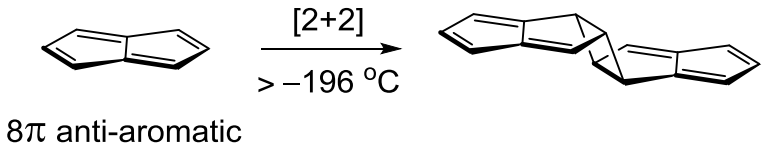


Figure 1.2. *Classical and non-classical carbocation nomenclature.*[5,6]

1.3 Synthesis of pentalene

The neutral pentalene molecule, C_8H_6, is the lower homologue of naphthalene and heptalene,[7,8] containing 8π-electrons which form a bond-alternant C_{2h} structure.[9–11] However, as would be expected for a planar 8π-electron system, it displays anti-aromatic character and rapidly dimerises above −196 °C *via* [2+2] cycloaddition to form the pentalene dimer, $[C_8H_6]_2$ (Scheme 1.1). [12–15]

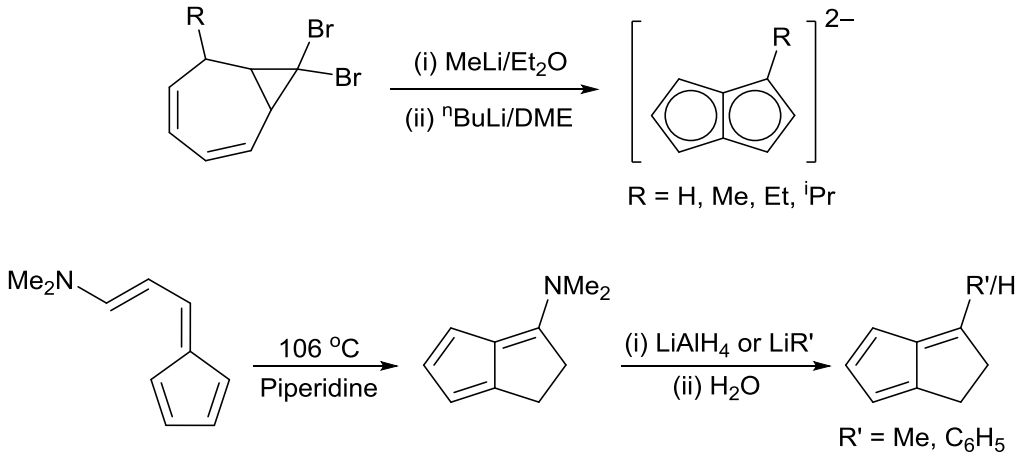


Scheme 1.1. *Pentalene dimerisation*[14,15]

Cyclooctatetraene (C_8H_8, COT) is isoelectronic to pentalene, but does not display the same thermal instability; in the absence of a transannular bond distortion to a tub-shaped conformation alleviates anti-aromaticity.[16,17] The organometallic chemistry of COT is easily accessed by alkali metal reduction of the neutral precursor, which forms a 10π-electron planar aromatic dianion, $[COT]^{2-}$. However, the instability of neutral pentalene with respect to dimerisation prevents access to aromatic $[Pn]^{2-}$ synthons by this route.

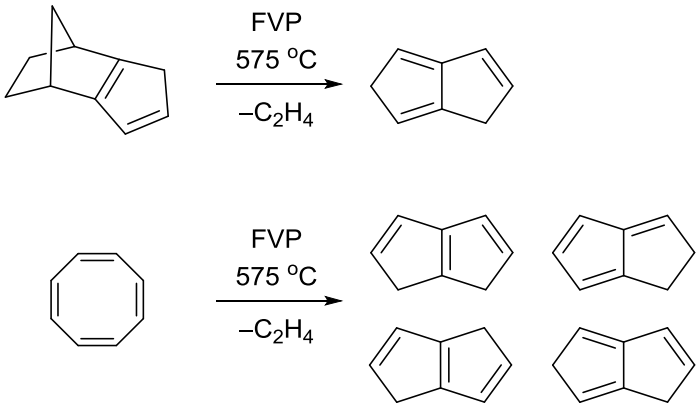
Instead, synthetic strategies for the isolation of dianionic pentalene derivatives generally target dihydropentalenes, which can be twice deprotonated to form $[Pn]^{2-}$. Skattebøl rearrangement of germinal dibromocyclopropane substituted cycloheptatrienes allows for

the synthesis of unsubstituted and mono-alkylated dihydropentalenes,[18,19] while intramolecular cyclisation of 6–(2–aminovinyl)fulvenes provides a second versatile route to synthesise dihydropentalenes by wet chemical methods (Scheme 1.2).[20,21]



Scheme 1.2. *Summary of wet chemical approaches to dihydropentalene synthesis.*[18–21]

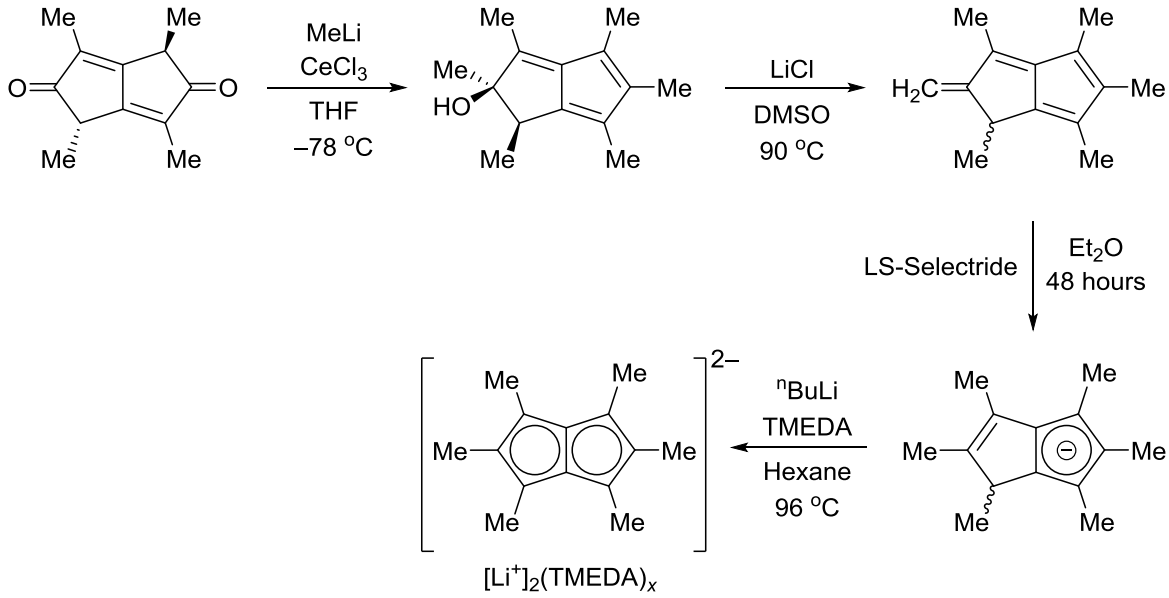
Alternatively, flash vacuum pyrolysis (FVP) of iso-dicyclopentadiene or COT allows for the isolation of dihydropentalenes in up to 90% yield on a 25 g scale (Scheme 1.3).[22–24] Following deprotonation, selective functionalisation of the pentalene framework with tri-alkylsilyl substituents in the 1,5– positions has been found to alleviate issues with solubility and diastereomer formation commonly encountered with Pn and $Pn^{1–R}$ derivatives respectively.[24,25]



Scheme 1.3. *Pyrolytic routes to dihydropentalene synthesis.*[22–24]

More recently, the solution-phase synthesis of permethylpentalene $[Pn^*]^{2–}$ was described by Ashley *et al.* (Scheme 1.4), which does not proceed *via* a dihydropentalene

intermediate. Instead, methylation-dehydration of the bicyclic bis(enone) shown in Scheme 1.4 allows for the synthesis of an exocyclic isomer of the neutral 8π-electron permethylpentalene molecule. Subsequent reduction can be realised by conjugate addition of H^- at the exocyclic double bond, which following deprotonation allows for the synthesis of Li_2[Pn*] on a 15 g scale.[3,26,27]



Scheme 1.4. *Synthesis of Li_2[Pn*] from trans-2,4,6,8-tetramethylbicyclo[3.3.0]octa-1,5-diene-3,7-dione.*[26,27]

1.4 Coordination chemistry of pentalene

The pentalene ligand displays rich coordination chemistry, with some commonly encountered bonding modes highlighted in Figure 1.3.[2,28]

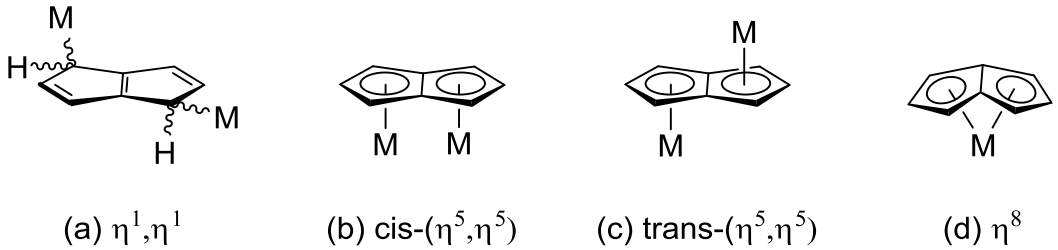


Figure 1.3. *Key bonding modes of pentalene*[2,2829]

The η^1–coordination mode is typically observed with p-block elements such as [1,5–Pn*($SnMe_3$)$_2$], which is employed as a "soft" source of $[Pn^*]^{2-}$ in the synthesis of

$[Pn^*TiCl(\mu\text{–}Cl)]_2$.[30] Using the covalent bonding classification, developed by Green, Green and Parkin the ligand can be described as an X donor to each heteroatom.[29,31]

Bound η^5, the pentalene ligand acts as an L_2X donor to each transition metal, which can be rationalised by considering the resonance structures shown in Figure 1.4.[29] The bridgehead double bond behaves as a (μ–L) ligand to each metal centre, with the anionic charges localised in allyl fragments at the ligand wingtips. Usually observed for mid-transition metals, both *cis*- and *trans*- conformations are known, although *trans*- complexes are more numerous in the literature.

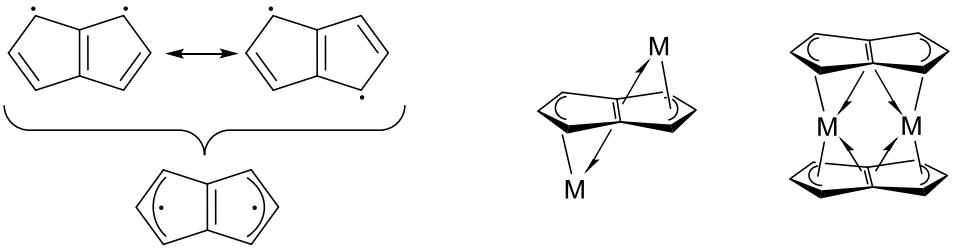


Figure 1.4. *Left: illustration of bis(allyl) resonance form of pentalene. Middle, right: pentalene as an $(L_2X)_2$ donor in trans- and cis- geometries.*[29,31]

Obtaining *cis*- geometries generally requires reaction with pre-organised multi-metallic fragments, as in the synthesis of *cis*-$[Cp_2V]_2Pn$ from $[CpVCl(THF)]_n$ and $[Li(DME)]_2Pn$.[25,32] As an extension of this, a number of "double-sandwich" compounds, $(Pn)_2M_2$, have been reported by salt-metathesis with metal derivatives already containing a metal-metal bonding interaction in appropriate stoichiometry with a source of $[Pn]^{2-}$.[33–36] Cloke *et al*. reported the synthesis of the hetero-bimetallic double-sandwich complex, $(\mu{:}\eta^5,\eta^5\text{–}Pn^\dagger)_2MoW$ ($Pn^\dagger$ = $[1,5\text{–}C_8H_4(Si^iPr_3)_2]^{2-}$), from the pre-organised bimetallic carboxylate, $MoW(^tBuCO_2)_4$ and two equivalents of $[K_2]Pn^\dagger$.[37]

Generally, in the presence of early transition or rare earths metals, the pentalene ligand will bend around the C–C bridgehead to allow all eight carbon atoms to bond with the metal centre acting as an L_3X_2 donor.[29,38–41] This is two fewer electrons than an equivalent bis(Cp) complex, which along with subtle changes to their frontier orbitals (*vide infra)*, leads η^8 complexes to display a surprising divergence in their reactivity when compared with Cp_2M analogues.

Folding of the pentalene ligand disrupts aromaticity, which is compensated for by the formation strong poly-haptic bonds. The deviation from planarity can therefore be a useful metric to gain insight into the steric and electronic environment of the metal complex, and is referred to as the "fold angle" (FA, Figure 1.5).

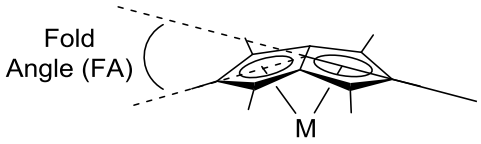


Figure 1.5. *Fold angle as defined for η^8-Pn complexes*

To a first approximation the fold angle decreases with increasing size of the metal. For example, Jonas *et al.* observed a decrease in the fold angle from V(III) to Ti(III) in PnMCp (M = V, Ti) from 43.0° to 37.0°,[42,43] which correlates with the contraction of ionic radii (0.670 *vs* 0.640 Å for 6-coordination M(III) ions).[44] In the series Pn*MCp(Cl) (M = Ti, Zr, Hf) reported by Chadwick *et al.*, the fold angle decreases from titanium to zirconium (31.0° to 30.7°), however, the hafnium complex demonstrated a fold angle of 30.9°.[45] This was suggested to result from improved metal-pentalene orbital overlap resulting from radial expansion of the 5d orbitals.

Beyond the effect of the metal, the electronic demands of the ligand set can impact the fold angle. A series of tantalum methyl complexes, $Pn^{\dagger}TaCl_xMe_{3-x}$ were reported by Cloke *et al.* to display a small increase in fold angle with increasing values of *x* in response to the presence of electron-withdrawing chloride ligands.[46] Similarly, substitution of the pentalene ring can have dramatic effects on the fold angle, which can be illustrated by considering the complexes PnZrCp(Cl) and Pn*ZrCp(Cl), which display fold angles of 33.0° and 30.7° respectively.[42,45] This is likely steric and electronic in origin; improved donor characteristics of Pn* may reduce electron deficiency at the metal centre, while the greater spatial requirements of the permethylated ancillary ligand would also encourage flattening of the Pn* rings.

1.5 Bonding in η^8–Pn* complexes

The frontier molecular orbitals of η^8–Pn* metal complexes qualitatively resemble those of a Cp_2M fragment (Figure 1.6).[47–50] Both possess C_{2v} symmetry, which gives rise to similar a_1 symmetric orbitals, while a b_2 symmetric orbital projects two lobes of opposite phase into the bonding cavity of both organometallic fragments. However, for η^8–Pn*M an additional, orthogonal orbital of b_1 symmetry is present, which manifests in a tendency to avoid co-planar ligand coordination as observed for Cp_2MX_3 complexes, in favour of trigonal or pyramidal geometries.[28]

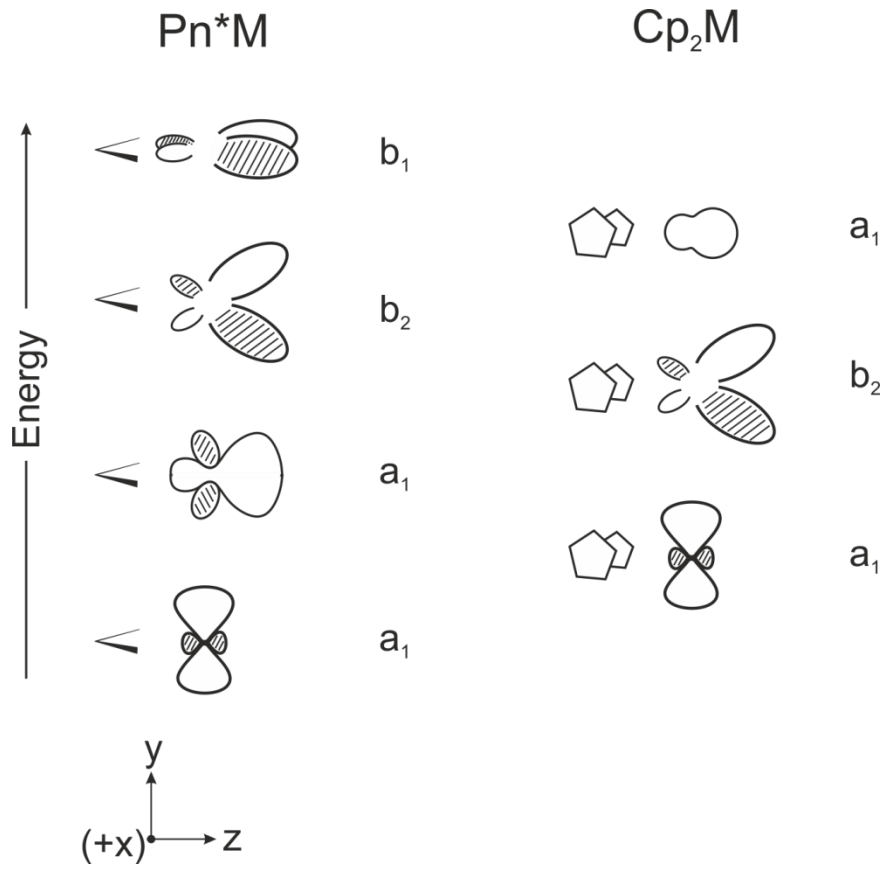


Figure 1.6. *Simplified illustration of frontier molecular orbitals for left: η^8-Pn*M, right: Cp_2M.*[28,48–51]

For example, $[Cp_2MoH_3]^+$ contains three hydride ligands arranged in a co-planar fashion,[52,53] while $Pn^{\dagger}TaMe_3$[46] and $PnZrCl_2(THF)_2$[42] form trigonal pyramidal and square pyramidal geometries respectively, with the metal at the pyramid apex (Figure 1.7).

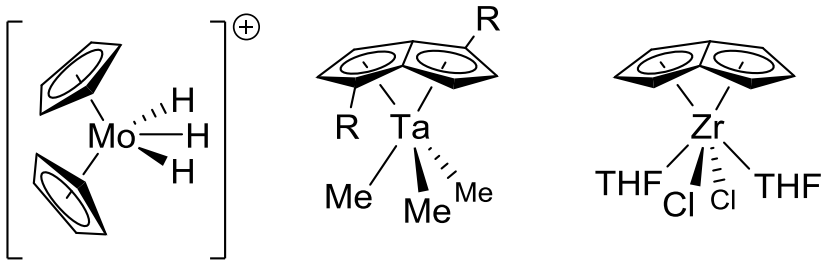


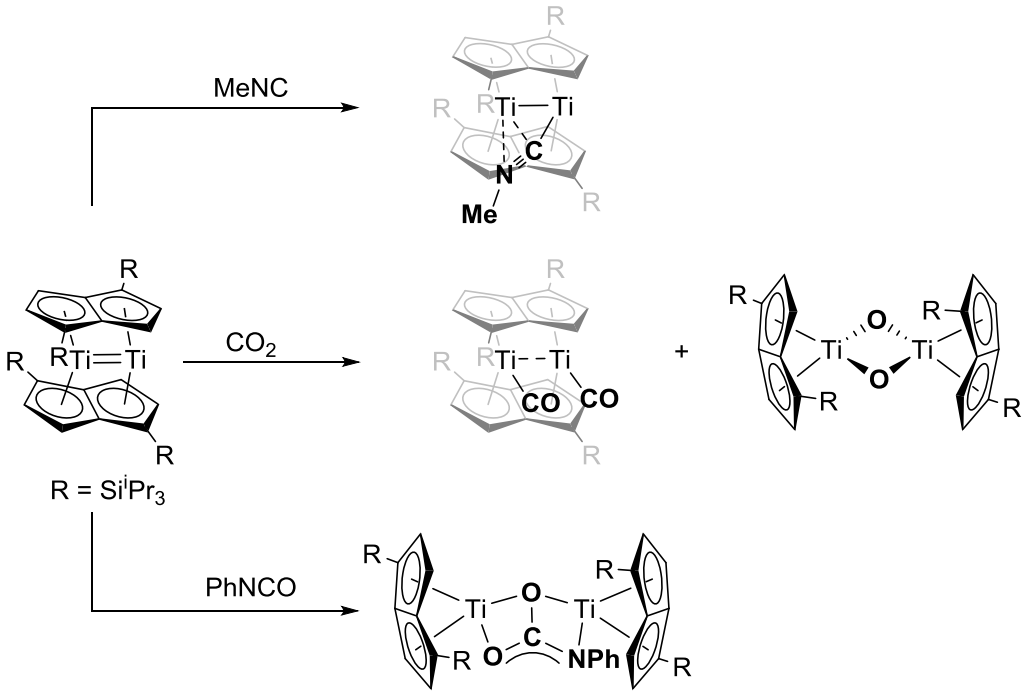
Figure 1.7. *Left: co-planar ligand coordination of Cp_2MX_3 complexes. Middle: Trigonal ligand coordination of $Pn^{\dagger}TaMe_3$. Right: Pyramidal ligand coordination of $PnZrCl_2.THF_2$.*[42,46,52,53]

This orthogonal displacement of the frontier molecular orbitals, alongside the relative electron deficiency of the pentalene ligand, means complexes tend to favour dimerisation. While Cp_2TiCl_2 is a monomeric 16 valence electron complex,[54] the Pn* analogue forms $[Pn^*TiCl(\mu–Cl)]_2$ where a 16 valence electron count is achieved by dimerisation with a trigonal disposition of co-ligands around the titanium centres.[30]

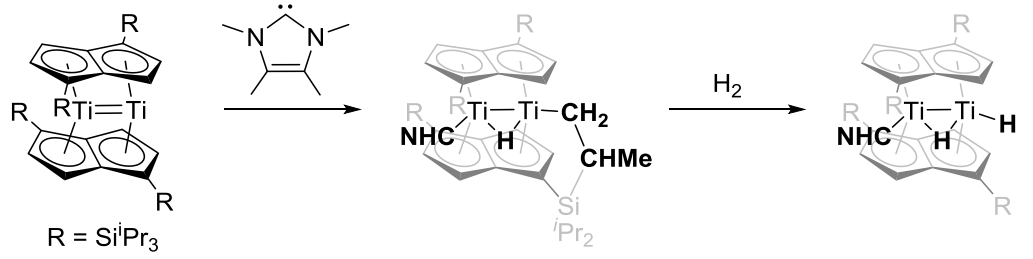
1.6 Small-molecule activation and catalysis with pentalene complexes

Kilpatrick *et al*. described an extended study on the bonding[55,56] and reactivity[57] of $Pn^{\dagger}{}_2Ti_2$ with a range of small molecules. With CO_2, reductive activation to form the dicarbonyl complex, $Pn^{\dagger}{}_2Ti_2(CO)_2$ was reported, alongside formation of the oxo-bridged dimer, $[\eta^8–Pn^{\dagger}Ti(\mu–O)]_2$.[58,59] Methyl isocyanide and 1,3–*N,N′*–di–*p*–tolylcarbodiimide formed thermally stable adducts, while phenyl isocyanates ruptured the double sandwich architecture to form an unusual phenyl-carbonimidate bridged complex, $[(\eta^8–Pn^{\dagger})Ti]_2(\mu,\kappa^2:\kappa^2–O_2CNPh)$ (Scheme 1.5).[60]

The remarkable reactivity of this system was further illustrated in recent reports by Tsoureas *et al*., of the first pentalene tuck-in complex, formed by addition of the N-heterocyclic carbene 1,3,4,5-tetramethylimidazol-2-ylidene to $(\mu{:}\eta^5,\eta^5–Pn^{\dagger})_2Ti_2$ (Scheme 1.6).[61] C–H activation of a ligand-bound tri-isopropylsilyl group installs a bridging hydride ligand across the titanium centres while forming a new Ti–C bond. Addition of H_2 leads to cleavage of the Ti–C bond although isotopic labelling experiments indicate this does not occur by σ-bond metathesis with H_2/D_2.

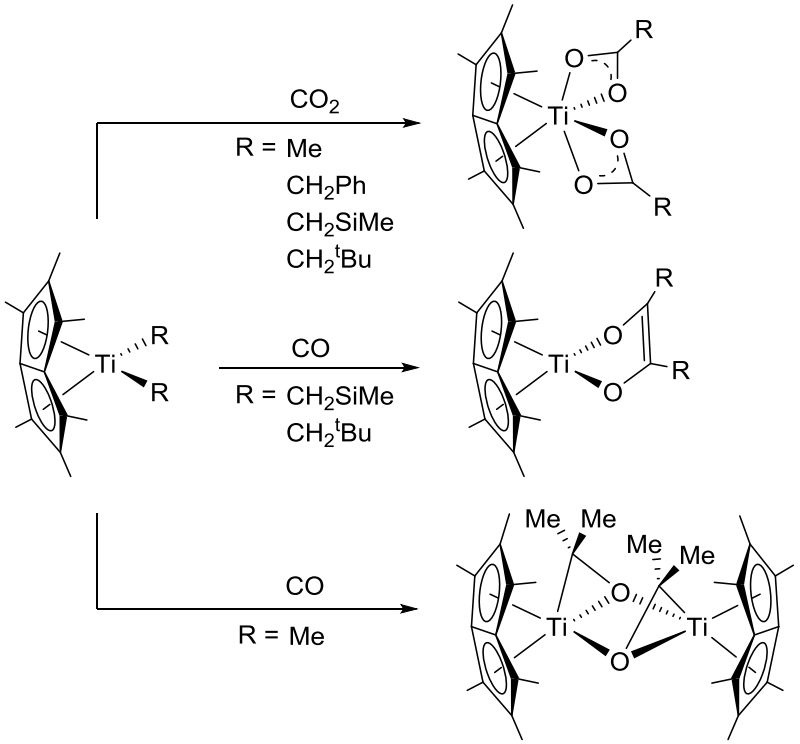


Scheme 1.5. *Reactivity of (μ:η^5,η^5–Pn†)$_2$Ti$_2$ with MeNC, CO$_2$ and PhNCO.*[58–60]



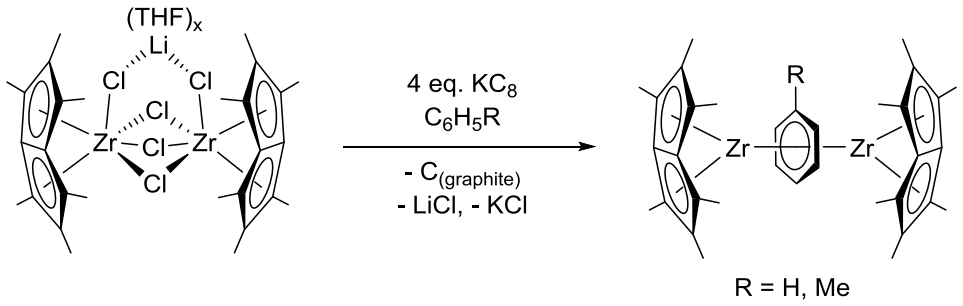
Scheme 1.6. *Reactivity of (μ:η^5,η^5–Pn†)$_2$Ti$_2$ with 1,3,4,5-tetramethylimidazol-2-ylidene.*[61]

In 2015, Cooper *et al*. reported the double insertion of CO_2 into the Ti–C bonds of Pn*TiR_2 (R = Me, CH_2Ph) to form Pn*Ti(κ^2–$O_2CR)_2$, which contrasts with the observed reactivity of Cp_2TiMe_2, where only a single CO_2 molecule is incorporated.[62] Insertion was also reported with CO, although the product of the reaction was found to be sensitive to the steric demands of alkyl ligand. With Pn*$TiMe_2$ formation of an unusual titanoxirane, [Pn*Ti(μ–η^1(O):η^2–OC(Me)$_2$)]$_2$, was observed while with Pn*TiR_2 (R = CH_2SiMe_3, $CH_2{}^tBu$) reductive coupling of two molecules of CO formed an ene-diolate complex, Pn*Ti(κ^2–O–C(R)=C(R)–O) (Scheme 1.7).[4]



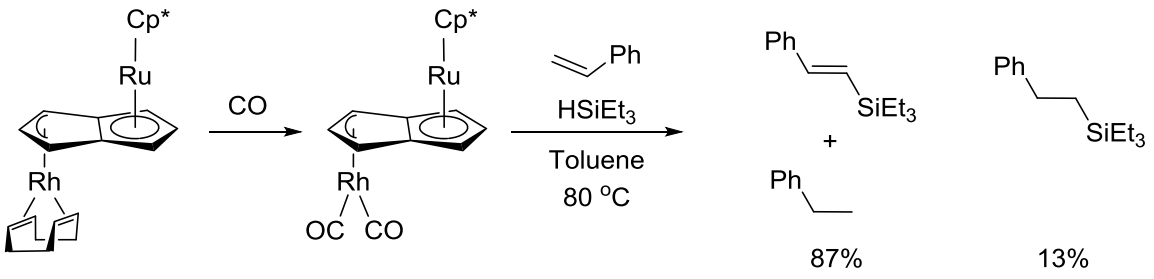
Scheme 1.7. *Reactivity of Pn*TiR$_2$ with CO$_2$ and CO.*[4,62]

There are fewer reports on small molecule reactivity with zirconium pentalene complexes. Reduction of the zirconium(IV) permethylpentalene chloride precursor, $[\eta^8$–Pn*Zr(μ–Cl)$_{3/2}]_2$(μ-Cl)$_2$Li·THF$_x$ with KC_8 leads to activation of aromatic solvents and the formation of triple-decker metallocenes (Scheme 1.8).[63] This reactivity was exemplified with the activation of benzene, toluene, cumene, *o*-xylene and *m*-xylene. However, it is interesting to note the divergent reactivity of Cp*$_2$ZrCl$_2$ under reducing conditions, which activates N_2 to form the dimeric complex, [(Cp*$_2$ZrN$_2$)$_2$(μ–N$_2$)].[64,65] Indeed, there are no reports of transition metal pentalene derivatives activating dinitrogen to date. In 2002, the Cloke group reported the reversible activation of N_2 with the uranium(III) complex, (η^8–Pn†)UCp* to form the oxidised U(IV) product, $[(\eta^8$–Pn†)UCp*$]_2$(μ–η^2:η^2–N$_2$).[66] Elongation of the N–N distance to 1.232(10) Å (c.f. 1.098 Å for free N_2) alongside DFT calculations led the authors to propose two electron reduction of N_2.



Scheme 1.8. *Synthesis of Pn*Zr "triple-decker" arene complexes.*[63]

Catalytic applications of pentalene complexes are largely focussed on polymerisation chemistry. The sole exceptions to this are the reports of Burgos *et al*., in which the synthesis of a heterobimetallic pentalene complex, [Cp*Ru(μ:η^5,η^3–Pn)Rh(η^4–COD)] is described by deprotonation and of the (hydro)pentalene complex, Cp*Ru(η^5–Pn(H)).[67] The dicarbonyl derivative, [Cp*Ru(μ:η^5,η^3–Pn)Rh(CO)$_2$] was reported to be one of the most active catalysts for the dehydrogenative silylation of styrene, as illustrated in Scheme 1.9.[68]



Scheme 1.9. *Synthesis of [Cp*Ru(μ:η^5,η^3–Pn)Rh(CO)$_2$] and its dehydrogenative silylation of styrene.*[67,68]

(Hydro)permethylpentalene complexes of titanium, zirconium and hafnium have been reported as competent initiators for lactide polymerisation, with the zirconium complexes, [Pn*(H)Zr[*S*–OCH(CH$_3$)C$_6$H$_5$]$_3$ and [Pn*(H)Zr[*rac*–OCH(CH$_3$)C$_6$H$_5$]$_3$ found to display activities comparable to the fastest initiators in the literature while retaining low polydispersities (1.14 – 1.15).[69] Although it was envisaged that stereocontrol could be imparted by the chiral, η^5-coordinated Pn*(H) ligand, only atactic polymers were obtained, indicating the limited influence of the distal chiral centre on the active site of the catalyst.[69]

Inspired by the rich chemistry of group 4 ethylene polymerisation catalysis based on Cp$_2$MX$_2$ (M = Ti, Zr, Hf, X = halide, alkyl, benzyl etc.) a number of analogous pentalene

alkyl and halide complexes have been tested. Pn*TiR_2 (R = Me, CH_2Ph, CH_2SiMe_3 and $CH_2{}^tBu$) display poor to moderate activity as measured on the Gibson scale[70] with the highest activity reported for Pn*$Ti(CH_2SiMe_3)_2$ in combination with $[CPh_3][B(C_6F_5)_4]$ (21.8 $kg_{PE}/(mol{\cdot}h{\cdot}bar)$).[4] The same general trend is observed for zirconium and hafnium congeners activated with methylaluminoxane (MAO): Pn*MR_2 (R = C_3H_5, CH_2Ph), $[Pn*M(\mu\text{–}Cl)_{3/2}]_2(\mu\text{-}Cl)_2Li{\cdot}THF_x$ and Pn*$MPh(\mu\text{–}Ph)_2Li$(dioxane) (M = Zr, Hf), all demonstrate moderate activities of less than 100 $kg_{PE}/(mol{\cdot}h{\cdot}bar)$.[71] Reports in the patent literature describe ethylene polymerisation with $PnZrCl_2.THF_2$ and $PnZr(C_3H_5)_2$ activated with 400 to 1000 equivalents of MAO, producing activities of 44 and 319 $kg_{PE}/(mol{\cdot}h{\cdot}bar)$ respectively,[72] the latter over five times the activity Pn*$Zr(C_3H_5)$ with 1000 equivalents of MAO (56 $kg_{PE}/(mol{\cdot}h{\cdot}bar)$) albeit with different dilutions and solvent.[71] A general observation can be made in light of these data, that ethylene polymerisation catalysts approximated as Pn^RMX_2 often produce poor to moderate activities.

Pn, $Pn^\dagger$ and Pn* variants of a second motif, $Pn^RMCp^{R'}(X)$ have also been reported. These 18 electron complexes contain only a single leaving group, which contradict the *a priori* design requirements for ethylene polymerisation catalysts (*vide infra)*. Nonetheless polymerisation activities one to two orders of magnitude greater than Pn^RMX_2 complexes are routinely observed (Figure 1.8). Ethylene polymerisation activities of $Pn^\dagger ZrCp(Cl)$ and $Pn^\dagger ZrCp*(Cl)$ were reported as 1117 and 1216 $kg_{PE}/(mol{\cdot}h{\cdot}bar)$ at 10 bar ethylene pressure with 2000 equivalents MAO,[73] while activities of 708 $kg_{PE}/(mol{\cdot}h{\cdot}bar)$ were recorded for PnZrInd(Cl) (2 bar ethylene, 1000 eq. MAO).[72] Pn*ZrCp(Cl) and Pn*ZrCp(η^1–Cp) produced activities of 4176 and 4194 $kg_{PE}/(mol{\cdot}h{\cdot}bar)$ respectively at [Al]/[Zr] = 1000, which was further optimised for Pn*ZrCp(Cl) to produce activities of 6993 $kg_{PE}/(mol{\cdot}h{\cdot}bar)$ at shorter reaction times of 15 minutes.[45,71] Hafnium analogues produce lower activities of 1009 and 247 $kg_{PE}/(mol{\cdot}h{\cdot}bar)$ for Pn*HfCp(Cl) and Pn*HfCp(η^1–Cp) respectively, although higher molecular weights were observed.[45] These data are summarised in Figure 1.8. It is interesting to note reports of very high ethylene polymerisation activities for the isoelectronic COT derivative, COT″ZrCp(Cl) (COT″ = [1,4–$C_8H_6(SiMe_3)_2$]) , up to 2188 $kg_{PE}/(mol{\cdot}h{\cdot}bar)$ at [Al]/[Zr] = 6000 and 10 bar ethylene pressure.[74] The retention of very high activities across different ligand architectures, all of which disobey traditional catalyst design strategies alludes to a common mechanism of polymerisation/activation distinct from the single-site catalysts studied to date.

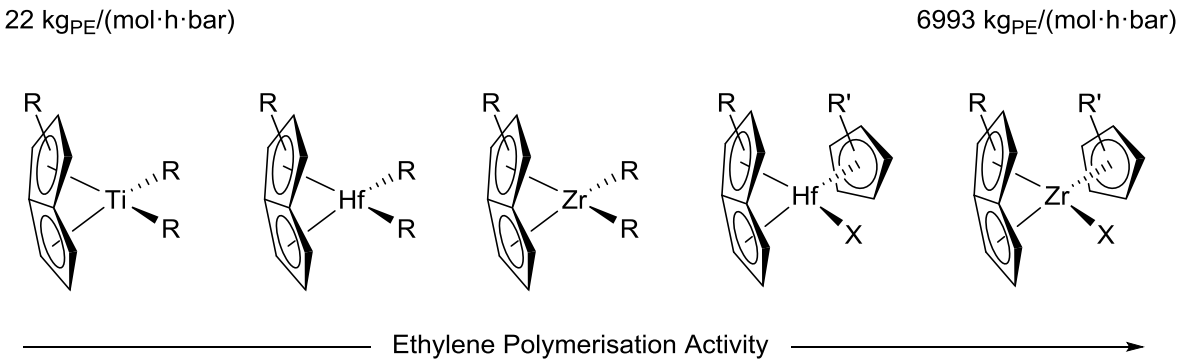


Figure 1.8. *Summary of ethylene polymerisation activity with pentalene complexes.*

1.7 Ethylene polymerisation mechanism

Transition-metal ethylene polymerisation catalysts have been demonstrated to function by a coordination-insertion mechanism, in which coordination of the monomer at a cationic, electrophilic metal centre is followed by migratory insertion into a metal-polymeryl bond (Figure 1.9).[75–78] Agostic interactions with the growing polymer chain have been proposed to stabilise the active catalyst and allow for control of polymer tacticity, which is of particular importance when polymerising higher α-olefins such as propene.[79–82] Pre-catalyst design strategies therefore require the inclusion of two viable leaving groups in order to accommodate both the polymeryl chain and a positive charge.

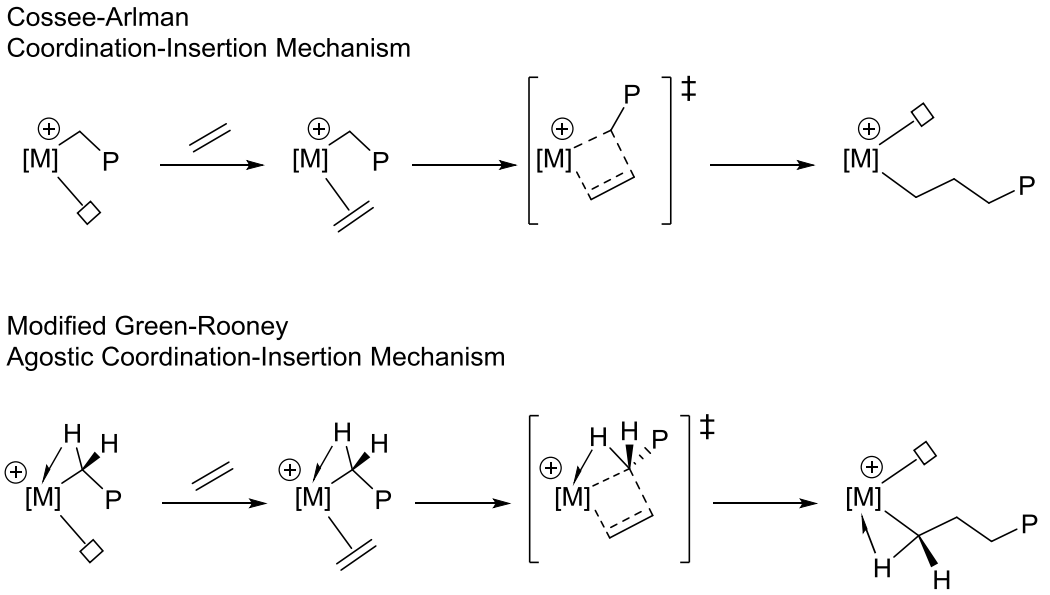


Figure 1.9. *α-olefin polymerisation mechanism with group 4 metal catalysts.*[76,77,79–81]

The pre-catalyst, typically employed as a metal-dihalide precursor requires activation to form the prerequisite cationic metal centre. One of the commonly employed co-catalysts is methylaluminoxane (MAO),[83–85] whose function is twofold: first to methylate the complex, then to abstract one of these methyl ligands to form a cationic complex.[86–89] The structure of MAO, formed by partial hydrolysis of $AlMe_3$,[83,90–92] is complex and ill-defined, usually approximated for simplicity as $[–Al(Me)O–]_n$. Studies on the structure of MAO indicate the formation of macromolecular aggregates, with cage-like motifs decorated at their exterior with $AlMe_X$ moieties (Figure 1.10).[93–96] Recent reports from researchers at Albermarle suggest the Lewis acidity of the co-catalyst arises in part from the ability of MAO to generate $[AlMe_2]^+$ fragments, which serve as potent electrophiles for halide/methide abstraction.[97–99]

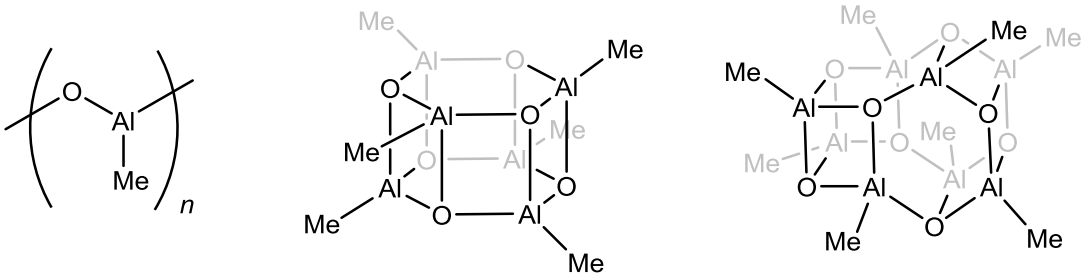


Figure 1.10. *Left: abbreviated structure of MAO. Middle, right: some proposed structures of MAO.*[84]

The practical application of MAO has limitations: these homogeneous polymerisations typically suffer from uncontrolled exothermic propagation, which leads to polymer aggregation, cessation of stirring, and a polymer product that can be challenging to process.[89,100] This can be overcome by immobilisation of the co-catalyst and pre-catalyst on an inorganic support, which serves to more effectively disperse the polymerisation exotherm, and provide a template for polymer growth.[89,100] One of the most widely studied support materials for these slurry-phase polymerisations is silica-supported MAO (ssMAO), in which covalent attachment of MAO occurs through Si–O–Al bond formation.[101–105] However, following pre-catalyst immobilisation large decreases in activity are typically observed relative to homogeneous MAO co-catalysed polymerisation,[106,107] which has stimulated efforts to find alternative, improved support materials. In principle, any material with surface hydroxyl functional groups is potentially a suitable candidate for catalyst immobilisation, and to that end layered double hydroxides

(LDHs) have more recently been investigated. LDHs have the general formula, $[M^{z+}_{1-x}M'^{y+}_{x}(OH)_2]^{a+}(A^{n-})_{a/n}\cdot bH_2O$, and form brucite-like layers of positively charged sheets braced by weakly-bound intercalated anions.[108] High surface area materials can be obtained by dispersion in aqueous-miscible organic (AMO) solvents, such as acetone, forming AMO-LDHs,[109,110] which following pre-treatment with MAO form superior inorganic supports for ethylene polymerisation catalysis than silica.[107,111,112] X-ray absorption spectroscopy data reported by Buffet *et al*., for LDH-MAO immobilised $EBIZrCl_2$ (EBI = *rac*-ethylenebis(1-indenyl)), indicated the expected formation of a cationic Zr–Me fragment either bound covalently, or closely approaching a surface aluminoxide environment, although the two bonding situations could not be adequately distinguished at the experimental resolution.[113]

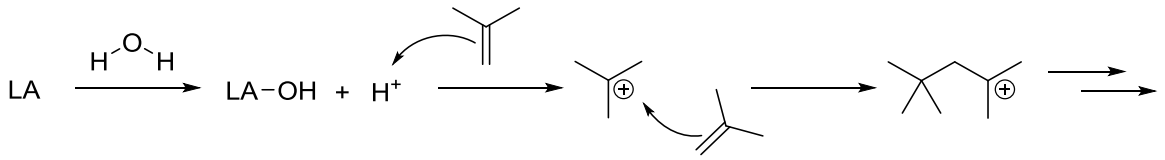
Alternatively, an insoluble form of MAO can be employed as a bifunctional material to both immobilise and activate the metal pre-catalyst. Polymethylaluminoxane (sMAO) can be formed by partial hydrolysis of $AlMe_3$ with benzoic acid to produce a proto-MAO, that following heat treatment oligomerises to form an insoluble support material.[114,115] Previous reports of sMAO-immobilised ethylene polymerisation catalysis suggest it to be one of the most active support materials known,[116] although its structure, like MAO, is poorly understood and ill-defined.[115] Pair-distribution function data suggests plausible formation of similar cage-like motifs as observed for MAO, although the limited resolution prevented definitive assignment of the structure.[115]

1.8 Cationic polymerisation

A number of other mechanisms are known for the polymerisation of ethylene beyond coordination-insertion. Radical initiation is employed industrially to produce branched polyethylene with wide molecular weight distributions.[117,118] While anionic initiation is also known with commercially available alkyl-lithium reagents, whose activities can be enhanced by inclusion of a tertiary amine base.[119,120] By contrast, cationic initiators for the polymerisation of ethylene to high molecular weight products are not known.

The mechanism of cationic initiation proceeds first with electrophilic activation of the olefin to produce a carbocation, which can then activate additional olefinic monomers to produce polymeric products. Traditional methods for cationic olefin polymerisation

employ a Lewis or Brønsted acid (e.g. $AlCl_3$, BF_3 or CF_3SO_3H) and an olefinic precursor such as isobutene (Scheme 1.10).[121–124] The active initiating species in both cases is H^+, which in the case of Lewis acids arises from the presence of trace H_2O or other exogenous proton sources; under strictly anhydrous conditions Lewis acids are poor or ineffective initiators for cationic polymerisation.[121,125,126] Given the central role played by adventitious moisture in the formation of active catalyst, experimental reproducibility is often poor, which can complicate interpretation of historical reports. However, polyisobutene, butyl rubber (isobutene-isoprene copolymer), polyvinyl ethers and isobutene-styrene copolymers are all produced commercially by cationic initiation, while styrene homopolymers and poly(*N*–vinyl carbazole) are also commonly investigated academically.[122,127] These monomers are generally considered well-suited to cationic initiation due to their ability to form stabilised carbocations either through hyperconjugation or mesomeric donation.[117,121]



Scheme 1.10. *Lewis acid (LA) initated polymerisation of isobutene in the presence of H_2O.*

Carbocations are highly reactive and prone to rearrangement by hydride shifts and proton eliminations. They also readily react with nucleophiles, which may arise from initiator or impurity, quenching the polymerisation activity. Nonetheless, "living" cationic polymerisations are now known for most commonly employed olefin substrates.[122] In order to achieve livingness a balance must be struck between the use of counteranions weakly-coordinating enough to avoid nucleophilic recombination, yet sufficiently coordinating to moderate the reactivity of the naked carbocation with respect to intramolecular rearrangement. For example, $[SiMe_3][B(C_6F_5)_4]$ does not allow for the observation of living polymerisation, due to the untempered promiscuity of the propagating carbocation.[128] Adventitious moisture is also a potent chain-transfer reagent, so non-nucleophilic, strongly basic additives such 2,6–di(tert-butyl)pyridine (DtBP) are frequently employed to sequester H_2O.[122,129] Faust and coworkers described the living polymerisation of isobutene initiated by BCl_3, DMSO and dicumyl alcohol in the presence of DtBP. Both DMSO and DtBP were proposed to facilitate "living-ness" by reducing the concentration of H_2O in solution.[129]

Although modern reviews consider the cationic polymerisation of α-olefins impossible,[117] this generalisation is misleading; propene requires neither extreme conditions nor catalysts in order to produce high molecular weight material. Fontana and coworkers investigated the cationic polymerisation of liquid propene at ambient pressure initiated by $AlBr_3$/HBr, and observed the formation of polypropylene with M_w = 138 kDa (polydispersity = 30.4).[130–133] Most remarkably, a 10% weight fraction was observed to contain polymer of molecular weight 829 kDa – a number at odds with the prevailing wisdom pertaining to cationic α-olefin polymerisation. Higher α-olefins beyond propylene tend towards low molecular weight material, which have found use in their own right as lubricants (*vide infra*), while with ethylene these initiators produce only oligomeric material (typically $<C_{40}$).[134–136]

This is not a thermodynamic limitation; the polymerisation of ethylene is significantly exergonic ($\Delta G_{298\ K} = -47$ kJ/mol).[117] Rather, ethylene is inactive towards proton initiated cationic polymerisation, which can be illustrated by considering the proton affinity of selected hydrocarbons, provided in Table 1.1.[137] A general trend can be observed where unsaturated substrates with large positive proton affinities are amenable to cationic polymerisation. By contrast the proton affinity of ethylene is closer to ethane than it is to isobutene, which illustrates the difficulty of its activation under protic conditions.

Substrate	Proton Affinity[137]	Cationic Polymerisation?
Ethane	596.3	None
Ethylene	680.5	Oligomers
Cyclopropane	750.3	Oligomers
Propene	751.4	Polymers (large PDI)
Isobutene	802.3	Polymers
Isoprene	826.4	Polymers
Styrene	839.5	Polymers
Methyl-vinyl-ether	859.2	Polymers

Table 1.1. *Proton affinity and cationic polymerisation of some saturated and unsaturated hydrocarbons.*[137]

Beyond the high energy barrier to its protic activation the lowest energy isomer of protonated ethylene, uniquely among α-olefins, is a C_{2v} symmetrical species with the proton bound by a 3-centre 2-electron bond across the olefin moiety.[138–141] The acid character of this compound is dominated by a low-lying empty MO anti-bonding with respect to the olefin–H^+ bond, which results in dominant Brønsted acid as opposed to Lewis acid behavior (Figure 1.11).[142–146] This contrasts with other protonated olefins, which due to their asymmetry, localise protons preferentially at 1° positions and formal cationic charges at 2° or 3° positions. The acid character of higher carbocations is consequently dominated by the resulting vacant p-orbital, which produces Lewis acidic behavior that allows for the activation and concatenation of additional olefin monomers.[6,134,143,147] This divergent reactivity can be illustrated by considering the reaction of protonated α-olefins with C_6D_6; addition of $C_2H_5^+$ to C_6D_6 leads primarily to H/D exchange, while addition of *i*-$C_3H_7^+$, produces alkylated benzenes.[142,143,145] To date, all attempts to produce polyethylene by cationic polymerisation have employed proton based initiators, adopting high-energy activation pathways, without producing the requisite Lewis-acidic carbocation. Therefore, in order to polymerise ethylene *via* a cationic mechanism a suitable initiator capable of asymmetrically activating ethylene exothermically would be required.

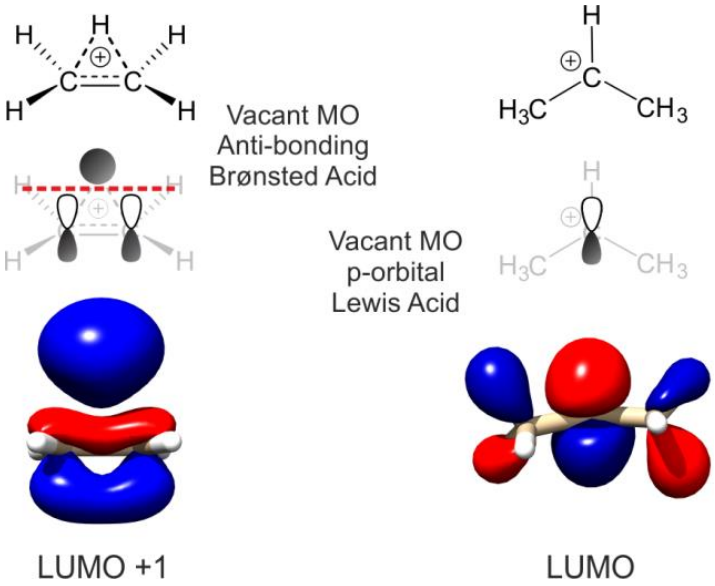


Figure 1.11. *Left: Non-classical carbonium ion $C_2H_5^+$ with LUMO +1 shown, contributing to Brønsted acid character. Right: Classical carbenium ion $C_3H_7^+$ with LUMO shown, contributing to Lewis acid character.*[148]

1.9 Transition-metal catalysed cationic polymerisation

Following the pioneering work Baird of coworkers, cationic d^0 metal catalysts are now recognised as viable initiators for the cationic polymerisation of olefinic monomers. $[Cp^*TiMe_2][MeB(C_6F_5)_3]$ was reported to polymerise ethylene by a proposed coordination-insertion mechanism, but also readily polymerised vinyl-ethers and *N*-vinyl carbazol, the latter of which is not considered amenable to coordination-insertion polymerisation.[149] Alcoholic quenching of the vinyl-ether polymerisations allowed for the observation of aldehydic end-groups by ^1H NMR spectroscopy, resulting from hydrolysis of the intermediate acetal formed by nucleophilic attack of the alcohol at the propagating carbocation, conclusively demonstrating cationic propagation.

Since then the monomer scope has been expanded to encompass isobutene,[150,151] styrenes,[152] isoprene[153] and 2,3-dihydrofuran.[154] Diverse metal initiators have been investigated, with $[Cp^*TiMe_2][MeB(C_6F_5)_3]$,[155] $[Zr\{N(SiMe_3)_2\}_3][MeB(C_6F_5)_3]$,[156] $[Cp'_4Zr_2H_3][B(C_6F_5)_4]$[157,158] and even $[Cp^*_2ZrMe][B(C_6F_4)_4]$[150] found to effectively initiate cationic polymerisation (Figure 1.12).

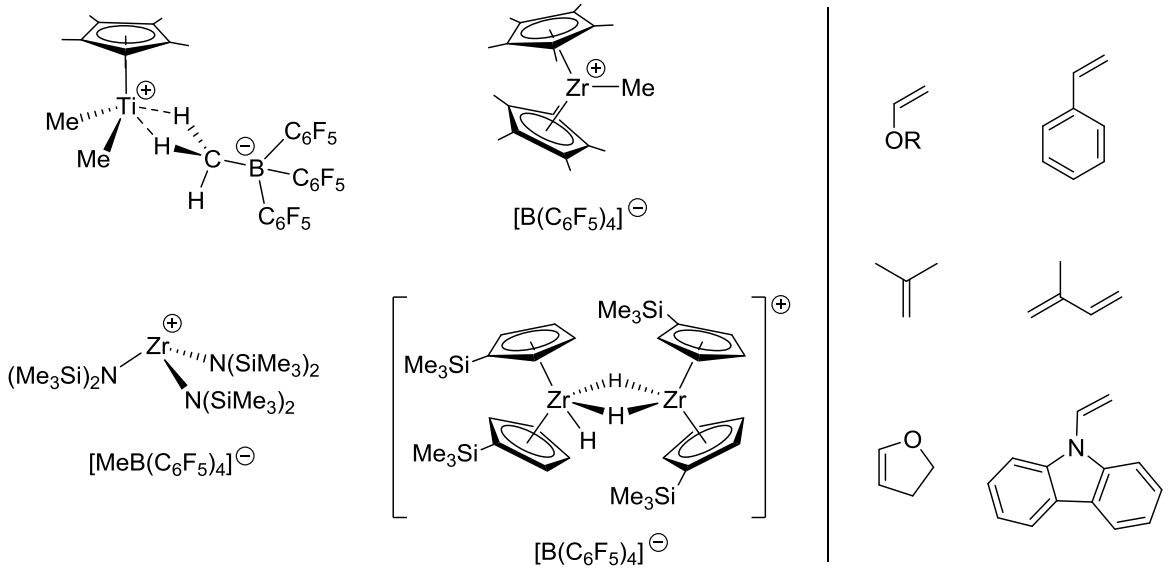


Figure 1.12. *Left: Transition metal initatiors for cationic polymerisation of olefins. Right: Olefin monomers polymerised cationically by transition metal metal complexes.*[149–158]

Mechanistic studies on the polymerisation of isobutene with $[Cp^*_2ZrMe][B(C_6F_4)_4]$ indicated these catalysts did not operate by proton initiation.[150] This was demonstrated by addition of excess 2,6–di(tert-butyl)pyridine (DtBP) as a non-nucleophilic strong base,

which behaves as a non-coordinating moisture trap.[150] Therefore, polymerisation in the presence of excess DtBP operates independently of H_2O. $[Cp^*_2ZrMe][B(C_6F_4)_4]$ was additionally compared to conventional main-group initiatiors under equivalent conditions, demonstrating the organometallic complex to produce materials with higher molecular weights and lower polydispersities at higher activities under equivalent conditions.[150] This has been ascribed in part to their improved initiation efficiency relative to main-group Lewis acids, which allows the organometallic complexes to be employed in greatly reduced concentrations, decreasing the probability of chain-transfer/termination.[158] Additionally, decoupling initiation from H_2O activation limits proton induced chain-transfer, which depresses molecular weights.[150]

The mechanism of isobutene polymerisation initiated by $[Cp'_4Zr_2H_3][B(C_6F_5)_4]$ was studied by NMR spectroscopy.[151,157,158] The possibility of proton-based initiation was investigated by monitoring the reaction of the pre-catalyst and 1,1-diphenylethylene at low temperature, whose cationation with triflic acid has been studied in detail by Sigwalt.[159] The authors reported formation of the expected indane dimerisation product, but no protonated intermediates, suggesting direct activation of the olefin at the metal.[158] The mechanism appeared complex, proceeding *via* a cascade of olefin-insertions, eliminations and oxidative additions, which prevented definitive assignment of the active species. A dimeric zirconium-vinyl complex was proposed to result from pre-catalyst activation, although conclusive evidence for its catalytic competence could not be obtained.[151,158] It is also interesting to note the robust activity of $[Zr\{N(SiMe_3)_2\}_3][MeB(C_6F_5)_3]$ towards isobutene polymerisation,[156] which illustrates the superfluous nature of alkyl or hydride substituents in cationic olefin polymerisation.

d^0 metal centres are potentially interesting candidates for cationic ethylene polymerisation. Their lack of d-electrons for back-bonding into the ethylene π^* orbital should favour unsymmetrical olefin coordination, with incipient positive charge developed at the β-position. The groups of Jordan, Baird and others have spectroscopically observed this unsymmetrical coordination approaching $[M(\eta^1-olefin)]^+$ in d^0 zirconocenes by NMR spectroscopy with diverse monomers.[155,160–165] Similarly, structurally characterised tethered-olefin metal complexes often demonstrate this asymmetry in the solid state (Figure 1.13).[162]

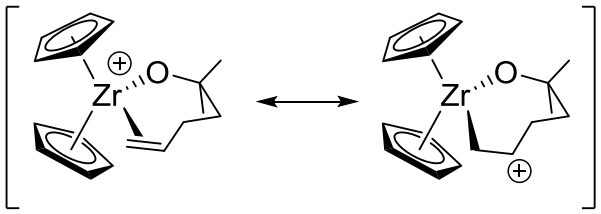
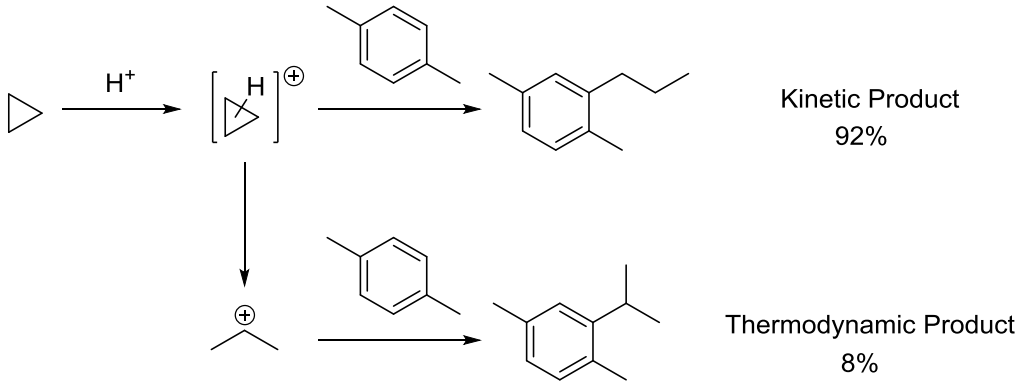


Figure 1.13. *Resonance structure describing the solid state structure of a tethered zirconium olefin complex. Anion = $[Me(B(C_6F_5)_3]^-$.*[162]

1.10 Cyclopropenium Cations

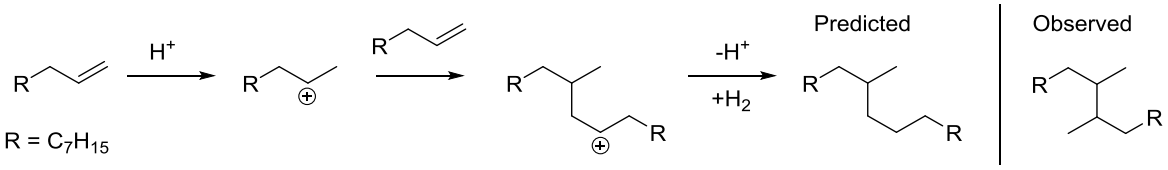
The cyclopropenium cation $(c\text{-}C_3H_7)^+$ is a relatively long-lived non-classical carbocation that can be formed by exposure of cyclopropane to Brønsted[166,167] or Lewis acids, the later acting as a masked proton source.[166] Although it is less thermodynamically stable than the secondary 2-propenium cation $(n\text{-}C_3H_7)^+$,[168,169] its persistence can be illustrated by considering its reactivity with nucleophiles. Its solvolysis in 8.4M H_2SO_4 exclusively forms *n*-propyl derivatives (*n*-propanol, *n*-propyl sulphate), with no *iso*-propyl byproducts observed.[166] More revealing is its reactivity with weak nucleophiles; the thermodynamic product expected following reaction with aromatics would be *iso*-propyl substituted arenes, while direct reaction with the cyclopropenium cation would form *n*-propyl substituted products. Addition of *p*-xylene to $(c\text{-}C_3H_7)^+$ was reported to produce near exclusive *n*-propyl substitution of the arene (*n*-:*iso*-propyl = 92:8), illustrating the preferred formation of the kinetic product (Scheme 1.11).[170]



Scheme 1.11. *Reactivity of weakly nucleophilic p-xylene and cyclopropenium cations.*[170]

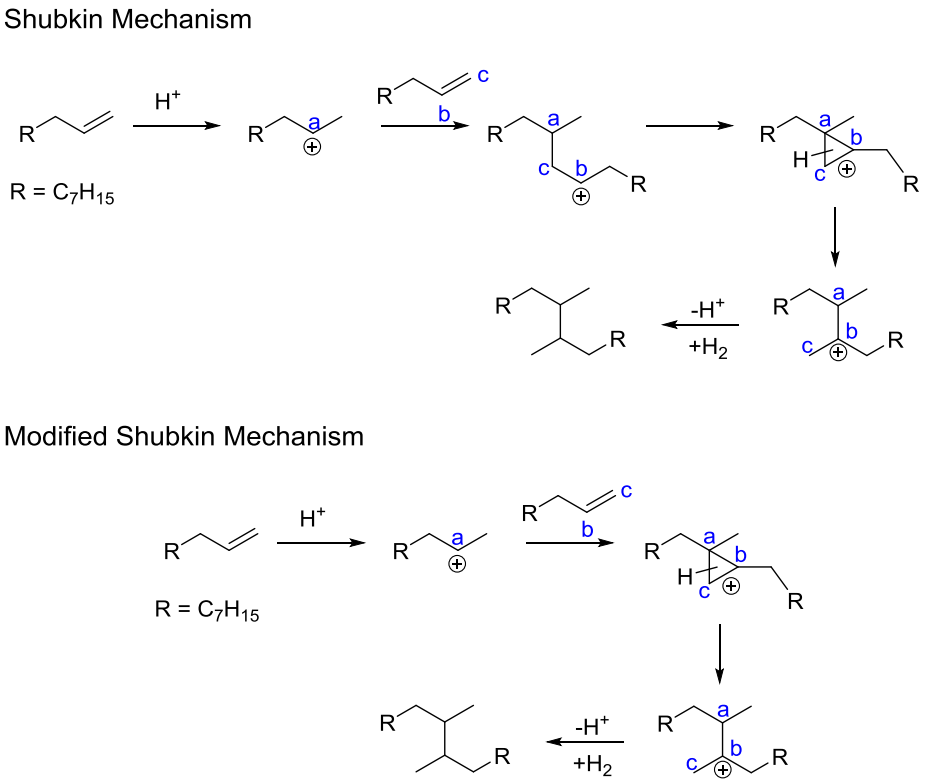
Alternatively, cyclopropenium derivatives can be formed by reaction of olefins and carbocations. The oligomerisation of 1-decene with Lewis acids such as BF_3 and $AlCl_3$ has been widely studied due the application of the paraffin products in high-performance

synthetic lubricants.[171,172] Given the relative stability of primary, secondary and tertiary cations,[5,6] a mechanism could be proposed that would predict formation of 3 methyl groups per dimer. However, the experimentally observed average methyl content is between 3.7 and 3.9 per dimer[171,173,174] indicating skeletal isomerisation, with the most abundant dimer component highlighted in Scheme 1.12.[175] Similarly, trimers would be expected to contain 4 methyl groups, while 4.7 are observed experimentally.[173]



Scheme 1.12. *Left: "Classical" carbocationic propagation predicting 3 methyl groups per dimer. Right: Most abundant dimerisation product observed experimentally (4 methyl groups per dimer).*[175,176]

The intermediacy of cycloproponium intermediates has been recognised as the likely cause of this anomalous methyl content since 1980 with the publication of the Shubkin mechanism.[173,176,177] The authors' proposed mechanism proceeds *via* initial addition of the α-olefin to the carbocation forming a secondary carbenium ion. This then rearranges to form a cycloproponium intermediate, which collapses to a methyl-rich tertiary carbocation (Scheme 1.13). However, no evidence for the secondary carbocation formed following olefin addition could be inferred from the product distribution.[175] Recent investigations of Gee *et al*., allowed for a more complete rationalisation of the product distribution by proposing *initial* cycloproponium cation formation following addition of the olefin to the carbocation (Scheme 1.13).[175]

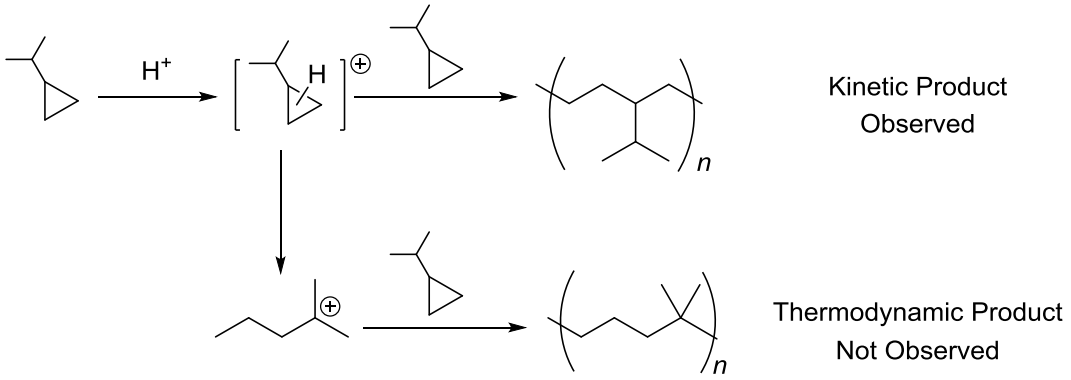


Scheme 1.13. *Top: Shubkin mechanism for 1-decene dimerisation.*[176] *Bottom: Modified Shubkin mechanism proposed by Gee et al..*[175]

The authors also note the absence of skeletal isomerisation beyond incorporation of three 1-decene molecules, indicating cyclopropenium formation does not occur for higher oligomers. Simultaneously, the rate of oligomerisation beyond trimerisation decreases rapidly, suggesting comparatively facile olefin addition to cyclopropenium cations relative to classical secondary/tertiary cations. Little evidence for cyclopropenium formation can be observed in more highly substituted olefins such as 2-butyl-1-octene and 2-methyl-1-pentene, while higher oligomers displaying this anomalous branch content are achieved readily with smaller α-olefins such as 1-pentene.[173] It is also interesting to note the divergent reactivity of propene and decene; propene forms high molecular weight polymer, albeit at lower temperatures (–44 °C *vs* 30 °C) and with a different catalyst ($AlBr_3$/HBr *vs* BF_3), while decene only produces oligomers. These reports illustrate the involvement of cyclopropenium cations in the concatenation of α-olefins, as well as the sensitivity of the degree of polymerisation towards the steric environment of the monomer and the initiator employed.

Carbocations are also frequently encountered biologically in isoprenoid biosynthetic pathways. Mg^{2+} catalysed dissociation of pyrophosphate forms carbocations that undergo diverse chemistry, with over 55 000 naturally occurring isoprenoids.[178–180] Cyclopropane motifs are commonly encountered in these natural products, such as the pyrethrin family of insectisides isolated from chrysanthemums, as well as intermediates en route to carotenoids and sterols, common to all eukaryota, archaea and some bacteria.[181,182] The prevalence of the cyclopropane moiety alludes to the intermediate formation of cycloproponium cations. However, more convincing evidence for their involvement in cyclopropanations, chain branching, and cyclobutanation was provided by Thulasiram *et al*., whose isotopic labelling studies found kinetic isotope effects that implicated initial cycloproponium formation as a branch point in product diversification, resulting from carbocation addition across an olefin bond.[183]

Uniquely among unactivated cycloalkanes, cyclopropane and its alkylated derivatives undergo acid-catalysed oligomerisation. In 1953, Ipatieff and co-workers observed the rapid polymerisation of 1,1–dimethyl cyclopropane,[184] chemistry uncharacteristic of saturated alkanes, although the polymeric materials were not characterised in detail. A further illustration of the kinetic stabilisation of cycloproponium derivatives can be found in the oligomerisation of *iso*-propyl cyclopropane with $AlBr_3$ reported by Naegele and Haubenstock (Scheme 1.14).[185] $AlBr_3$, acting as masked a proton source, would be expected to induce rearrangement to the tertiary carbocationic intermediate before concatenation with the weakly nucleophilic cycloalkane would form geminal-dimethyl substituted oligo-butane. Instead near complete retention of the intact *iso*-propyl moiety is observed by NMR spectroscopy, which can now be understood to result from addition of *iso*-propyl cyclopropane to the cycloproponium cation. Despite this unusual acid catalysed chain growth observed with weakly nucleophilic cyclopropane derivatives, no reports on the reactivity of α-olefins and cycloproponium cations have been made to date.



Scheme 1.14. *iso-propyl cyclopropane oligomerisation under acidic conditions.*[185]

1.11 Cationic ethylene polymerisation

Very few modern investigations have been undertaken examining the cationic polymerisation/oligomerisation of ethylene. Studies by Ipatieff and coworkers in the 1930s found the reaction of $AlCl_3$ and ethylene produced a complex mixture of organic compounds, some of which had an odd number of carbon atoms indicating C–C bond scission, while other components were identified as aromatic and napthalenic.[135,136,186] Unfortunately, the limited characterisation techniques available 80 years ago places the minutiae of these reactions beyond reach; for example solid polymeric material and "Friedels-Crafts sludge" that could not be purified by distillation is disregarded as "bottoms" in discussions of the time.

It is known that exposure of olefins to ionising radiation can generate charged species, initiating ionic polymerisations. Exposure of liquid ethylene to Co^{60}, a source of γ-radiation, was observed to initiate the cationic polymerisation of ethylene at low temperatures, although little characterising data for the polymer is provided.[187,188]

In 2002, Reed, Sen and co-workers synthesised $[Et_2Al][CB_{11}H_6Br_6]$ ($[CB_{11}H_6Br_6]^-$ = weakly coordinating carborane anion), which when exposed to ethylene, produced oligomers catalytically (M_w = 525 g/mol). Isotopic labelling studies with C_2D_4 demonstrated no insertion into Al–Et bonds, leading the authors to propose a cationic initiation mechanism with chain-growth at aluminium.[189] The catalytic formation of 1-butene was reported alongside ethyl/*sec*-butyl benzene formed in ~1:10 ratio. However, these observations are less consistent with chain-growth at aluminium than proton-

mediated ethylene oligomerisation. Indeed, improved yields were reported under similar conditions for $AlCl_3$, which is known to operate by activation of protic impurities. Later investigations by Klis *et al.*, examined the activation of 1-hexene with [Dipp*AlEt][$CH_6B_{11}I_6$], [DcpAlEt][$CH_6B_{11}I_6$] and [$AlEt_2$][$CB_{11}H_6Br_6$], (Dipp* = 2,6-(2,6-*i*-$Pr_2C_6H_3)_2C_6H_3$), Dcp = 2,6-(2,6-$Cl_2C_6H_3)_2C_6H_3$) finding activation of trace moisture, postulated to leech from glassware, was responsible for alkene activation.[190] In the presence of a proton trap, DtBP, reaction with 1-hexene was prevented with no coordination observed between aluminium and the bulky Lewis base.

1.12 Scope of Thesis

In the first section of this thesis, the non-classical polymerisation motif, Pn*MCp^R(X) is exemplified with a series of complexes investigating substitution of the ancilliary ligand and leaving group. The ethylene polymerisation activity of these complexes is investigated both in solution, activated by MAO, and immobilised on inorganic supports. The mechanism of polymerisation is then considered, supported by the synthesis of proposed intermediates, measurement of *in-situ* gas uptake rates, and small-molecule reactivity studies.

In the second section of this thesis the synthesis and characterisation of metal-hydride complexes is described and preliminary results on their small-molecule reactivity is presented. Finally the chemistry of reduced permethylpentalene titanium complexes is investigated.

1.13 References

(1) Cloke, F. G. N.; Green, J. C.; Kilpatrick, A. F. R.; O'Hare, D. *Coord. Chem. Rev.* **2017**, *344*, 238–262.
(2) Summerscales, O. T.; Cloke, F. G. N. *Coord. Chem. Rev.* **2006**, *250* (9–10), 1122–1140.
(3) Ashley, A. E. D.Phil Thesis, University of Oxford, 2006.
(4) Cooper, R. T. D.Phil Thesis, University of Oxford, 2012.
(5) Olah, G. A. *J. Am. Chem. Soc.* **1972**, *94* (3), 808–820.
(6) Olah, G. A. *J. Org. Chem.* **2001**, *66* (18), 5943–5957.
(7) Dauben, H. J.; Bertelli, D. J. *J. Am. Chem. Soc.* **1961**, *83* (22), 4659–4660.
(8) Dauben, H. J.; Bertelli, D. J. *J. Am. Chem. Soc.* **1961**, *83* (22), 4657–4659.
(9) den Boer-Veenendaal, P. C.; den Boer, D. H. W. *Mol. Phys.* **1961**, *4* (1), 33–38.
(10) den Boer, P. C.; den Boer, D. H. W.; Coulson, C. A.; Goodwin, T. H. *Tetrahedron*

1963, *19* (12), 2163–2170.
(11) Bally, T.; Chai, S.; Neuenschwander, M.; Zhu, Z. *J. Am. Chem. Soc.* **1997**, *119* (8), 1869–1875.
(12) Dewar, M. J. S.; De Llano, C. *J. Am. Chem. Soc.* **1969**, *91* (4), 789–795.
(13) Hess, B. A.; Schaad, L. J. *J. Am. Chem. Soc.* **1971**, *93* (2), 305–310.
(14) Hafner, K.; Dönges, R.; Goedecke, E.; Kaiser, R. *Angew. Chem. Int. Ed.* **1973**, *12* (4), 337–339.
(15) Bally, T.; Chai, S.; Neuenschwander, M.; Zhu, Z. *J. Am. Chem. Soc.* **1997**, *119* (8), 1869–1875.
(16) Kaufman, H. S.; Fankuchen, I.; Mark, H. *Nature* **1948**, *161* (4083), 165–165.
(17) Klärner, F.-G. *Angew. Chem. Int. Ed.* **2001**, *40* (21), 3977.
(18) Baird, M. S.; Reese, C. B. *Tetrahedron Lett.* **1976**, *17* (33), 2895–2898.
(19) Jones, S. C.; Roussel, P.; Hascall, T.; O'Hare, D. *Organometallics* **2006**, *25* (1), 221–229.
(20) Kaiser, R.; Hafner, K. *Angew. Chem. Int. Ed.* **1970**, *9* (11), 892–893.
(21) Kaiser, R.; Hafner, K. *Angew. Chem.* **1973**, *85* (8), 361–362.
(22) Katz, T. J.; Rosenberger, M.; O'Hara, R. K. *J. Am. Chem. Soc.* **1964**, *86* (2), 249–252.
(23) Jones, M.; Schwab, L. O. *J. Am. Chem. Soc.* **1968**, *90* (23), 6549–6550.
(24) Cloke, F. G. N.; Kuchta, M. C.; Harker, R. M.; Hitchcock, P. B.; Parry, J. S. *Organometallics* **2000**, *19* (26), 5795–5798.
(25) Jones, S. C. D.Phil Thesis, University of Oxford, 2003.
(26) Ashley, A. E.; Cowley, A. R.; O'Hare, D. *Eur. J. Org. Chem.* **2007**, *2007* (14), 2239–2242.
(27) Ashley, A. E.; Cowley, A. R.; O'Hare, D. *Chem. Commun.* **2007**, No. 15, 1512–1514.
(28) Cloke, F. G. N.; Green, J. C.; Kilpatrick, A. F. R.; O'Hare, D. *Coord. Chem. Rev.* **2017**, *344*, 238–262.
(29) Green, J. C.; Green, M. L. H.; Parkin, G. *Chem. Commun.* **2012**, *48* (94), 11481.
(30) Cooper, R. T.; Chadwick, F. M.; Ashley, A. E.; O'Hare, D. *Organometallics* **2013**, *32* (7), 2228–2233.
(31) Green, M. L. H. *J. Organomet. Chem.* **1995**, *500* (1–2), 127–148.
(32) Jones, S. C.; O'Hare, D. *Chem. Commun.* **2003**, *0* (17), 2208–2209.
(33) Ashley, A. E.; Cooper, R. T.; Wildgoose, G. G.; Green, J. C.; O'Hare, D. *J. Am. Chem. Soc.* **2008**, *130* (46), 15662–15677.
(34) Kuchta, M. C.; Cloke, F. G. N.; Hitchcock, P. B. *Organometallics* **1998**, *17* (10), 1934–1936.
(35) Cloke, F. G. N.; Green, J. C.; Jardine, C. N.; Kuchta, M. C. *Organometallics* **1999**, *18* (6), 1087–1090.
(36) Balazs, G.; Cloke, F. G. N.; Gagliardi, L.; Green, J. C.; Harrison, A.; Hitchcock, P. B.; Shahi, A. R. M.; Summerscales, O. T. *Organometallics* **2008**, *27* (9), 2013–2020.
(37) Smith, A. D. M.Chem. Dissertation, Univeristy of Sussex, 2012.
(38) Gleiter, R.; Bethke, S.; Okubo, J.; Jonas, K. *Organometallics* **2001**, *20* (20), 4274–4278.
(39) King, R. B. *Appl. Organomet. Chem.* **2003**, *17* (6–7), 393–397.
(40) Bendjaballah, S.; Kahlal, S.; Costuas, K.; Bévillon, E.; Saillard, J.-Y. *Chem. Eur. J.* **2006**, *12* (7), 2048–2065.

(41) Cloke, F. G. N. *Pure Appl. Chem.* **2001**, *73* (2), 233–238.
(42) Jonas, K.; Kolb, P.; Kollbach, G.; Gabor, B.; Mynott, R.; Angermund, K.; Heinemann, O.; Krüger, C. *Angew. Chem. Int. Ed.* **1997**, *36* (16), 1714–1718.
(43) Jonas, K.; Gabor, B.; Mynott, R.; Angermund, K.; Heinemann, O.; Krüger, C. *Angew. Chem. Int. Ed.* **1997**, *36* (16), 1712–1714.
(44) Shannon, R. D. *Acta Crystallogr. Sect. A* **1976**, *32* (5), 751–767.
(45) Chadwick, F. M.; Cooper, R. T.; Ashley, A. E.; Buffet, J.-C.; O'Hare, D. M. *Organometallics* **2014**, *33* (14), 3775–3785.
(46) Cloke, F. G. N.; Hitchcock, P. B.; Kuchta, M. C.; Morley-Smith, N. A. *Polyhedron* **2004**, *23* (17), 2625–2630.
(47) Green, J. C.; Green, M. L. H.; Prout, C. K. *J. Chem. Soc., Chem. Commun.* **1972**, *0* (7), 421–422.
(48) Petersen, J. L.; Dahl, L. F. *J. Am. Chem. Soc.* **1975**, *97* (22), 6422–6433.
(49) Long, N. J. *Metallocenes : an introduction to sandwich complexes*; Blackwell Science, 1998.
(50) C. Green, J. *Chem. Soc. Rev.* **1998**, *27* (4), 263–271.
(51) Green, J. C.; Green, M. L. H.; Prout, C. K. *J. Chem. Soc., Chem. Commun.* **1972**, *0* (7), 421–422.
(52) Green, M. L. H.; McCleverty, J. A.; Pratt, L.; Wilkinson, G. *J. Chem. Soc.* **1961**, *0* (0), 4854–4859.
(53) Green, M. L. H. *Pure Appl. Chem.* **1972**, *30* (3–4), 373–388.
(54) Clearfield, A.; Warner, D. K.; Saldarriaga-Molina, C. H.; Ropal, R.; Bernal, I. *Can. J. Chem.* **1975**, *53* (11), 1622–1629.
(55) Kilpatrick, A. F. R.; Green, J. C.; Cloke, F. G. N. *Organometallics* **2015**, *34* (20), 4830–4843.
(56) Kilpatrick, A. F. R.; Green, J. C.; Cloke, F. G. N.; Tsoureas, N. *Chem. Commun.* **2013**, *49* (82), 9434.
(57) Kilpatrick, A. F. R. Ph.D Thesis, University of Sussex, 2014.
(58) Kilpatrick, A. F. R.; Cloke, F. G. N. *Chem. Commun.* **2014**, *50* (21), 2769.
(59) Kilpatrick, A. F. R.; Green, J. C.; Cloke, F. G. N. *Organometallics* **2015**, *34* (20), 4816–4829.
(60) Kilpatrick, A. F. R.; Green, J. C.; Cloke, F. G. N. *Organometallics* **2017**, *36* (2), 352–362.
(61) Tsoureas, N.; Green, J. C.; Cloke, F. G. N. *Chem. Commun.* **2017**, *53* (98), 13117–13120.
(62) Cooper, R. T.; Chadwick, F. M.; Ashley, A. E.; O'Hare, D. *Chem. Commun.* **2015**, *51* (59), 11856–11859.
(63) Kilpatrick, A. F. R.; Green, J. C.; Turner, Z. R.; Buffet, J.-C.; O'Hare, D. *Chem. Commun.* **2017**, *53* (88), 12048–12051.
(64) Manriquez, J. M.; Bercaw, J. E. *J. Am. Chem. Soc.* **1974**, *96* (19), 6229–6230.
(65) Manriquez, J. M.; Sanner, R. D.; Marsh, R. E.; Bercaw, J. E. *J. Am. Chem. Soc.* **1976**, *98* (10), 3042–3044.
(66) Cloke, F. G. N.; Hitchcock, P. B. *J. Am. Chem. Soc.* **2002**, *124* (32), 9352–9353.
(67) Burgos, F.; Arancibia, V.; Manríquez, J. M.; Chávez, I. *Boletín la Soc. Chil. Química* **2000**, *45* (4).
(68) Burgos, F.; Chávez, I.; Manriquez, J. M.; Valderrama, M.; Lago, E.; Molins, E.; Delpech, F.; Castel, A.; Rivière, P. *Organometallics* **2001**, *20* (7), 1287–1291.
(69) Turner, Z. R.; Buffet, J.-C.; O'Hare, D. *Organometallics* **2014**, *33* (14), 3891–3903.

(70) Britovsek, G. J. P.; Gibson, V. C.; Wass, D. F. *Angew. Chem. Int. Ed.* **1999**, *38* (4), 428–447.
(71) Chadwick, F. M. D.Phil Thesis, University of Oxford, 2013.
(72) Jonas, K.; Kolb, P.; Kollbach, G. Mononuclear and polynuclear transition metal complexes with pentalene ligands bound to single metal atoms. US 5959132 A, 1999.
(73) Cloke, F. G. N.; Parry, J. S. Novel transition metal complexes. WO 1999007716 A1, 1998.
(74) Cloke, F. G. N. Polymerization catalysts. EP0672676 A2, 1995.
(75) Cossee, P. *J. Catal.* **1964**, *3* (1), 80–88.
(76) Kaminsky, W.; Laban, A. *Appl. Catal. A Gen.* **2001**, *222* (1–2), 47–61.
(77) Collins, R. A.; Russell, A. F.; Mountford, P. *Appl. Petrochemical Res.* **2015**, *5* (3), 153–171.
(78) Pellecchia, C.; Grassi, A.; Zambelli, A. *Organometallics* **1994**, *13* (1), 298–302.
(79) Grubbs, R. H.; Coates, G. W. *Acc. Chem. Res.* **1996**, *29* (2), 85–93.
(80) Bochmann, M. *J. Chem. Soc., Dalton Trans.* **1996**, No. 3, 255.
(81) Brookhart, M.; Green, M. L. H.; Parkin, G. *Proc. Natl. Acad. Sci.* **2007**, *104* (17), 6908–6914.
(82) Piers, W. E.; Bercaw, J. E. *J. Am. Chem. Soc.* **1990**, *112* (25), 9406–9407.
(83) Sinn, H.; Kaminsky, W.; Vollmer, H.-J.; Woldt, R. *Angew. Chem. Int. Ed.* **1980**, *19* (5), 390–392.
(84) Zijlstra, H. S.; Harder, S. *Eur. J. Inorg. Chem.* **2015**, *2015* (1), 19–43.
(85) Brintzinger, H. H.; Fischer, D.; Mülhaupt, R.; Rieger, B.; Waymouth, R. M. *Angew. Chem. Int. Ed.* **1995**, *34* (11), 1143–1170.
(86) Tritto, I.; Li, S.; Sacchi, M. C.; Zannoni, G. *Macromolecules* **1993**, *26* (26), 7111–7115.
(87) Kaminsky, W. *Macromol. Symp.* **1995**, *97* (1), 79–89.
(88) Kaminsky, W. *Macromol. Chem. Phys.* **1996**, *197* (12), 3907–3945.
(89) Severn, J. R.; Chadwick, J. C. *Tailor-made polymers : via immobilization of alpha-olefin polymerization catalysts*; Wiley-VCH, 2008.
(90) Obrey, S. J.; Barron, A. R. *J. Chem. Soc., Dalton Trans.* **2001**, *0* (17), 2456–2458.
(91) Andresen, A.; Cordes, H.-G.; Herwig, J.; Kaminsky, W.; Merck, A.; Mottweiler, R.; Pein, J.; Sinn, H.; Vollmer, H.-J. *Angew. Chem. Int. Ed.* **1976**, *15* (10), 630–632.
(92) Resconi, L.; Bossi, S.; Abis, L. *Macromolecules* **1990**, *23* (20), 4489–4491.
(93) Atwood, J. L.; Hrncir, D. C.; Priester, R. D.; Rogers, R. D. *Organometallics* **1983**, *2* (8), 985–989.
(94) Mason, M. R.; Smith, J. M.; Bott, S. G.; Barron, A. R. *J. Am. Chem. Soc.* **1993**, *115* (12), 4971–4984.
(95) Harlan, C. J.; Mason, M. R.; Barron, A. R. *Organometallics* **1994**, *13* (8), 2957–2969.
(96) Harlan, C. J.; Bott, S. G.; Barron, A. R. *J. Am. Chem. Soc.* **1995**, *117* (24), 6465–6474.
(97) Luo, L.; Sangokoya, S. A.; Xiao, W.; Diefenbach, S. P.; Kneale, B. Aluminoxane Catalyst Activators Derived From Dialkylaluminum Cation Precursor Agents, Processes For Making Same, And Use Thereof In Catalysts And Polymerization Of Olefins. US20090062492 A1, 2008.
(98) Ghiotto, F.; Pateraki, C.; Tanskanen, J.; Severn, J. R.; Luehmann, N.; Kusmin, A.; Stellbrink, J.; Linnolahti, M.; Bochmann, M. *Organometallics* **2013**, *32* (11), 3354–

3362.
(99) Klosin, J.; Roof, G. R.; Chen, E. Y.-X.; Abboud, K. A. *Organometallics* **2000**, *19* (23), 4684–4686.
(100) Severn, J. R.; Chadwick, J. C.; Duchateau, R.; Friederichs, N. *Chem. Rev.* **2005**, *105* (11), 4073–4147.
(101) Bartram, M. E.; Michalske, T. A.; Rogers, J. W. *J. Phys. Chem.* **1991**, *95* (11), 4453–4463.
(102) Soga, K.; Kaminaka, M. *Die Makromol. Chemie* **1993**, *194* (6), 1745–1755.
(103) Panchenko, V. N.; Semikolenova, N. V.; Danilova, I. G.; Paukshtis, E. A.; Zakharov, V. A. *J. Mol. Catal. A Chem.* **1999**, *142* (1), 27–37.
(104) Welborn, H. C. Supported polymerization catalyst. US 4808561 A, February 28, 1989.
(105) Takahashi, T. Process for producing ethylene copolymers. US 5026797 A, June 25, 1991.
(106) Angpanitcharoen, P.; Hay, G.; Buffet, J.-C.; Turner, Z. R.; Arnold, T. A. Q.; O'Hare, D. *Polyhedron* **2016**, *116*, 216–222.
(107) Buffet, J.-C.; Arnold, T. A. Q.; Turner, Z. R.; Angpanitcharoen, P.; O'Hare, D. *RSC Adv.* **2015**, *5* (106), 87456–87464.
(108) Zhang, J.; Zhang, F.; Ren, L.; Evans, D. G.; Duan, X. *Mater. Chem. Phys.* **2004**, *85* (1), 207–214.
(109) Wang, Q.; O'Hare, D. *Chem. Commun.* **2013**, *49* (56), 6301.
(110) Chen, C.; Yang, M.; Wang, Q.; Buffet, J.-C.; O'Hare, D. *J. Mater. Chem. A* **2014**, *2* (36), 15102–15110.
(111) Buffet, J.-C.; Turner, Z. R.; Cooper, R. T.; O'Hare, D. *Polym. Chem.* **2015**, *6* (13), 2493–2503.
(112) Wright, C. M. R.; Turner, Z. R.; Buffet, J.-C.; O'Hare, D. *Chem. Commun.* **2016**, *52* (13), 2850–2853.
(113) Buffet, J.-C.; Wanna, N.; Arnold, T. A. Q.; Gibson, E. K.; Wells, P. P.; Wang, Q.; Tantirungrotechai, J.; O'Hare, D. *Chem. Mater.* **2015**, *27* (5), 1495–1501.
(114) Kaji, E.; Yoshioka, E. Solid polymethylaluminoxane composition and process for producing same. WO2010055652, May 20, 2010.
(115) Kilpatrick, A. F. R.; Buffet, J.-C.; Nørby, P.; Rees, N. H.; Funnell, N. P.; Sripothongnak, S.; O'Hare, D. *Chem. Mater.* **2016**, *28* (20), 7444–7450.
(116) Arnold, T. A. Q.; Turner, Z. R.; Buffet, J.-C.; O'Hare, D. *J. Organomet. Chem.* **2016**, *822*, 85–90.
(117) Odian, G. G. *Principles of polymerization*, 4th ed.; John Wiley & Sons, Inc.: Hoboken, New Jersey, 2004.
(118) Mark, H. F.; Bikales, N. M.; Overberger, C. G.; Menges, G. *Encyclopedia of Polymer Science and Engineering, Volume 6*, 2nd ed.; Kroschwitz, J. I., Ed.; Wiley-Interscience: New York, 1986.
(119) Marshall, W. B.; Brewbaker, J. L.; Delaney, M. S. *J. Appl. Polym. Sci.* **1991**, *42* (2), 533–541.
(120) Eberhardt, G. G.; Davis, W. R. *J. Polym. Sci. Part A Gen. Pap.* **1965**, *3* (11), 3753–3762.
(121) Kennedy, J. P.; Maréchal, E. *Carbocationic polymerization*; Wiley, 1982.
(122) Aoshima, S.; Kanaoka, S. *Chem. Rev.* **2009**, *109* (11), 5245–5287.
(123) Plesch, P. H. *The Chemistry of Cationic Polymerization.*; Elsevier Science, 2013.
(124) Matyjaszewski, K. *Cationic polymerizations: mechanisms, synthesis, and*

applications; Marcel Dekker, 1996.
(125) Evans, A. G.; Meadows, G. W. *Trans. Faraday Soc.* **1950**, *46* (0), 327.
(126) Kennedy, J. P. *J. Polym. Sci. Polym. Symp.* **1976**, *56* (1), 1–11.
(127) Pazur, R. J.; Greve, H.-H. In *Ionic Polymerizations and Related Processes*; Springer Netherlands: Dordrecht, 1999; pp 13–29.
(128) Pi, Z.; Jacob, S.; Kennedy, J. P. In *Ionic Polymerizations and Related Processes*; Springer Netherlands: Dordrecht, 1999; pp 1–12.
(129) Balogh, L.; Faust, R. *Polym. Bull.* **1992**, *28* (4), 367–374.
(130) Fontana, C. M. *J. Phys. Chem.* **1959**, *63* (7), 1167–1174.
(131) Fontana, C. M.; Herold, R. J.; Kinney, E. J.; Miller, R. C. *Ind. Eng. Chem.* **1952**, *44* (12), 2955–2962.
(132) Fontana, C. M.; Kidder, G. A.; Herold, R. J. *Ind. Eng. Chem.* **1952**, *44* (7), 1688–1695.
(133) Fontana, C. M.; Kidder, G. A. *J. Am. Chem. Soc.* **1948**, *70* (11), 3745–3751.
(134) Kennedy, J. P. *Cationic polymerization of olefins: a critical inventory*; Wiley, 1975.
(135) Ipatieff, V. N.; Grosse, A. V.; Pines, H.; Komarewsky, V. I. *J. Am. Chem. Soc.* **1936**, *58* (6), 913–915.
(136) Ipatieff, V. N.; Grosse, A. V. *J. Am. Chem. Soc.* **1936**, *58* (6), 915–917.
(137) Hunter, E. P. L.; Lias, S. G. *J. Phys. Chem. Ref. Data* **1998**, *27* (3), 413–656.
(138) Andrei, H.-S.; Solcà, N.; Dopfer, O. *Angew. Chem. Int. Ed.* **2008**, *47* (2), 395–397.
(139) Lischka, H.; Koehler, H. J. *J. Am. Chem. Soc.* **1978**, *100* (17), 5297–5305.
(140) Ricks, A. M.; Douberly, G. E.; Schleyer, P. v. R.; Duncan, M. A. *Chem. Phys. Lett.* **2009**, *480* (1–3), 17–20.
(141) Perera, S. A.; Bartlett, R. J.; Schleyer, P. von R. *J. Am. Chem. Soc.* **1995**, *117* (32), 8476–8477.
(142) Chiavarino, B.; Crestoni, M. E.; Di Rienzo, B.; Fornarini, S. *J. Am. Chem. Soc.* **1998**, *120* (42), 10856–10862.
(143) Cerichelli, G.; Crestoni, M. E.; Fornarini, S. *J. Am. Chem. Soc.* **1992**, *114* (6), 2002–2009.
(144) Angelini, G.; Bucci, R.; Laguzzi, G.; Siciliano, C.; Segre, A. L. *J. Phys. Chem. A* **1998**, *102* (32), 6464–6469.
(145) Fornarini, S.; Crestoni, M. E. *Acc. Chem. Res.* **1998**, *31* (12), 827–834.
(146) Chiavarino, B.; Crestoni, M. E.; Fornarini, S. *J. Am. Chem. Soc.* **1999**, *121* (11), 2619–2620.
(147) Attina, M.; Giacomello, P. *J. Am. Chem. Soc.* **1979**, *101* (20), 6040–6045.
(148) Calculations carried out at the B3LYP level of theory using Ahlrichs split-valence basis set.
(149) Quyoum, R.; Wang, Q.; Tudoret, M.-J.; Baird, M. C.; Gillis, D. J. *J. Am. Chem. Soc.* **1994**, *116* (14), 6435–6436.
(150) Shaffer, T. D.; Ashbaugh, J. R. *J. Polym. Sci. Part A Polym. Chem.* **1997**, *35* (2), 329–344.
(151) Bochmann, M. *Acc. Chem. Res.* **2010**, *43* (9), 1267–1278.
(152) Wang, Q.; Quyoum, R.; Gillis, D. J.; Tudoret, M.-J.; Jeremic, D.; Hunter, B. K.; Baird, M. C. *Organometallics* **1996**, *15* (2), 693–703.
(153) Barsan, F.; Baird, M. C. *J. Chem. Soc., Chem. Commun.* **1995**, *25* (10), 1065–1066.
(154) Wang, Q.; Baird, M. C. *Macromolecules* **1995**, *28* (24), 8021–8027.
(155) Baird, M. C. *Chem. Rev.* **2000**, *100* (4), 1471–1478.
(156) Carr, A. G.; Dawson, D. M.; Bochmann, M. *Macromol. Rapid Commun.* **1998**, *19*

(4), 205–207.
(157) Carr, A. G.; Dawson, D. M.; Thornton-Pett, M.; Bochmann, M. *Organometallics* **1999**, *18* (16), 2933–2935.
(158) Garratt, S.; Carr, A. G.; Langstein, G.; Bochmann, M. *Macromolecules* **2003**, *36* (12), 4276–4287.
(159) Sigwalt, P.; Sauvet, G. *Polym. J.* **1980**, *12* (9), 651–659.
(160) Stoebenau, E. J.; Jordan, R. F. *J. Am. Chem. Soc.* **2006**, *128* (26), 8638–8650.
(161) Stoebenau, E. J.; Jordan, R. F. *J. Am. Chem. Soc.* **2006**, *128* (25), 8162–8175.
(162) Wu, Z.; Jordan, R. F.; Petersen, J. L. *J. Am. Chem. Soc.* **1995**, *117* (21), 5867–5868.
(163) Vatamanu, M.; Stojcevic, G.; Baird, M. C. *J. Am. Chem. Soc.* **2008**, *130* (2), 454–456.
(164) Casey, C. P.; Carpenetti, D. W.; Sakurai, H. *J. Am. Chem. Soc.* **1999**, *121* (40), 9483–9484.
(165) Sauriol, F.; Wong, El.; Leung, A. M. H.; Donaghue, I. E.; Baird, M. C.; Wondimagegn, T.; Ziegler, T. *Angew. Chem. Int. Ed.* **2009**, *48* (18), 3342–3345.
(166) Baird, R. L.; Aboderin, A. A. *J. Am. Chem. Soc.* **1964**, *86* (2), 252–255.
(167) Baird, R. L.; Aboderin, A. *Tetrahedron Lett.* **1963**, *4* (4), 235–237.
(168) Radom, L.; Pople, J. A.; Schleyer, P. v. R. *J. Am. Chem. Soc.* **1972**, *94* (17), 5935–5945.
(169) Koch, W.; Liu, B.; Schleyer, P. v. R. *J. Am. Chem. Soc.* **1989**, *111* (9), 3479–3480.
(170) Deno, N. C.; LaVietes, D.; Mockus, J.; Scholl, P. *J. Am. Chem. Soc.* **1968**, *90* (23), 6457–6460.
(171) Shubkin, R. L.; Kerkemeyer, M. E. *J. Synth. Lubr.* **1991**, *8* (2), 115–134.
(172) Driscoll, G. L.; Linkletter, S. J. G. *Synthesis of Synthetic Hydrocarbons Via Alpha Olefins.*; Defense Technical Information Centre, ADA160386, 1985.
(173) Onopchenko, A.; Cupples, B. L.; Kresge, A. N. *Ind. Eng. Chem. Prod. Res. Dev.* **1983**, *22* (2), 182–191.
(174) Kapur, G. S.; Sarpal, A. S.; Sarin, R.; Jain, S. K.; Srivastava, S. P.; Bhatnagar, A. K. *J. Synth. Lubr.* **1998**, *15* (3), 177–191.
(175) Gee, J. C.; Small, B. L.; Hope, K. D. *J. Phys. Org. Chem.* **2012**, *25* (12), 1409–1417.
(176) Shubkin, R. L.; Baylerian, M. S.; Maler, A. R. *Ind. Eng. Chem. Prod. Res. Dev.* **1980**, *19* (1), 15–19.
(177) Lahtela, M.; Pakkanen, T. A.; Nissfolk, F. *J. Phys. Chem.* **1995**, *99* (25), 10267–10271.
(178) Sacchettini, J. C.; Poulter, C. D. *Science* **1997**, *277* (5333), 1788–1789.
(179) Tantillo, D. J. *Nat. Prod. Rep.* **2011**, *28* (6), 1035.
(180) Oldfield, E.; Lin, F.-Y. *Angew. Chem. Int. Ed.* **2012**, *51* (5), 1124–1137.
(181) Poulter, C. D. *Acc. Chem. Res.* **1990**, *23* (3), 70–77.
(182) Godin, P. J.; Thain, E. M. *Proc. Chem. Soc.* **1961**, *9*, 441.
(183) Thulasiram, H. V.; Erickson, H. K.; Poulter, C. D. *J. Am. Chem. Soc.* **2008**, *130* (6), 1966–1971.
(184) Pines, H.; Huntsman, W. D.; Ipatieff, V. N. *J. Am. Chem. Soc.* **1953**, *75* (10), 2315–2317.
(185) Naegele, W.; Haubenstock, H. *Tetrahedron Lett.* **1965**, *6* (48), 4283–4290.
(186) Ipatieff, V. N.; Pines, H. *Ind. Eng. Chem.* **1935**, *27* (11), 1364–1369.
(187) Wagner, C. D. *J. Phys. Chem.* **1961**, *65* (12), 2276–2277.
(188) Tabata, Y.; Shibano, H.; Sobue, H.; Hara, K. *J. Polym. Sci. Part A Gen. Pap.* **1963**,

1 (3), 1049–1053.
(189) Kim, K.-C.; Reed, C. A.; Long, G. S.; Sen, A. *J. Am. Chem. Soc.* **2002**, *124* (26), 7662–7663.
(190) Klis, T.; Powell, D. R.; Wojtas, L.; Wehmschulte, R. J. *Organometallics* **2011**, *30* (9), 2563–2570.

Chapter 2: Synthesis and Characterisation of Pn*MCp^R(X) Complexes

2.1 Introduction

Altering the ligand environment of ethylene polymerisation pre-catalysts can allow for improvement of polymerisation activity and the modification of polymer properties.[1–4] Typically, the most significant changes will result from changes to ancillary ligand fragments; variation of leaving groups can improve activities where pre-catalyst activation is rate-limiting, but in general the persistent ligands assert a more significant effect given their proximity to every chain propagation event throughout the whole polymerisation. Nonetheless, substitution of the chloride leaving group provides access to a variety of new chemistry that is required to effectively understand the mechanism of polymerisation, which is discussed in detail in Chapter 4.

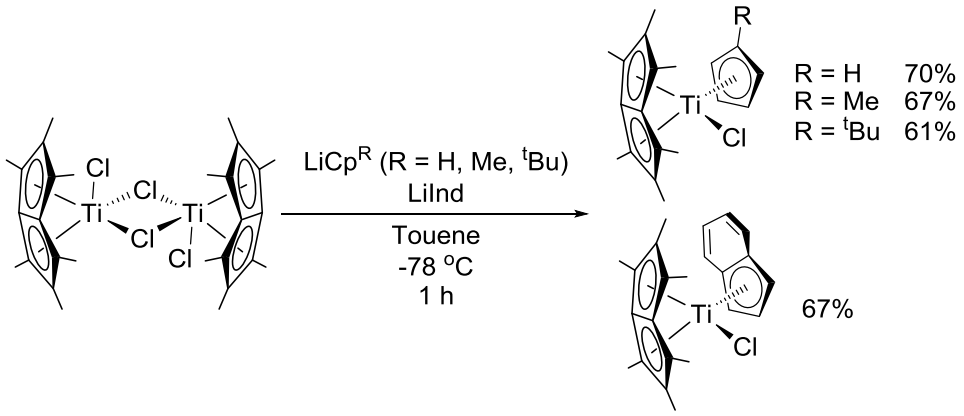
Catalysts based on the archetypal zirconocene polymerisation catalyst, Cp_2ZrCl_2, illustrate the impact of even minor variations to the ancilliary ligand set. Mono-substitution of both Cp rings produces $Cp^R{}_2ZrCl_2$ (R = H, Me, ^{n}Bu, ^{t}Bu). In the presence of 1000 eq MAO the lowest activities are observed for R = ^{t}Bu (3750 $kg_{PE}/(mol\cdot h\cdot bar)$), followed by R = Me and H (7150 and 8850 $kg_{PE}/(mol\cdot h\cdot bar)$ respectively), while R = ^{n}Bu demonstrates significantly improved activities of 11700 $kg_{PE}/(mol\cdot h\cdot bar)$, a 212% increase relative to R = ^{t}Bu.[5] However, substitution of halide ligands for more labile substituents can lead to significant increases in activity, such as the observed 135% increase in activity observed for *meso*-EBI*$ZrCl_2$ when compared to the bis-benzyl derivative.[6]

This chapter describes the modification of the Pn*MCp^R(X) motif in order to explore the effect of ligand substitution on polymerisation activity. The synthesis and characterisation of 8 new Cp^R and 11 leaving group derivatives is described. The complexes are fully characterised by elemental analysis, single crystal X-ray diffraction, multinuclear NMR spectroscopy and, where relevant, EPR spectroscopy.

2.2 Synthesis of Pn*MCp^R(Cl) (M = Ti, Zr)

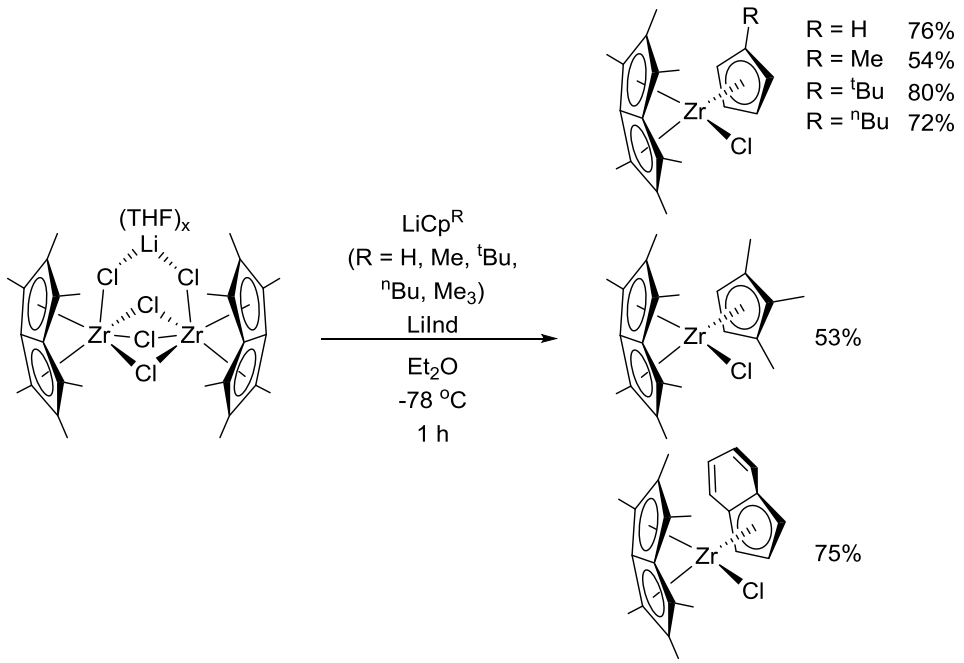
Pn*TiCp^R(Cl) complexes were synthesised by the reaction of $[TiPn^*Cl(\mu\text{–}Cl)]_2$[7] and LiCp^R (Cp^R = Cp, Cp^{Me}, Cp^{tBu}, Ind) in toluene at −78 °C over 1 hour, producing orange to dark red solids in good yields (61–70%) (Scheme 2.1). As the steric demand of the Cp^R ligand increased, reduction of the Ti(IV) dimer was observed to compete with the desired

salt metathesis producing an intractable mixture of Ti(IV) and Ti(III). This can be readily demonstrated with the attempted synthesis of Pn*TiCp*(Cl); at room temperature in toluene minimal reaction was observed to occur with LiCp*, while heating to 60 °C for 2–16 h produced a complex ^{1}H NMR spectrum indicating a mixture of diamagnetic and paramagnetic components that could not be assigned. Use of more polar solvents encouraged further side-reactivity, presumably favouring reduction given the broad featureless NMR spectrum obtained. Attempts to disfavour this reductive pathway by using the softer reagent, Cp*SnMe$_3$, led to no reaction, while extended sonication or addition of crown-ether to solubilise LiCp* did not permit the synthesis of the target compound. It was therefore concluded that the small, first-row group 4 metal was simply too crowded to accommodate these sterically demanding ligands.



Scheme 2.1. *Synthesis of Pn*TiCp^{R}Cl (Cp^R = Cp, Cp^{Me}, Cp^{tBu}, Ind).*

Synthesis of the analogous zirconium complexes was achieved by reaction of [Pn*Zr(μ–Cl)$_{3/2}$]$_2$(μ–Cl)$_2$Li.THF$_x$[7] with LiCp^R (Cp^R = Cp, Cp^{Me}, Cp^{tBu}, Cp^{nBu}, Cp^{Me3}, Ind) at –78 °C in diethyl ether over 1 hour to afford Pn*ZrCp^{R}Cl in moderate to good yields (54–80%) (Scheme 2.2). The reaction is accelerated by employing a more polar solvent, Et$_2$O or THF; in toluene high temperatures (80 °C) and long reaction times (2 - 4 days) are required to achieve full conversion. By comparison to the titanium analogues, the increased ionic radius of zirconium allows more sterically demanding cyclopentadienyl derivatives to be appended to the metal (0.42 and 0.59 Å for Ti(IV) and Zr(IV) respectively).[8]



Scheme 2.2. *Synthesis of Pn*ZrCp^R(Cl) (Cp^R = Cp, Cp^{Me}, Cp^{tBu}, Cp^{nBu}, Cp^{Me3}, Ind).*

2.3 Solid state structural analysis

The solid-state molecular structures were obtained for all Pn*MCp^R(Cl) complexes, which are shown in Figure 2.1, with a comparison of some key structural features provided in Table 2.1. Of particular interest when interpreting solid-state structures of η^8-pentalene complexes is the fold angle (FA), defined as the deviation from planarity of the two pentalenic rings. This can inform understanding of the electronic and steric requirements of the metal, and is generally larger for small, electron deficient metals with minimal steric hindrance. With pseudo-tetrahedral Pn* derivatives asymmetric coordination is observed with canting of the carbocycle away from the "X" ligand. This can be measured by taking the average difference between the M–C1/C3 and M–C5/C7 bond lengths, and is referred to as Δ_{CNT}.

Similarly, distortion of the indenyl ligand can provide insight into electronic and spatial demands of the metal. Aromatic character in the benzannulated ligand is enhanced by slippage of the metal to η^3 from η^5 coordination, the so-called "indenyl effect", while structural distortions of the planar system are measured by the hinge angle (HA) and fold angle (FA). Collectively these slip-fold characteristics can be used to categorise the indenyl hapticity as true or distorted η^5, or η^3 coordination. These metrics are summarised in Figure 2.2.

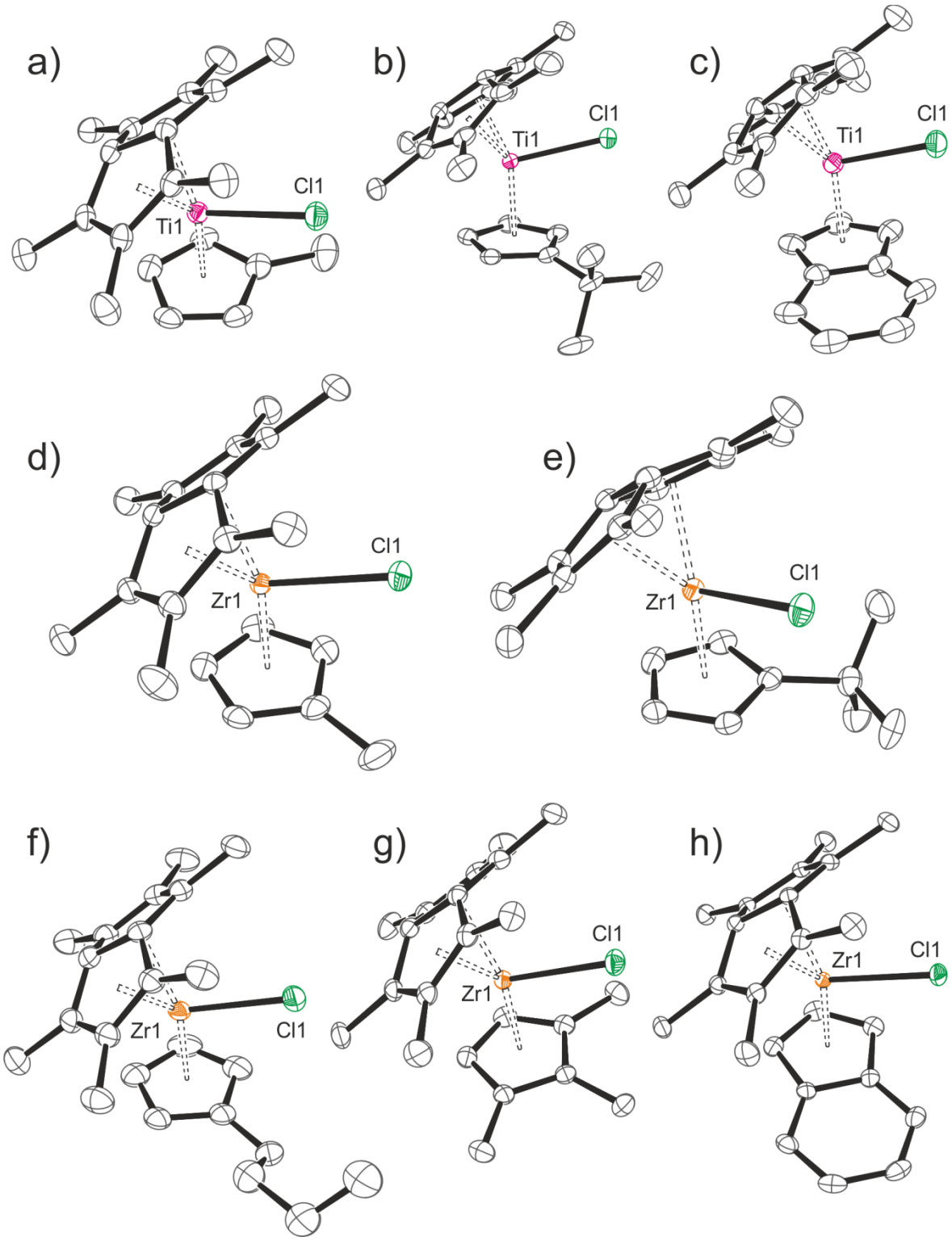
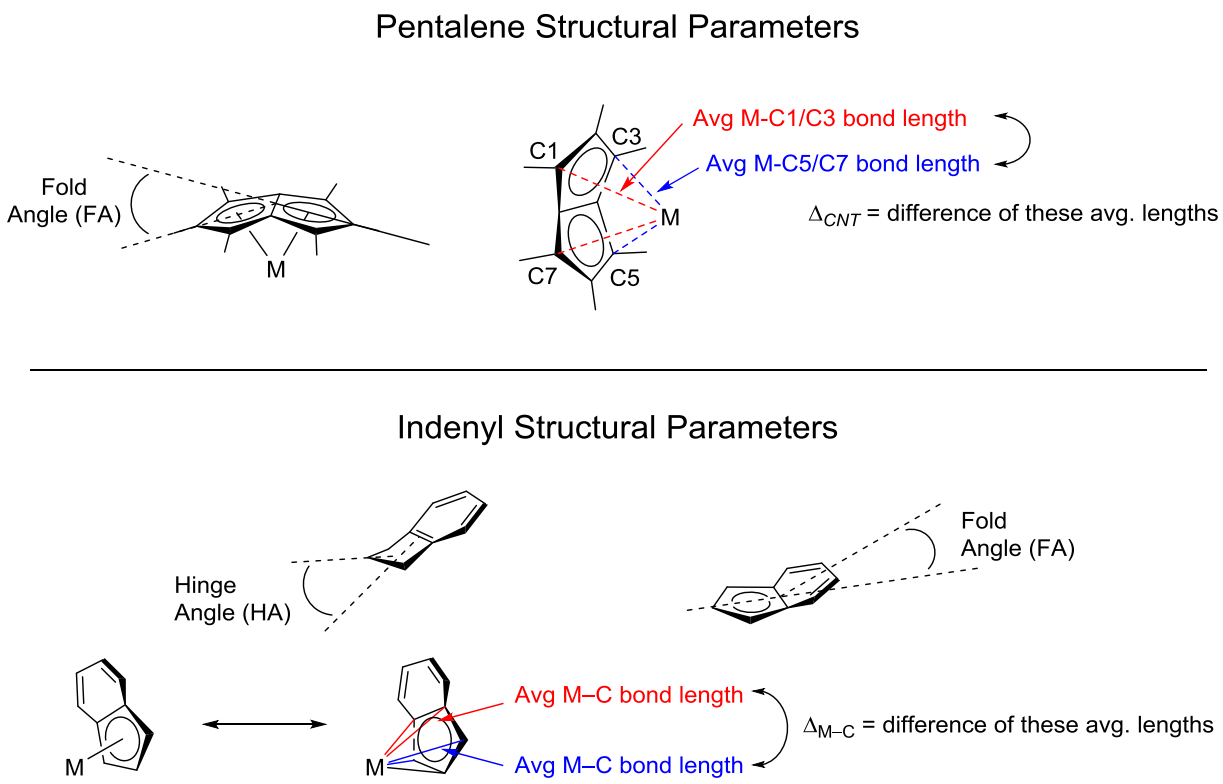


Figure 2.1. *Thermal displacement ellipsoid plots (50% probability) of a) Pn*TiCp^{Me}(Cl), b) Pn*ZrCp^{tBu}(Cl), c) Pn*TiInd(Cl), d) Pn*ZrCp^{Me}(Cl), e) Pn*ZrCp^{tBu}(Cl) f) Pn*ZrCp^{nBu}(Cl), g) Pn*ZrCp^{Me3}(Cl), h) Pn*ZrInd(Cl). H atoms are omitted for clarity.*



Slip-Fold Parameter	"True η^5"	Distorted η^5	η^3
HA	2.5	7 – 14	-
FA	4.4	6 – 13	28
Δ_{M-C}	0 – 0.03	0.11 – 0.42	0.8

Figure 2.2. *Summary of key structural parameters.*

In the solid state, all of the complexes are C_1 symmetric with pseudo-tetrahedral geometry about the metal centre. The Pn* ligand is bound asymmetrically, canting away from chloride ligand. The effects of this tilt are amplified by the Pn*−*Me* groups, which leads to a strong steric preference for substituents appended to the Cp ligand to point away from the downward cant of the Pn*, whilst avoiding eclipsing interactions with the chloride group. The magnitude of Δ_{CNT} appears much more sensitive to the nature of Cp^R substituent than metal centre.

The Ti–Cl bond lengths fall in the range 2.4608(6)–2.4769(6) Å and are slightly shorter than both the parent pentalene analogue PnTiCp(Cl) (2.512(1) Å)[9] and Pn*TiCp(Cl)

(2.5068(8) Å).[10] They are all, however, long compared to typical terminal Ti(IV)−Cl bonds; the longest example can be found in $TiCp_2$(4–MeO–TEMPO)Cl (2.5346(12) Å).[11] Although bond length does not always correlate exactly with bond strength when sterics are limiting, this does suggest a rather activated Ti–Cl bond. The indenyl ligand in Pn*TiInd(Cl) has slip-fold characteristics consistent with distorted η^5-coordination,[12,13] implying steric congestion around the metal centre (Δ_{M-C} = 0.16, HA = 5.95°, FA = 3.42°).

By comparison, the Zr–Cl bond lengths (2.5285(14)–2.5340(5) Å) are somewhat shorter than expected based on consideration of the ionic radii of the metal centres (4 coordinate Zr(IV) - 0.59 Å; Ti(IV) - 0.42 Å).[8] Zr–Cl bond lengths for structurally related compounds generally fall in the range 2.3–2.5 Å.[14,15] The slip-fold characteristics of Pn*ZrInd(Cl) indicate a slightly less distorted η^5-coordination relative to the titanium analogue, which reflects the radially expanded and less crowded coordination sphere of the metal centre (Δ_{M-C} = 0.10, HA = 4.82°, FA = 3.89°).

The Pn* fold-angle is marginally smaller for the zirconium complexes than the titanium analogues, correlating inversely with the ionic radius of the metal centre as has previously been observed.[10] However, in all cases the fold angle of the Pn* ligand is less than the Pn analogues, which is likely a result of the improved donor characteristics of Pn*; inductive donation of electron density from the six methyl groups around the pentalene framework allows the ligand to satisfy electron deficiency at the metal centre with less extreme distortion of the wingtip positions.

Complex	d(M–Cl)	Pn* Fold Angle	d(M–Pn*$_{cent}$)		d(M–Cp$^{R}_{cent}$)	Δ_{CNT}	^{1}H NMR δ		
							NWT		WT
*Pn*TiCp(Cl)*[a]	*2.5068(8)*	*30.98(12)*	*1.9924(11)*	*1.9967(12)*	*2.0631(14)*	*0.1240*	*1.51*	*1.64*	*2.19*
PnTiCp(Cl)[b]	*2.512(1)*	*33.57*	*1.969*	*1.969*	*2.057*	*0.1120*	-	-	-
Pn*TiCp^{Me}(Cl)	2.4769(6)	31.29(10)	1.9912(9)	1.9942(10)	2.0704(10)	0.1339	1.51	1.68	2.20
Pn*TiCp^{tBu}(Cl)[c]	2.4608(6)	31.9(2)	1.991(2)	1.993(2)	2.056(2)	0.1240	1.58	1.69	2.16
Pn*TiInd(Cl)[c]	2.4668(13)	31.7(2)	1.981(2)	1.993(2)	2.119(2)	0.0953	1.35	1.83	2.00
*Pn*ZrCp(Cl)*[a]	*2.5484(8)*	*30.33(14)*	*2.1094(13)*	*2.1099(11)*	*2.2189(17)*	*0.1125*	*1.64*	*1.75*	*2.10*
PnZrCp(Cl)[b]	*2.540(1)*	*32.64*	*2.095*	*2.095*	*2.215*	*0.1130*	-	-	-
Pn*ZrCp^{Me}(Cl)	2.5309(4)	30.56(7)	2.1062(6)	2.1065(7)	2.2219(7)	0.1206	1.66	1.81	2.12
Pn*ZrCp^{tBu}(Cl)	2.5319(5)	30.00(9)	2.1117(8)	2.1181(8)	2.2338(8)	0.1372	1.71	1.83	2.09
Pn*ZrCp^{nBu}(Cl)[c]	2.5285(14)	30.7(2)	2.1028(18)	2.1058(23)	2.2192(23)	0.1358	1.70	1.84	2.11
Pn*ZrCp^{Me3}(Cl)	2.5340(5)	30.56(9)	2.0984(8)	2.1259(8)	2.2310(8)	0.1211	1.64	1.90	2.14
Pn*ZrInd(Cl)	2.5317(4)	30.42(7)	2.0880(7)	2.1172(7)	2.2515(7)	0.1020	1.49	1.91	1.94

Table 2.1. *Comparison of selected bond lengths (Å), angles (°) and selected ^{1}H NMR spectroscopic chemical shifts (ppm) given in C_6D_6. NWT and WT correspond to "non-wingtip" and "wingtip" environments. Relevant literature comparisons are provided in italics. a) see ref 9; b) see ref 8. c) Solid state parameters are given as averages of the two independent molecules in the asymmetric unit.*

2.4 NMR spectroscopic characterisation

The ^{1}H NMR spectra of the complexes display 3 sharp singlets of intensity 6:6:6 corresponding to the Pn*–*Me* groups, which is expected for these pseudo-tetrahedral complexes of the general formula Pn*MXY; two singlets correspond to the non-wingtip (NWT) positions and a further singlet is observed for the wingtip (WT) methyl substituents. This is consistent with C_s molecular symmetry in solution due to rotation of the Cp^R ligand; a complex of C_1 symmetry would result in 6 discrete resonances in a 3:3:3:3:3:3 ratio for the Pn*–*Me* groups. There are no clear relationships between the observed ^{1}H NMR resonances and either the donor capacity of the Cp^R substituent, or structural parameters in the solid state. Complexes bearing indenyl ligands show large differences in the chemical shifts of the Pn*−*Me* resonances relative to compounds with alkyl-Cp substituents. This is presumably due to nascent aromatic character at the benzannulated position producing ring-currents that influence the chemical shifts of the Pn* protons. On breaking the five-fold symmetry of the Cp ligand fragment by functionalising one or more positions, the ^{1}H NMR spectra show the expected splitting resulting from reduced symmetry of a rotating ring. For example, in complexes with a Cp^R ligand (R = Me, ^{t}Bu, ^{n}Bu), the AA'XX' spin system leads to the observation of two pseudo-triplets with typical coupling constants in the range 2.6 – 2.7 Hz (Figure 2.3).[16]

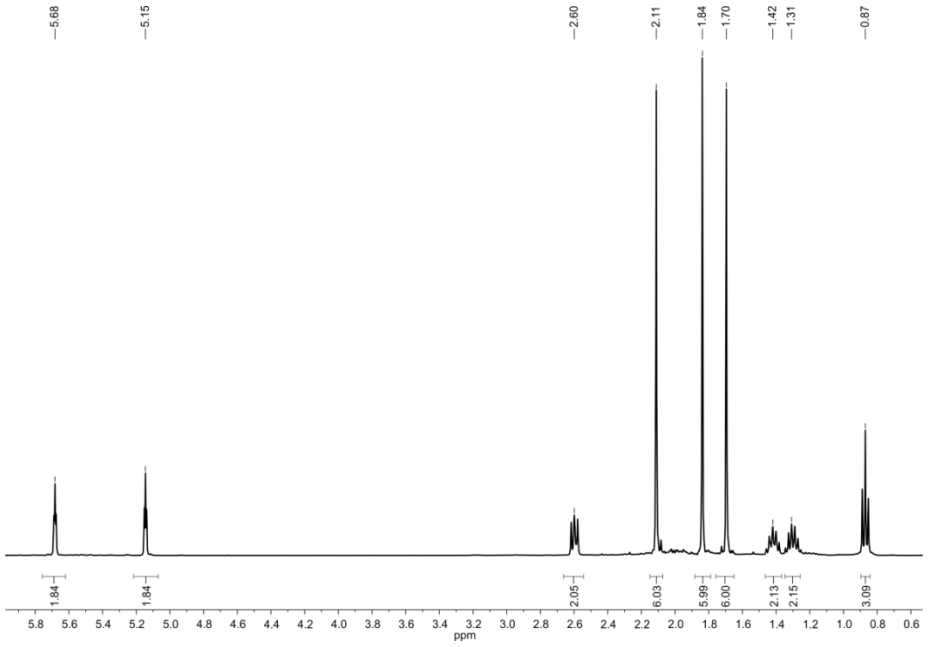


Figure 2.3. *^{1}H NMR spectrum of Pn*ZrCp^{nBu}(Cl) (C_6D_6, 298 K, 400 MHz).*

2.5 Density Function Theory calculations

Density functional theory calculations were performed at the BP86[17–19] and B3LYP[17,20,21] level of theory by Dr Zoë Turner. Geometry optimisations were generally found to reproduce the metrical data established experimentally well, though reproduction of the C20–Cp$^{R}_{centroid}$–M1–Cl1 torsion angle did appear to be more sensitive to the functional in use. The calculations indicated that, for all Pn*MCp^{R}(Cl) complexes, the HOMO primarily consisted of M–Pn* π-bonding interactions, whilst the LUMO was centred on metal d-orbitals (Figure 2.4).

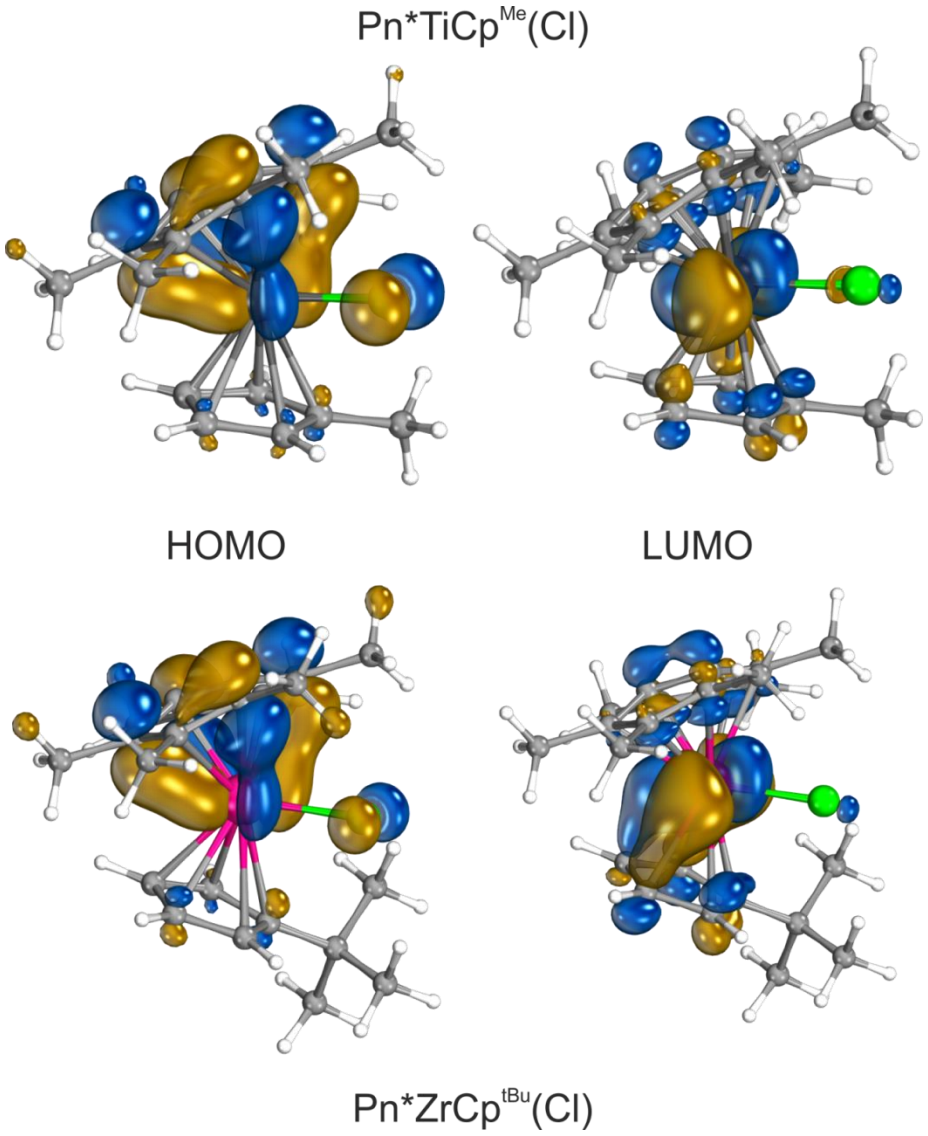


Figure 2.4. *Frontier molecular orbitals of top: Pn*TiCp^{Me}(Cl) bottom: Pn*ZrCp^{tBu}(Cl).*

2.6 Synthesis and characterisation of Pn*MCp^{R}(Me) (M = Ti, Zr)

Pn*TiCp(Me) can be synthesised by addition of 1.05 eq MeLi in toluene at −78 °C to Pn*TiCp(Cl). Crystallisation from pentane at –78 °C affords a pure brown solid in 86% yield. Pn*ZrCp(Me) and Pn*ZrCp^{Me}(Me) can by synthesised by an analogous route to the titanium analogue, using MeLi in toluene, with the products isolated in 55% and 50% yields respectively (Figure 2.5). Pn*ZrCp(Me) was also synthesised using the Grignard reagent, MeMgI, although this led to a significant decrease in isolated yield (12 %). Single crystals were grown by slow-evaporation of a benzene solution; comparison of bond lengths, fold angles and selected NMR spectroscopic resonances of Pn*MCp^{R}(X) complexes are given in Table 2.2.

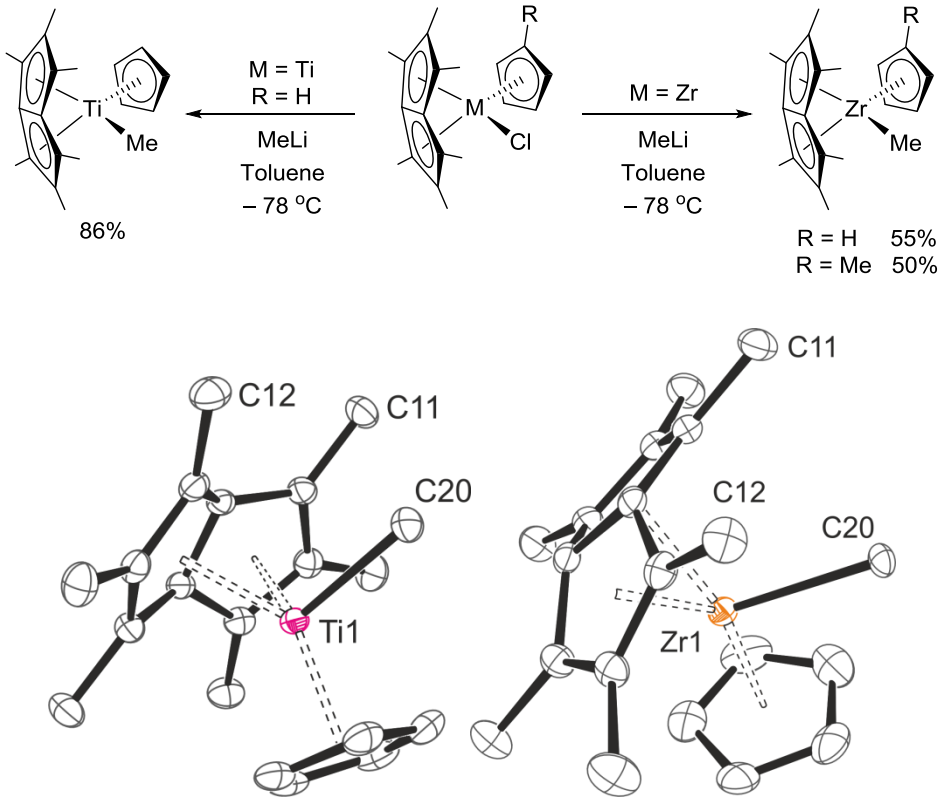


Figure 2.5. *Synthesis and thermal displacement ellipsoid plots of Pn*MCp(Me)(M = Ti, Zr). Ellipsoids shown at 50% probability, H atoms omitted for clarity.*

As expected, NMR spectroscopy indicates the complexes are C_s symmetric in solution, with 3 Pn*-*Me* resonances of equal intensity observed. Interestingly, the ^{13}C–^{1}H HMBC spectrum of the methyl complexes indicates a correlation between M–CH_3 and one Pn*−CH_3 environment. Given that an interaction is observed and that the proton only interacts with one

Pn*–CH_3 environment, it can be concluded that ring-whizzing of the Pn* is not operative on the NMR timescale. Similar features have previously been noted by Kilpatrick *et al*. in (μ:η^5,η^5–Pn†)$_2$Ti$_2$(μ:η^2-^{13}CO) (Pn† = [1,4–C$_8$H$_4$(Si^{i}Pr$_3$)$_2$]$^{2-}$). In this case, coupling was observed between ^{13}CO and the proximal non-wingtip substituents (Si and H) of the Pn† ring ($J_{C\text{-}H}$ = 3.2 Hz; $J_{C\text{-}Si}$ = 1.5 Hz), and was attributed to through-space scalar coupling.[22] For Pn*MCp^{R}(Me) the coupling is proposed to result from an analogous interaction of M–CH_3 with C11/C12 (Figure 2.5).

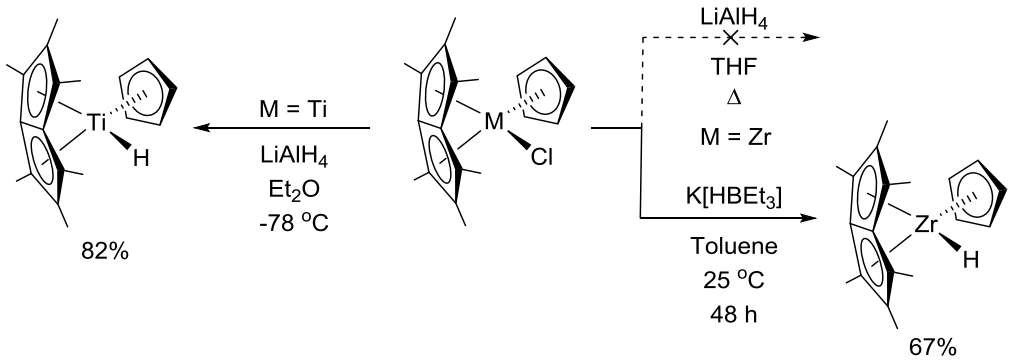
2.7 Synthesis and characterisation of Pn*MCp(H) (M = Ti, Zr)

Transition metal hydrides have long been of interest due to their ability to reduce small molecules of environmental importance, such as CO[23,24] and CO$_2$[25–27] as well as their proposed intermediacy in olefin polymerisation following β-hydride elimination of the growing polymer chain.[28,29] Strategies for their synthesis use either H$_2$ as a hydride source, or an exogenous hydride-transfer reagent. With H$_2$, hydride formation can result either from oxidative addition, as in the synthesis of Cp*$_2$ZrH$_2$ from (Cp*$_2$ZrN$_2$)$_2$N$_2$,[24] or from sigma-bond metathesis with metal alkyl precursors such as [Cp$_2$ZrMe(THF)][BPh$_4$] to form [Cp$_2$ZrH(THF)][BPh$_4$].[30] Alternatively, hydride transfer reagents such as LiAlH$_4$ or LiAlH(O^{t}Bu)$_3$ can be employed, with the latter used to synthesise many Cp$^{R}_2$Zr hydride derivatives such as [Cp$^{Me}_2$ZrH(μ–H)]$_2$ from the corresponding chloride complex.[31]

Given Ti(II)/Zr(II) complexes incorporating η^8-Pn* and Cp ligands are not expected to be accessible on electron-counting grounds, Pn*MCp(Me) (M = Ti, Zr) were exposed to 2 bar H$_2$ and monitored by ^{1}H NMR spectroscopy. At room temperature, minimal reaction was observed, however, heating to 80 °C led to very slow consumption of the starting material along with the formation of Pn*MCp(H). In the case of Pn*ZrCp(Me) complete conversion required 21 days of heating, so hydride transfer agents were investigated in pursuit of a more practical synthesis.

Pn*TiCp(H) was successfully synthesised from Pn*TiCp(Cl) using LiAlH$_4$ as the hydride transfer reagent at −78 °C in Et$_2$O. No reaction was observed to occur until approximately −20 °C at which point the colour changed from brown to pale orange. This contrasts with the reactivity observed in C$_6$D$_6$, where elevated temperatures and long reaction times are required, which leads to darkening of the solution to green-brown, perhaps due to partial reduction to Ti(III). However, following recrystallisation of the ethereal mixture from

pentane, pure Pn*TiCp(H) was obtained in 82% yield. Although a number of alternative hydride reagents were tested ($NaBH_4$, KH, LiH) in both polar and non-polar solvents, at a variety of different temperatures and durations, reactivity was only observed with $LiAlH_4$. Within this series of hydrides, $[AlH_4]^-$ has been reported to be the most potent hydride-donor (ΔG = 43 kcal/mol) followed by $[BH_4]^-$ (50 kcal/mol).[32] By comparison the binary hydrides KH and LiH are basic, but are generally poor hydride donors. Attempts to synthesise Pn*ZrCp(H) using $LiAlH_4$ as a hydride donor were unsuccessful, presumably as a result of stronger metal-ligand bonds encountered on descending group 4. However, moving to the more potent hydride donor, $K[HBEt_3]^-$ ($[HBEt_3]^-$ ΔG = 24 kcal/mol) Pn*ZrCp(H) can be successful synthesised from Pn*ZrCp(Cl) at 25 °C over 48 hours in 67% yield (Figure 2.6).



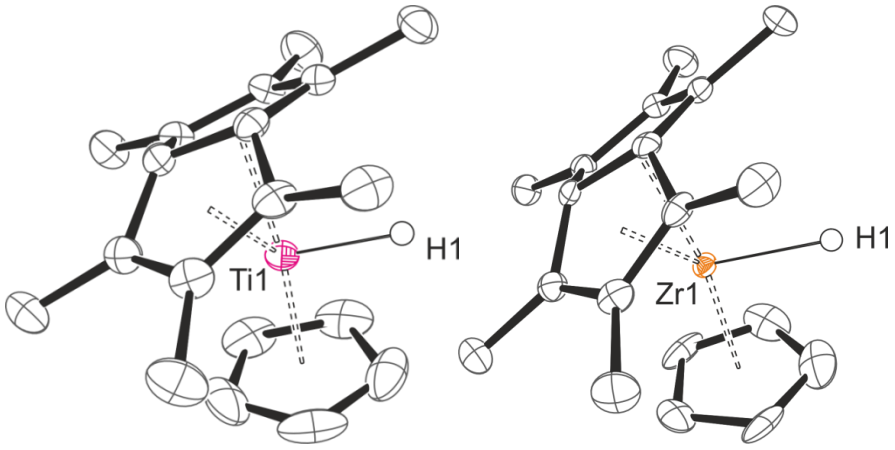


Figure 2.6. *Synthesis and thermal displacement ellipsoid plots of Pn*MCp(H) (M = Ti, Zr). Ellipsoids shown at 50% probability, Pn* and Cp H atoms omitted for clarity, hydride atoms crystallographically located.*

NMR spectra of these hydride complexes show a similar coupling between M–*X* and the Pn* periphery as observed for Pn*MCp^{R}(Me). A through-space coupling is observed between M–*H* and one set of Pn*–*Me* NWT resonances, which are resolved as a doublet

(J_{H-H} = 1.6 and 1.7 Hz for Pn*TiCp(H) and Pn*ZrCp(H) respectively). Although the carbocyclic resonances remain similar upon variation of the metal centre, the hydridic resonance of Pn*ZrCp(H) is somewhat deshielded relative to that of Pn*TiCp(H) (0.69 and −1.50 ppm respectively). Single crystals were grown by slow evaporation of benzene solutions; the data collected were of sufficient quality to crystallographically locate the hydride atoms. The solid state structures are discussed in more detail in section 2.12 along with a comparison of key metrics of all Pn*MCp(X) derivatives.

2.8 Synthesis and characterisation of Pn*MCp(R) (M = Ti, Zr, R = Et, ^{n}Bu)

Following the failure of $LiAlH_4$ to furnish Pn*ZrCp(H), an alternative synthetic route was initially pursued, involving the transient synthesis of Pn*ZrCp(^{n}Bu) from Pn*ZrCp(Cl) and ^{n}BuLi, that was expected to β–hydride eliminate to form the target hydride and butene. Surprisingly the zirconium *n*-butyl complex was found to be remarkably stable with respect to elimination. Heating a C_6D_6 solution of the complex to 80 °C for 1 week leads to 5% conversion to Pn*ZrCp(H). It is known that β–hydride elimination is retarded in electronically saturated complexes (*vide infra)*, so this impressive thermal stability is likely a consequence of the 18-electron configuration attained by Pn*ZrCp(^{n}Bu). Scaling up the alkylation in toluene allows for the synthesis of pure Pn*ZrCp(^{n}Bu) in 57% yield. In the case of the titanium analogue, while there was some indication of alkylation of the metal, the major product observed by ^{1}H NMR spectroscopy was Pn*TiCp(H). Broad features in the NMR spectrum allude also to the formation of reduced titanium by-products. Low temperature synthesis did not allow for the clean isolation of the desired titanium-alkyl complex, and attempts at its isolation were abandoned.

Given the successful synthesis of Pn*ZrCp(^{n}Bu), the ethyl analogue was targeted by an analogous route. Following the reaction by ^{1}H NMR spectroscopy the product was observed to form less readily, requiring two equivalents of EtLi to fully consume the Pn*ZrCp(Cl) starting material. In the presence of this excess alkyl-lithium reagent Pn*ZrCp(Et) appeared to be more susceptible to β-hydride elimination. Although the solubility characteristics of Pn*ZrCp(H) and Pn*ZrCp(Et) are very similar, Pn*ZrCp(Cl) is only slightly soluble in alkane solvents. Therefore by extracting the reaction mixture into pentane after 6 hours, before significant quantities of Pn*ZrCp(H) had formed, a crude mixture consisting of

Pn*ZrCp(Cl) and Pn*ZrCp(Et) (30:70) could be obtained, which could be further crystallised to obtain the ethyl complex as a pure yellow solid in 25% yield (Figure 2.7).

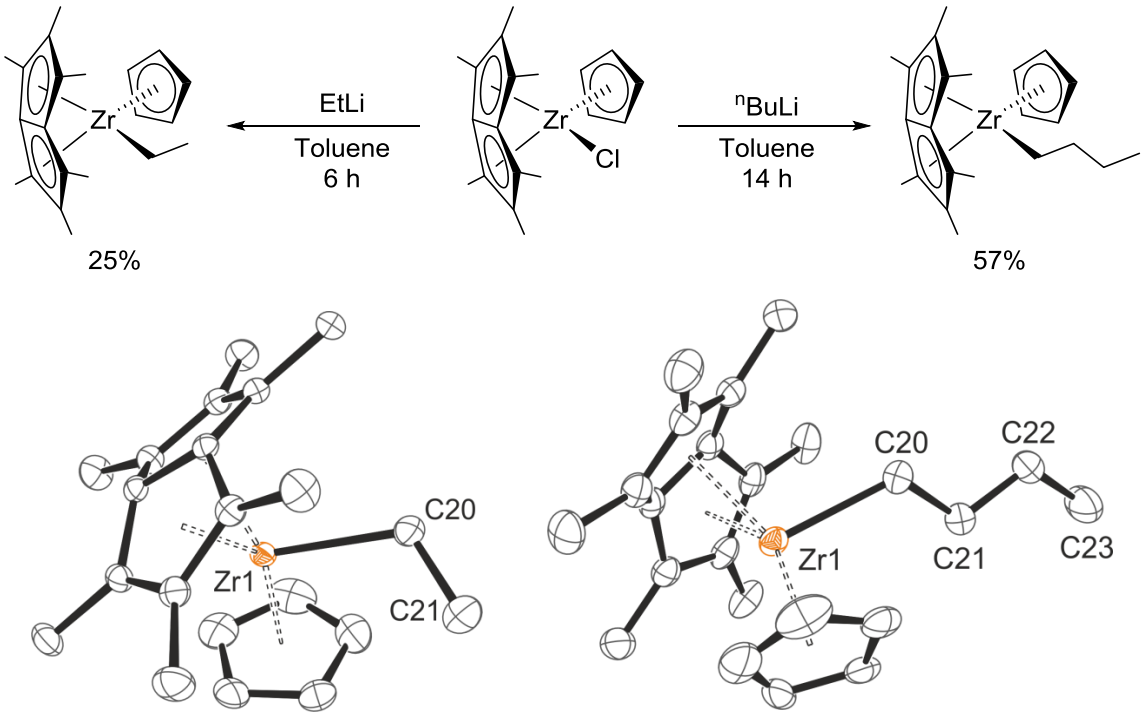


Figure 2.7. *Synthesis and thermal displacement ellipsoid plots of Pn*ZrCp(R) (R = Et, ^{n}Bu). Ellipsoids shown at 50% probability, H atoms omitted for clarity.*

The stability of these metal *n*-alkyl complexes is particularly significant in the context of this study given their expected formation during ethylene polymerisation. However, interest in these compounds is not limited to the field of olefin polymerisation; $Cp_2Zr(^{n}Bu)_2$ and $Cp_2Zr(Et)_2$ have been investigated for the last 30 years as precursors to the "Negishi reagent". This Zr(II) synthon is generally formulated as an olefin complex, $Cp_2Zr(\eta^2\text{-}C{=}C\text{-}R)$ resulting from β-hydride abstraction of the transient dialkyl, that is active towards cyclometallation, hydrosilylation and activation of other small molecules.[33–35] Despite the intensity with which these compounds have been studied only a handful of zirconium ethyl/*n*-butyl complexes have been crystallographically characterised. This is due to the kinetic accessibility of decomposition pathways, particularly β-hydride elimination, which typically renders these complexes thermally unstable. However, this can be inhibited by stabilising the complex electronically or sterically. $[2,6{-}(CH_2C_5H_4)_2C_5H_3N]Zr^{n}Bu_2$ inhibits decomposition by attaining a filled set of d-orbitals,[36] while $(Cy_2N)_3Zr^{n}Bu$ relies instead on steric preclusion by large cyclohexyl substituents leading to thermolytic stability up to 100 °C.[37] Perhaps the most

pertinent example is COT″CpZr(Et) (COT″ = 1,4–$(SiMe_3)_2$–COT), which was synthesised from the parent halide and $EtMgBr(MeOCMe_3)_{0.5}$ (Figure 2.8).[38,39] Given the desired application of Pn*MCp^{R}(X) complexes as ethylene polymerisation catalysts it is interesting to note the very high activities of the halide complex, COT″CpZr(Cl), alongside the similar coordination chemistry clearly accessible to these related dianionic carbocyclic motifs.

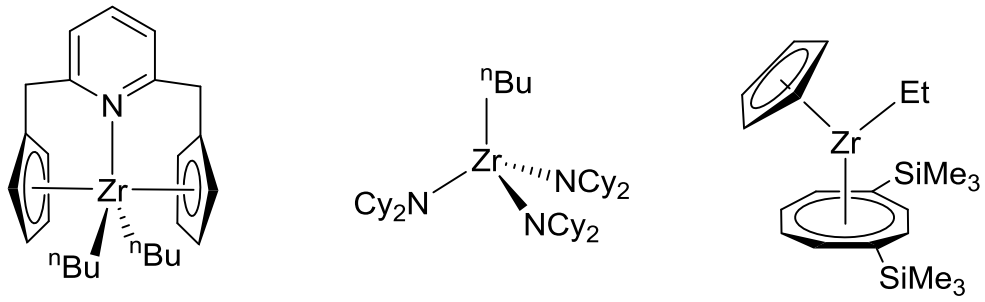


Figure 2.8. *Selected stable zirconium n-alkyl complexes (left to right): [2,6−$(CH_2C_5H_4)_2C_5H_3N$]Zr^{n}Bu$_2$[36], $(Cy_2N)_3Zr^{n}Bu$[37] and COT″CpZr(Et).*[38,39]

2.9 Synthesis and characterisation of Pn*ZrCp(CH_2Ph)

The benzyl complex, Pn*ZrCp(CH_2Ph) was made by salt metathesis with potassium benzyl and Pn*ZrCp(Cl) in toluene followed by crystallisation from cold pentane to give the product as a yellow microcrystalline solid in 43% yield. Single crystals suitable for an X-ray diffraction study were grown by slow evaporation of a benzene solution (Figure 2.9). The benzylic C*H*$_2$ protons are resolved as a singlet at 1.16 ppm, while C_s molecular symmetry is inferred in solution by the observed 6:6:6 relative integration of Pn*−*Me* environments by ^{1}H NMR spectroscopy.

Benzyl ligands are known to display varied coordination modes, where electron donation from the aromatic system to the metal centre can lead to increased hapticity. There are some key spectroscopic and structural features that allow for classification of the bonding mode. NMR spectra of $\eta^{(>1)}$ isomers should exhibit shielded resonances corresponding to the *ortho*-protons of the aromatic ring (<6.8 ppm) and the methylene carbon position (<75 ppm) while increased $^{1}J_{C\text{-}H}$ coupling constants should be observed for the methylene environment (> 130 Hz) as the hapticity increases.[40–42] Structurally, the M–CH_2–Ph bond angle should contract below 97°, and the difference between d(M–*C*H$_2$) and d(M–C$_{ortho}$) (δ_{ipso}) should be less than 0.5 Å.[43]

NMR spectra of Pn*ZrCp(CH_2Ph) display an *ortho*-proton resonance as 6.93 ppm, and methylene-carbon resonance at 37.3 ppm ($^{1}J_{C\text{-}H}$ = 121.5 Hz). In the solid state M–CH_2–Ph angles of 115.34(12)° are observed and δ_{ipso} is calculated as 0.922 Å. Taken together these data point conclusively to η^1-coordination of the benzyl ligand, to give the 18-electron complex, Pn*ZrCp(η^1–CH_2Ph).

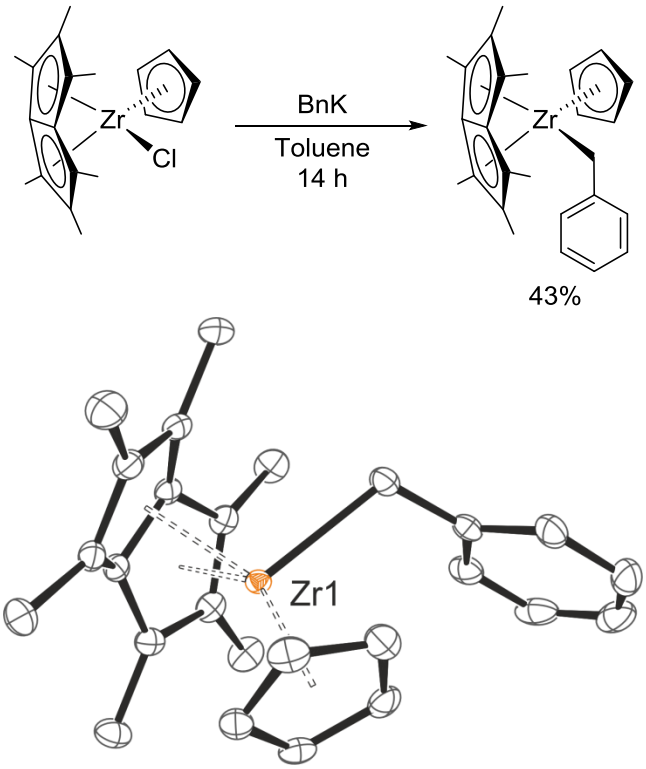
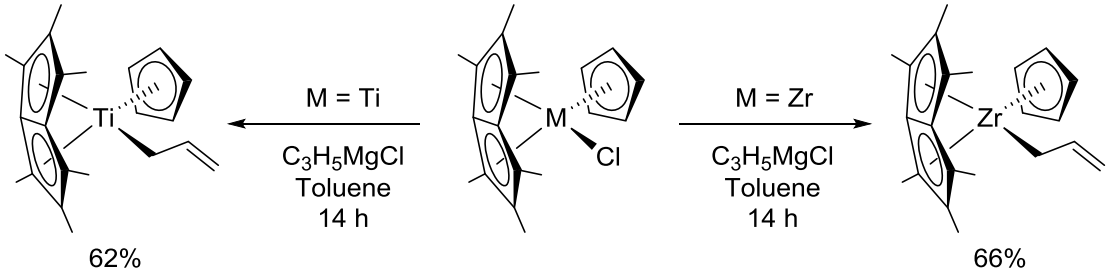


Figure 2.9. *Synthesis and thermal displacement ellipsoid plot of Pn*ZrCp(CH_2Ph). Ellipsoids shown at 50% probability, H atoms omitted for clarity.*

2.10 Synthesis and characterisation of Pn*MCp(C_3H_5) (M = Ti, Zr)

The allyl complex, Pn*TiCp(C_3H_5), was synthesised by the reaction of Pn*TiCp(Cl) and C_3H_5MgCl in toluene over 8 hours. Crystallisation from pentane at −78 °C allows for the isolation of the allyl complex in 62% yield as a deep red, thermally unstable, crystalline solid. The zirconium analogue, Pn*ZrCp(C_3H_5) can be made by a similar route, giving the product as a yellow crystalline solid in 66% yield (Scheme 2.3). When this latter reaction is carried out in THF instead of toluene, the previously reported bis(allyl) complex, Pn*Zr(C_3H_5)$_2$, is formed as a byproduct. This is perhaps unsurprising given the previously reported preparation of PnZr(C_3H_5)$_2$ involves the addition of LiC_3H_5 to PnZrCp(Cl) in Et_2O.[44]



Scheme 2.3. *Synthesis of Pn*MCp(C_3H_5) (M = Ti, Zr).*

2.11 Spectroscopic studies of Pn*MCp(C_3H_5)

The allyl ligand (C_3H_5) is a interesting not just because of its variable hapticity and frequently encountered fluxional behaviour; metal-allyl intermediates have also been observed as intermediates in the titanium and zirconium catalysed polymerisation of olefins.[45–47] The solution state behaviour of allyl complexes falls into three broad categories: at one extreme is static η^1-coordination, which is straightforwardly identified by the presence of a doublet resonating generally <1 ppm in the ^{1}H NMR spectrum corresponding to the M–CH_2– environment; at the other extreme of static η^3-coordination this environment adjacent to the metal centre is now lost, forming AM_2X_2 spin systems due to magnetic inequivalence of the terminal protons, H_{syn} and H_{anti}; in the intermediate regime, rapid isomerisation from η^1-η^3 leads to magnetic equivalence of all four terminal protons on the NMR timescale, which are resolved as a single resonance, coupling to the central methine proton to produce a quintet (AX_4).

In the case of Pn*ZrCp(C_3H_5) the room temperature ^{1}H NMR spectrum in C_7D_8 contains a C_s symmetric Pn* fragment with corresponding Cp resonance (Figure 2.10: b, f, g, h), a quintet (6.0 ppm, $^3J_{H\text{-}H}$ = 11.1 Hz, Figure 2.10, a) and a very broad feature at 4.30 ppm ($\nu_{1/2}$ = 840 Hz). On cooling the solution to 211 K, a non-binomial sextet is observed at 6.03 ppm (Figure 2.10: a), and the broad resonance decoalesces into a doublet (0.83 ppm) and two diastereotopic doublets at 4.96 and 4.81 ppm (Figure 2.10: i, c, d). This corresponds to static η^1-coordination to form the 18-electron Pn*ZrCp(η^1-C_3H_5). Heating the solution to 373 K, the methine proton is resolved as a non-binomial quintet, and the terminal positions are observed as a broadened singlet (2.06 ppm, $\nu_{1/2}$ = 40 Hz, Figure 2.10: e).

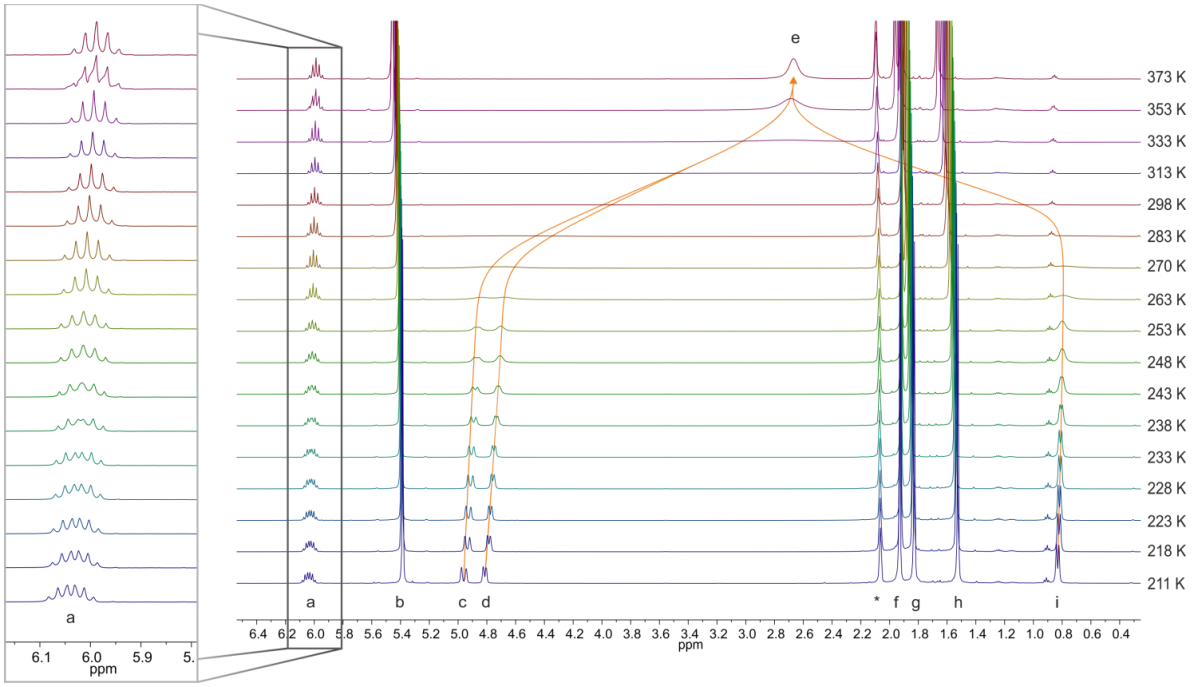


Figure 2.10. *Variable temperature ^{1}H NMR spectrum of Pn*ZrCp(C$_3$H$_5$). * = C$_7$D$_8$; a = M–CH$_2$–C**H**=CH$_2$, b = Cp, c = M–CH$_2$–CH=CH**H**$_{anti}$,d = M–CH$_2$–CH=CH**H**$_{syn}$, e = M–C**H**$_2$–CH–C**H**$_2$, f,g,h = Pn*–Me, i = M-C**H**$_2$–.*

This corresponds to rapid isomerisation of the allyl ligand, as shown in Figure 2.11. The intermediate Pn*ZrCp(η^3-C$_3$H$_5$) is formally a 20-electron complex, which though unusual, is known for the carbocyclic zirconium derivatives (η^5-Cp^{Me})$_3$Zr(η^1-Cp^{Me})[48], Pn$_2$Zr[49] and Pn*$_2$Zr.[50] Alternatively, the transiently formed η^3-allyl moiety may be accommodated by ring-slippage of the Cp ring to form Pn*Zr(η^3-Cp)(η^3-C$_3$H$_5$).

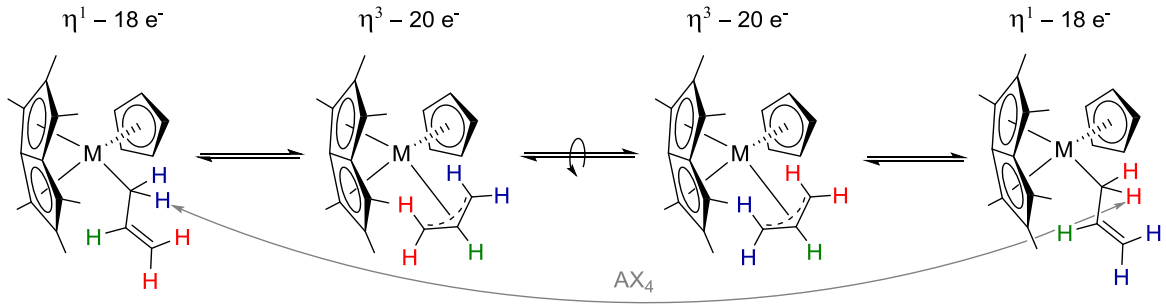


Figure 2.11. *Proposed Mechanism of Allyl Fluxionality.*

Although the η^3 isomer could not be directly observed by ^{1}H NMR spectroscopy, fourier transform infra-red (FTIR) spectroscopy can be a useful tool for differentiating between allylic isomers due to the faster timescale of the experiment. Characteristic C=C stretching

frequencies are typically observed at 1500 – 1600 cm^{-1} for η^1 isomers, with η^3-isomers demonstrating reduced stretching frequencies in the range 1400-1500 cm^{-1} resulting from the decreased bond order of the delocalised π-system. The solid state FTIR spectrum (KBr pellet) displays a C=C bond stretch at 1589 cm^{-1} consistent with η^1 coordination, while a tetrachloroethylene solution shows a similar stretch at 1594 cm^{-1}. Variable temperature FTIR was attempted in C_2Cl_4, however, even at elevated temperatures no lower frequency stretch was observed, demonstrating the short-lived nature of the η^3-isomer. Single crystals suitable for an X-ray diffraction study were grown by slow evaporation of a benzene solution (Figure 2.12). These confirmed η^1-coordination, with clear localisation of the double bond between C20–C22 (1.331(3) Å. c.f. C20–C21: 1.466(3) Å).

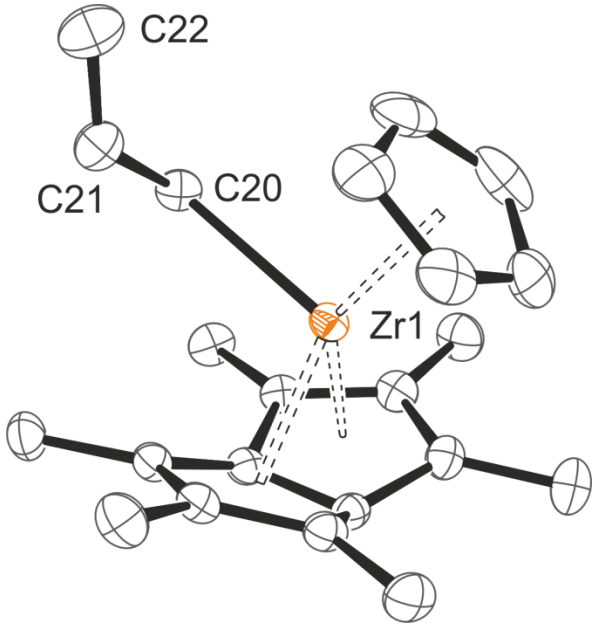


Figure 2.12. *Thermal displacement ellipsoid plot (50% probability) of Pn*ZrCp(C_3H_5). H atoms omitted for clarity.*

The titanium analogue shows rather different variable temperature behaviour. At room temperature the ^{1}H NMR spectrum clearly indicates the retention of static η^1-coordination; a non-binomial sextet at 5.90 ppm (Figure 2.13, a), a characteristic doublet at 0.83 ppm and two olefinic resonances for the *–syn* and *–anti* terminal protons at 4.68 and 4.80 ppm respectively (Figure 2.13: k, f, e). FTIR spectroscopy confirms this proposed structure, with a C=C stretch observed at 1590 cm^{-1} (KBr pellet).

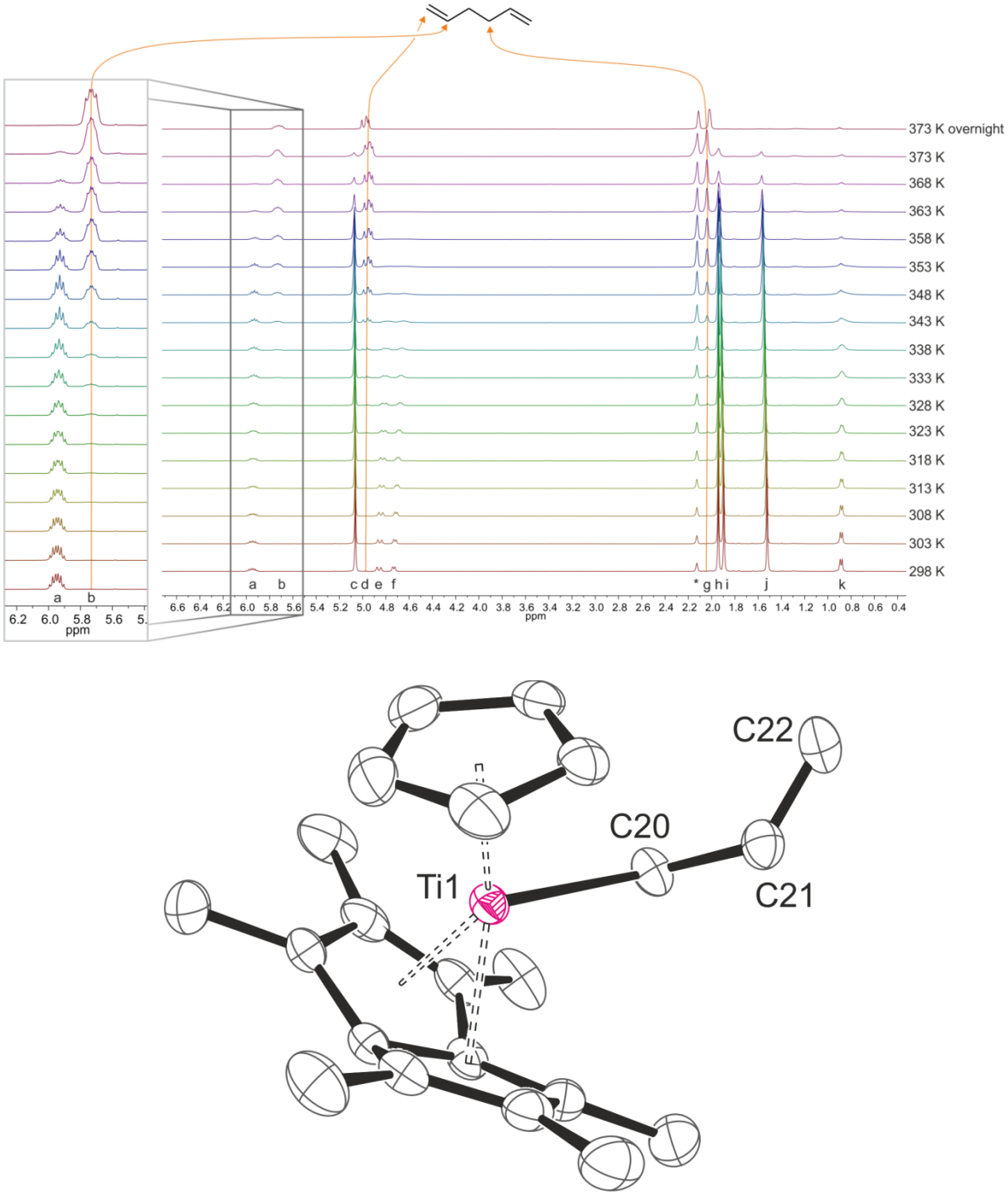


Figure 2.13. *Top: Variable temperature ^{1}H NMR spectrum of Pn*TiCp(C_3H_5). * = C_7D_8; a = M–CH_2–C**H**=CH_2, b = CH_2=C**H**–CH_2–, c = Cp, d = C**H**$_2$=CH–, e = M–CH_2–CH=CH**H**$_{anti}$, f = M–CH_2–CH=CH**H**$_{syn}$, g = CH_2=C**H**–CH_2–, h, i, j = Pn*–Me, k = M–C**H**$_2$–. Peaks b, d and g correspond to 1,5-hexadiene. Bottom: Thermal displacement ellipsoid plots (50% probability) of Pn*ZrCp(C_3H_5). Pn* and Cp H atoms omitted for clarity.*

Single crystals, grown by slow evaporation of a benzene solution, exhibit the same structural features as the zirconium analogue, with localisation of the double bond between C21–C22 (Figure 2.13, 1.329(3) Å. c.f. Pn*ZrCp(C_3H_5) C20–C21: 1.470(3) Å). Additional bond metrics are discussed in more detail in section 2.12 .

Upon warming a C_7D_8 solution and following the reaction by ^{1}H NMR spectroscopy, the allyl resonances are observed to broaden up to 363 K, alongside a decrease in the intensity of both the allyl environments and the carbocyclic framework. Simultaneously three new resonances appear at 5.73, 4.93 and 2.03 ppm, which were confirmed to correspond to 1,5−hexadiene by comparison to a genuine sample in C_7D_8 (Figure 2.13: b, d, g).

This is proposed to form by the coupling of allylic radicals resulting from homolytic bond cleavage of the Ti–C_{allyl} bond. Single crystals of the reduced titanium by-product were obtained by cooling a pentane solution of the purple thermolysed mixture to −80 °C, which were crystallographically identified as Pn*TiCp (Figure 2.14). The Pn* ligand was disordered over at least two positions, and the Cp ring disordered over two positions, which prevented a complete solution of the structure, with multiple data-sets displaying the same disorder. A ball-and-stick model produced from this data is shown in Figure 2.14 to illustrate connectivity. Further chemical confirmation of the product was desirable to eliminate the possibility that the disordered Cp-ring was a coordinated arene; re-oxidation to Pn*TiCp(Cl) was achieved using CPh_3Cl in C_6D_6, allowing for the confident assignment of the thermolysis product as Pn*TiCp. Interestingly, early attempts to synthesise $Cp_2Ti(C_3H_5)_2$ observed similar reductive decomposition to $Cp_2Ti(C_3H_5)$ with postulated formation of an organic radical, while the more redox-inactive zirconium congener, $Cp_2Zr(C_3H_5)_2$ could be synthesised straightforwardly.[51,52] Given the desired application of these complexes as ethylene polymerisation catalysts, the thermal accessibility of this decomposition pathway alludes to the potential limitations of the Pn*TiCp(X) motif.

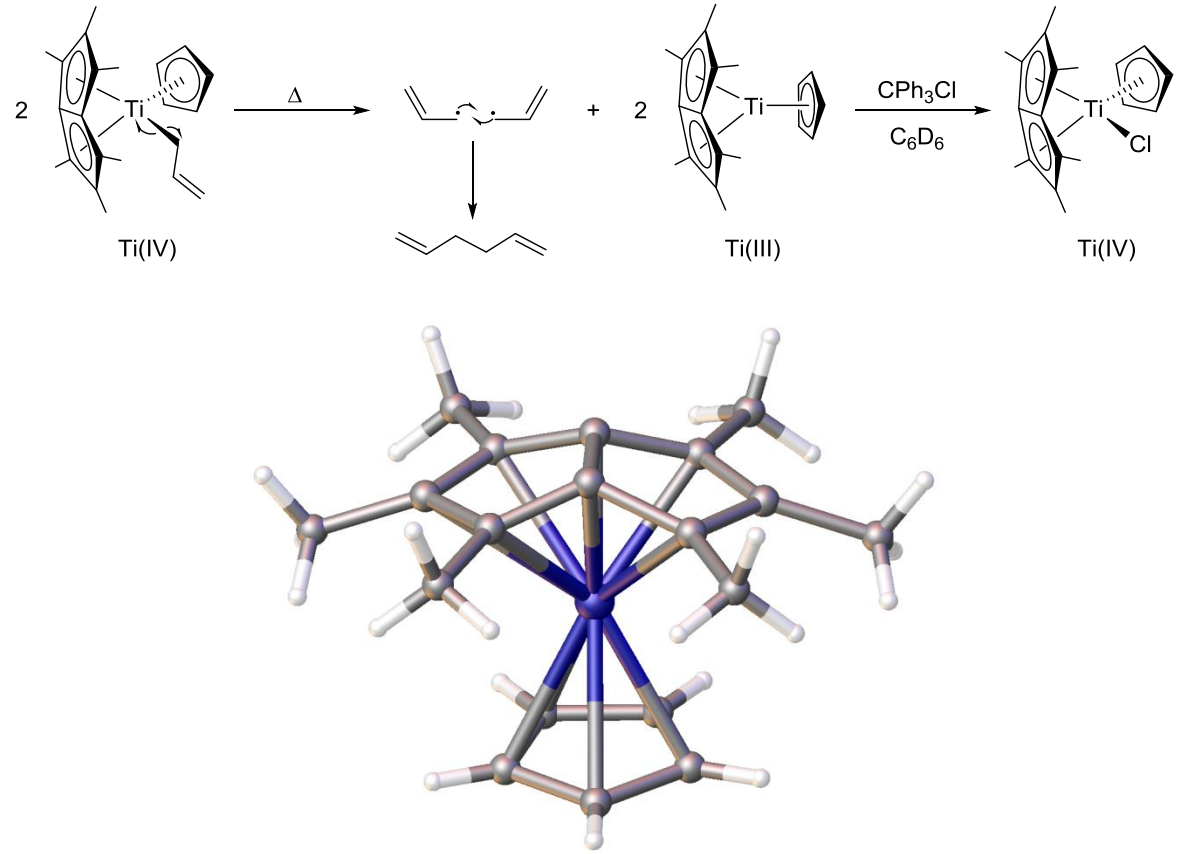


Figure 2.14. *Synthesis of PnTiCp via thermolysis of Pn*TiCp(C_3H_5) and subsequent re-oxidation with CPh_3Cl. Ball-and-stick model of Pn*TiCp produced from single crystal X-ray diffraction data.*

Pn*TiCp is silent by NMR spectroscopy, but can be further characterised by EPR spectroscopy. X-band measurements were carried out at 298 K in a 5 mM toluene solution. A single isotropic resonance was observed at g = 1.9946 with no coupling observed to spin-active titanium nuclei Ti^{47} and Ti^{49} (S = $\frac{5}{2}$ and $\frac{7}{2}$ respectively). This contrasts with the observed isotropic g value of isoelectronic Ti(COT)Cp, which is more significantly shifted from the free electron value (g_e = 2.0023) to g = 1.981.[53] In this latter case, unresolved hyperfine coupling to both titanium nuclei and carbocyclic protons at room temperature leads to the observation of a very broad resonance (20G) compared to 2G found for Pn*TiCp. Upon cooling Pn*TiCp to 120 K the anisotropic g tensors are resolved, and the complex appears axially symmetric ($g_z > g_x = g_y$), however, this could not be simulated adequately. W-band measurements were therefore carried out at 85 K to investigate whether this was due to unresolved hyperfine coupling.

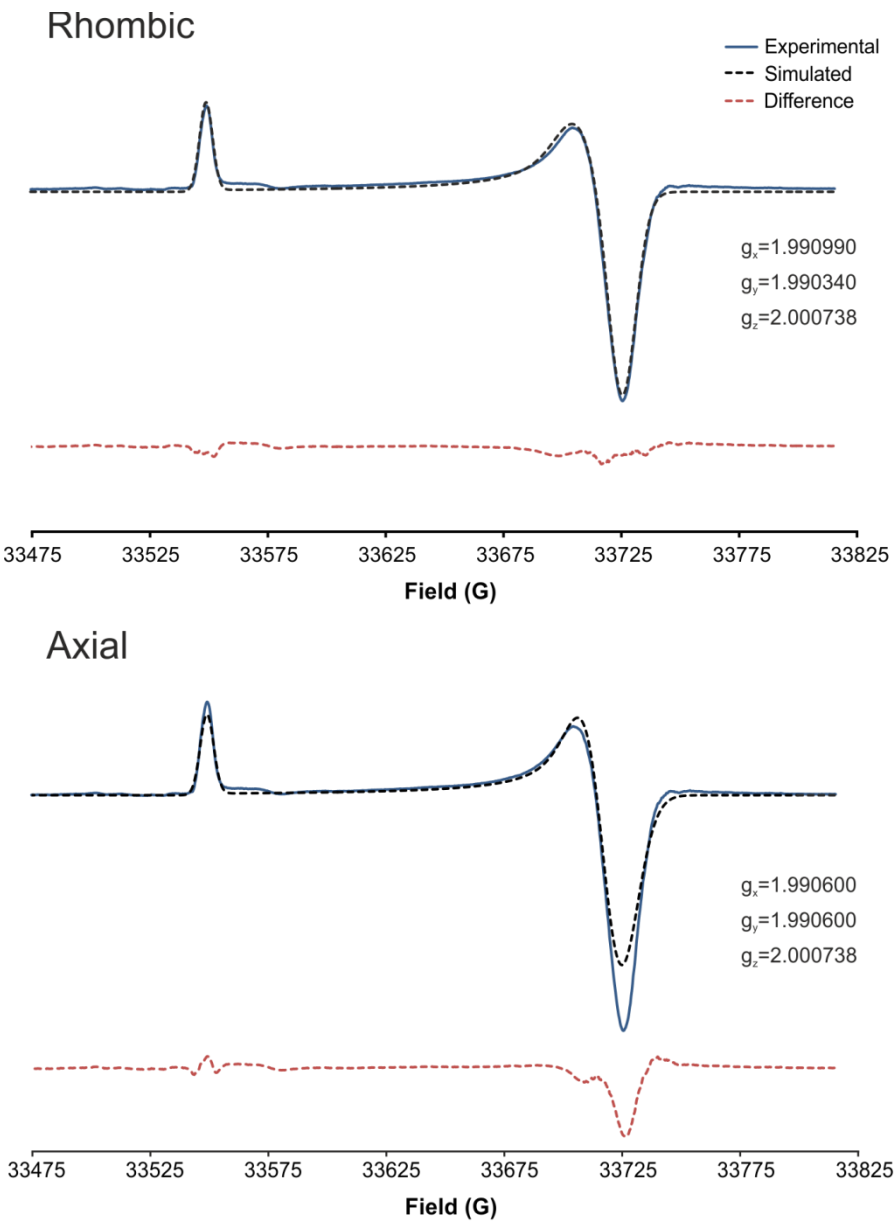


Figure 2.15. *Experimental and Simulated EPR Spectrum of Pn*TiCp as rhombic (top) or axially symmetric (bottom).*

Again no interaction with spin-active nuclei was resolved and the spectrum could not be adequately simulated as axially symmetric, with the peak at 33725 G poorly reproduced. A more convincing fit was achieved by allowing a slight rhombic distortion of g_x and g_y as shown in Figure 2.15. This contrasts with the COT analogue, which is well reproduced as axially symmetric with $g_{\parallel} = 1.998$ and $g_{\perp} = 1.969$.[53,54]

Despite the appearance of C_{2h} symmetry in the solid state structure, the Pn* ligand is in fact bound unsymmetrically. The distances between titanium and NWT ring carbon atoms are not equivalent in experimental or calculated structures (*vide infra*) although the accuracy of the former is limited by structural disorder. Regardless, this shift away from axial structural symmetry may be responsible for this slight rhombic distortion of the *g*-tensor. Indeed the COT ligand in Ti(COT)Cp lies on a crystallographic mirror plane that bisects the ligand through the centre, and therefore axial symmetry is definitively retained in the solid-state.[55] However, these structural and electronic distortions cannot be correlated with certainty on the basis of available data.

Density functional theory calculations were carried out at the B3LYP level of theory, which reproduced the bond metrics well given the disordered experimental structure, confirming the validity of the diffraction data. The SOMO, shown in Figure 2.16, is primarily metal-based (86%), of predominant d_{z^2} and $d_{x^2-y^2}$ character (22 and 62% respectively.), with the spin density localised on the titanium atom (96%). Simulation of the anisotropic *g*-tensors reproduces the magnitude of the experimentally observed rhombic distortion to a high degree of accuracy (g_x = 1.989044, g_y = 1.989744, g_z = 2.001033), however, further work will be required to understand the origins of this rhombicity.

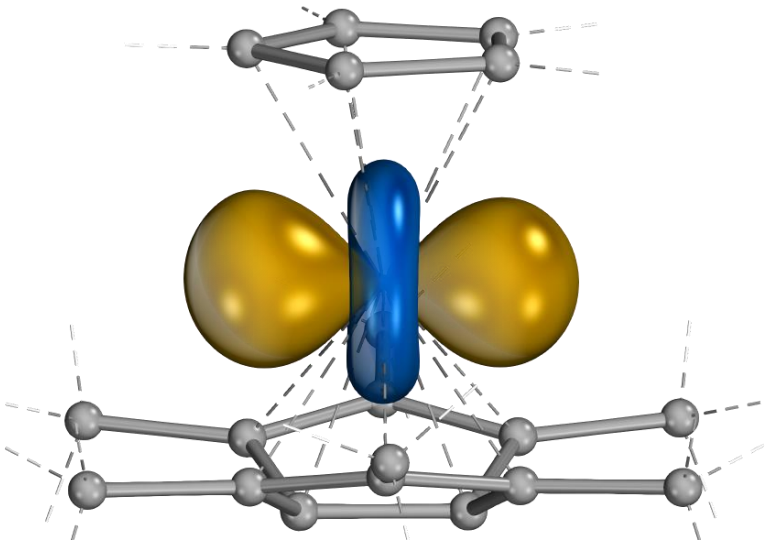


Figure 2.16. *Calculated singularly occupied molecular orbital (SOMO) of Pn*TiCp.*

It is interesting to compare the behavior of Pn*MCp(C_3H_5) with the di-substituted analogues Pn*M(C_3H_5)$_2$ (M = Ti, Zr). The ^{1}H NMR spectrum of Pn*ZrCp(C_3H_5)$_2$ demonstrates static

η^3-coordination to give the 18-electron complex Pn*Zr(η^3-C_3H_5)$_2$. Haptropic shifts were inferred from the formation of an AX_4 spin system on heating to 333 K. In the case of Pn*Ti(C_3H_5)$_2$ an AX_4 spin system is observed at room temperature corresponding to rapid $\eta^1 \leftrightarrow \eta^3$ isomerisation. However, the product was thermally unstable, decomposing in solution over 12 hours. In light of the reductive decomposition of Pn*TiCp(C_3H_5), a comparable mechanism may be responsible; in the future this could provide an interesting entry point to the chemistry of reduced Pn*Ti complexes.

2.12 Solid state structural analysis of Pn*MCp(X) complexes

A summary of some key bond lengths and angles for Pn*MCp(X) complexes are provided in Table 2.2. In the solid state, Pn*MCp(X) (X = H, Me) are C_s symmetric, with the remaining M(IV) complexes demonstrating C_1 symmetry, with pseudo-tetrahedral geometry observed at the metal centre. As before, the Pn* ligand cants away from the "X" ligand with the magnitude of this canting generally greater for zirconium than titanium. Typical values for Δ_{CNT} Pn*ZrCp(X) are >0.1 Å, with titanium analogues around 0.08 Å. Exceptions to this are the hydride complexes, Pn*MCp(H), where the minimal steric requirement of H^- causes a levelling of the Pn* moiety. The largest cant is observed for Pn*ZrCp(CH_2Ph), which may be an indication of crowding of the metal centre.

As before, elongation of metal ligand bond distances is observed in zirconium relative to titanium, along with a general decrease in Pn* fold-angle as a result of the increased ionic radius of the 4d metal. The hydride complexes, Pn*MCp(H), display more severe folding of the pentalene ligand, which is presumably both steric and electronic in origin. Weaker inductive electron donation from H^- relative to R^- leaves the metal centre more electron deficient, which is accommodated by an enhanced metal–Pn* bonding interaction. Contraction of the M–Pn*$_{cent}$ distances and the increased fold-angle are likely facilitated by the minimal steric repulsions imposed by the hydride ligand. It is unclear whether the deshielded NWT resonances observed for these Pn*MCp(H) complexes are a result of this structural change; as observed for PnMCp^R(Cl) complexes, no significant correlation is observed between these key crystallographic parameters and the spectroscopic data.

Complex	d(M–X)	Pn* Fold Angle	d(M–Pn*$_{cent}$)		d(M–Cp$^{R}_{cent}$)	Δ_{CNT}	^{1}H NMR δ		
							NWT		WT
*Pn*TiCp(Cl)*[a]	*2.5068(8)*	*30.98(12)*	*1.9924(11)*	*1.9967(12)*	*2.0631(14)*	*0.1240*	*1.51*	*1.64*	*2.19*
Pn*TiCp(Me)	2.2666(14)	31.55(6)	1.9853(6)	1.9903(6)	2.0778(7)	0.0806	1.52	1.92	1.94
Pn*TiCp(H)	1.69(4)	33.56(10)	1.9477(4)	1.9490(4)	2.0328(4)	0.0535	1.51	2.05	2.55
Pn*TiCp(C_3H_5)*	2.312(2)	31.90(9)	1.9885(9)	1.9896(9)	2.0639(9)	0.0861	1.45	1.84	1.92
*Pn*ZrCp(Cl)*[a]	*2.4668(13)*	*31.7(2)*	*1.981(2)*	*1.993(2)*	*2.119(2)*	*0.1125*	*1.35*	*1.83*	*2.00*
Pn*ZrCp(Me)	2.3735(18)	30.65(10)	2.101(1)	2.1209(9)	2.2323(12)	0.1167	1.64	1.97	1.97
Pn*ZrCp^{Me}(Me)	2.348(2)	30.10(11)	2.1089(9)	2.1203(10)	2.2262(11)	0.0986	1.63	1.99	2.00
Pn*ZrCp(H)	1.97(7)	31.26(19)	2.0888(18)	2.0946(15)	2.216(11)	0.0895	1.69	2.05	2.59
Pn*ZrCp(Et)	2.3634(18)	30.51(7)	2.1106(7)	2.1146(7)	2.2294(7)	0.1071	1.65	1.96	1.96
Pn*ZrCp(^{n}Bu)	2.3461(16)	30.24(7)	2.1133(7)	2.1163(7)	2.2388(12)	0.1000	1.63	1.96	1.99
Pn*ZrCp(CH_2Ph)	2.3782(18)	30.22(8)	2.1119(9)	2.1339(8)	2.2218(9)	0.1498	1.65	1.88	2.03
Pn*ZrCp(C_3H_5)	2.3836(19)	30.58(8)	2.1150(7)	2.1167(8)	2.2210(7)	0.1198	1.59	1.90	1.94

Table 2.2. *Comparison of selected bond lengths (Å), angles (°) and selected ^{1}H NMR spectroscopic chemical shifts (ppm). Relevant literature comparisons are provided in italics. a) see ref 9. *Solid state parameters are given as averages of the two independent molecules in the asymmetric unit.*

Reduction of the titanium centre from Ti(IV) to Ti(III) leads to a flattening of the Pn* ligand, as the less electropositive metal centre provides reduced compensation for distortion of the carbocyclic framework. Unsurprisingly, this is accompanied by an increase in the metal-centroid distances.

2.13 Conclusion

19 new complexes have been synthesised and fully characterised based on the Pn*MCp^{R}(X) motif. The smaller ionic radius of titanium prevents ligation of bulky Cp derivatives such as Cp^{Me3} and Cp*, which are more readily accommodated by zirconium.

A series of leaving group variants were synthesised, including unusually stable zirconium *n*-alkyl complexes that could be accessed *via* the corresponding alkyl-lithium reagent, although facile β-hydride elimination prevented the synthesis of analogous titanium *n*-alkyl derivatives. Metal-hydride complexes were not readily accessible by hydrogenation of these alkyl derivatives, but could be successfully synthesised from $LiAlH_4$ and K[$HBEt_3$] for titanium and zirconium respectively.

The fluxional behaviour of Pn*MCp(C_3H_5) (M = Zr, Ti) was studied by variable temperature NMR spectroscopy, which illustrated unexpected η^1–η^3 isomerisation for M = Zr, while thermolytic decomposition was observed for Pn*TiCp(C_3H_5). This decomposition is proposed to occur *via* allyl radical generation with concomitant formation of Pn*TiCp and 1,5–hexadiene. Despite the initial appearance of axial molecular symmetry in Pn*TiCp, canting of the Pn* ligand desymmetrises the complex, and the anistropic EPR spectrum displays rhombic symmetry. This was corroborated by DFT calculations, which reproduce the rhombic distortion well, although insufficient data is available to indicate if canting is the root cause of this electronic asymmetry.

2.14 References

(1) Bochmann, M. *J. Chem. Soc., Dalton Trans.* **1996**, No. 3, 255.
(2) Collins, R. A.; Russell, A. F.; Mountford, P. *Appl. Petrochemical Res.* **2015**, *5* (3), 153–171.
(3) Britovsek, G. J. P.; Gibson, V. C.; Wass, D. F. *Angew. Chem. Int. Ed.* **1999**, *38* (4), 428–447.
(4) Möhring, P. C.; Coville, N. J. *J. Organomet. Chem.* **1994**, *479* (1–2), 1–29.
(5) Bryliakov, K. P.; Semikolenova, N. V; Yudaev, D. V; Zakharov, V. A.; Brintzinger, H. H.; Ystenes, M.; Rytter, E.; Talsi, E. P. *J. Organomet. Chem.* **2003**, *683* (1), 92–102.
(6) Arnold, T. A. Q.; Turner, Z. R.; Buffet, J.-C.; O'Hare, D. *J. Organomet. Chem.* **2016**,

822, 85–90.
(7) Cooper, R. T.; Chadwick, F. M.; Ashley, A. E.; O'Hare, D. *Organometallics* **2013**, *32* (7), 2228–2233.
(8) Shannon, R. D. *Acta Crystallogr. Sect. A* **1976**, *32* (5), 751–767.
(9) Jonas, K.; Kolb, P.; Kollbach, G.; Gabor, B.; Mynott, R.; Angermund, K.; Heinemann, O.; Krüger, C. *Angew. Chem. Int. Ed.* **1997**, *36* (16), 1714–1718.
(10) Chadwick, F. M.; Cooper, R. T.; Ashley, A. E.; Buffet, J.-C.; O'Hare, D. M. *Organometallics* **2014**, *33* (14), 3775–3785.
(11) Huang, K.-W.; Han, J. H.; Cole, A. P.; Musgrave, C. B.; Waymouth, R. M. *J. Am. Chem. Soc.* **2005**, *127* (11), 3807–3816.
(12) Westcott, S. A.; Kakkar, A. K.; Stringer, G.; Taylor, N. J.; Marder, T. B. *J. Organomet. Chem.* **1990**, *394* (1–3), 777–794.
(13) Kakkar, A. K.; Taylor, N. J.; Marder, T. B.; Shen, J. K.; Hallinan, N.; Basolo, F. *Inorg. Chim. Acta* **1992**, *198–200*, 219–231.
(14) Bruno, I. J.; Cole, J. C.; Edgington, P. R.; Kessler, M.; Macrae, C. F.; McCabe, P.; Pearson, J.; Taylor, R. *Acta Crystallogr. Sect. B Struct. Sci.* **2002**, *58* (3), 389–397.
(15) Allen, F. H. *Acta Crystallogr. Sect. B Struct. Sci.* **2002**, *58* (3), 380–388.
(16) Newmark, R. A.; Boardman, L. D.; Siedle, A. R. *Inorg. Chem.* **1991**, *30* (4), 853–856.
(17) Becke, A. D. *J. Chem. Phys.* **1986**, *84* (8), 4524–4529.
(18) Perdew, J. P. *Phys. Rev. B* **1986**, *33* (12), 8822–8824.
(19) Perdew, J. P.; Yue, W. *Phys. Rev. B* **1986**, *33* (12), 8800–8802.
(20) Lee, C.; Yang, W.; Parr, R. G. *Phys. Rev. B* **1988**, *37* (2), 785–789.
(21) Becke, A. D. *J. Chem. Phys.* **1993**, *98* (7), 5648–5652.
(22) Kilpatrick, A. F. R.; Green, J. C.; Cloke, F. G. N. *Organometallics* **2015**, *34* (20), 4830–4843.
(23) Wolczanski, P. T.; Bercaw, J. E. *Acc. Chem. Res.* **1980**, *13* (4), 121–127.
(24) Manriquez, J. M.; McAlister, D. R.; Sanner, R. D.; Bercaw, J. E. *J. Am. Chem. Soc.* **1978**, *100* (9), 2716–2724.
(25) Jessop, P. G.; Ikariya, T.; Noyori, R. *Chem. Rev.* **1995**, *95* (2), 259–272.
(26) Wang, W.; Wang, S.; Ma, X.; Gong, J. *Chem. Soc. Rev.* **2011**, *40* (7), 3703.
(27) Wang, W.-H.; Himeda, Y.; Muckerman, J. T.; Manbeck, G. F.; Fujita, E. *Chem. Rev.* **2015**, *115* (23), 12936–12973.
(28) Siedle, A. R.; Lamanna, W. M.; Newmark, R. A.; Schroepfer, J. N. *J. Mol. Catal. A Chem.* **1998**, *128* (1–3), 257–271.
(29) Chirik, P. J.; Bercaw, J. E. *Organometallics* **2005**, *24* (22), 5407–5423.
(30) Jordan, R. F.; Bajgur, C. S.; Dasher, W. E.; Rheingold, A. L. *Organometallics* **1987**, *6* (5), 1041–1051.
(31) Jones, S. B.; Petersen, J. L. *Inorg. Chem.* **1981**, *20* (9), 2889–2894.
(32) Heiden, Z. M.; Lathem, A. P. *Organometallics* **2015**, *34* (10), 1818–1827.
(33) Negishi, E.-I.; Takahashi, T. *Acc. Chem. Res.* **1994**, *27* (5), 124–130.
(34) Keaton, R. J.; Koterwas, L. A.; Fettinger, J. C.; Sita, L. R. *J. Am. Chem. Soc.* **2002**, *124* (21), 5932–5933.
(35) Fischer, R.; Walther, D.; Gebhardt, P.; Görls, H. *Organometallics* **2000**, *19* (13), 2532–2540.
(36) Paolucci, G.; Pojana, G.; Zanon, J.; Lucchini, V.; Avtomonov, E. *Organometallics* **1997**, *16* (24), 5312–5320.
(37) Adler, C.; Tomaschun, G.; Schmidtmann, M.; Beckhaus, R. *Organometallics* **2014**, *33* (24), 7011–7014.

(38) Cloke, F. G. N. Polymerization catalysts. EP0672676 A2, 1995.
(39) Cloke, F. G. N. Polymerization catalysts. US 5536690 A, 1995.
(40) Hughes, A. K.; Meetsma, A.; Teuben, J. H. *Organometallics* **1993**, *12* (5), 1936–1945.
(41) Latesky, S. L.; McMullen, A. K.; Niccolai, G. P.; Rothwell, I. P.; Huffman, J. C. *Organometallics* **1985**, *4* (5), 902–908.
(42) Brookhart, M.; Green, M. L. H. *J. Organomet. Chem.* **1983**, *250* (1), 395–408.
(43) Rong, Y.; Al-Harbi, A.; Parkin, G. *Organometallics* **2012**, *31* (23), 8208–8217.
(44) Gabor, B.; Jonas, K.; Mynott, R. *Inorg. Chim. Acta* **1998**, *270* (1–2), 555–558.
(45) Babushkin, D. E.; Panchenko, V. N.; Brintzinger, H.-H. *Angew. Chem. Int. Ed.* **2014**, *53* (36), 9645–9649.
(46) Vatamanu, M.; Stojcevic, G.; Baird, M. C. *J. Am. Chem. Soc.* **2008**, *130* (2), 454–456.
(47) Karl, J.; Dahlmann, M.; Erker, G.; Bergander, K. *J. Am. Chem. Soc.* **1998**, *120* (23), 5643–5652.
(48) Palmer, E. J.; Strittmatter, R. J.; Thornley, K. T.; Gallucci, J. C.; Bursten, B. E. *Polyhedron* **2013**, *58*, 120–128.
(49) Gleiter, R.; Bethke, S.; Okubo, J.; Jonas, K. *Organometallics* **2001**, *20* (20), 4274–4278.
(50) Chadwick, F. M.; Cooper, R. T.; O'Hare, D. *Organometallics* **2016**, *35* (12), 2092–2100.
(51) Martin, H. A.; Jellinek, F. *J. Organomet. Chem.* **1967**, *8* (1), 115–128.
(52) Martin, H. A.; Lemaire, P. J.; Jellinek, F. *J. Organomet. Chem.* **1968**, *14* (1), 149–156.
(53) Samuel, E.; Labauze, G.; Vivien, D. *J. Chem. Soc., Dalton Trans.* **1979**, *0* (6), 956.
(54) Thomas, J. L.; Hayes, R. G. *Inorg. Chem.* **1972**, *11* (2), 348–350.
(55) Kool, L. B.; Rausch, M. D.; Rogers, R. D. *J. Organomet. Chem.* **1985**, *297* (3), 289–299.

Chapter 3: Ethylene Polymerisation with Pn*MCp^R(X) Catalysts

3.1 Introduction

Investigations into single-site ethylene polymerisation catalysis has allowed for the development of unprecedented mechanistic understanding of coordination-insertion olefin polymerisation.[1–6] Facile catalyst modification by functionalisation of ancillary ligands or substitution of leaving groups has provided a canvass for vast experimentation over the last 60 years in pursuit of increased activities and improved control over polymer properties.[7–10] Homogeneous ethylene polymerisation with excess methyl aluminoxane (MAO) as a co-catalyst is one of the most common methods employed to test ethylene polymerisation activity.[4,7,11–13] The most significant limitations are poor polymerisation control leading to reactor fouling and unsatisfactory morphology resulting from aggregation of polymer particles.[14,15] Immobilisation of catalysts on MAO-activated inorganic supports has previously been reported to alleviate these issues, albeit at the expense of reduced activities.[16–18]

This chapter describes an investigation into the activity of selected Pn*MCp^R(X) catalysts in homogeneous ethylene polymerisation with MAO as a co-catalyst. The slurry-phase ethylene polymerisation catalysis of the more active zirconium series, Pn*ZrCp^R(X), is then investigated, immobilised on and activated by silica-supported MAO, layered double hydroxide-supported MAO and solid polymethylaluminoxane. The immobilised complexes are characterised by solid-state NMR spectroscopy and their ethylene polymerisation activity measured. Polymerisations in the presence of H_2 are described to investigate the suitability of these complexes as PE-wax catalysts, and subsequently the copolymerisation of ethylene/1-hexene is discussed. Large scale polymerisations, carried out in collaboration with SCG Chemicals, are presented, which assess the effect of scale on polymer properties and activities. The polymer produced is characterised by GPC, SEM, DSC, powder XRD and NMR spectroscopy.

3.2 Solution phase ethylene polymerisation studies

[TiPn*Cl(μ-Cl)]$_2$, Pn*TiCp^{R}(Cl) (Cp^{R} = Cp, Cp^{Me}, Cp^{tBu}, Ind) and Pn*TiCp(H) were tested as ethylene polymerisation catalysts in solution, using MAO as a co-catalyst in a modest ratio ([Ti]:[MAO] = 1:250). The polymerisation activities were moderate on the Gibson scale,[19] and no significant difference is observed across the series (Figure 3.1). The highest activity was recorded at 35 kg$_{PE}$/(mol·h·bar) for Pn*TiCp^{tBu}(Cl). The moderate activity of [TiPn*Cl(μ-Cl)]$_2$ is particularly noteworthy given that it is more electron deficient and sterically available than the other complexes. These activities are significantly lower than those reported for Pn*HfCp(Cl) and Pn*ZrCp(Cl) (1009 and 4176 kg$_{PE}$/(mol·h·bar)) albeit at higher co-catalyst loadings ([M]:[MAO] = 1000).[20,21]

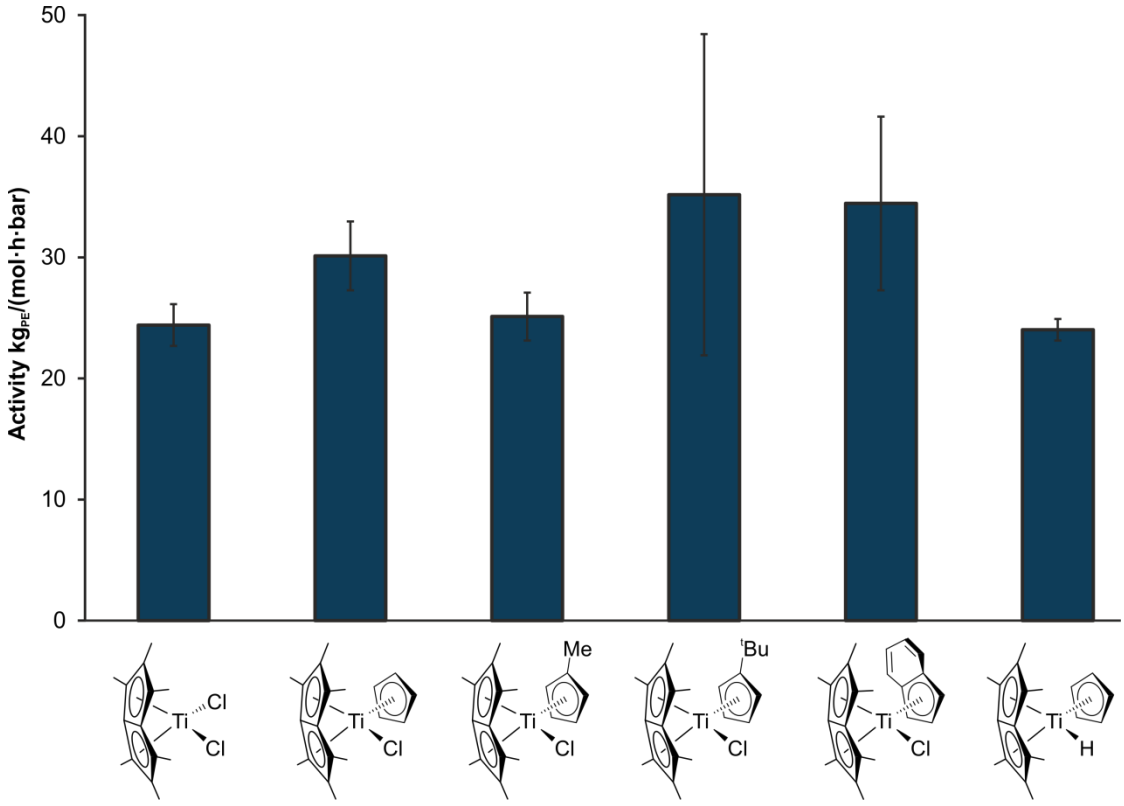


Figure 3.1. *Solution phase ethylene polymerisation activities of (left to right) [Pn*TiCl(μ-Cl)]$_2$, Pn*TiCp^{R}(Cl) (Cp^{R} = Cp, Cp^{Me}, Cp^{tBu}, Ind) and Pn*TiCp(H). [Ti]:[MAO] = 1:250; 2 bar ethylene; 0.5 mg catalyst loading; 50 mL toluene; 60 °C; 30 minutes.*

Pn*ZrCp^{R}(Cl) (Cp^{R} = Cp, Cp^{Me}, Cp^{tBu}, Cp^{nBu}, Cp^{Me3}, Ind), Pn*ZrCp^{Me}(Me) and Pn*ZrCp(^{n}Bu) were tested under identical conditions to those used for the titanium analogues. By contrast, the zirconium complexes are very active on the Gibson scale, with

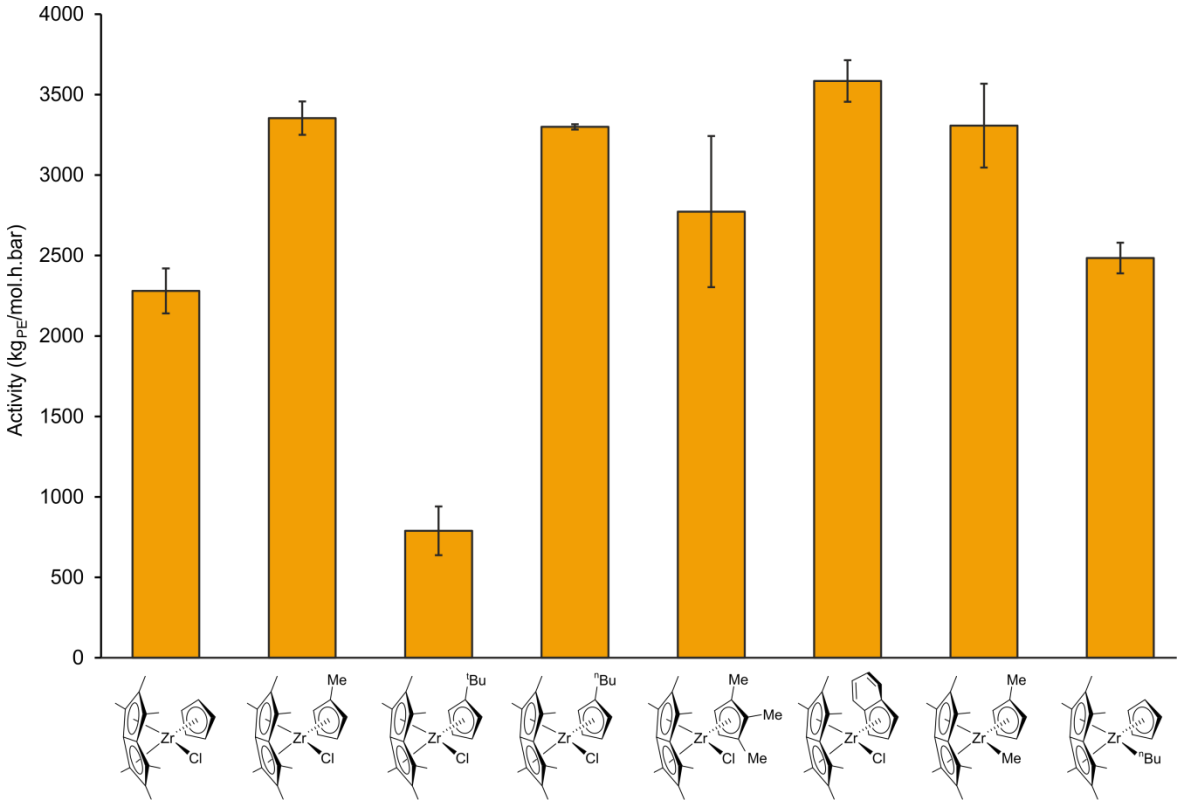


Figure 3.2. *Ethylene polymerisation activities of Pn*ZrCp^{R}(Cl) (Cp^{R} = Cp, Cp^{Me}, Cp^{tBu}, Cp^{nBu}, Cp^{Me3}, Ind), Pn*ZrCp^{Me}(Me) and Pn*ZrCp(^{n}Bu). Conditions: [Zr]:[MAO] = 1:250; 2 bar ethylene; 0.5 mg catalyst loading; 50 mL toluene; 60 °C; 5 minutes.*

most complexes two orders of magnitude more active than their titanium congeners (Figure 3.2). The highest activity is observed for Pn*ZrInd(Cl), which shows an increase in activity of 57% relative to Pn*ZrCp(Cl) (3585 and 2281 kg$_{PE}$/(mol·h·bar) respectively). Direct comparison of activities with previous reports should be treated with caution due to the significant effect reaction conditions (e.g. co-catalyst ratio, dilution, stirring efficiency) can have on the observed activities. The ethylene polymerisation activity of the unsubstituted parent pentalene complex PnZrInd(Cl) has previously been described in the patent literature as 5423 kg$_{PE}$/(mol·h·bar), albeit at much higher co-catalysts loadings of [Zr]:[MAO] = 1000 and on a larger scale.[22] The indenyl ligand is often observed to increase the rate of reaction in transformations that involve associative rate-determining steps due to the ease with which the indenyl ligand can transiently adopt an η^3-configuration, allowing for the coordination of additional ligands such as ethylene.[23–25] However, in this case it would appear that this is not the major factor that dictates the increased activity. Pn*ZrCp^{Me}(Cl) and Pn*ZrCp^{nBu}(Cl) are similar in activity to

Pn*ZrInd(Cl), but instead contain *n*-alkyl-substituted Cp^{R} ligands. Electron-donating substituents are known to inhibit ring-slippage so a rate decrease relative to Pn*ZrCp(Cl) would be expected.[26] It is more likely that these substituents aid in the stabilization of charged intermediates in the polymerisation as a result of their improved donor capacity. The more sterically demanding *t*-alkyl derivative, Pn*ZrCp^{tBu}(Cl), demonstrates a 66% decrease in activity relative to Pn*ZrCp(Cl) (789 and 2281 kg_{PE}/(mol·h·bar) respectively), with the steric requirements of the *t*-butyl group now appearing to dominate the rate of polymerisation over any favorable physical or electronic advantages.

Interestingly when the chloride ligand is substituted for an alkyl group (Pn*ZrCp(^{n}Bu) and Pn*ZrCp^{Me}(Me)), no statistically significant change in activity is observed, implying facile activation of the pre-catalysts under polymerisation conditions.

3.3 Synthesis and characterisation of solid-supported zirconium complexes, and preliminary slurry-phase ethylene polymerisation studies

Given the high activities of the zirconium pre-catalysts in solution, Pn*ZrCp^{Me}(Cl) was immobilised on MAO-modified silica (SSMAO), MAO-modified aqueous miscible organic solvent treated layered double hydroxide (LDH-MAO) and on polymethylaluminoxane (sMAO) for further study as slurry-phase polymerisation catalysts. To achieve immobilisation, Pn*ZrCp^{Me}Cl and the appropriate support material were swirled in toluene at 60 °C for 1 h, before the coloured solid was allowed to settle leaving a colourless supernatant (Figure 3.3). This was decanted and the solid dried under vacuum to furnish the supported complexes as pale-yellow pyrophoric powders in good isolated yields (64–75%).

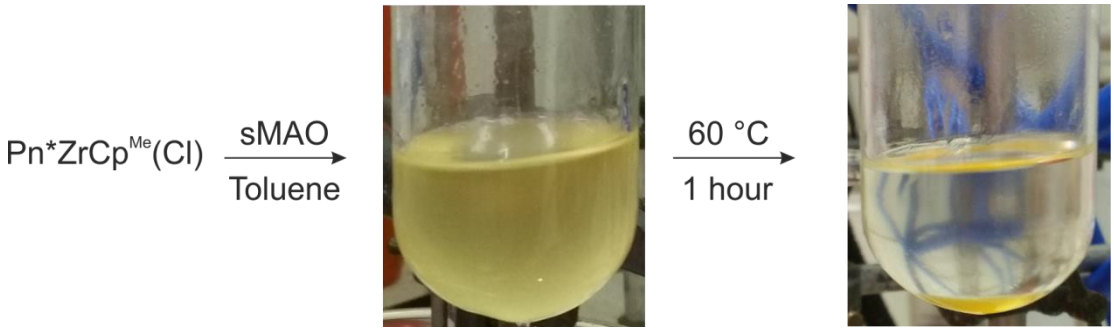


Figure 3.3. *Procedure for immobilisation of pre-catalysts on inorganic support.*

MAO-modified silica (SSMAO) has been well documented as an effective support in surface organometallic chemistry,[27–29] and is commonly employed to support olefin polymerisation catalysts.[30,31] By comparison AMO–LDH, which has the general formula $[M^{z+}_{1-x}M'^{y+}_{x}(OH)_2]^{a+}(A^{n-})_{a/n}\cdot bH_2O\cdot c$(AMO–solvent), has only recently been demonstrated as an effective support for the immobilisation of single-site olefin polymerisation and oligomerisation catalysts following pre-treatment with MAO.[32–34] sMAO is a polymeric, porous aluminoxane that is a solid, insoluble form of MAO suitable for supporting complexes. The structure, like MAO, is poorly defined, with some recent studies on this material discussed in section 1.7.

The polymerisation activity of the immobilised catalysts was measured over the temperature range 40–80 °C to investigate the effect of the support material (Figure 3.4).

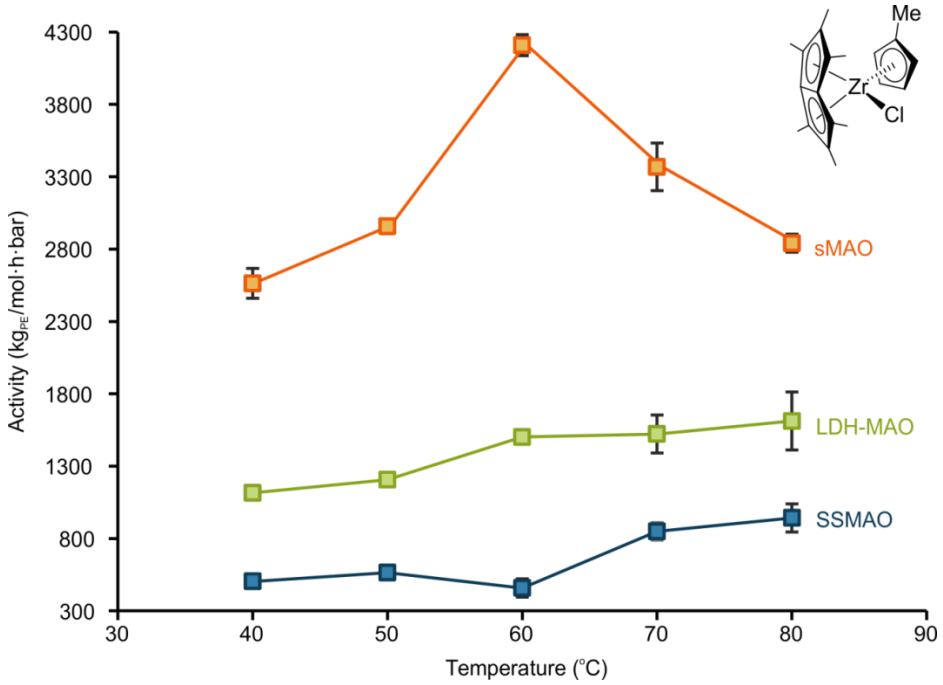


Figure 3.4. *Comparison of ethylene polymerisation activities of Pn*ZrCp^{Me}(Cl)immobilised on: (top to bottom) sMAO, LDH-MAO and SSMAO. Slurry conditions: [Zr]:[Al] = 1:200; 150 mg TiBA co-catalyst; 2 bar ethylene; 10 mg catalyst loading; 50 mL toluene; 30 minutes.*

The silica-supported catalyst demonstrated the lowest activities (504–943 kg$_{PE}$/(mol·h·bar)), whilst Pn*ZrCp^{Me}(Cl)$_{LDH\text{-}MAO}$ produced activities generally twice as large (1116–1612 kg$_{PE}$/(mol·h·bar)) with both showing a general increase in activity with increasing temperature. Pn*ZrCp^{Me}(Cl)$_{LDH\text{-}MAO}$ is one of the most active known

zirconocene LDH-MAO catalysts, only marginally slower than $(Cp^{nBu})_2ZrCl_{2LDH\text{-}MAO}$ (2141 $kg_{PE}/(mol{\cdot}h{\cdot}bar)$) and over 18 times faster than the (hydro)permethylpentalene complex $[Pn^*(H)ZrCl_3]_{2LDH\text{-}MAO}$ (89 $kg_{PE}/(mol{\cdot}h{\cdot}bar)$).[32] The polymethylaluminoxane catalyst Pn*ZrCp^{Me}(Cl)$_{sMAO}$ demonstrated up to a three-fold increase in activity relative to the same complex supported on LDH-MAO, with a maximum activity of 4209 $kg_{PE}/(mol{\cdot}h{\cdot}bar)$ observed at 60 °C. Given the superior polymerisation activity of the polymethylaluminoxane support, a series of zirconium-sMAO catalysts were synthesised. Pn*ZrCp^{R}(Cl) (Cp^{R} = Cp, Cp^{Me}, Cp^{nBu}, Cp^{Me3}, Ind), Pn*ZrCp^{Me}(Me) and Pn*ZrCp(X) (X = Me, H, ^{n}Bu, CH_2Ph, C_3H_5); the complexes were also isolated as pale-yellow pyrophoric powders in excellent yields (71–80%).

Characterisation of the polymethylaluminoxane–supported complexes was achieved by solid state ^{13}C CPMAS and ^{27}Al DPMAS NMR spectroscopy (Figure 3.5). The ^{13}C CPMAS spectrum of sMAO exhibits a major, broad resonance at approximately −7 ppm corresponding to the sMAO–*Me* environments, while benzoate resonances can be observed at 119–130 ppm for the aromatic environments and 179 ppm for α-*C*(O)O (benzoic acid is used as a mild oxygen source in the synthesis of sMAO). Additionally, all catalysts display a resonance at around 13 ppm corresponding to Pn*−*Me* environments, which are no longer resolved as discrete resonances due to line broadening in the solid state. Further resonances are observed around 112–118 ppm due to Cp ring-carbon environments. These resonances are best resolved in complexes with minimally substituted Cp^{R} ligands containing multiple $C_{Cp\text{-}ring}$–H bonds due to magnetisation transfer from the protons in these cross-polarisation experiments, such as Pn*ZrCp^{R}(Cl) (R = H, Me, ^{t}Bu, ^{n}Bu). By contrast, the indenyl resonances of Pn*ZrInd(Cl)$_{sMAO}$ are split over a larger frequency range, while for Pn*ZrCp^{Me3}(Cl)$_{sMAO}$, fewer $C_{Cp\text{-}ring}$–H bonds are present in the Cp ligand and do not produce readily observable signals in this region. Nonetheless complexation can still be confirmed by the presence of the characteristic Pn*–Me resonances at 13 ppm. In the case of Pn*ZrCp^{tBu}(Cl)$_{sMAO}$ and Pn*ZrCp^{nBu}(Cl)$_{sMAO}$ resonances can be observed for the Cp^{R} *t*-butyl and *n*-butyl groups at 40 ppm and 22–35 ppm respectively, with the latter showing three well resolved resonances for the carbon environments along the chain (Figure 3.5). The solid state ^{27}Al DPMAS NMR spectra for the supported species are complicated with four major resonances around 340, 200, –80 and –245 ppm, which correspond to the different aluminum environments within the polymethylaluminoxane.

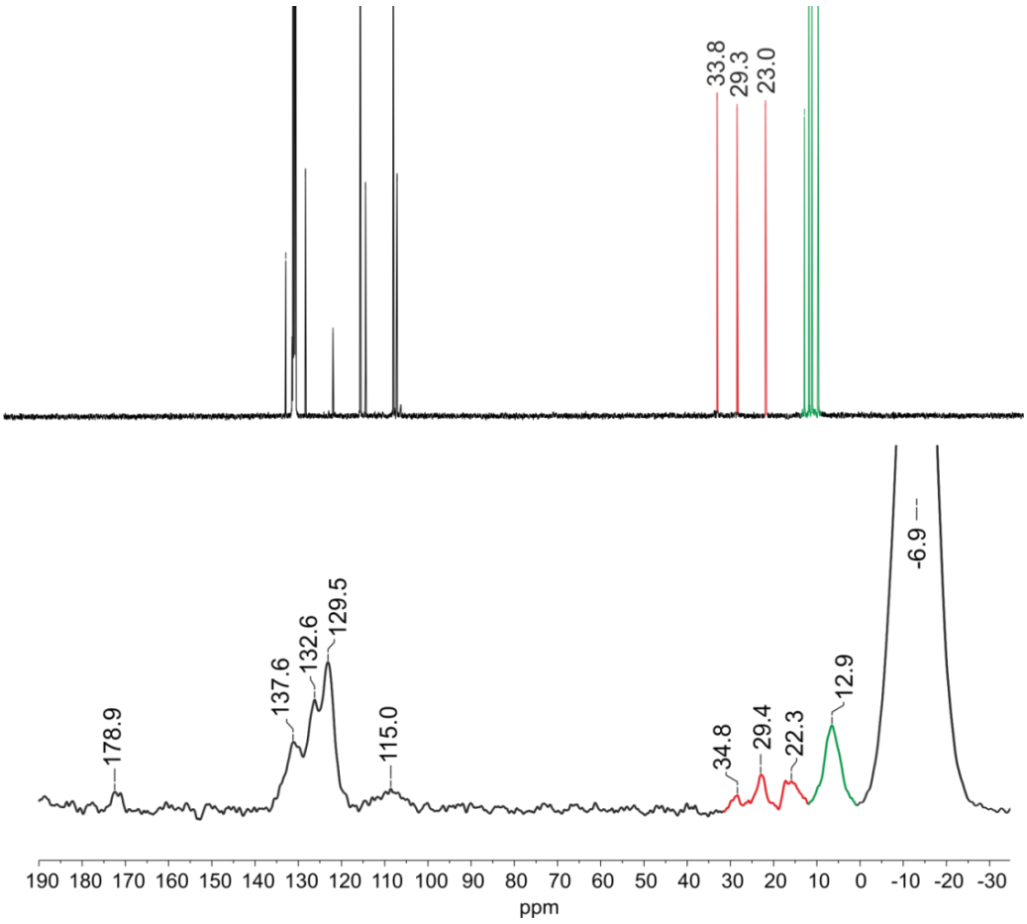


Figure 3.5. *Top: Solution $^{13}C\{^{1}H\}$ NMR spectrum (400 MHz, C_6D_6) of Pn*ZrCp^{nBu}(Cl). Bottom: Solid state ^{13}C CPMAS NMR spectrum (10 kHz, contact time 3000 µs) of Pn*ZrCp^{nBu}(Cl)$_{sMAO}$. Highlighted in red: ^{n}Bu resonances; highlighted in green: Pn*–Me resonances.*

Previously the surface structure of (EBI)ZrCl$_{2LDH\text{-}MAO}$ {EBI = *rac*-ethylenebis(1-indenyl)} was investigated using Zr K-edge EXAFS; the zirconium is in a tetrahedral environment bound to the zirconocene ligand, with a close contact to a surface oxygen and a single Zr–Me bond.[35] Studies on the immobilisation of W(NDipp)Cl$_4$(THF) {Dipp = 2,6-(^{i}Pr)$_2$C$_6$H$_3$)} on sMAO indicated that three methylations occur *in situ*, whilst a W-Cl-Al interaction stabilises the resulting species.[34] For Pn*ZrCp^{R}(X)$_{SMAO}$ catalysts, a resonance corresponding to a Zr-*Me* environment cannot be observed in the ^{13}C CPMAS NMR spectra; it is unclear whether the metal site is methylated or persists as a cation with close-contact to a surface oxygen. Attempts to observe any Zr–C bond by FTIR spectroscopy were unsuccessful – only stretches arising from polymethylaluminoxane could be resolved.

The catalyst loading was subsequently increased to 100:1 (from 200:1), however peaks corresponding to the supported complex could still not be observed.

3.4 Pre-catalyst screening of polymethylaluminoxane complexes

The slurry phase ethylene polymerisation activities of the supported Pn*ZrCp^{R}(X) complexes were measured at [Zr]:[sMAO] = 1:200. Where data is available for both homogeneous and slurry phase polymerisations, this is presented in (Figure 3.6). Within this series the highest activities were observed for Pn*ZrCp^{Me}(Cl)$_{sMAO}$, Pn*ZrCp^{nBu}(Cl)$_{sMAO}$ and Pn*ZrCp^{Me}(Me)$_{sMAO}$ (4206, 4096, and 4486 kg$_{PE}$/(mol·h·bar) respectively). This can be compared with the unsubstituted analogue Pn*ZrCp(Cl)$_{sMAO}$, which demonstrated lower activities of 3624 kg$_{PE}$/(mol·h·bar). A general trend can be observed in which the supported pre-catalysts with no substitution or *n*-alkyl substitution of one position of the Cp ring were found to be the most effective ethylene polymerisation catalysts.

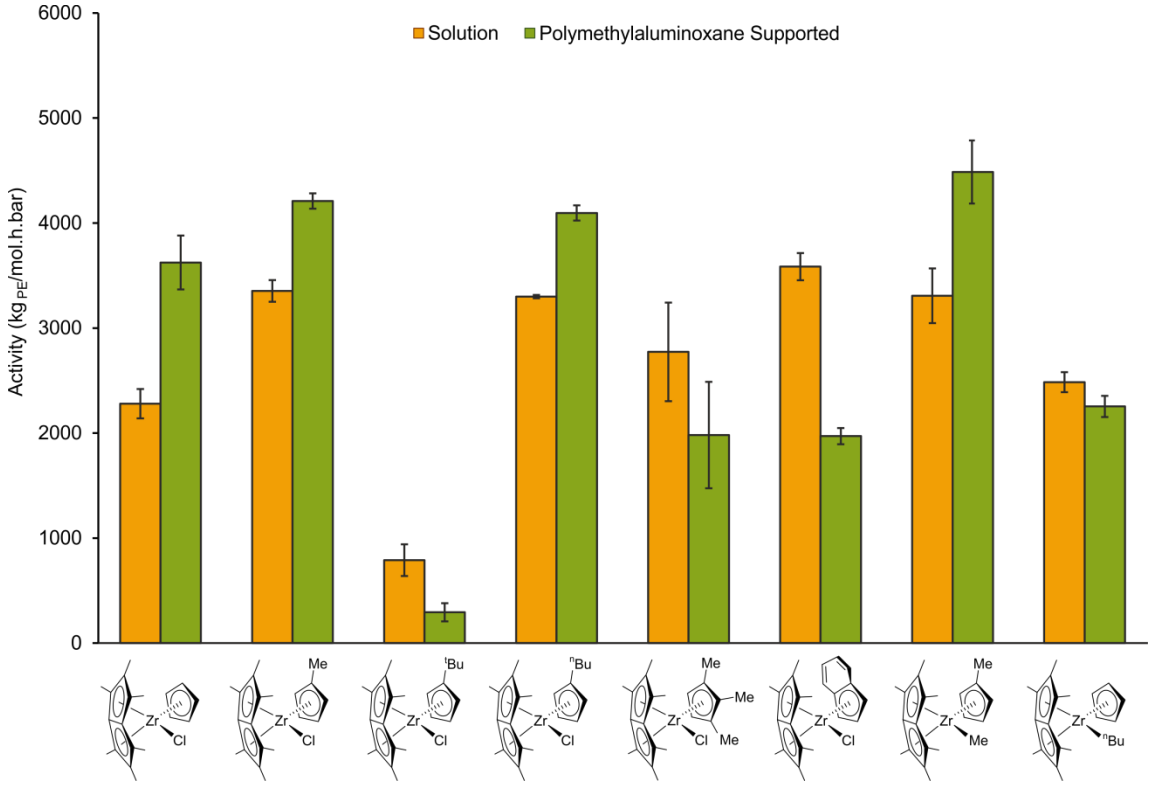


Figure 3.6. *Comparison of solution and slurry phase ethylene polymerisation activities of Pn*ZrCp^{R}(Cl) (Cp^{R} = Cp, Cp^{Me}, Cp^{tBu}, Cp^{nBu}, Cp^{Me3}, Ind), Pn*ZrCp^{Me}(Me) and Pn*ZrCp(^{n}Bu). Solution conditions: [Zr]:[MAO] = 1:250; 2 bar ethylene; 0.5 mg catalyst loading; 50 mL toluene; 60 °C; 5 minutes. Supported conditions: [Zr]:[MAO] = 1:200; 2 bar ethylene; 10 mg catalyst loading; 50 mL toluene; 60 °C; 150 mg TiBA; 30 minutes.*

This can be compared with cases where there is substitution of multiple positions of the Cp ring (Pn*ZrInd(Cl)$_{sMAO}$ and Pn*ZrCp^{Me3}(Cl)$_{sMAO}$). Here, a significant decrease in rate is observed, with both catalysts approximately 53% slower than Pn*ZrCp^{Me}(Cl)$_{sMAO}$ (1981 and 1971 kg$_{PE}$/(mol·h·bar) compared to 4206 kg$_{PE}$/(mol·h·bar)). However, the most dramatic effect is found for *t*-alkyl substitution of the Cp ring, echoing the trend observed for the solution phase pre-catalysts, with activities of 294 kg$_{PE}$/(mol·h·bar) recorded for Pn*ZrCp^{tBu}(Cl)$_{sMAO}$; a 94% decrease compared to Pn*ZrCp^{Me}(Me)$_{sMAO}$.

An interesting comparison can be made between these data and the solution phase polymerisations. In general, complexes bearing Cp^{R} ligands with no substitution or *n*-alkyl substitution at only a single position (Pn*ZrCp(Cl)$_{sMAO}$, Pn*ZrCp^{Me}(Cl)$_{sMAO}$, Pn*ZrCp^{nBu}(Cl)$_{sMAO}$ and Pn*ZrCp^{Me}(Me)$_{sMAO}$) display an increase in activity relative to the MAO co-catalysed analogues. The largest increase is 59% from 2281 kg$_{PE}$/(mol·h·bar) (Pn*ZrCp(Cl)) to 3624 kg$_{PE}$/(mol·h·bar) (Pn*ZrCp(Cl)$_{sMAO}$). This is surprising given the general trend that supported polymerisation catalysts usually demonstrate lower activities compared to their homogeneous counterparts. The solid surface can be assumed to occupy a large volume and inhibit approach of monomer units to the metal centre. When supported complexes bearing larger Cp^{R} ligands are employed (Pn*ZrCp^{tBu}(Cl), Pn*ZrCp^{Me3}(Cl), Pn*ZrCpInd(Cl)), the steric requirements of the support have a noticeable impact, and the activities are found to decrease relative to the homogenous analogues as expected. For example, there is a 63% decrease from Pn*ZrCp^{tBu}(Cl) (789 kg$_{PE}$/(mol·h·bar)) to Pn*ZrCp^{tBu}(Cl)$_{sMAO}$, **(**294 kg$_{PE}$/(mol·h·bar)). This more conventional trend is also clearly observed in the comparison of Pn*ZrCp^{Me}(Cl)$_{LDH\text{-}MAO}$ and Pn*ZrCp^{Me}(Cl)$_{ssMAO}$ with the solution phase polymerisation activity of Pn*ZrCp^{Me}(Cl).

The polyethylene produced from selected catalysts was characterised by gel-permeation chromatography, with the experimental molecular weights and polydispersities (PDI) found to vary significantly across the series (Figure 3.7). Although Pn*ZrCp^{Me}(Cl) and Pn*ZrInd(Cl) displayed the highest activities of any solution-phase system, the polymers produced were inhomogenous in 1,2,3-$C_6Cl_3H_3$ on heating at 140 °C for 4 h followed by 160 °C for 2 h. Supporting these catalysts on sMAO allows for the production of a homogenous polymer at the expense of a lower M_w. In general, the supported catalysts

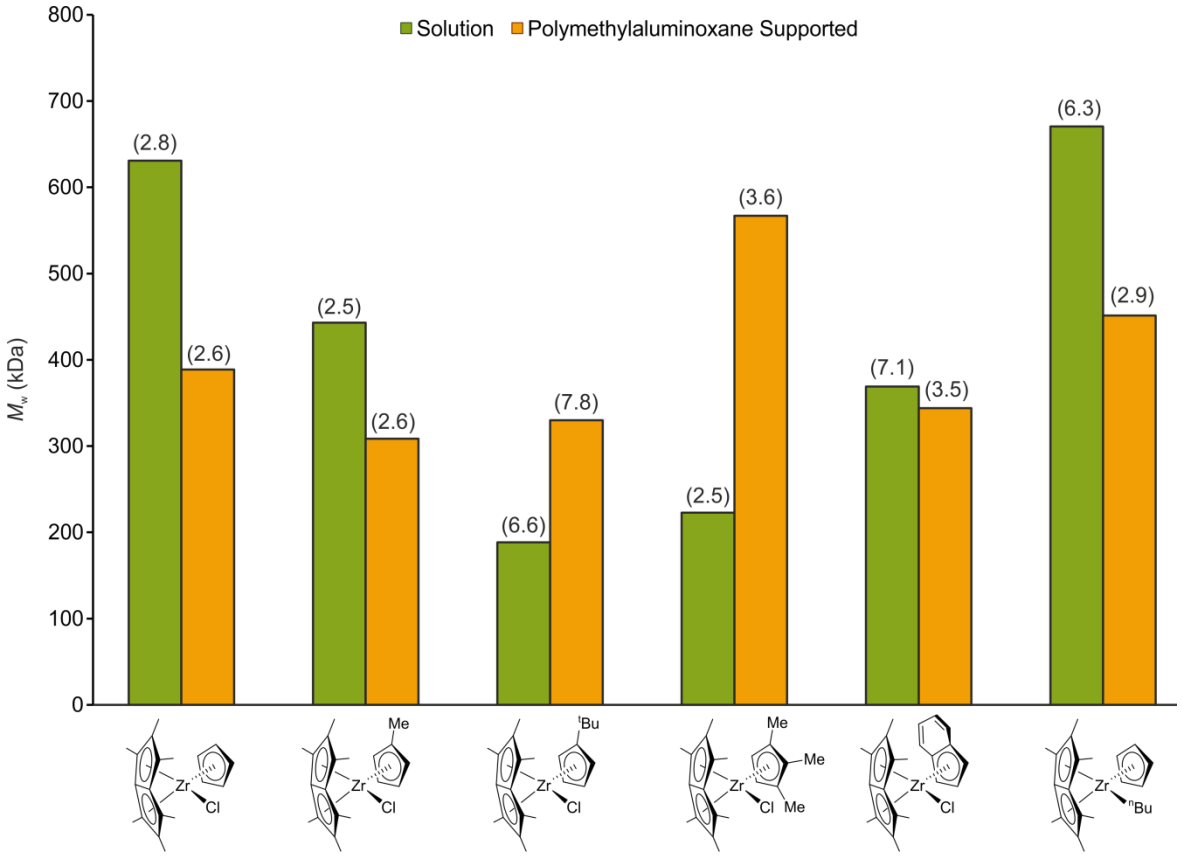


Figure 3.7. *Polymer molecular weight, M_w for solution and polymethylaluminoxane supported ethylene polymerisation at 60 °C with Pn*ZrCp^{R}(Cl) (Cp^{R} = Cp, Cp^{Me}, Cp^{tBu}, Cp^{Me3}, Ind) and Pn*ZrCp(^{n}Bu). PDIs are given in parentheses.*

produce polymers with larger PDIs, although this appears sensitive to the nature of the complex immobilised. The highest M_w observed was for Pn*ZrCp(^{n}Bu) employed as a solution phase pre-catalyst, which produced a polymer M_w of 670 kDa, while the highest M_w for a supported catalyst was Pn*ZrCp^{Me3}(Cl) (567 kDa), although an increased PDI (3.6) is also observed for the latter.

The polymers produced using Pn*ZrCp^{tBu}(Cl) and Pn*ZrCp^{tBu}(Cl)$_{sMAO}$ were found to exhibit a bimodal molecular weight distribution (Figure 3.8); Pn*ZrCp^{tBu}(Cl) exhibits a major peak at 40 kDa and a minor peak at 136 kDa, while Pn*ZrCp^{tBu}(Cl)$_{sMAO}$ has maxima at 61 and 579 kDa.

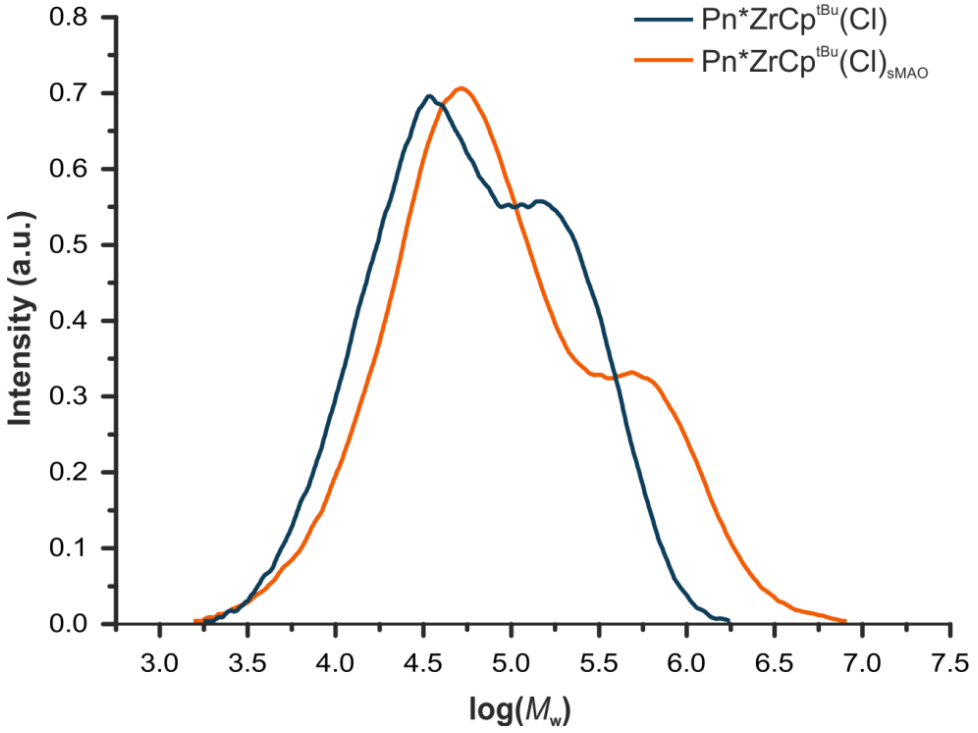


Figure 3.8. *Molecular weight distribution of polymer produced by pre-catalysts Pn*ZrCp^{tBu}(Cl) (blue) and Pn*ZrCp^{tBu}(Cl)$_{sMAO}$ (orange), determined by GPC.*

3.5 Slurry-phase ethylene polymerisation studies with polymethylaluminoxane supported zirconium pre-catalysts

Following the promising results obtained with sMAO-immobilised catalysts, an extended study of was undertaken investigating the effect of temperature on activity and polymer properties. Examining Pn*ZrCp(Cl)$_{sMAO}$ across the temperature range 40 – 80 °C in toluene, peak activity is found at 60 °C (Figure 3.9, 3624 kg$_{PE}$/(mol·h·bar)). The molecular weight is observed to decrease with increasing temperature, due to increased rates of chain termination relative to propagation at high temperature.[36] Measuring the polymerisation activity at different time intervals, a decrease in activity is observed with increasing duration. This is likely due to inactivation of the catalyst, either due to the envelopment of the active centre in polymer, or by complex decomposition.[37] However, the molecular weight remains rather constant across the series, which is a clear indication of chain-growth polymerisation.[38]

By contrast, in hexane, the polymerisation activity generally decreases with increasing temperature (Figure 3.10). Maximum activity is observed at 40 °C, which is 20% lower than the corresponding maximum observed in toluene.

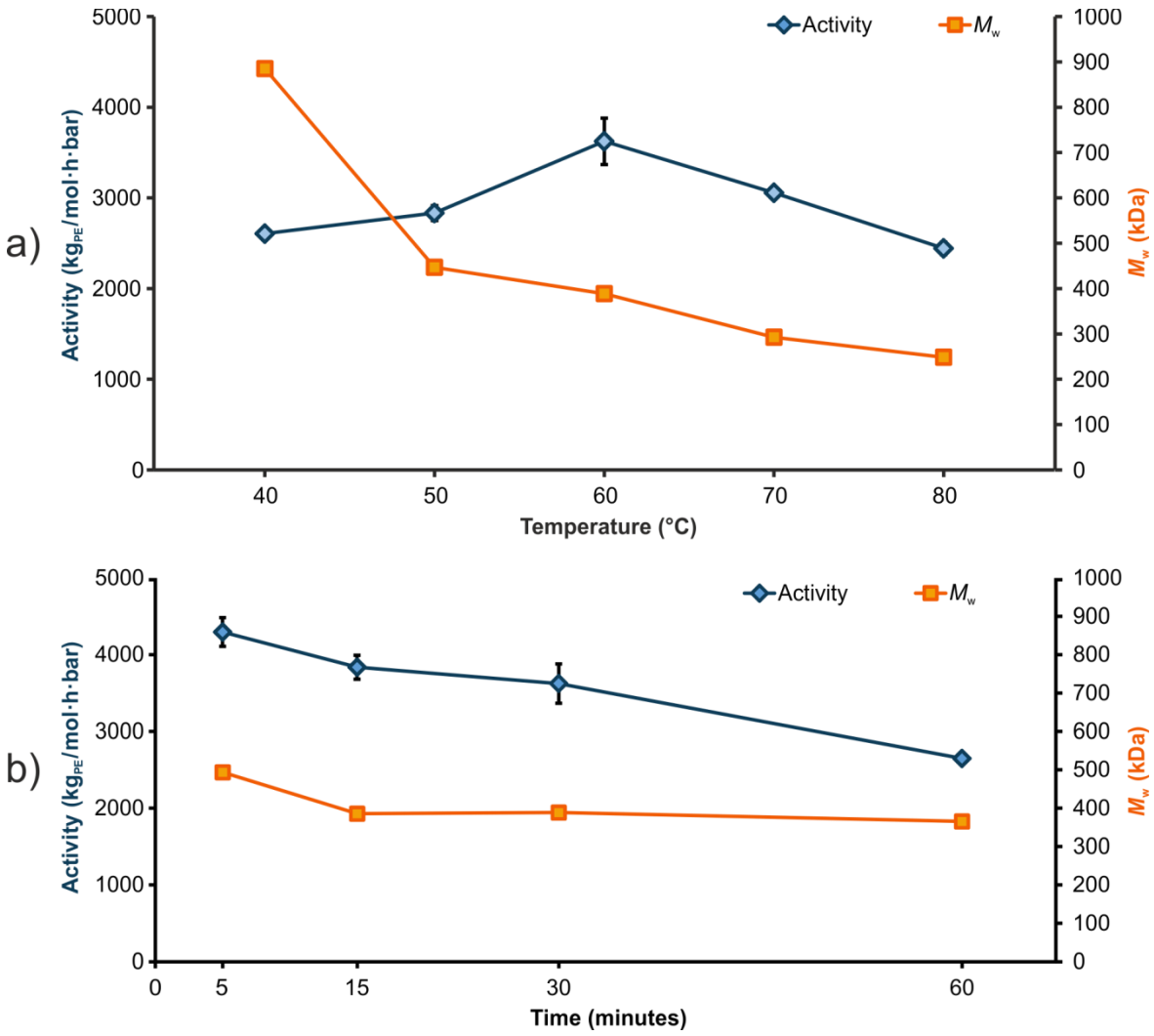


Figure 3.9. *Slurry phase ethylene polymerisation activity (blue) and polyethylene M_w (orange) using Pn*ZrCp(Cl)$_{sMAO}$ a) across the temperature range 40 – 80 °C; b) at time intervals between 5 and 60 minutes. Conditions: [Zr]:[sMAO] = 1:200; 2 bar ethylene; 10 mg catalyst loading; 50 mL toluene;150 mg TiBA.*

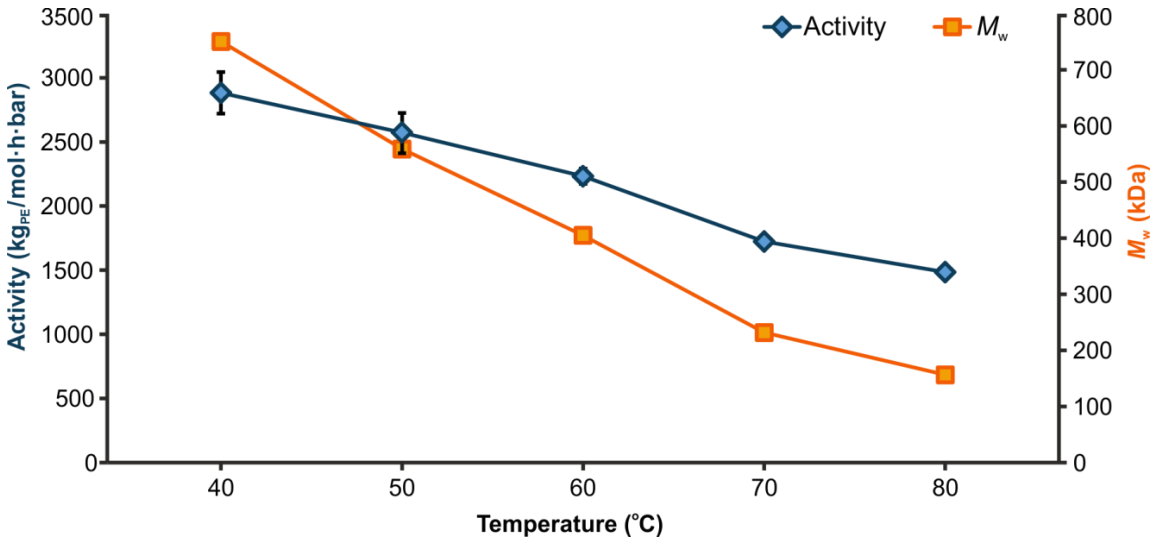


Figure 3.10. *Slurry phase ethylene polymerisation activity (blue) and polyethylene M_w (orange) Pn*ZrCp(Cl) in hexane across the temperature range 40 – 80 °C. Conditions: [Zr]:[sMAO] = 1:200; 2 bar ethylene; 10 mg catalyst loading; 50 mL toluene;150 mg TiBA; 30 minutes.*

Pn*ZrCp^{Me}(Cl)$_{sMAO}$ displays peak activity at 60 °C as observed for the Cp derivative, however, Pn*ZrCp^{nBu}(Cl)$_{sMAO}$ shows its maximum activity at lower temperatures (Figure 3.11). These activities recorded at 50 °C are the largest activities of any Pn* complex, and correspond to a 39% increase with respect to Pn*ZrCp(Cl)$_{sMAO}$ peak activity (5024 and 3624 kg_{PE}/mol·h·bar respectively). By comparison the ethylene polymerisation activity of Pn*ZrInd(Cl)$_{sMAO}$ is positively correlated with increasing temperature, with a maximum at 70 °C (3144 kg_{PE}/mol·h·bar). An interesting contrast is provided by Pn*ZrCp^{Me3}(Cl)$_{sMAO}$, which is markedly less active than the other Cp-derivatives. In this case the temperature profile is rather flat showing a slight peak at 50 °C (Figure 3.11). Clearly functionalisation of the Cp ring has a very significant effect on activity; the maximum activity of the best and worst performing catalysts in this series vary by 3114 kg_{PE}/mol·h·bar. Comparison to Pn*ZrCp^{tBu}(Cl)$_{sMAO}$ is even more dramatic, with activities 23 times smaller than the ^{n}Bu isomer (Figure 3.6). This would suggest a role for the Cp-fragment as an ancilliary ligand, and not as a leaving group, which has mechanistic implications discussed in more detail in Chapter 4. As expected, the molecular weight decreases with increasing temperature. A significant decrease in the measured molecular weight is observed for Pn*ZrCp^{Me}(Cl)$_{sMAO}$ between 40 and 50 °C (820 to 523 kDa). However, at higher temperatures the measured values are more similar to Pn*ZrCp^{nBu}(Cl)$_{sMAO}$.

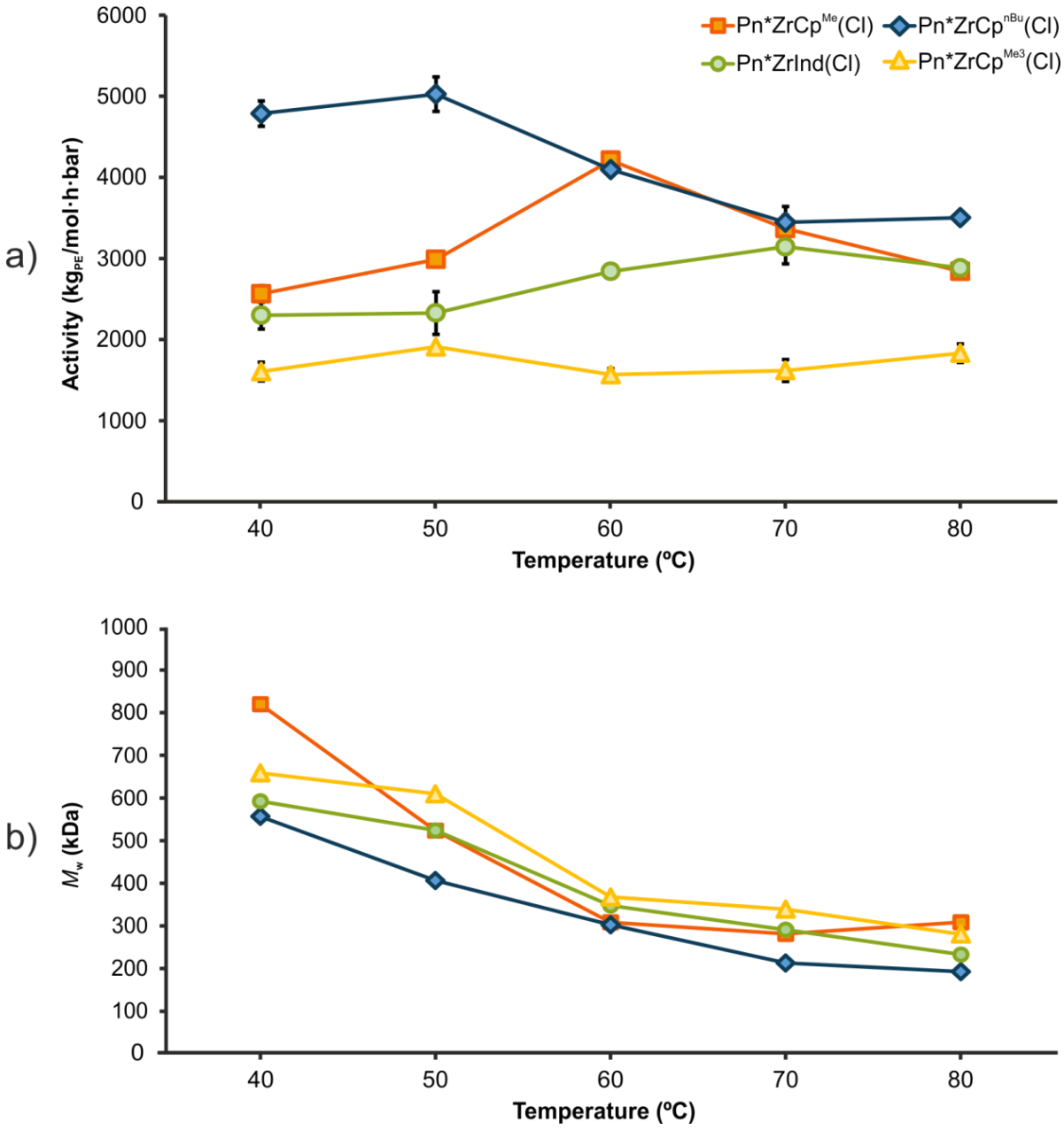


Figure 3.11. *a) slurry phase ethylene polymerisation activity and b) polyethylene M_w of sMAO-activated Pn*ZrCp^{Me}(Cl) (orange), Pn*ZrCp^{nBu}(Cl) (blue), Pn*ZrInd(Cl) (green) and Pn*ZrCp^{Me3}(Cl) (yellow) across the temperature range 40 – 80 °C. Conditions: [Zr]:[sMAO] = 1:200; 2 bar ethylene; 10 mg catalyst loading; 50 mL toluene;150 mg TiBA; 30 minutes.*

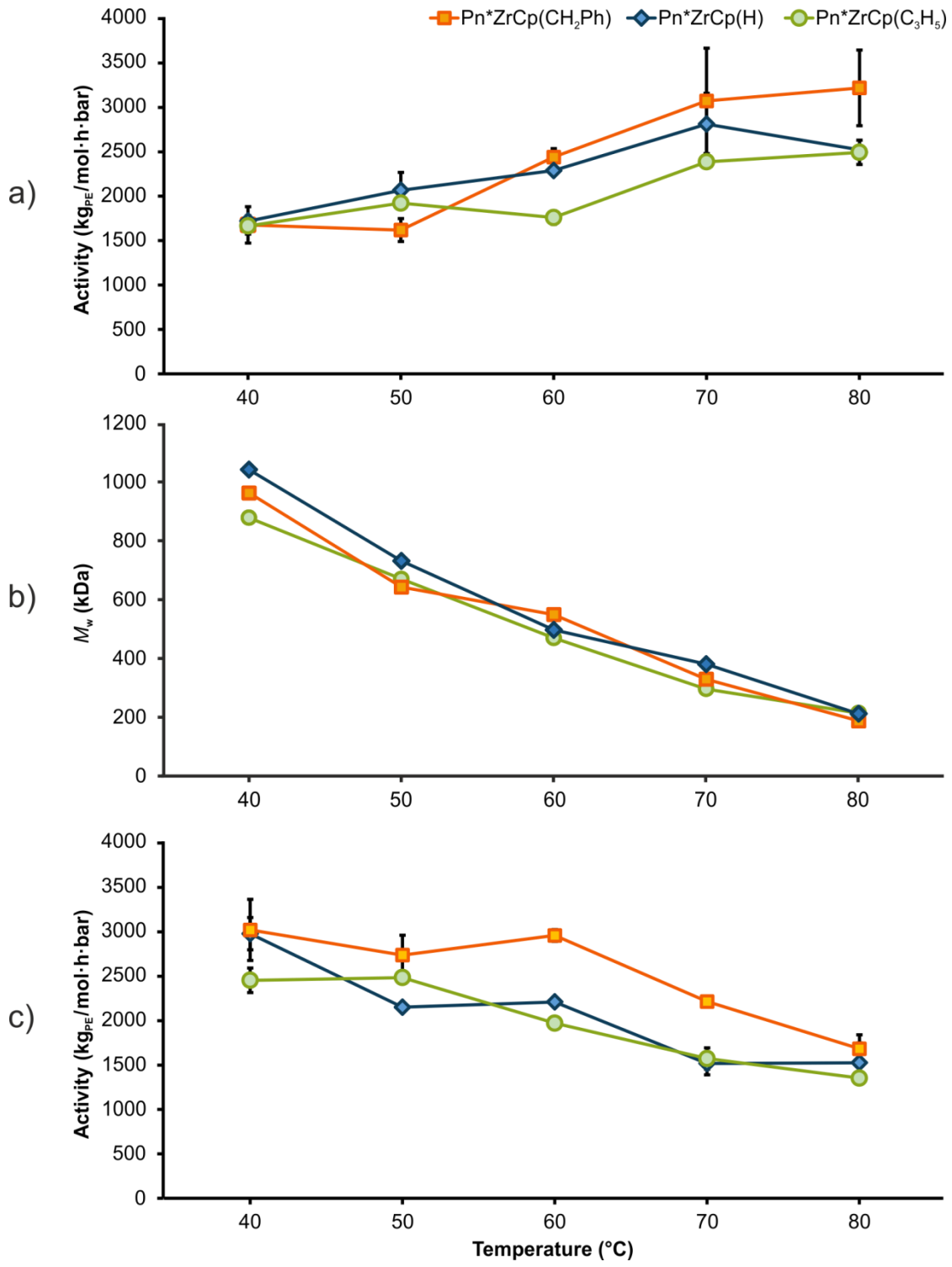


Figure 3.12. *a) slurry phase ethylene polymerisation activity and b) polymer M_w of sMAO-activated Pn*ZrCp(CH$_2$Ph) (orange), Pn*ZrCp(H) (blue) and Pn*ZrCp(C$_3$H$_5$) (green) in toluene across the temperature range 40 – 80 °C. b) slurry phase ethylene polymerisation activity of the above catalysts in hexane. Conditions: [Zr]:[sMAO] = 1:200; 2 bar ethylene; 10 mg catalyst loading;150 mg TiBA; 30 minutes.*

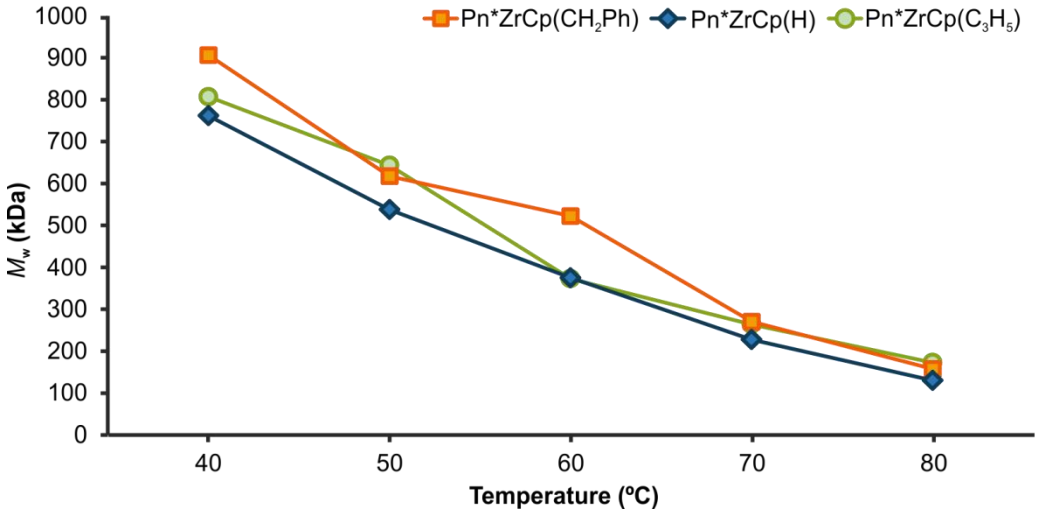


Figure 3.13. *M_w of polymer produced by sMAO-activated Pn*ZrCp(CH_2Ph) (orange), Pn*ZrCp(H) (blue) and Pn*ZrCp(C_3H_5) (green) across the temperature range 40 – 80 °C in hexane. Conditions: [Zr]:[sMAO] = 1:200; 2 bar ethylene; 10 mg catalyst loading; 50 mL hexane;150 mg TiBA; 30 minutes.*

Pn*ZrCp(X)$_{sMAO}$ derivatives were also tested, both in toluene and hexane (Figure 3.12). In toluene, activity was observed to increase with increasing temperature, while in hexane the reverse trend is observed; the activity correlates inversely with temperature. This may be due to the reduced solubility of gases in hot solvents, especially as the boiling point of the liquid is approached. In both solvents, there is a rather narrow spread of activities for the different catalysts, although more significant divergence is observed in hexane. In general, the highest activities observed in hexane and toluene are very similar for each catalyst, despite the large temperature difference of these maxima.

The molecular weights of the polyethylene formed by these catalyst show the expected temperature response and are very similar to each other (Figure 3.13). Higher molecular weight polymer is formed in toluene, as opposed to hexane, although the difference is smaller than those caused by varying temperature. For example at 40 °C Pn*ZrCp(C_3H_5)$_{sMAO}$ produced polymer of molecular weight 874 kDa in toluene and 807 kDa in hexane. Over the 40 °C temperature range investigated, molecular weights are observed to decrease by 600-700 kDa.

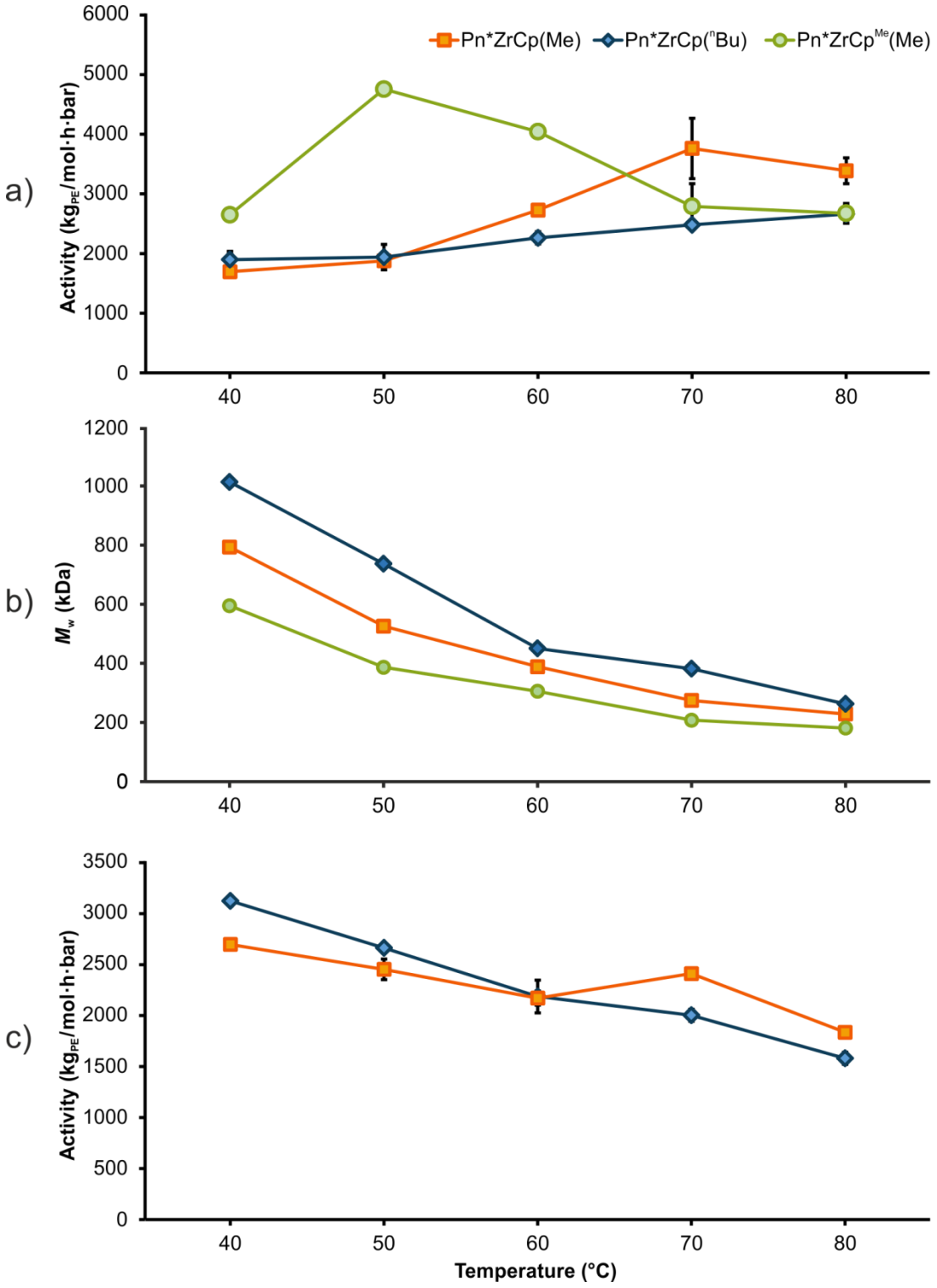


Figure 3.14. *a) slurry phase ethylene polymerisation activity and b) polymer M_w of sMAO-activated Pn*ZrCp(Me) (orange), Pn*ZrCp(^{n}Bu) (blue) and Pn*ZrCp^{Me}(Me) (green) in toluene at 40 – 80 °C. c) Pn*ZrCp(Me)and Pn*ZrCp(^{n}Bu) as above in hexane. Conditions: [Zr]:[sMAO] = 1:200; 2 bar ethylene; 10 mg catalyst loading;150 mg TiBA; 30 minutes.*

The ethylene polymerisation activity of Pn*ZrCp(X)$_{sMAO}$ (X = Me, ^{n}Bu) display similar trends to the other leaving group variants (Figure 3.14). In toluene activity increases with increasing temperature, while in hexane the reverse is true. As before a rather narrow spread of activities is generally observed. The highest activity for any of these Pn*ZrCp(X) derivatives is observed for X = Me in toluene at 70 °C, (3746 kg$_{PE}$/(mol.h.bar)). However, this does not correspond to a statistically significant increase relative to the maximum activity found for the chloride analogue, Pn*ZrCp(Cl)$_{sMAO}$ at 60 °C.

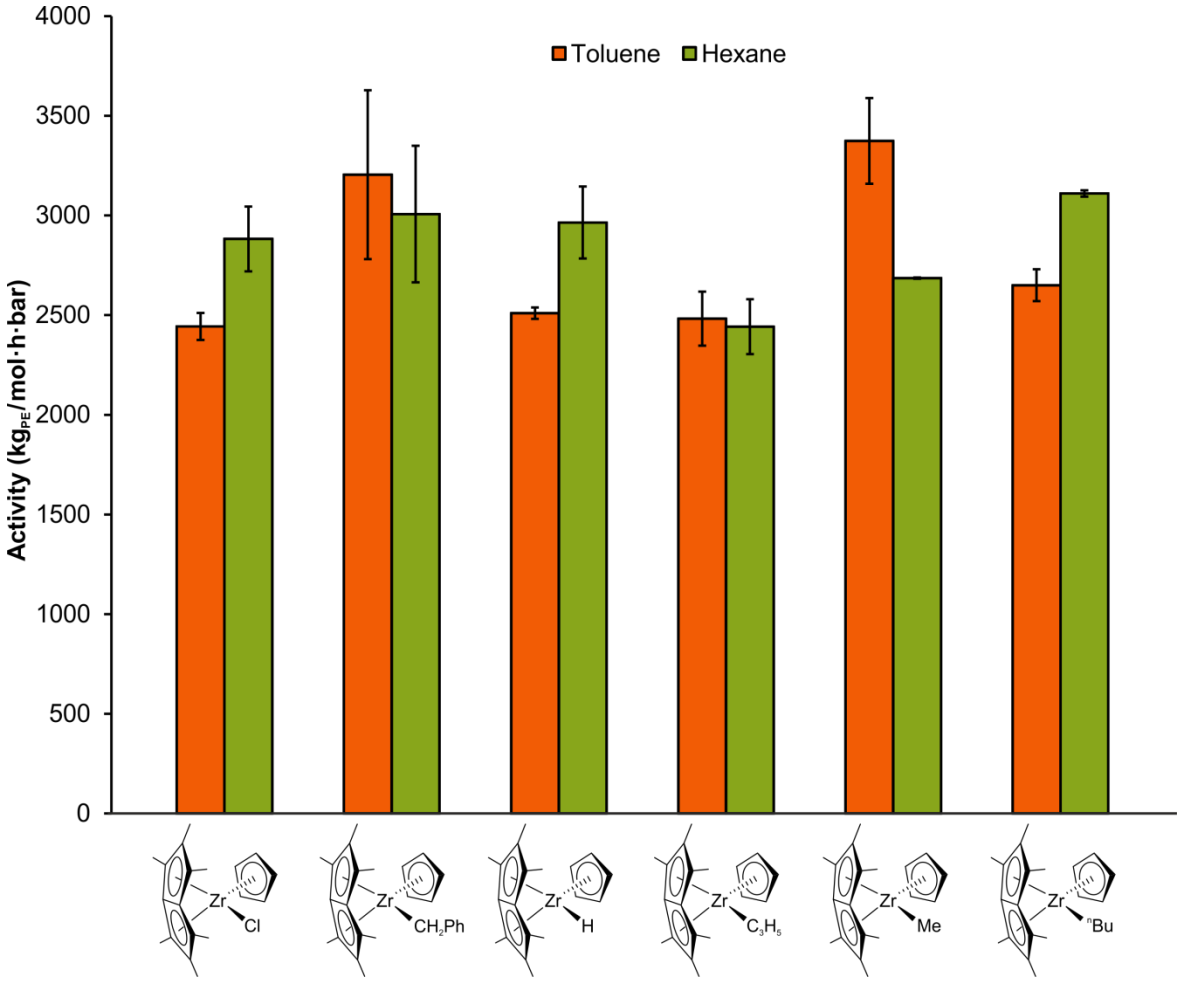


Figure 3.15. *Summary of ethylene polymerisation data for Pn*ZrCp(X)$_{sMAO}$ catalysts in toluene (80 °C) and hexane (40 °C). Conditions: [Zr]:[sMAO] = 1:200; 2 bar ethylene; 10 mg catalyst loading;150 mg TiBA; 30 minutes.*

Figure 3.15 shows the activity of Pn*ZrCp(X) complexes in hexane and toluene at 40 and 80 °C respectively, given maximum activity generally occurred at these temperatures. Although some variation is clearly observed, this never exceeds 1000 kg/(mol·h·bar), and

is rarely statistically significant. This contrasts markedly with the behaviour of Pn*ZrCp^{R}(X), where activities vary over 4700 kg/(mol·h·bar).

Given the small changes that result from variation of this ligand, it is reasonable to suggest its role as a leaving group during pre-catalyst activation, which is generally not rate-limiting. Further evidence for this proposed formulation of Cp^{R} as ancilliary ligand, and "X" as leaving group can be found in the temperature response of Pn*ZrCp^{Me}(Me)$_{sMAO}$ in toluene (Figure 3.14). The profile is altered relative to Pn*ZrCp(Me)$_{sMAO}$, apparently dominated by the nature of the Cp^{R} moiety, demonstrating a maximum activity at 50 °C. This corresponds to a 12% increase in activity relative to Pn*ZrCp^{Me}(Cl)$_{sMAO}$ at 60 °C.

3.6 Polymer Characterisation

The polymer was further characterised by FTIR spectroscopy. Analysis of the polymer formed by Pn*ZrCp(Cl)$_{sMAO}$ using attenuated total reflection (ATR) FTIR spectroscopy allowed for the observation of peaks at 2917 and 2849 cm^{-1} corresponding to CH_2 stretching, 1473 and 1461 cm^{-1}, which corresponds to CH_2 bending and 730 and 718 cm^{-1}, which results from CH_2 rocking.[39] No peaks could be observed that correspond to terminal CH_3 groups, suggesting small amounts of branching in the polymer chain.

Analysis of the polymer by differential scanning calorimetry allows for the characterisation of thermal behaviour and percentage crystallinity. The peak melting temperature is observed at 138.6 °C, which is consistent with high molecular weight, high density polyethylene with small amounts of short chain branching (Figure 3.16). The percentage crystallinity is calculated by taking the difference between the areas underneath the melting and crystallisation curves, then dividing this by a reference value for 100% crystalline polyethylene. Pn*ZrCp(Cl)$_{sMAO}$ produced polyethylene of 30% crystallinity, while Pn*ZrCp^{nBu}(Cl)$_{sMAO}$ formed 28% crystalline PE.

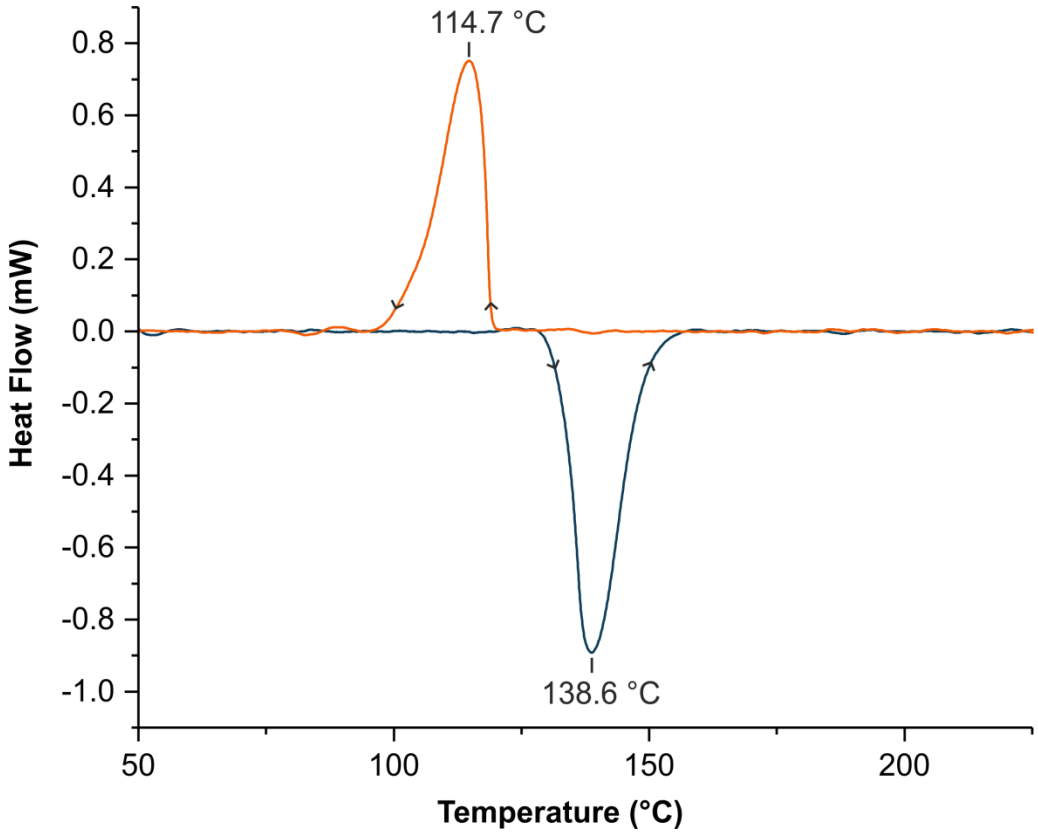


Figure 3.16. *DSC plot of polyethylene produced by Pn*ZrCp(Cl)$_{sMAO}$. Heating shown in blue, cooling shown in orange.*

These crystalline regions can be further characterised by powder X-ray diffraction, with major features at 21.9° and 23.9° for the (110) and (200) peaks respectively (Figure 3.17). Amorphous polyethylene can also be observed as a broad feature between 15 and 26 °. The lattice parameter, *a*, is most sensitive to structural variation within the polymer chain. In the case of polymer synthesised by Pn*ZrCp(Cl), this is calculated as 7.4291 Å, which is slightly elongated relative to recrystallised polyethylene, but comparable to unmodified HDPE (7.4241 Å).[40,41]

The branch content can be determined by NMR spectroscopy in 1,2-$C_6H_4Cl_2$. The number of methyl groups is expressed as a ratio of CH_2 backbone linkages; for Pn*ZrCp(Cl)$_{sMAO}$ (80 °C, toluene) CH_3/1000 CH_2 is calculated to be 0.8. This is consistent with the findings of the other characterisation techniques, which all point to the formation of HDPE with small amounts of short-chain branching.

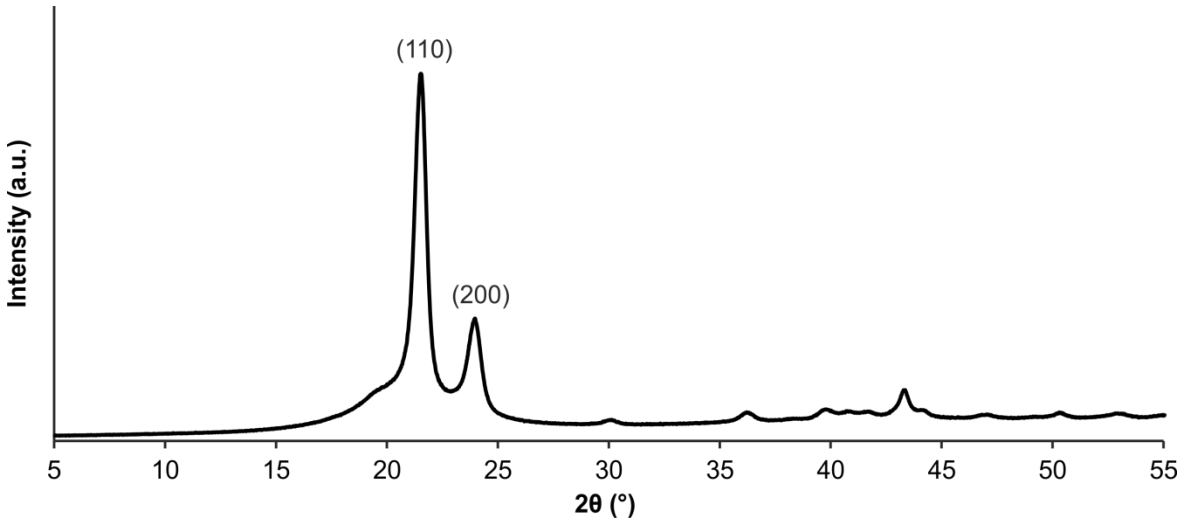


Figure 3.17. *Powder X-ray diffraction pattern of polyethylene produced by Pn*ZrCp(Cl)$_{sMAO}$.*

The improvement in polymer morphology following catalyst immobilisation can be seen by scanning electron microscopy (SEM). Figure 3.18 shows SEM images of the polymer produced by Pn*ZrCp^{Me}(Cl) (a) and Pn*ZrCp^{Me}(Cl)$_{sMAO}$ (b) at x100 magnification. Clearly, aggregation is significantly decreased following immobilisation of the catalyst on sMAO, producing a polymer with typical particle size 13–23 μm, compared to > 1 mm, as seen with the product of homogeneous conditions. This aggregation is caused by poor control of the polymerisation exotherm leading to the partial melting and adhesion of polymer particles, which is the same root cause as for reactor fouling.

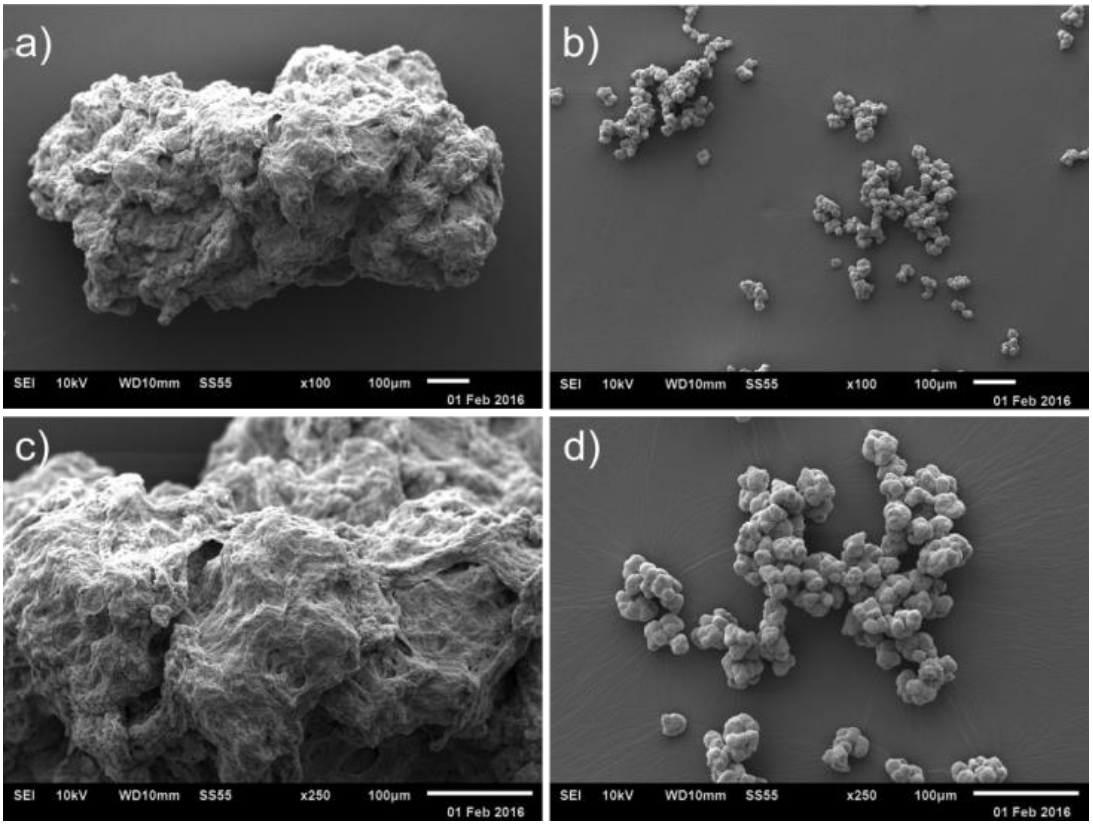


Figure 3.18. *SEM of polymer produced: a) Pn*ZrCp^{Me}(Cl) at x100 magnification; b) Pn*ZrCp^{Me}(Cl)$_{sMAO}$ at x100; c) Pn*ZrCp^{Me}(Cl) at x250; d) Pn*ZrCp^{Me}(Cl)$_{sMAO}$ at x250 magnification.*

3.7 High-throughput catalyst testing with polymethylaluminoxane supported zirconium complexes

In collaboration with Prof Vincenzo Busico at HTExplore (Naples), hydrogen response and ethylene/1-hexene co-polymerisation were investigated. 48-well micro-reactors were used to test selected catalysts for either α-olefin incorporation or H_2 response in three separate libraries; while reproducibility within each library was acceptable, results collected across different libraries are not necessarily comparable. These data therefore allow for a semi-quantitative assessment of trends, but the absolute values are treated with caution. All of the polymerisations were carried out at 80 °C until a finish condition was met: either 1 hour duration or 120 psi ethylene consumed (80 psi for hexene copolymerisations). The high temperature was chosen due to its industrial relevance; in a plant setting it is cheaper to maintain equilibrium by providing less heat to a reaction to

than it is to refrigerate coolant. The reactions were also carried out at higher pressures of 120 psi (8.27 bar), which is again more typical of industrial conditions.

The first library examined the effect of Cp^{R} substitution (Figure 3.19). Activities were observed to increase in the order R = H < Me < ^{n}Bu. Rather unusually, in the presence of 0.8% H_2 a rate acceleration is observed, which is most dramatic for Pn*ZrCp^{nBu}(Cl)$_{sMAO}$. Doubling the H_2 concentration to 1.6% leads to a relative decrease in activity, where Pn*ZrCp(Cl)$_{sMAO}$ appears the least robust. Under these conditions a large decrease in molecular weight is observed from approximately 400 kDa to 10 – 65 kDa (0.8% H_2) and 10 – 20 kDa (1.6% H_2). For Pn*ZrCp^{nBu}(Cl)$_{sMAO}$, these low molecular weights are achieved even at 0.8% H_2 concentration with some broadening of the polydispersity (17 kDa, PDI = 5.7). By contrast Pn*ZrCp(Cl)$_{sMAO}$ achieves molecular weights of only 63 kDa under identical conditions with PDI = 17.4. These changes in polymer microstructure affect the thermal properties of the polymer. This can be characterised by crystallisation-elution fractionation (CEF), which is a two-component separation procedure based on fractional crystallisation, and subsequent column chromatography.[42] As melting point and crystallinity decrease, the measured elution temperature ($T_{el,max}$) will also decrease. The amorphous fraction, not crystallised under experimental conditions, is eluted first and expressed as %AF. The elution temperature is therefore found to correlate inversely with % H_2 concentration, as is %AF.

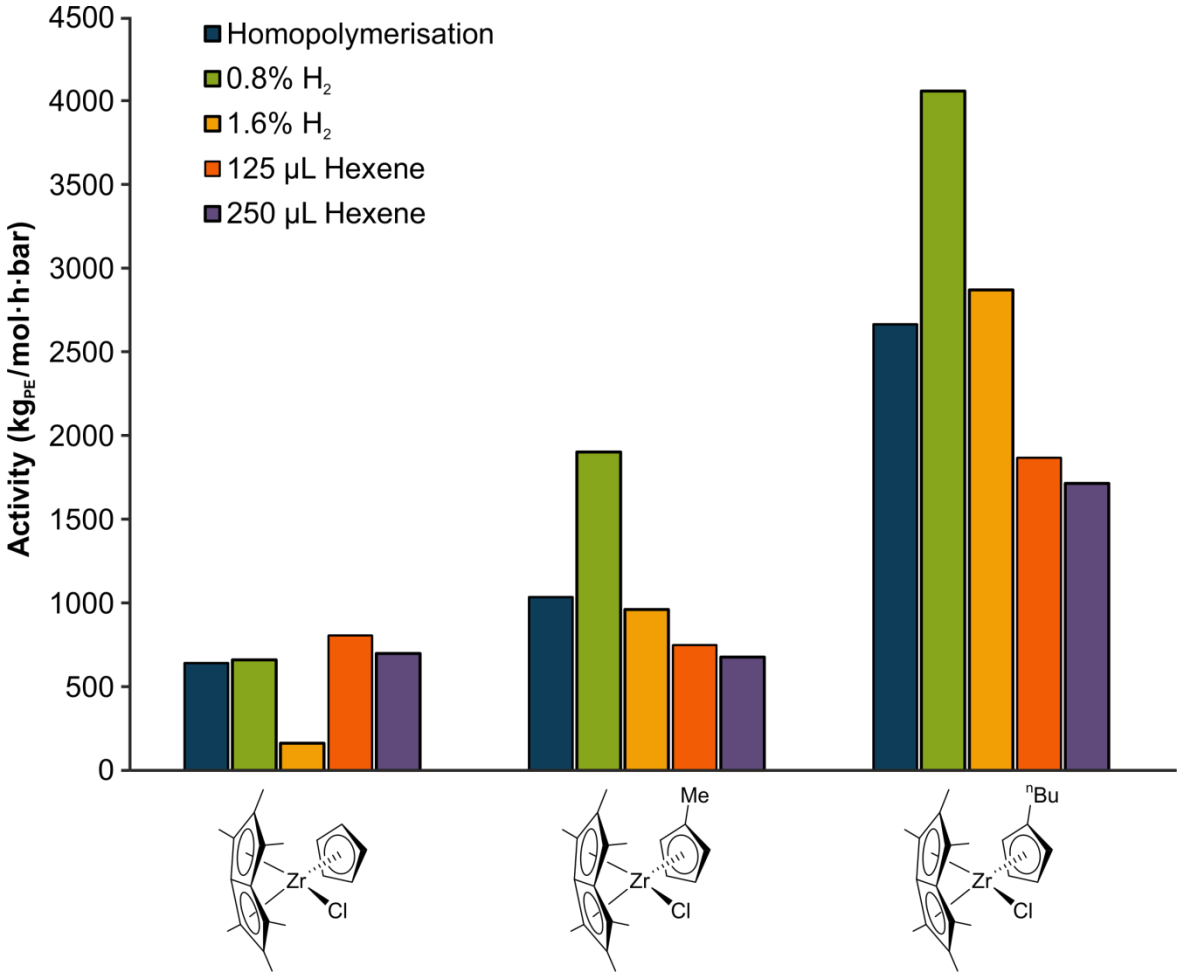


Figure 3.19. *Slurry phase ethylene polymerisation activity of Pn*ZrCp(Cl)$_{sMAO}$, Pn*ZrCp^{Me}(Cl)$_{sMAO}$ and Pn*ZrCp^{nBu}(Cl)$_{sMAO}$. Conditions: [Zr]:[sMAO] = 1:200; 120 psi ethylene; 5 mL heptane; typical loading 0.2 mg;10 µM TiBA; 80 °C.*

Given the very wide polydispersities found for Pn*ZrCp(Cl)$_{sMAO}$ in the presence of H_2 it is perhaps unsurprising to observe the largest %AF in this case (21% at 1.6% H_2 concentration). At 0.8% H_2, the elution temperature is found to respond most significantly in Pn*ZrCp^{nBu}(Cl)$_{sMAO}$ (111.6 °C to 109.8 °C) although the lowest elution temperature is found for Pn*ZrCp^{Me}(Cl)$_{sMAO}$ at 1.6% H_2 concentration (107.5 °C).

All Pn* catalysts investigated demonstrate low incorporation of 1-hexene into the polymer chain. The mol% incorporation is typically 0.6% in the presence of 125 µL 1-hexene and 1.1% for 250 µL 1-hexene, as determined by ^{13}C NMR spectroscopy. However, even at these low hexene concentrations, we observe modification of the thermal behaviour of the polymer. Unlike in the presence of H_2, the amorphous fraction is generally less than 1%, with elution temperatures more significantly affected by hexene incorporation. The

minimum observed $T_{el,max}$ is observed for Pn*ZrCp^{nBu}(Cl)$_{sMAO}$ at 250 µL hexene loading (104.4 °C), however Pn*ZrCp(Cl)$_{sMAO}$ also demonstrates a similar elution temperature under equivalent conditions (104.7 °C).

Within this series the most competent catalyst across a range of measures appears to be Pn*ZrCp^{nBu}(Cl)$_{sMAO}$; robust response of the polymer molecular weight to even low hydrogen concentrations is accompanied by a very unusual rate increase. These results may suggest useful application in the synthesis of PE-wax, which is further investigated in section 3.8.

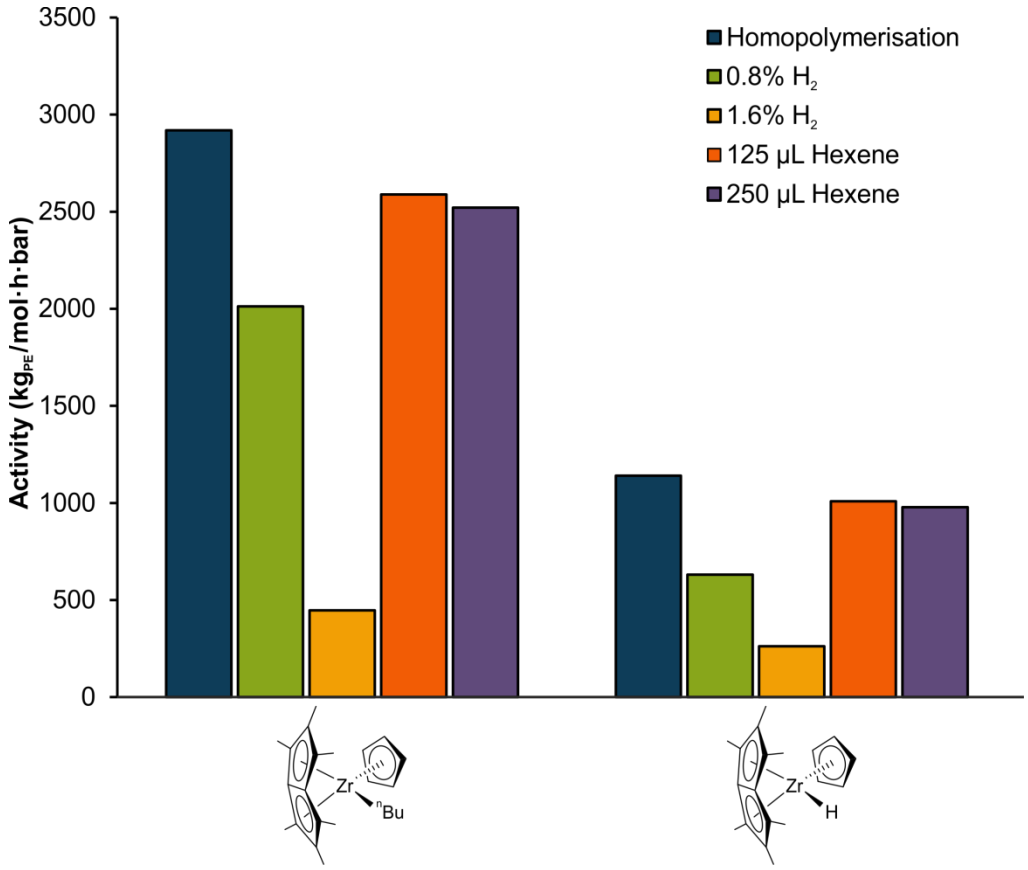


Figure 3.20. *Slurry phase ethylene polymerisation activity of Pn*ZrCp(^{n}Bu)$_{sMAO}$ and Pn*ZrCp(H)$_{sMAO}$. Conditions: [Zr]:[sMAO] = 1:200; 120 psi ethylene; 5 mL heptane; typical loading 0.2 mg;10 µM TiBA; 80 °C.*

The second library investigated the effect of substitution of the leaving group examining the catalysts Pn*ZrCp(X)$_{sMAO}$ (X = ^{n}Bu, H) (Figure 3.20). The hydride complex displays lower activities than the alkyl complex, which is interesting given the very similar activities described in section 3.5. This may be due to the different conditions employed, in particular the increased pressure of these polymerisations, although catalyst decomposition

in transit cannot be discounted. Both catalysts exhibit a drop in activity in the presence of H_2, as expected, but in contrast to the previous examples. This is accompanied by a drop in molecular weight from approximately 300 kDa to 15 – 30 kDa and 6-7 kDa with 0.8% and 1.6% H_2 respectively.

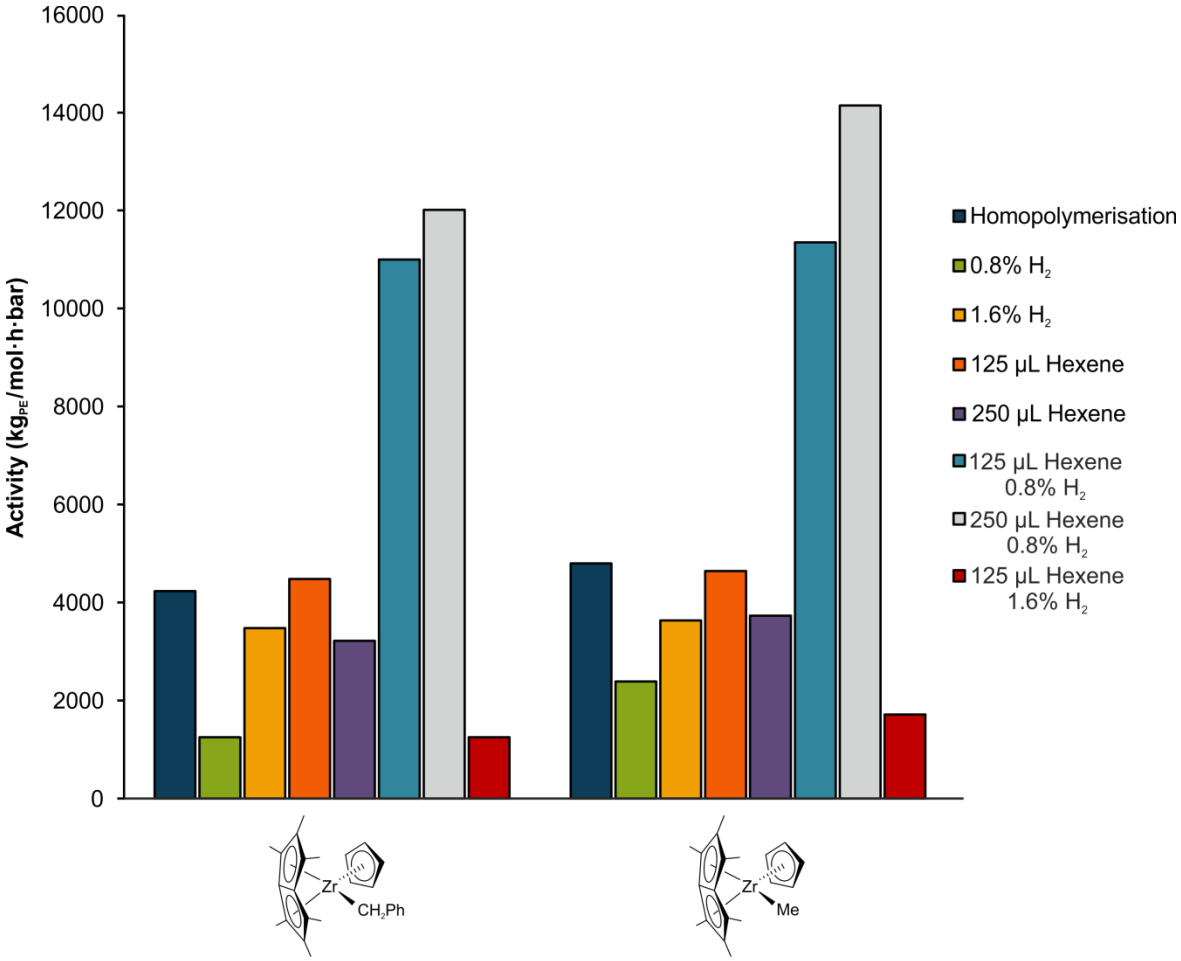


Figure 3.21. *Slurry phase ethylene polymerisation activity of Pn*ZrCp(CH$_2$Ph)$_{sMAO}$, and Pn*ZrCp(Me)$_{sMAO}$. Conditions: [Zr]:[sMAO] = 1:200; 120 psi ethylene; 5 mL heptane; typical loading 0.2 mg;10 µM TiBA; 80 °C.*

Addition of 1-hexene leads to a small drop in activity, alongside small amount of comonomer incorporation. 0.5% and 1% incorporation is observed with 125 and 250 µL hexene respectively, which produces a drop in the elution temperature measured by CEF. This is most significant for Pn*ZrCp(^{n}Bu), which displays a maximum elution temperature of 105.3 °C in the presence of 250 µL hexene.

A third library investigated two further leaving group variants, Pn*ZrCp(X)$_{sMAO}$ (X = CH_2Ph, Me) (Figure 3.21). In the presence of hydrogen a decrease in activity is

observed alongside a concomitant decrease in molecular weight from approximately 300 kDa to 20-30 kDa and 12 kDa in the presence of 0.8% and 1.6% H_2 respectively. Addition of 1-hexene generally leads to a small decrease in activity, with small amounts of comonomer incorporation observed by NMR spectroscopy. In the presence of 250 µL 1-hexene, similar decreases in elution temperature are observed by CEF in both cases from 111.9 °C and 111.7 °C to 103.9 °C and 103.7 °C for the benzyl and methyl catalysts respectively.

In this library, slurry phase ethylene polymerisations were also carried out in the combined presence of H_2 and hexene. In both cases, addition of 0.8% H_2 alongside hexene leads to remarkable increases in activity, which can be enhanced further by increasing 1-hexene concentration allowing for a near tripling of the observed activity. The origins of this unusual behavior are unknown and similar examples in the literature could not be found. Under these conditions a decrease in molecular weight is observed to approximately 10 kDa with rather narrow polydispersities of 3 – 3.3. This contrasts with the molecular weights found in the absence of hexene in the presence of 0.8% H_2, which are both higher (approx. 20 – 30 kDa) and more polydisperse (PDI = 7 – 8). Given the H_2/hexene/ethylene ternary system displays PDIs approaching single-site behavior, the hexene comonomer may play a role in stabilising reactive species formed in the presence of H_2. As a liquid, the entropic penalty associated with coordination of hexene to a metal centre is reduced relative to ethylene, while its donor characteristics are enhanced by *n*-alkyl substitution of the terminal position. Unfortunately time constraints prevented further detailed investigation of this phenomenon.

3.8 Large-scale polymerisation of polymethylaluminoxane-supported zirconium catalysts.

Pn*ZrCp^{nBu}(Cl) and Pn*ZrCp(^{n}Bu) were studied in collaboration with SCG Chemicals Co, Ltd. (Thailand), to investigate the effect of scale on these polymerisations. Using a 2 L polymerisation reactor, the solvent volume could be increased from 50 mL to 850 mL, which is facilitated by more efficient mechanical stirring (as opposed to the use of magnetic stir bars). This increases maximum polymer yield to 300 g, compared to approximately 7 g using glass ampoules. In addition, the presence of flow meters allows

for the collection of more precise gas uptake data, as opposed to limited point measures of polymerisation such as activity.

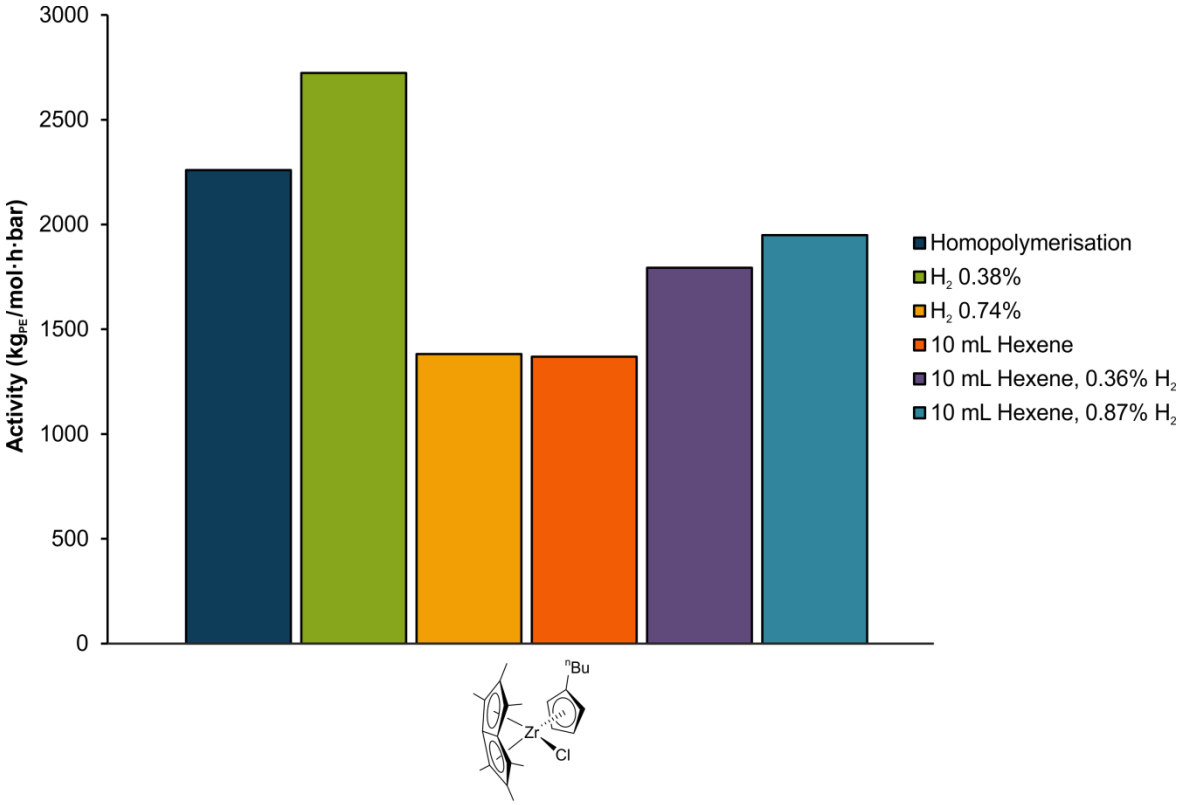


Figure 3.22. *Ethylene polymerisation activity of Pn*ZrCp^{nBu}(Cl)$_{sMAO}$. Conditions: [Zr]:[sMAO] = 1:200; 8 bar ethylene; 850 mL hexane; 25-70 mg catalyst loading;2.5 mL AlEt$_3$. Homopolymersation and H$_2$ response at 70 °C, all hexene polymerisations at 60 °C.*

Surprisingly, under these conditions the activity of Pn*ZrCp^{nBu}(Cl)$_{sMAO}$ was observed to decrease relative to the activities reported in section 3.5 (Figure 3.22). There may be a number of reasons for this decrease. Activity is reported in units of reciprocal bar, so if the rate of polymerisation does not scale linearly with pressure, a decrease in activity will be recorded. Secondly, the scavenger employed in this system is $AlEt_3$, where $Al^{i}Bu_3$ was previously used, which may negatively affect the polymerisation rate. Finally, catalyst decomposition in transit cannot be entirely discounted. Although comparison with values reported in section 3.7should be treated with caution, the same decrease in activity was not observed in this case. $AlEt_3$ has previously been reported to decrease activity relative to $Al^{i}Bu_3$ in Cp_2ZrCl_2 catalysed polymerisation of ethylene,[43] however it is difficult to assign this disparity to the modified scavenger with certainty.

Relative to the activity observed for ethylene homopolymerisation, an increase in activity is observed in the presence of 0.38% H_2, however, increasing the H_2 content further to 0.74% leads to a decrease in activity. In fact, this decrease highlights the limitations of activity as a crude point measure of polymerisation. Figure 3.23 shows the gas uptake rate for these polymerisations. In the presence of 0.38% H_2 the gas uptake trace is translated up the *y*-axis reflecting the higher activity observed. The behaviour in the presence of 0.74% is more complex. Although the steady-state region of the graph (from 1400 seconds) displays gas uptake rates equivalent to, or greater than the homopolymerisation trace, the decrease in activity in fact results from a long period of inactivity, perhaps an intiation period, which lasts over 10 minutes.

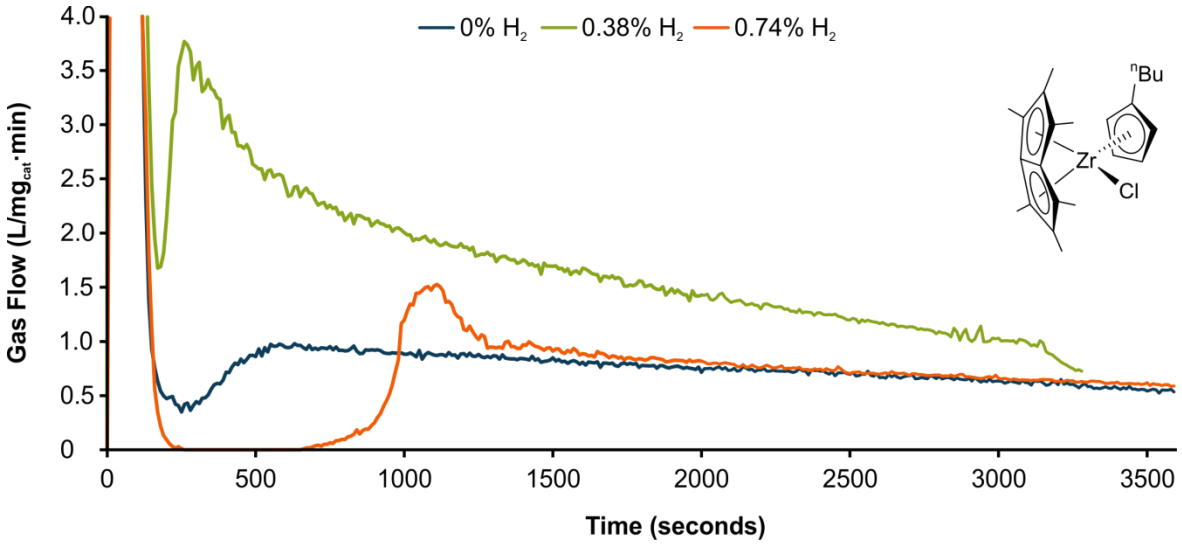


Figure 3.23. *Ethylene uptake rate for Pn*ZrCp^{nBu}(Cl)$_{sMAO}$ with pure ethylene feed (blue), 0.38% H_2 (green) and 0.74% H_2 (orange). Conditions: [Zr]:[sMAO] = 1:200; 8 bar ethylene; 850 mL hexane; 25-70 mg catalyst loading;2.5 mL $AlEt_3$;70 °C.*

A similar initiation was not observed in data described in 3.7, for which gas uptake rates are also available. Neither were similar initiation periods observed for Pn*ZrCp(^{n}Bu) discussed below. This may have arisen from an experimental limitation such as blockage of the gas-feed, or may be a result from the different scavenger employed in this set-up. Regardless, in the presence of H_2 the molecular weight is observed to decrease, although to a lesser extent than observed in section 3.7. In the absence of H_2 molecular weights of 390 kDa are observed, which decreases to 122 kDa with 0.38% H_2 and 101 kDa with 0.74% H_2. The polydispersity also increases significantly from 5.7 to 10.9 and 19.9 for

homopolymerisation, 0.38% and 0.74% H_2 respectively, indicating a significant divergence from single site behaviour.

Addition of hexene leads to a decrease in polymerisation activity, despite the small extent of comonomer incorporation (0.16 mol%). However, simultaneous addition of both hexene and H_2 (0.36% and 0.87%) leads to the observation of an unusual rate acceleration. Unlike the data described in section 3.7, this does not exceed the activity recorded for ethylene homopolymerisation. However, this does lead to the formation of lower molecular weight polyethylene (77 kDa and 47 kDa) with a narrowing of the PDIs (7.8, 9.2).

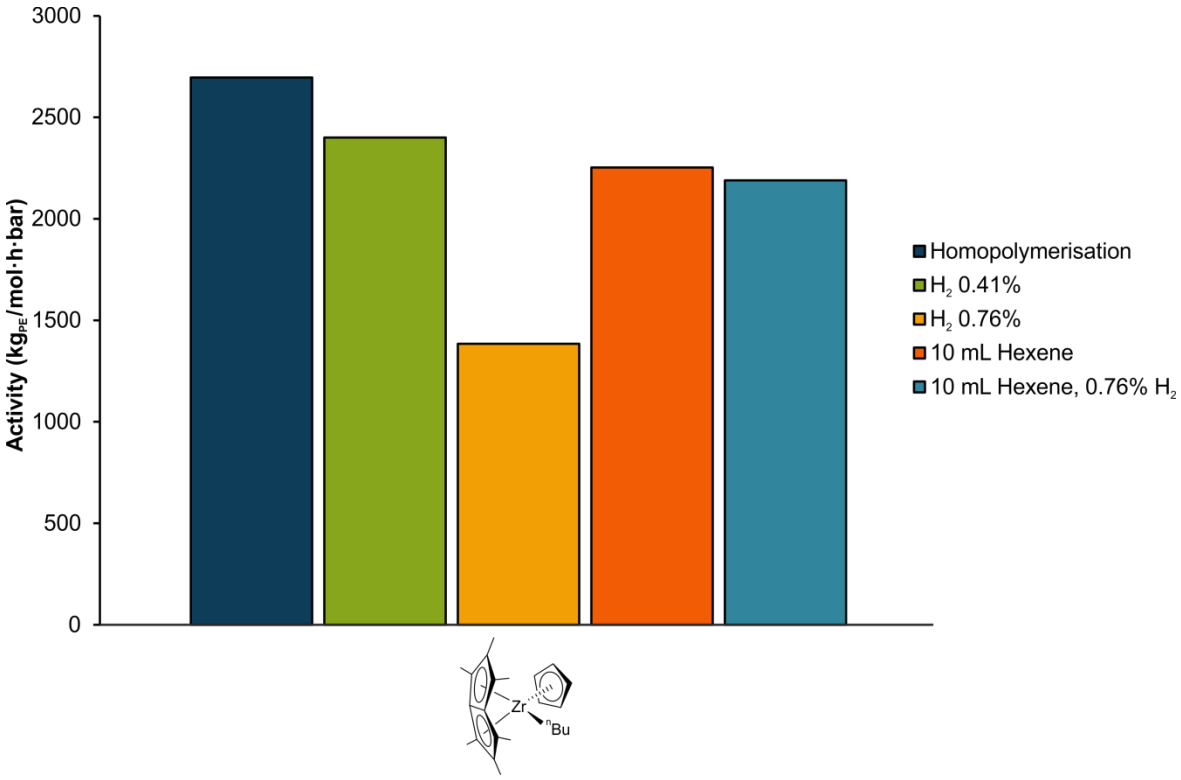


Figure 3.24. *Ethylene polymerisation activity of Pn*ZrCp(^{n}Bu)$_{sMAO}$. Conditions: [Zr]:[sMAO] = 1:200; 8 bar ethylene; 850 mL hexane; 25-70 mg catalyst loading;2.5 mL AlEt$_3$; Homopolymersation and H$_2$ response at 70 °C, all hexene polymerisations at 60 °C.*

Pn*ZrCp(^{n}Bu)$_{sMAO}$, shows a decrease in activity with increasing H_2 concentration, which correlates well with the data reported in section 3.7(Figure 3.24). The gas uptake rate does not show the same prolonged inactivity during the early stages of reaction with 0.76% H_2, as observed for Pn*ZrCp^{nBu}(Cl) although addition of the gas does appear to delay the onset of steady-state gas consumption (Figure 3.25). There is a concomitant decrease in molecular weight observed from 418 kDa to 46 kDa and 37 kDa for homopolymerisation,

0.41% and 0.76% H_2 respectively. A broadening of the PDIs is also observed, which is much less dramatic than for Pn*ZrCp^{nBu}(Cl) (4.5, 4.5 and 7.7 for homopolyemrisation, 0.41% and 0.76% H_2 respectively). In the presence of hexene a small rate decrease is observed relative the homopolymerisation activity, with little comonomer incorporation measured by ^{13}C NMR Spectroscopy (0.15 mol%). As observed for Pn*ZrCp^{nBu}(Cl), simultaneous addition of hexene and 0.76% H_2 leads to a rate increase relative to the hexene-free analogue, although the measured activity does not exceed that found for ethylene homopolymersation.

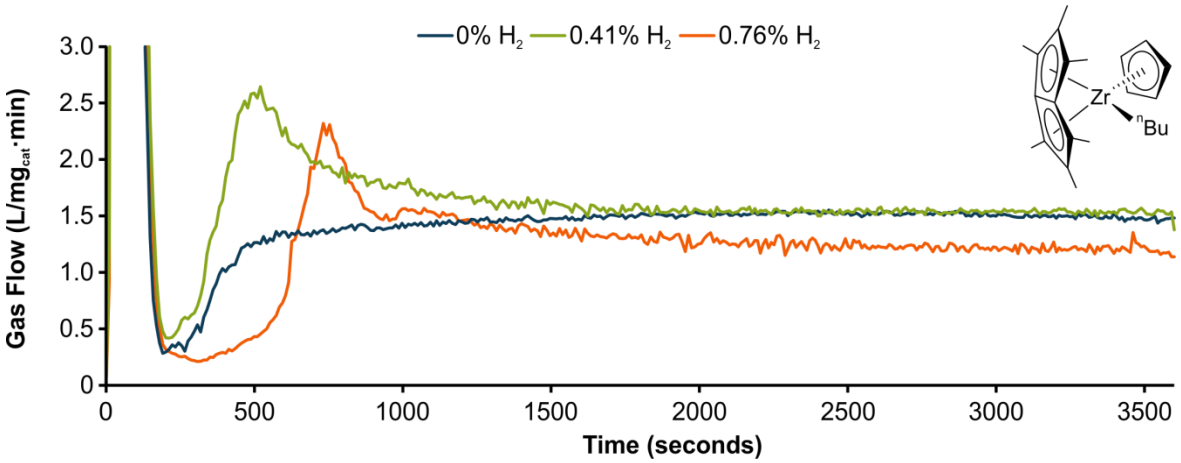


Figure 3.25. *Ethylene uptake rate for Pn*ZrCp(^{n}Bu)$_{sMAO}$ with pure ethylene feed (blue), 0.41% H_2 (green) and 0.76% H_2 (orange). Conditions: [Zr]:[sMAO] = 1:200; 8 bar ethylene; 850 mL hexane; 25-70 mg catalyst loading;2.5 mL $AlEt_3$;70 °C.*

All of the raw data for polymerisation and characterising data described in this chapter is provided in Appendix A for reference.

Conclusion

Fifteen new permethylpentalene group 4 complexes have been tested as ethylene polymerisation catalysts. The titanium pre-catalysts were found to demonstrate activities two orders of magnitude smaller than the zirconium analogues. Given their high activities, these zirconium pre-catalysts were tested on three different inorganic supports designed to improve polymer morphology and eliminate reactor fouling. The best performing support material was found to be polymethylaluminoxane, and was therefore studied in greater detail with the zirconium pre-catalysts. The supported complexes were characterised by

solid-state NMR spectroscopy, which confirmed the immobilisation of the Pn*ZrCp motif on the surface, although the detailed structure of the surface-organometallic complex remains unknown.

These catalysts were very active, with the exception of sterically hindered Pn*ZrCp^{tBu}(Cl), and in many cases more active than the solution-phase counterparts. Maximum activities were recorded for Pn*ZrCp^{nBu}(Cl) of 5025 kg_{PE}/mol·h·bar, which corresponds to a 39% increase relative to the parent complex, Pn*ZrCp(Cl) at its maximum activity. The polyethylene produced is characterised by a range of different techniques: GPC, SEM, DSC, NMR spectroscopy, powder XRD, and FTIR spectroscopy. These demonstrate the formation of high molecular weight, high density polyethylene with low branch densities.

Selected immobilised complexes were also investigated as potential PE-Wax catalysts, exposed to ethylene/H_2 mixtures in order to target low molecular weight polymer. In general, good hydrogen response was observed with significant decreases in M_w, typically accompanied by an increase in polydispersity, and in some cases, a very unusual increase in activity. All of the catalysts demonstrated poor 1-hexene incorporation, although activities were generally robust to the presence of high co-monomer concentrations. Some catalysts also demonstrated remarkable rate accelerations in the presence of ethylene/H_2/hexene mixtures, which may be due to stabilisation of reactive intermediates.

3.9 References

(1) Breslow, D. S.; Newburg, N. R. *J. Am. Chem. Soc.* **1957**, *79* (18), 5072–5073.
(2) Natta, G.; Pino, P.; Mazzanti, G.; Giannini, U. *J. Am. Chem. Soc.* **1957**, *79* (11), 2975–2976.
(3) Cossee, P. *J. Catal.* **1964**, *3* (1), 80–88.
(4) Kaminsky, W.; Laban, A. *Appl. Catal. A Gen.* **2001**, *222* (1–2), 47–61.
(5) Collins, R. A.; Russell, A. F.; Mountford, P. *Appl. Petrochemical Res.* **2015**, *5* (3), 153–171.
(6) Pellecchia, C.; Grassi, A.; Zambelli, A. *Organometallics* **1994**, *13* (1), 298–302.
(7) Chen, E. Y.-X.; Marks, T. J. *Chem. Rev.* **2000**, *100* (4), 1391–1434.
(8) Delferro, M.; Marks, T. J. *Chem. Rev.* **2011**, *111* (3), 2450–2485.
(9) Alt, H. G.; Köppl, A. *Chem. Rev.* **2000**, *100* (4), 1205–1222.
(10) McKnight, A. L.; Waymouth, R. M. *Chem. Rev.* **1998**, *98* (7), 2587–2598.
(11) Andresen, A.; Cordes, H.-G.; Herwig, J.; Kaminsky, W.; Merck, A.; Mottweiler, R.; Pein, J.; Sinn, H.; Vollmer, H.-J. *Angew. Chem. Int. Ed.* **1976**, *15* (10), 630–632.
(12) Sinn, H.; Kaminsky, W.; Vollmer, H.-J.; Woldt, R. *Angew. Chem. Int. Ed.* **1980**, *19* (5), 390–392.
(13) Harlan, C. J.; Bott, S. G.; Barron, A. R. *J. Am. Chem. Soc.* **1995**, *117* (24), 6465–

6474.
(14) Severn, J. R.; Chadwick, J. C.; Duchateau, R.; Friederichs, N. *Chem. Rev.* **2005**, *105* (11), 4073–4147.
(15) Severn, J. R.; Chadwick, J. C. *Tailor-made polymers : via immobilization of alpha-olefin polymerization catalysts*; Wiley-VCH, 2008.
(16) Ribeiro, M. R.; Deffieux, A.; Portela, M. F. *Ind. Eng. Chem. Res.* **1997**, *36* (4), 1224–1237.
(17) Jenny, C.; Maddox, P. *Curr. Opin. Solid State Mater. Sci.* **1998**, *3* (1), 94–103.
(18) Soares, J. B. P.; Hamielec, A. E. *Polym. React. Eng.* **1995**, *3* (2), 131–200.
(19) Britovsek, G. J. P.; Gibson, V. C.; Wass, D. F. *Angew. Chem. Int. Ed.* **1999**, *38* (4), 428–447.
(20) Chadwick, F. M.; Cooper, R. T.; Ashley, A. E.; Buffet, J.-C.; O'Hare, D. M. *Organometallics* **2014**, *33* (14), 3775–3785.
(21) Chadwick, F. M. Uranium, Zirconium and Hafnium η8-permethylpentalene chemistry, University of Oxford, 2013.
(22) Jonas, K.; Kolb, P.; Kollbach, G. Mononuclear and polynuclear transition metal complexes with pentalene ligands bound to single metal atoms. US 5959132 A, September 28, 1999.
(23) Hart-Davis, A. J.; White, C.; Mawby, R. J. *Inorg. Chim. Acta* **1970**, *4*, 441–446.
(24) Rerek, M. E.; Basolo, F. *J. Am. Chem. Soc.* **1984**, *106* (20), 5908–5912.
(25) Veiros, L. F. *Organometallics* **2000**, *19* (16), 3127–3136.
(26) Basolo, F. *Polyhedron* **1990**, *9* (13), 1503–1535.
(27) Bartram, M. E.; Michalske, T. A.; Rogers, J. W. *J. Phys. Chem.* **1991**, *95* (11), 4453–4463.
(28) Soga, K.; Kaminaka, M. *Die Makromol. Chemie* **1993**, *194* (6), 1745–1755.
(29) Panchenko, V. N.; Semikolenova, N. V.; Danilova, I. G.; Paukshtis, E. A.; Zakharov, V. A. *J. Mol. Catal. A Chem.* **1999**, *142* (1), 27–37.
(30) Welborn, H. C. Supported polymerization catalyst. US 4808561 A, February 28, 1989.
(31) Takahashi, T. Process for producing ethylene copolymers. US 5026797 A, June 25, 1991.
(32) Buffet, J.-C.; Turner, Z. R.; Cooper, R. T.; O'Hare, D. *Polym. Chem.* **2015**, *6* (13), 2493–2503.
(33) Buffet, J.-C.; Arnold, T. A. Q.; Turner, Z. R.; Angpanitcharoen, P.; O'Hare, D. *RSC Adv.* **2015**, *5* (106), 87456–87464.
(34) Wright, C. M. R.; Turner, Z. R.; Buffet, J.-C.; O'Hare, D. *Chem. Commun.* **2016**, *52* (13), 2850–2853.
(35) Buffet, J.-C.; Wanna, N.; Arnold, T. A. Q.; Gibson, E. K.; Wells, P. P.; Wang, Q.; Tantirungrotechai, J.; O'Hare, D. *Chem. Mater.* **2015**, *27* (5), 1495–1501.
(36) Andresen, A.; Cordes, H.-G.; Herwig, J.; Kaminsky, W.; Merck, A.; Mottweiler, R.; Pein, J.; Sinn, H.; Vollmer, H.-J. *Angew. Chem. Int. Ed.* **1976**, *15* (10), 630–632.
(37) D'Agnillo, L.; Soares, J. B. P.; Penlidis, A. *Macromol. Chem. Phys.* **1998**, *199* (6), 955–962.
(38) Odian, G. G. *Principles of polymerization*, 4th ed.; John Wiley & Sons, Inc.: Hoboken, New Jersey, 2004.
(39) Krimm, S.; Liang, C. Y.; Sutherland, G. B. B. M. *J. Chem. Phys.* **1956**, *25* (3), 549–562.
(40) Alsaygh, A. A.; Al-hamidi, J.; Alsewailem, F. D.; Al-Najjar, I. M.; Kuznetsov, V.

L. *Appl. Petrochemical Res.* **2014**, *4* (1), 79–84.
(41) Fontana, L.; Vinh, D. Q.; Santoro, M.; Scandolo, S.; Gorelli, F. A.; Bini, R.; Hanfland, M. *Phys. Rev. B* **2007**, *75* (17), 174112.
(42) Monrabal, B.; Sancho-Tello, J.; Mayo, N.; Romero, L. *Macromol. Symp.* **2007**, *257* (1), 71–79.
(43) Götz, C.; Rau, A.; Luft, G. *Macromol. Mater. Eng.* **2002**, *287* (1), 16–22.

Chapter 4: Mechanism of Ethylene Polymerisation with Pn*MCp^{R}(X) Complexes

4.1 Introduction

In the previous chapter, very high activities are reported for Pn*ZrCp^{R}(X) catalysts activated with MAO or polymethylaluminoxane.[1–4] The zirconium congeners were the best performing catalysts with activities up to 5025 $kg_{PE}/(mol \cdot h \cdot bar)$ observed, producing high molecular weight PE up to 1000 kDa.

Unusually, these Pn*ZrCp^{R}(X) complexes are all 18-electron, oxidatively saturated compounds, containing only a single leaving-group, which contradicts the accepted structural design requirements for transition metal coordination-insertion catalysts.

Similar examples are very rare with a few known examples in the patent literature. PnZrInd(Cl) has previously been noted as a very active catalyst,[5] as has Pn″ZrCp(Cl) (Pn″ = $[1,5\text{-}C_8H_4(SiMe_3)_2]^{2-}$)[6] and COT″ZrCp(Cl) (COT″ = $[1,4\text{−}C_8H_6(SiMe_3)_2]^{2-}$).[7]

The rarity of transition metal pre-catalysts similar to Pn*ZrCp^{R}(X) can be attributed to their inability to form cationic metal alkyl complexes without severe and energetically unfavourable ligand reorganisations. The hypothetical complex, $[Pn*ZrCp(alkyl)]^{+}$, would require zirconium in the (+5) oxidation state, which is not accessible for zirconium or any of the group 4 metals (Figure 4.1).

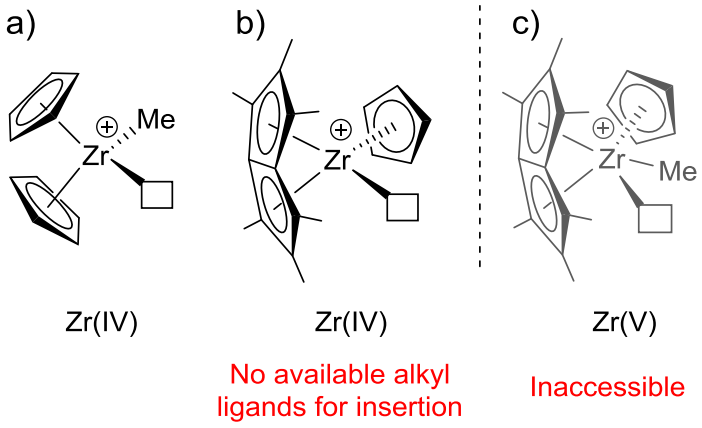


Figure 4.1. *Comparison of active species for a) coordination insertion pre-catalyst Cp_2ZrX_2, b) hypothetical activation product of Pn*ZrCp(X), c) inaccessible cationic alkyl active species with Pn*ZrCp(X) pre-catalyst.*

In this chapter the mechanism of polymerisation with this non-classical motif is investigated. Synthesis of proposed intermediates, small molecule reactivity studies and *in-situ* gas uptake measurements lead to the proposal of a cationic polymerisation mechanism capable of producing high molecular weight polyethylene.

4.2 Ethylene polymerisation with permethylpentalene zirconium complexes

O'Hare and coworkers have previously reported the synthesis of the Zr(IV) halide dimer, $[Pn^*Zr(\mu{-}Cl)_{3/2})]_2(\mu{-}Cl)_2Li(THF)_x$,[8] and a number of Pn^*ZrX_2 complexes (X = allyl, benzyl),[9,10] which can be considered broadly analogous to the bent metallocene olefin polymerisation pre-catalysts, Cp_2ZrX_2. All of the complexes contain two labile ligands groups that could, in principle, be converted in the presence of a MAO to a cationic alkyl complex suitable for coordination-insertion catalysis. It is therefore surprising to find comparatively poor ethylene polymerisation activities across the series of 56–90 $kg_{PE}/(mol{\cdot}h{\cdot}bar)$ compared to 5195 $kg_{PE}/(mol{\cdot}h{\cdot}bar)$ for $Pn^*ZrCp^{nBu}(Cl)$ (Table 4.1).

Entry	Complex	Activity $kg_{PE}/(mol{\cdot}h{\cdot}bar)$
1	$[Pn^*Zr(\mu{-}Cl)_{3/2})]_2(\mu{-}Cl)_2Li(THF)_x$ [a]	84 ± 7
2	$Pn^*Zr(C_3H_5)_2$ [a]	56 ± 6
3	$Pn^*Zr(Bz)_2$ [a]	90 ± 8
4	$Pn^*ZrCp(Cl)$ [b]	4497 ± 168
5	$Pn^*ZrCp^{nBu}(Cl)$ [b]	5195 ± 24
6	Cp_2ZrMe_2 [b]	5533 ± 66

Table 4.1. *Comparison of solution phase ethylene polymerisation activities of some Pn*Zr complexes. Polymerisation conditions: [Zr]:[MAO] = 1:1000, 50 mL hexane, 2 bar ethylene, 80 °C; a) 1 mg catalyst loading, 60 mins. Data obtained from ref (10) b) 0.5 mg catalyst loading, 2 mins.*

It can be inferred that pentalene complexes pre-disposed to coordination-insertion catalysis produce low activities (Table 4.1, entries 1 – 3), while those structurally prohibited from operating by the same mechanism produce high activities (Table 4.1, entries 4 and 5), comparable to traditional zirconocene polymerisation catalysts.

4.3 Identifying the products of activation

Exposure of Pn*ZrCp(Cl) to ethylene does not lead to polyethylene formation, therefore the active species is formed only following reaction with a co-catalyst such as MAO. Pn*ZrCp(Cl) was reacted with 50 eq. MAO in C_6D_6 at room temperature. Within 5 minutes phase separation of a yellow oil could be observed, which settled over a further 10 minutes leaving a near colourless supernatant. Similar phase separation is often encountered with cationic zirconocenes, although these oils are generally soluble in halo-aromatic solvents. After decanting the supernatant and re-dissolving the oil in C_6D_5Cl a surprisingly simple ^{1}H NMR spectrum was obtained (Figure 4.2). An intense broad resonance corresponding to the Al–Me environments of MAO can be observed at –0.17 ppm alongside a set of sharp singlets corresponding to an η^{8}–Pn*ZrCp fragment at 1.84, 1.86, 1.94 and 5.52 ppm. From HMBC and HSQC NMR spectra it is observed that both these ^{1}H signals and their corresponding ^{13}C environments are similar to those found for [(Pn*ZrCp)$_2$(μ–Cl)][B(C$_6$F$_5$)$_4$] (1.75, 1.78, 1.85, 5.44 ppm, *vide infra*), bearing less resemblance to Pn*ZrCp(X) (X = Cl, Me) or [(Pn*ZrCp)$_2$(μ–Me)][B(C$_6$F$_5$)$_4$] in C_6D_5Cl.

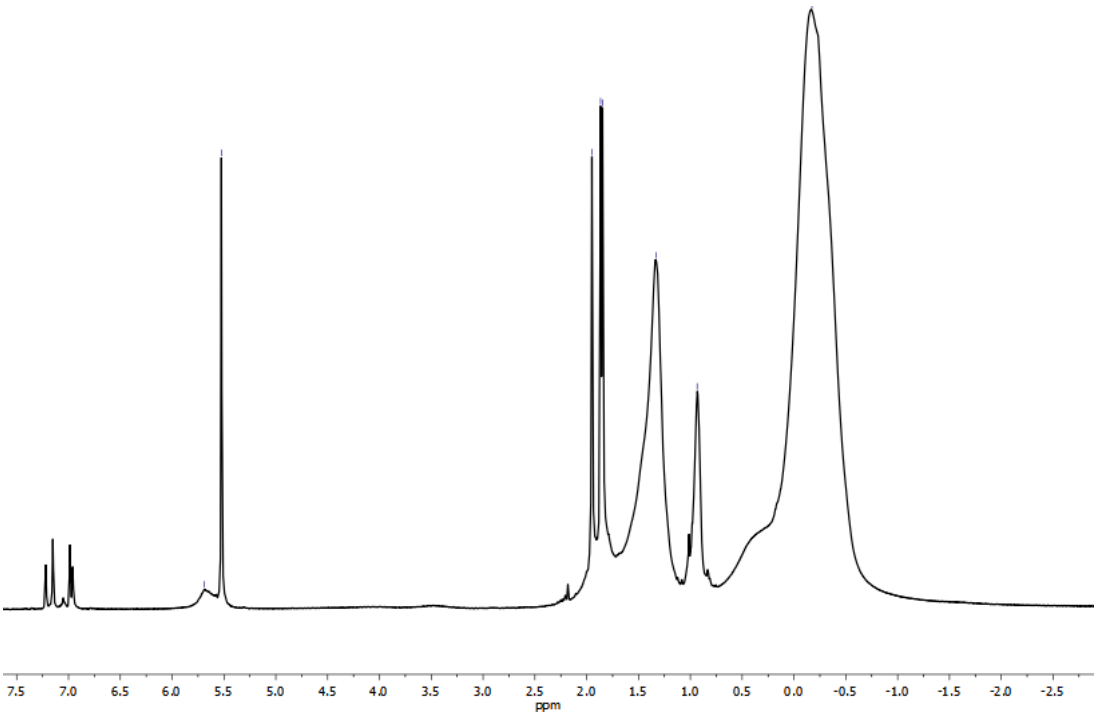


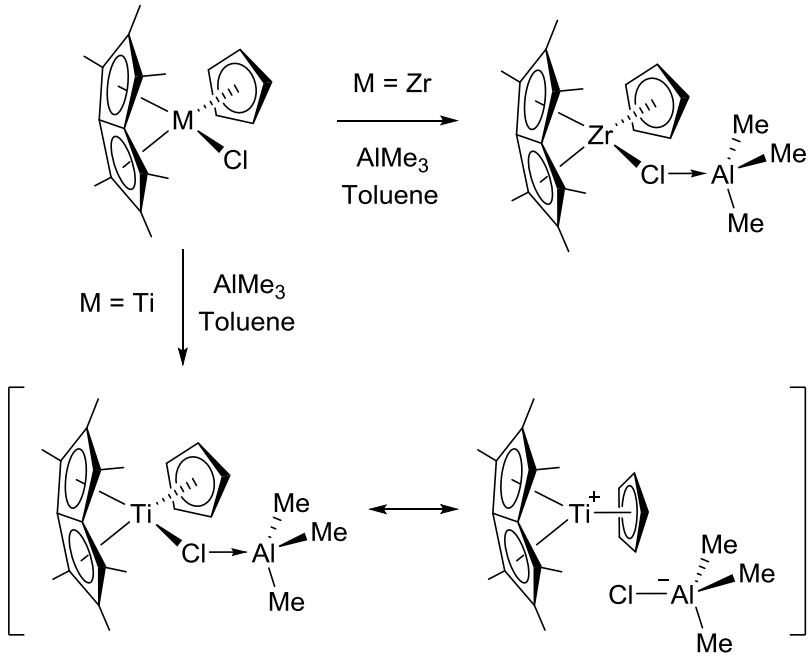
Figure 4.2. *^{1}H NMR spectrum (400 MHz, C_6D_5Cl, 298 K) of Pn*ZrCp(Cl) activated with 50 eq. MAO.*

Some additional broad features are also observed at 0.93, 1.34, 5.69 ppm, the latter of which is in a region typically found for Cp rings. Due to the ill-defined nature of MAO, cationation often produces broad NMR spectra that are challenging to interpret. Inner- and outer-sphere $[Zr]^+[MAO–X]^–$ species have previously been proposed following activation of $Cp^R_2ZrX_2$, with outer-sphere ion pairs, $[Cp^RZrMe]$- - -[X–MAO] producing significant broadening in particular.[11–15] On the basis of these data conclusive assignment of either component is not possible, although they allude to the formation of cationic zirconium species.

In pursuit of discrete molecular species, MAO was substituted for the well-defined alkylaluminium co-catalyst $AlMe_3$. Although less Lewis-acidic than MAO, the use of $AlMe_3$ in mechanistic studies has provided useful insights into the reactivity of metallocenes and MAO previously.[16,17] Weaker M–L bonds in titanium homologues can also provide a useful approximation for the reactivity of zirconium complexes under more forcing, Lewis acidic conditions.

On addition of 1 eq. $AlMe_3$ to a C_7D_8 solution of Pn*ZrCp(Cl) in an NMR tube, three Pn*–*Me* resonances were observed by ^{1}H NMR spectroscopy alongside a new singlet at –0.31 ppm corresponding to the Al–*Me* environment. The time-averaged C_s symmetry is consistent with the formation of an adduct, Pn*ZrCp(μ–Cl)$AlMe_3$ (Scheme 4.1).

Variable temperature ^{1}H NMR spectroscopy indicated the persistence of this adduct up to 380 K, with no evidence for halide abstraction observed. The adduct can be synthesised in bulk simply by the addition of Pn*ZrCp(Cl) and $AlMe_3$ in toluene, before drying under vacuum. Pn*ZrCp(μ–Cl)$AlMe_3$ was isolated as a yellow microcrystalline solid in 82% yield (Scheme 4.1); the aluminium fragment is evidently strongly bound as accurate elemental analysis was obtained following exposure to dynamic vacuum.



Scheme 4.1. *Reactivity of Pn*MCp(Cl) complexes with $AlMe_3$ (M = Ti, Zr).*

By contrast addition of 1 eq. $AlMe_3$ to a C_7D_8 solution of Pn*TiCp(Cl) leads to abstraction of the halide ligand at room temperature. Two Pn*–*Me* resonances are observed in a ratio 12:6 indicating C_{2v} time-averaged symmetry, which suggests the formation of the ion-pair [Pn*TiCp][$AlMe_3Cl$] (Figure 4.3). This halide abstraction was observed to be reversible, with a broadened C_s symmetric Pn* moiety observed at 212 K. The free energy change of the transition was calculated at the coalescence point of 232 K ($\Delta G^{\ddagger}_{232K}$ = 47 kJ/mol, Figure 4.3).

Bulk synthesis was achieved by the addition of Pn*TiCp(Cl) and 1 eq. $AlMe_3$ in pentane. After drying under vacuum, the product was isolated as a pure red solid in 78% yield. The $AlMe_3$ fragment was found to be more labile than in Pn*ZrCp(μ–Cl)$AlMe_3$, requiring exposure to vacuum for a minimum duration, and the substitution of toluene for pentane. Single crystals of both complexes suitable for X-ray diffraction were obtained by slow evaporation of benzene solutions, which demonstrated the formation of $AlMe_3$ adducts in the solid state, Pn*MCp(μ–Cl)$AlMe_3$ (M = Ti, Zr) (Figure 4.4). A comparison of some key structural parameters are given in Table 4.2.

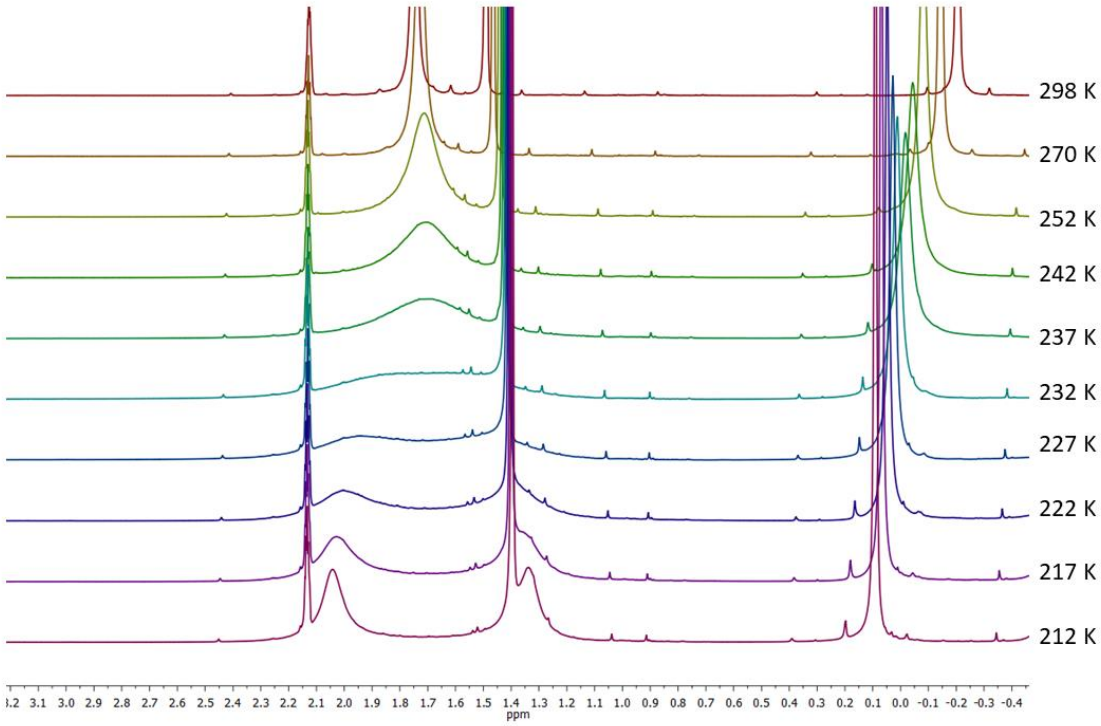


Figure 4.3. *Variable temperature ^{1}H NMR spectra of Pn*TiCpCl.AlMe$_3$ (C_7D_8).*

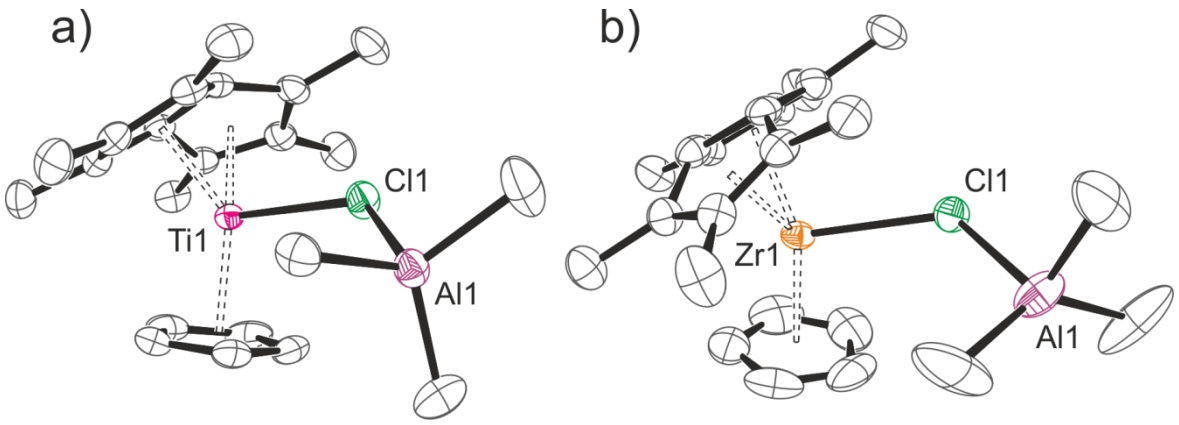


Figure 4.4. *Thermal displacement ellipsoid plot (50% probability) of a) Pn*TiCp(μ−Cl)AlMe$_3$ b) Pn*ZrCp(μ−Cl)AlMe$_3$. H atoms omitted for clarity.*

	Fold Angle	M–Cl	Al–C	M–Cl–Al	Al–$C_{3\text{-plane}}$
Pn*TiCp(Cl)	30.98(12)	2.5068(8)	-	-	-
Pn*TiCp(μ–Cl)$AlMe_3$	31.52(7)	2.5531(5)	2.3337(6)	130.35(2)	0.4326(12)
Pn*ZrCp(Cl)	30.33(14)	2.5484(8)	-	-	-
Pn*ZrCp(μ–Cl)$AlMe_3$	29.85(19)	2.6112(9)	2.3713(16)	124.93(5)	0.422(7)

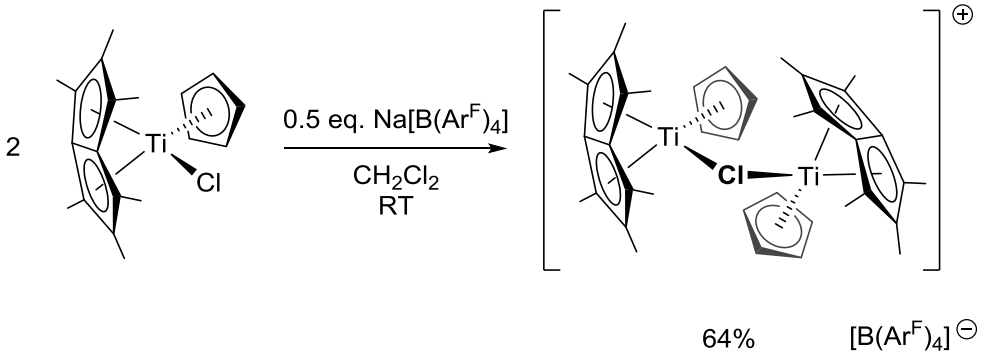
Table 4.2. *Comparison of selected bond lengths (Å) and angles (°) for Pn*MCp(μ–Cl)$AlMe_3$ complexes (M = Ti, Zr). Al–$C_{3\text{-plane}}$ is the distance between Al and the mean plane of the adjacent terminal carbon atoms.*

Elongation of the M–Cl bonds is observed following coordination of $AlMe_3$, which is slightly more pronounced for zirconium relative to titanium. This is despite the observation of a longer Al–Cl bond in the former case, which might allude to a stronger Al–Cl bonding interaction for the zirconium congener. This would qualitatively correlate with the increased volatility of the $AlMe_3$ fragment observed for Pn*TiCp(μ–Cl)$AlMe_3$ under vacuum. The pyramidalisation of the organo-aluminium fragment can be quantified by measuring the distance from aluminium to the mean plane of adjacent terminal carbon atoms. A slight decrease in pyramidalisation is observed for zirconium relative to titanium, which suggests reduced electron donation from the chloride ligand into the vacant aluminium p-orbital.

In light of the apparent involvement of cationic metal complexes following activation with alkyl aluminium reagents, it was postulated that cationation precedes polymerisation. Therefore rational routes to the synthesis of cationic metal Pn* complexes were sought.

4.4 Attempted synthesis of cationic complexes by halide abstraction

Pn*TiCp(Cl) was reacted with 0.5 eq. Na[B(3,5–$C_6H_3(CF_3)_2)_4$] in CH_2Cl_2 at room temperature for 30 minutes, during which time NaCl was observed to precipitate. Following filtration, the green solution was cooled to –80 °C, yielding a dark green crystalline solid of [(Pn*TiCp)$_2$(μ–Cl)][(B(3,5–$C_6H_3(CF_3)_2)_4$] in 64% yield, determined pure by elemental analysis (Scheme 4.2). Single crystals suitable for an X-ray diffraction study were obtained by slow evaporation of a benzene solution (Figure 4.5), with key bond lengths and angles given in Table 4.3.



Scheme 4.2. *Synthesis of [(Pn*TiCp)$_2$(μ–Cl)][(B(Ar^F)$_4$] B(Ar^F)$_4$ = (B(3,5–C$_6$H$_3$(CF$_3$)$_2$)$_4$.*

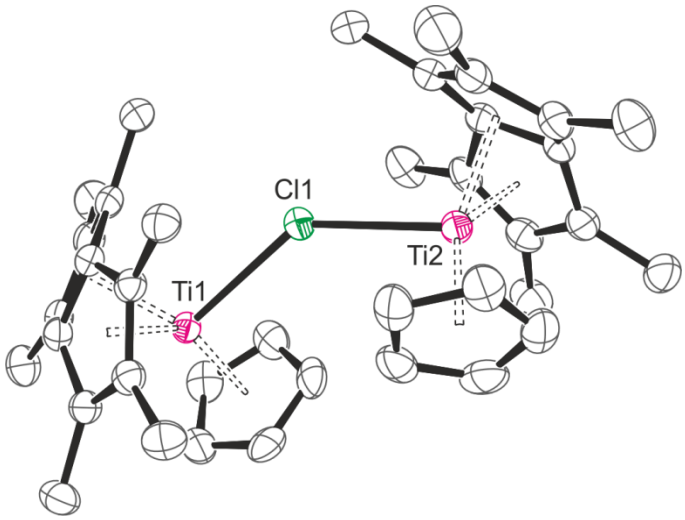


Figure 4.5. *Thermal displacement ellipsoid plot of [(Pn*TiCp)$_2$(μ–Cl)][(B(3,5–C$_6$H$_3$(CF$_3$)$_2$)$_4$]. Anion and H atoms omitted for clarity, ellipsoids shown at 50% probability.*

The fold angles are slightly contracted relative to Pn*TiCp(Cl) (30.98(12)°), but are similar in magnitude to those observed for Pn*TiCp(μ–Cl)AlMe$_3$. This is presumably a result of more extensive electron donation from Pn* to titanium in order to compensate for the positive charge in [(Pn*TiCp)$_2$(μ–Cl)][(B(3,5–C$_6$H$_3$(CF$_3$)$_2$)$_4$]. Further evidence for this can be found in the contraction of the Ti–Pn*$_{cent}$ distances, with a less significant decrease in Ti–Cp$_{cent}$ bond lengths also observed (Pn*TiCp(Cl) average Ti–Pn*$_{cent}$ = 1.9946(12) Å, Ti–Cp$_{cent}$ = 2.0631(14) Å). Unsurprisingly, elongation of the Ti–Cl bond is found upon dimerisation, from 2.0568(8) Å in the neutral monomer, to 2.6227(7) Å and 2.6340(7) Å in the cationic dimer. The two Pn*TiCp fragments are twisted relative to one another, which can be measured by considering the twist angle made by mean planes of each Pn* bridgehead centroid, Ti and

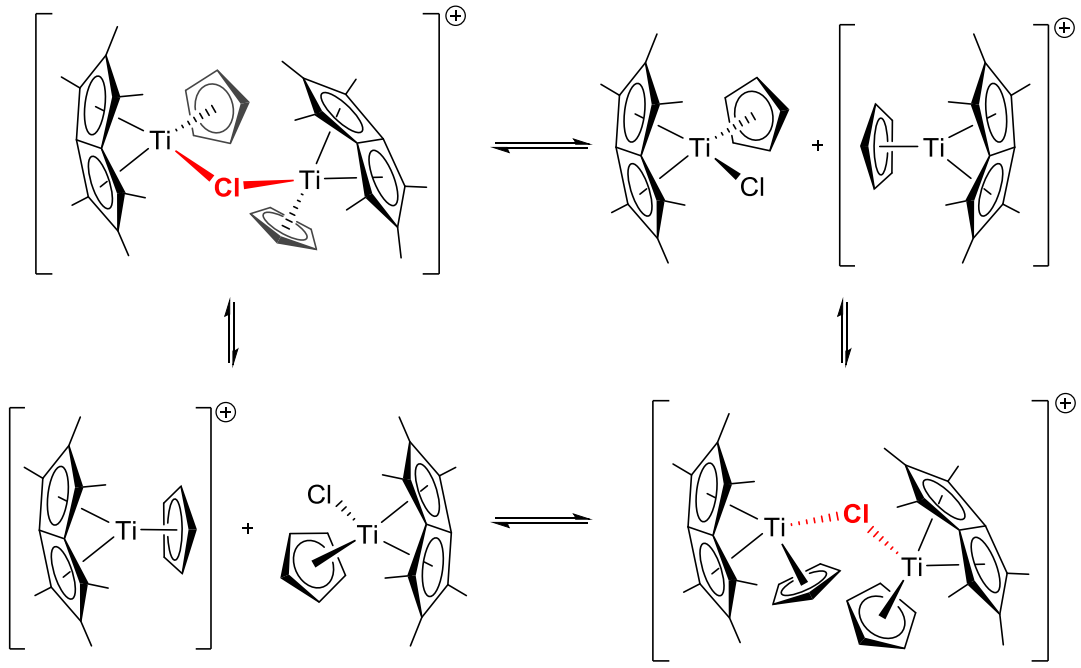
Cp centroid. The twist found in [(Pn*TiCp)$_2$(μ–Cl)][(B(3,5–$C_6H_3(CF_3)_2)_4$] is close to 90°, which minimises any steric clashes arising from neighboring carbocycles.

[(Pn*TiCp)$_2$(μ–Cl)][(B(3,5–$C_6H_3(CF_3)_2)_4$]	
Fold Angle	31.68(15)
	31.15(13)
Ti–Pn*$_{cent}$	1.9862(13)
Ti–Cp$_{cent}$	2.0545(14)
Ti–Cl	2.6227(7)
	2.6340(7)
Ti–Cl–Ti	138.2(3)
Twist Angle	84.53(6)

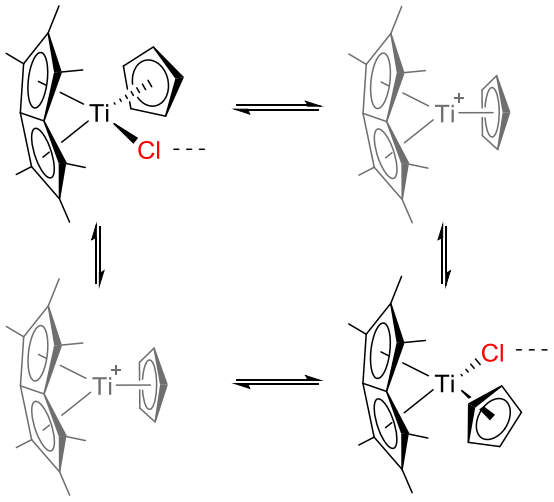
Table 4.3. *Comparison of selected bond lengths (Å) and angles (°) for [(Pn*TiCp)$_2$(μ–Cl)][(B(3,5–$C_6H_3(CF_3)_2)_4$]. Twist angle = angle made by the mean planes of Pn*$_{bridgehead\text{-}cent}$–Ti–Cp$_{cent.}$*

The ^{1}H NMR spectrum in C_6D_5Cl displays two Pn*–*Me* resonances in a 12:6 ratio (1.49 and 1.56 ppm). This C_{2v} solution-state symmetry is inconsistent with the C_1 symmetry observed for this complex in the solid state, which is likely due to a rapid and reversible dimerisation process producing time-averaged C_{2v} symmetry around the titanium centre (Scheme 4.3). This is most straightforwardly visualised by considering the dynamic behaviour of a single Pn*Ti fragment (Scheme 4.4).

Following formal cleavage of one Ti–Cl bond, there should be no preferred orientation for nucleophilic attack of an additional Pn*TiCp(Cl) molecule, which approaching from the opposite face of the complex would form a second unique isomer. This process recurring rapidly would generate equivalent NWT resonances averaged over time, and the appearance of C_{2v} symmetry in solution by NMR spectroscopy.



Scheme 4.3. *Monomer/dimer equilibrium responsible for time-averaged C_{2v} symmetry of [(Pn*TiCp)$_2$(μ–Cl)][(B(3,5–C$_6$H$_3$(CF$_3$)$_2$)$_4$].*



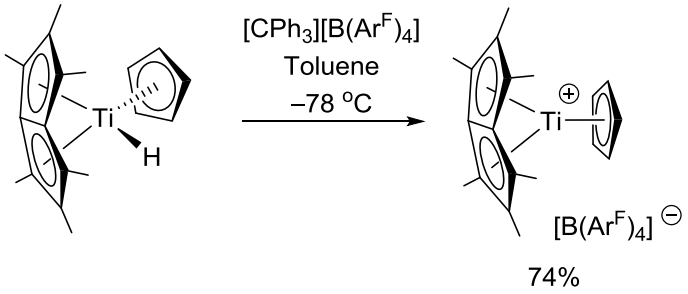
Scheme 4.4. *Illustration of monomer/dimer fluxionality of [(Pn*TiCp)$_2$(μ–Cl)][(B(3,5–C$_6$H$_3$(CF$_3$)$_2$)$_4$] over time from the perspective of a single titanium centre.*

Attempts to abstract the remaining halide ligand with Na[B(3,5–C$_6$H$_3$(CF$_3$)$_2$)$_4$] by varying solvent, temperature and stoichiometry were unsuccessful. Similarly, AgPF$_6$ only allowed for the synthesis of the [PF$_6$]$^-$ stabilised homobimetallic complex as judged by NMR spectroscopy. For Pn*ZrCp(Cl), stronger metal-ligands bonds encountered on moving down group 4 prevents halide abstraction with either AgPF$_6$ or Na[B(3,5–C$_6$H$_3$(CF$_3$)$_2$)$_4$] in

polar or non-polar solvents between room temperature and 80 °C. Given the limited success achieved by chloride abstraction, an alternative route of hydride/alkyl abstractions was pursued, which has generally been a reliable method for the synthesis of base-free cationic metal complexes.

4.5 Synthesis of cationic complexes by hydride/alkyl abstraction

Synthesis of the target cationic complexes was achieved using the trityl cation salts, $[CPh_3][B(Ar^F)_4]$ (Ar^F = C_6F_5, 3,5–$C_6H_3(CF_3)_2$). [Pn*TiCp][B(3,5–$C_6H_3(CF_3)_2)_4$] was synthesised from Pn*TiCp(X) (X = H, Me) and 1 eq. $[CPh_3][B(Ar^F)_4]$ in toluene at −78 °C. After warming to room temperature and precipitating with pentane, the product was isolated as a brown powder in 74% yield, determined pure by elemental analysis (Scheme 4.5).



Scheme 4.5. *Synthesis of [(Pn*TiCp)][(B(3,5–$C_6H_3(CF_3)_2)_4$].*

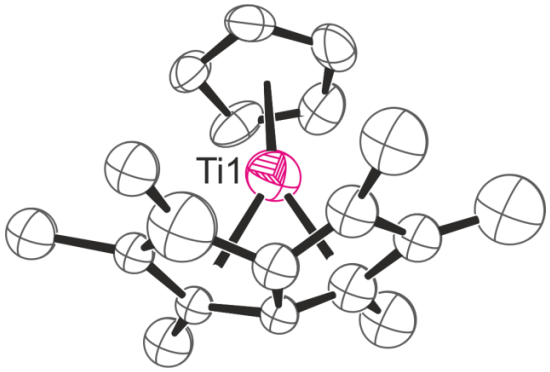
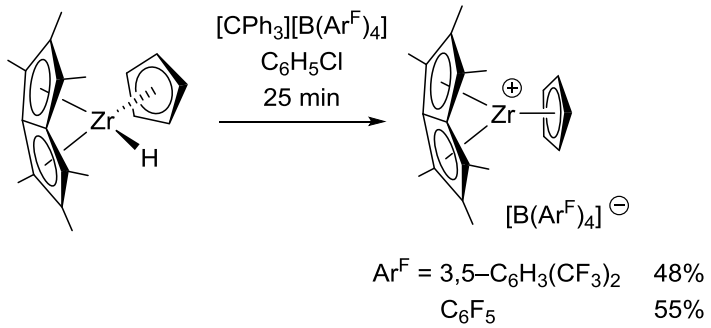


Figure 4.6. *Thermal displacement ellipsoid plot of [(Pn*TiCp)][(B(3,5–$C_6H_3(CF_3)_2)_4$]. Anion and H atoms omitted for clarity, ellipsoids shown at 50% probability.*

The ^{1}H NMR spectrum in C_6D_5Cl indicates C_{2v} symmetry in solution with no observable interaction between the anion and the metal centre. Deshielded Pn*–*Me* environments resonate at 1.47 and 0.84 ppm for NWT and WT protons respectively (c.f. Pn*TiCp(H)

NWT 2.06, 1.70; WT 2.60 ppm). Single crystals suitable for an X-ray diffraction study were grown by slow evaporation of a chlorobenzene solution (Figure 4.6). Both the Pn* ligand and Ar–CF_3 groups were disordered over two positions; for Pn* each resolved part displays a large variation in M–Pn*$_{cent}$ distances (up to 0.2 Å) and fold angles (4.5°). The data is therefore only suitable for the assignment of connectivity, which indicates the same molecular symmetry in the solid state as in solution, with no interaction observed to either solvent or borate anion.

By comparison to [Pn*TiCp][B(Ar^{F})$_4$], the zirconium congener is more reactive, displaying a shorter lifetime both in solution and the solid-state. Chlorobenzene was added to a dry mixture of Pn*ZrCp(X) (X = H, Me) and [CPh_3][B(Ar^{F})$_4$] and stirred for 25 minutes, during which time the colour darkened slightly from orange to orange brown. The cationic complex was precipitated by the addition of pentane and the solution cooled for 10 minutes at –20 °C to encourage flocculation of the solid, which was then isolated by filtration and dried under vacuum. The target compounds were obtained as brown powders in 48% and 55% yield for Ar^{F} = 3,5–$C_6H_3(CF_3)_2$ and C_6F_5 respectively, with purity confirmed by combustion analysis (Scheme 4.6).



Scheme 4.6. *Synthesis of [Pn*ZrCp][B(Ar^{F})$_4$] (Ar^{F} = 3,5–$C_6H_3(CF_3)_2$, C_6F_5).*

[Pn*ZrCp][B(3,5–$C_6H_3(CF_3)_2$)$_4$] is less stable than the perfluorinated analogue, decomposing completely in 12 h in chlorobenzene, immediately in ethereal or chlorinated aliphatic solvents, and over 1 week in the solid state. [Pn*ZrCp][B(C_6F_5)$_4$] is somewhat more stable, with resonances in ^{1}H NMR spectra corresponding to the cationic complex still clearly resolved after 12 h in chlorobenzene among unidentified decomposition products, although similar instability was observed in ethereal and chlorinated aliphatic solvents. ^{1}H NMR spectra of freshly prepared samples in C_6D_5Cl display the same C_{2v}

symmetry as seen for the titanium analogue for both borate counteranions. Deshielding of NWT resonances was observed relative to the neutral complexes (1.72 ppm for [Pn*ZrCp][B(3,5–$C_6H_3(CF_3)_2)_4$] *vs*. 2.09 ppm for Pn*ZrCp(H)).

Attempts to isolate X-ray quality single-crystals of base-free [Pn*ZrCp]$^+$ were repeatedly unsuccessful. Slow diffusion of hexane into chlorobenzene solutions at room temperature and –30 °C only resulted in the formation of brown oils, while the reduced stability of this cationic complex in 1,2-dichlorobenzene, fluorobenzene and bromobenzene limited the scope for variation of the solvent. However, single-crystalline material was obtained by slow evaporation of a concentrated chlorobenzene solution of [Pn*ZrCp][$B(C_6F_5)_4$] over 72 hours. The isolated crystals were identified as [$(Pn*ZrCp)_2(\mu–Cl)$][$(B(C_6F_5)_4$], which is structurally analogous to the titanium complex described in section 4.4, and is proposed to form from the reaction of [Pn*ZrCp]$^+$ with chlorobenzene (Figure 4.7, Table 4.4).

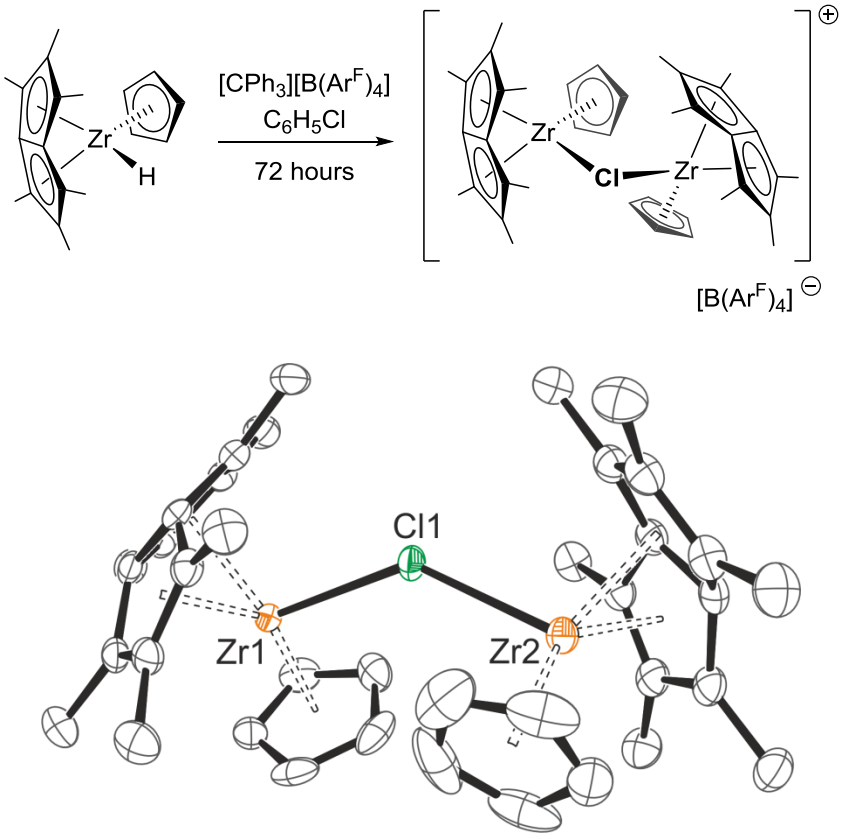


Figure 4.7. *Serendipitous synthesis and thermal displacement ellipsoid plot of [(Pn*ZrCp)(μ–Cl)][$B(Ar^F)_4$], isolated from solvolytic decomposition of [Pn*ZrCp][$B(Ar^F)_4$] in C_6H_5Cl. Ar^F = C_6F_5, anion and H atoms omitted for clarity, ellipsoids shown at 50% probability.*

	[(Pn*ZrCp)$_2$(μ–Cl)][(B(C$_6$F$_5$)$_4$]
Fold Angle	31.64(17)
	30.86(18)
Zr–Pn*$_{cent}$	2.0966(16)
Zr–Cp$_{cent}$	2.212(3)
Zr–Cl	2.6457(9)
	2.6567(9)
Zr–Cl–Zr	139.07(3)
Twist Angle	89.02(9)

Table 4.4. *Comparison of selected bond lengths (Å) and angles (°) for [(Pn*ZrCp)$_2$(μ–Cl)][(B(C$_6$F$_5$)$_4$]. Twist angle = angle made by the mean planes of Pn*$_{bridgehead\text{-}cent}$–Zr–Cp$_{cent.}$*

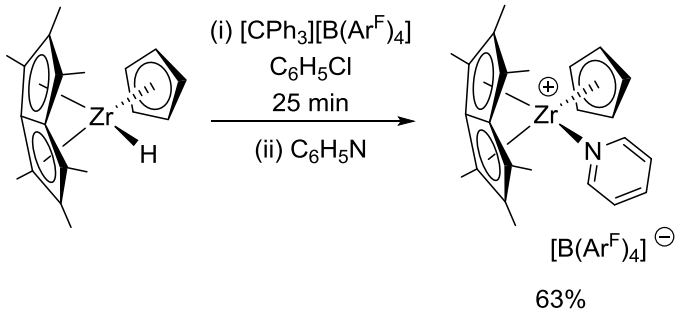
A slight contraction of the fold angles is observed relative to Pn*ZrCp(Cl) (30.33(14)°), which is accompanied by a decrease in the Zr–Pn*$_{cent}$ distances (c.f. 2.11097(12) Å for Pn*ZrCp(Cl)). The Zr–Cl bonds are elongated on dimerisation by approximately 0.1 Å, which is to be expected as electron donation from the chloride ligand is diminished, bridging between two metal centres. The bond metrics are very similar to those observed for [(Pn*TiCp)$_2$(μ–Cl)][(B(3,5–C$_6$H$_3$(CF$_3$)$_2$)$_4$], with a slight opening of the fold angle and increase in metal ligand bond lengths observed as would be expected given the larger ionic radius of zirconium relative to titanium.[18] The twist angle of 89.02(9)° is greater than the observed twist in the titanium congener of 84.53(6)°, which is likely due to similar avoidance of unfavourable steric interactions.

[(Pn*ZrCp)$_2$(μ–Cl)][(B(C$_6$F$_5$)$_4$] was synthesised rationally by the addition of Pn*ZrCp(Cl) to *in-situ* generated [Pn*ZrCp][B(C$_6$F$_5$)$_4$] in C$_6$D$_5$Cl. The ^{1}H NMR spectrum displays three Pn*–*Me* resonances at 1.85, 1.77 and 1.76 ppm, which are not markedly deshielded relative to Pn*ZrCp(Cl) (2.10, 1.75, 1.64 ppm). This contrasts with the pseudo C_{2v} solution-state symmetry found for titanium analogue, which may reflect the relative ease with which the Ti–Cl bond is broken.

Similar solvent-mediated decomposition has previously been observed with cationic zirconocenes.[19,20] For example, Harney *et al*. reported the facile decomposition of cationic zirconium amidinates {Cp*ZrR[N(Et)C(Me)N(^{t}Bu)]}[B(C$_6$F$_5$)$_4$] (R = Et, ^{n}Pr, ^{i}Pr, ^{n}Bu, ^{i}Bu

and 2-ethylbutyl) in chlorobenzene at 30 °C to give dichloro dications, $\{Cp^*Zr(\mu–Cl)[N(Et)C(Me)N(^tBu)]\}_2[B(C_6F_5)_4]_2$ by an analogous pathway.[21]

Further evidence for the successful formation of $[Pn^*ZrCp]^+$ can be obtained by addition of 1 eq. pyridine to a chlorobenzene solution of Pn*ZrCp(H) and $[CPh_3][B(3,5–C_6H_3(CF_3)_2)_4]$, which stabilises the cationic complex to form $[Pn^*ZrCp(Py)][B(3,5–C_6H_3(CF_3)_2)_4]$. Precipitation with pentane and filtration of the supernatant allows for the isolation of the donor stabilised cation in 63% yield, as a pale green powder determined pure by elemental analysis (Scheme 4.7). ^{1}H NMR spectra display C_s symmetry with 3 Pn*–*Me* resonances observed at 1.82, 1.77 and 1.34 ppm, deshielded relative to Pn*ZrCp(Cl) (2.10, 1.75 and 1.64 ppm). Slow evaporation of a chlorobenzene solution yielded single crystals suitable for X-ray diffraction (Figure 4.8).



Scheme 4.7. *Synthesis of [Pn*ZrCp(Py)][B(3,5–C$_6$H$_3$(CF$_3$)$_2$)$_4$].*

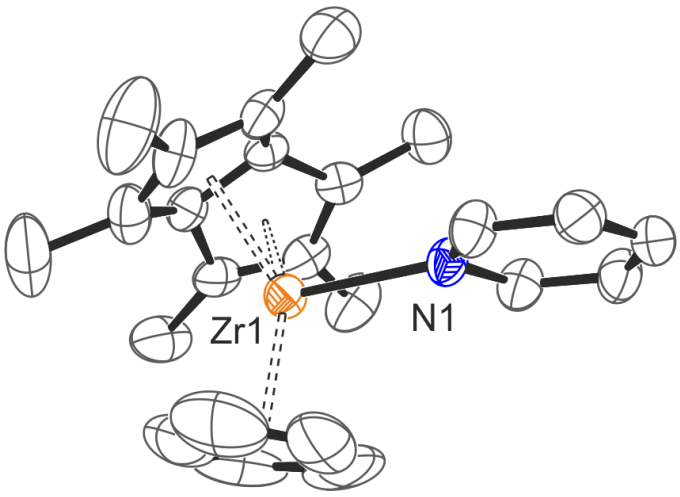


Figure 4.8. *Thermal displacement ellipsoid plot of [Pn*ZrCp(Py)][B(3,5–C$_6$H$_3$(CF$_3$)$_2$)$_4$]. Anion and H atoms omitted for clarity, ellipsoids shown at 50% probability.*

The Cp ring was disordered over two positions, as were two of the borate CF_3 groups. However, the data was of sufficient quality to extract bond metrics, shown in Table 4.5. The fold angle and Zr–carbocycle$_{cent}$ distances are very similar to those observed in $[(Pn^*ZrCp)_2(\mu–Cl)][(B(C_6F_5)_4]$, and the Zr–N bond is contracted relative to the Zr–Cl bond.

[(Pn*ZrCp(Pyr)][(B(3,5–$C_6H_3(CF_3)_2)_4$]	
Fold Angle	30.9(2)
Zr–Pn*$_{cent}$	2.0993(17)
Zr–Cp$_{cent}$	2.221(5)
Zr–N	2.361(4)

Table 4.5. *Comparison of selected bond lengths (Å) and angles (°) for [Pn*ZrCp(Py)][B(3,5–$C_6H_3(CF_3)_2)_4$].*

With access to $[Pn^*MCp]^+$ complexes, their reactivity with ethylene was tested (Table 4.6). Most remarkably exposure of $[Pn^*ZrCp][B(Ar^F)_4]$ to 2 bar ethylene leads to the production of polyethylene with high activities (up to 547 $kg_{PE}/(mol·h·bar)$ for $Ar^F = C_6F_5$) despite the lack of alkyl group into which the monomer can insert. By contrast, the donor-stabilised cation $[Pn^*ZrCp(Py)][BArF_4]$ does not polymerise ethylene in the absence of co-catalyst and $[Pn^*TiCp][BArF_4]$ is also inactive.

4.6 Probing the mechanism of polymerisation

A number of mechanisms now can be discounted: a metallocycle mechanism would require oxidation of the group 4 metal centre to the (+6) oxidation state following cycloaddition. Heterobimetallic Zr(μ–Me)Al complexes can be also be discounted as active species given the inhibitory effect of $AlMe_3$ (Table 4.6).

A bimetallic mechanism could be proposed, where olefin insertion proceeds *via* a 5-membered transition state, as opposed to usual the 4-membered alternative. This has previously been suggested, on the basis of computational studies, to account for the polymerisation activity of dimeric yttrium alkyl and scandium hydride complexes.[22,23] A similar mechanism could be envisaged in the case of $[Pn^*ZrCp]^+$, proceeding with initial formation of a bimetallic, cationic metal-alkyl complex, $[(Pn^*ZrCp)_2(\mu–R)]^+$ (R = alkyl).

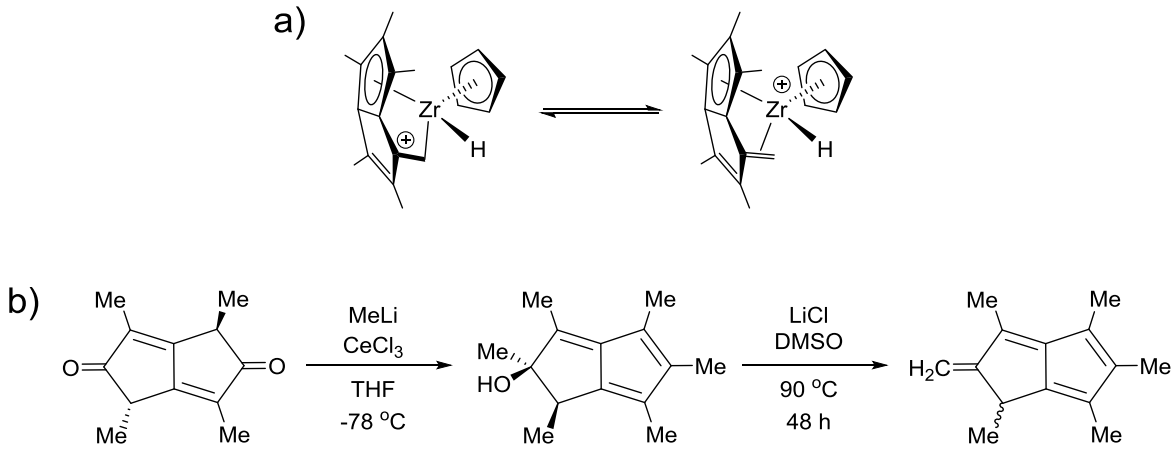
Complex	Co-catalyst	Activity $kg_{PE}/(mol \cdot h \cdot bar)$
Pn*ZrCp(Cl)[a]	250 eq MAO	1106
[Pn*ZrCp][B(Ar^F)$_4$] [b]	–	345
[Pn*ZrCp][B(Ar^F)$_4$][c]	250 eq MAO	767
[Pn*ZrCp][B(C$_6$F$_5$)$_4$][b]	–	547
[(Pn*ZrCp)$_2$(μ–Me)][(B(C$_6$F$_5$)$_4$] [d]	–	71
[Pn*ZrCp][B(Ar^F)$_4$] [b]	1 eq $AlMe_3$	Trace
[Pn*ZrCp][B(Ar^F)$_4$] [b]	100 eq $AlMe_3$	0
[Pn*ZrCp(Py)][B(Ar^F)$_4$][b]	–	0
[Pn*ZrCp(Py)][B(Ar^F)$_4$][e]	250 eq MAO	350
[Pn*TiCp][B(Ar^F)$_4$] [b]	–	0

Table 4.6. *Ethylene polymerisation activities of [Pn*MCp]$^+$ complexes. [B(Ar^F)$_4$]$^-$ corresponds to [B(3,5–C$_6$H$_3$(CF$_3$)$_2$)$_4$]. Conditions: 50 mL C$_6$H$_5$Cl, 2 bar ethylene, 25 °C a) 1.2 μmol$_{Zr}$, 5 mins b) 4.4 μmol$_{Zr}$, 5 mins c) 1.5 μmol$_{Zr}$, 5 mins; d) 8.9 μmol$_{Zr}$, 5 mins; e) 3.1 μmol$_{Zr/Ti}$ catalyst loading, 30 mins.*

Pn*ZrCp(Me) was added to a solution of [Pn*ZrCp][B(C$_6$F$_5$)$_4$] in C$_6$D$_5$Cl forming the bimetallic complex, [(Pn*ZrCp)$_2$(μ–Me)][(B(C$_6$F$_5$)$_4$]. The ^{1}H NMR spectrum displays 6 Pn*–*Me* groups observed, presumably reflecting restricted rotation about the Zr–Me–Zr bond, in contrast to the chloride analogue described in section 4.5. Addition of ethylene to a chlorobenzene solution of *in-situ* generated [(Pn*ZrCp)$_2$(μ–Me)][(B(C$_6$F$_5$)$_4$] produced polyethylene with activities of 71 $kg_{PE}/(mol \cdot h \cdot bar)$ corresponding to an 87% decrease relative to [Pn*ZrCp][B(C$_6$F$_5$)$_4$]. This is accompanied by additional polymer aggregation, with the polymer obtained as a single congealed sheet.

Alternatively, a bimolecular mechanism could be considered, which has been proposed to rationalise the unexpected ethylene polymerisation activity of cationic aluminium alkyl complexes.[24–26] However, a bimolecular mechanism is difficult to reconcile with the very high activities reported for immobilised catalysts in Chapter 3, which would require very close proximity of metal centres on the inorganic surface. It is also interesting to note that these cationic aluminium catalysts almost exclusively produce polyethylene with activities $\leq$ 1 $kg_{PE}/(mol \cdot h \cdot bar)$.[27–31] A bimolecular mechanism is therefore unlikely responsible for the unusual polymerisation activity of these catalysts.

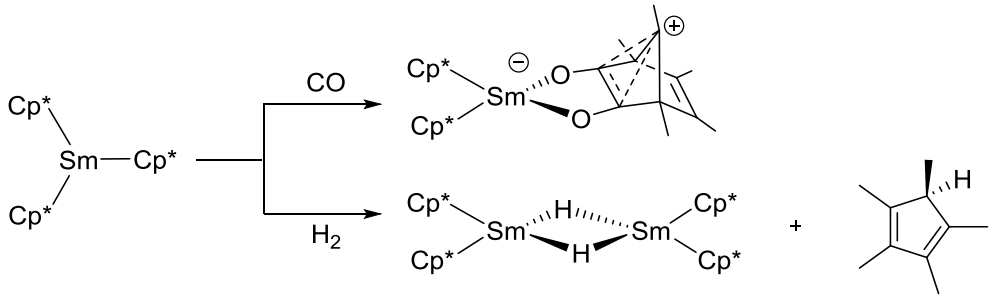
Any alternative mechanism to accommodate coordination-insertion requires functionalisation of either the Pn* or Cp rings. C–H activation of the Pn* periphery could be envisaged, forming a fulvene/ "tuck-in" complex that formally oxidises the carbocycle. Indeed during the synthesis of Pn*, a fulvene derivative is formed following methylation and dehydration of 2,4,6,8-tetramethylbicyclo[3.3.0]octa-1,5-diene-3,7-dione, which is subsequently reduced to Li_2[Pn*].[32,33] Cp* fulvene/"tuck-in" derivatives are also well known for zirconium[34,35] and titanium, such as Cp^*_2Ti which exists as an equilibrium mixture of fulvene and Cp* isomers[36,37]. In the context of [Pn*ZrCp]$^+$, a similar equilibrium could be considered (Scheme 4.8).



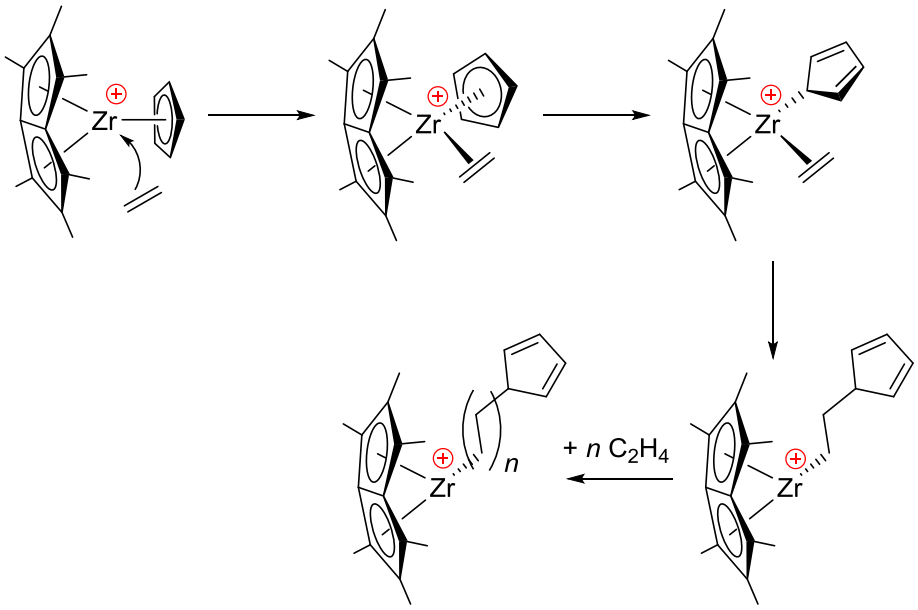
Scheme 4.8. *a) hypothetical tuck-in/fulvene [Pn*ZrCp]$^+$complex. b) fulvene intermediate formed during Pn* synthesis.*

Although the hydride resonance of the proposed fulvene intermediate may be difficult to observe by ^{1}H NMR spectroscopy, the desymmetrised Pn* fragment should be diagnostic for ring functionalised intermediates and well-separated from the starting complex. However, no evidence for the formation of such a complex could be observed in C_6D_5Cl in the temperature range 237 K – 310 K. Assuming the lifetime of such an intermediate is short, it may not be resolved by NMR spectroscopy, although it should, nonetheless, be possible to trap out these derivatives using small molecules such as CO or CO_2. Alternatively, addition of D_2 should lead to deuterium incorporation into the Pn* periphery.[38–41]

Instead of functionalisation of the Pn* moiety, Cp-ring non-innocence could be considered. Cp*$_3$Sm produces polyethylene in the absence of co-catalyst, despite no obvious metal alkyl bonds into which the olefin can insert.[42,43] The mechanism was confirmed to proceed *via* transient formation of (η^5–Cp*)$_2$(η^1–Cp*)Sm, which could not be observed spectroscopically, by inserting a variety of small molecules into the short-lived mixed-hapticity samarocene, including H_2 and CO (Scheme 4.9). An analogous mechanism could be envisaged to be operative in the case of [Pn*ZrCp]$^+$, as illustrated in Scheme 4.10. If either Cp or Pn* functionalisation are relevant to the polymerisation of [Pn*ZrCp]$^+$, the ring-functionalised derivatives should react with these small molecules.



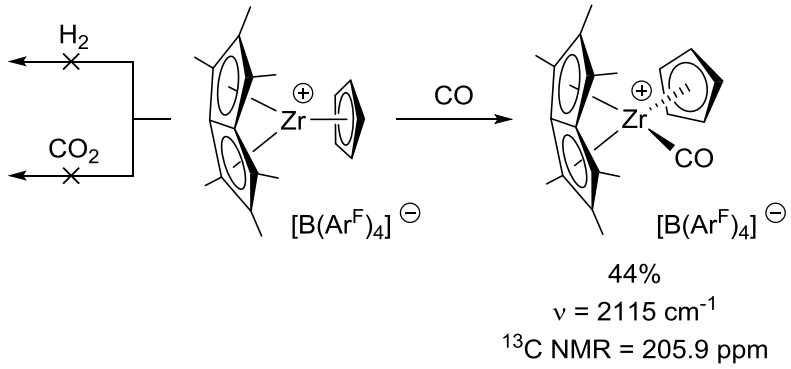
Scheme 4.9. *Small molecule reactivity of Cp*$_3$Sm demonstrating lability of Cp* ligand.*



Scheme 4.10. *Hypothetical ethylene polymerisation mechanism of [Pn*ZrCp]$^+$ following olefin insertion into Cp ring.*

Exposing [Pn*ZrCp][B(3,5–$C_6H_3(CF_3)_2)_4$] to an atmosphere of CO leads to complete consumption of the starting complex, and the formation of a new C_s symmetric product observed by NMR spectroscopy. However, this was determined to correspond to the carbonyl complex [Pn*ZrCp(CO)][B(3,5–$C_6H_3(CF_3)_2)_4$] and not an insertion product. The $^{13}C\{^1H\}$ NMR spectrum shows the presence of a sharp singlet at 205.9 ppm corresponding to the terminal carbonyl environent, and a single Cp resonance in both ^1H and $^{13}C\{^1H\}$ NMR spectra indicates η^5-Cp coordination is maintained. A carbonyl stretching frequency was observed at 2115 cm^{-1} by FTIR spectroscopy (c.f. 2143 cm^{-1} for free CO),[44] consistent with very weak back-donation expected from d^0 metal-centres. [Pn*ZrCp(CO)][B(3,5–$C_6H_3(CF_3)_2)_4$] was synthesised on a preparative scale by addition of CO at 0.1 bar overpressure to *in-situ* generated [Pn*ZrCp][B(3,5–$C_6H_3(CF_3)_2)_4$] in C_6H_5Cl. The complex was precipitated in pentane, isolated by filtration and dried under dynamic vacuum, to afford the target compound in 44% yield (Scheme 4.11). The product was obtained as a brown powder whose bulk purity was confirmed by elemental analysis.

Exposed instead to an atmosphere of hydrogen, the cationic complex did not react, and with D_2, no deuterium incorporation into the pentalene or Cp rings was observed. Similarly, no reaction was observed with CO_2, which suggests metal-hydrides or η^1–Cp isomers are not formed under these conditions (Scheme 4.11). More convincing evidence in contradiction of the fulvene hypothesis can be found in the very high activities of PnZrInd(Cl);[5] in this case a fulvene intermediate is not accessible in the absence of ring-methyl substituents. Assuming both Pn and Pn* complexes act by a common mechanism, and in light of the inactivity towards small molecules, intermediate fulvene formation can be discounted as catalytically relevant.



Scheme 4.11. *Reactivity of [Pn*ZrCp][B(Ar^F)$_4$] with H_2, CO_2 and CO (Ar^F = 3,5–$C_6H_3(CF_3)_2$).*

Retention of the Cp ring can be further demonstrated by considering gas uptake rates for Pn*ZrCp^{R}(Cl) catalysts. If the Cp ring is behaving as an electron-rich leaving group, as in the case of Cp*$_3$Sm, variation of Cp for Cp^{R} would only affect the initial reaction rates, subsequently being removed from the metal centre to the far end of a polymer chain. At this stage, any modification of the Cp ligand becomes redundant and all Cp-variants should tend towards a degenerate gas uptake rate.

Graphs illustrating the gas uptake rate of three solid polymethylaluminoxane activated Pn*ZrCp^{R}(Cl) catalysts, Pn*ZrCp(Cl)$_{sMAO}$, Pn*ZrCp^{Me}(Cl)$_{sMAO}$ and Pn*ZrCp^{nBu}(Cl)$_{sMAO}$, are shown in Figure 4.9.

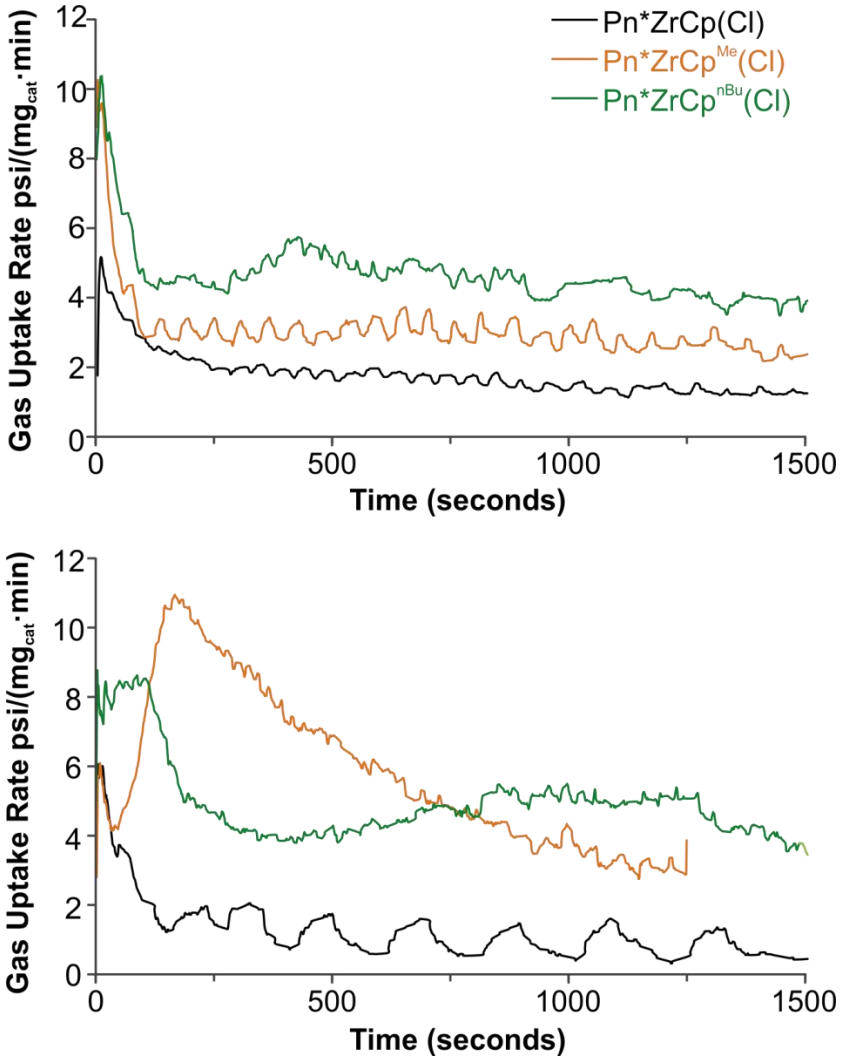


Figure 4.9. *Ethylene uptake rates for Pn*ZrCp(Cl) (black), Pn*ZrCp^{Me}Cl (orange), Pn*ZrCp^{nBu}Cl (green). Conditions: [Zr]:[sMAO] = 1:200; 120 psi ethylene; 5 mL heptane; typical catalyst loading 0.2 mg;10 µM TiBA; 80 °C.Top: ethylene homopolymerisation; bottom: 1.6% H$_2$.*

The rate of gas uptake increases in the order Pn*ZrCp(Cl) < Pn*ZrCp^{Me}(Cl) < Pn*ZrCp^{nBu}(Cl), and the profiles do not become degenerate over the course of polymerisation. The average gas uptake for the best performing catalyst is 2.5 times greater than for the worst performing. This variation is even more dramatic when H_2 is added to the gas feed; modification of the Cp ligand leads to large changes in gas uptake over the whole course of polymerisation, with average gas uptake rates nearly 14 times greater for Pn*ZrCp^{nBu}(Cl) than for Pn*ZrCp(Cl). Moreover, not only are activities altered by Cp-ring substitution, the polymer properties are also not constant across the series. The percentage amorphous fraction of the polymer nearly doubles from Pn*ZrCp^{nBu}(Cl) to Pn*ZrCp(Cl), as does the polymer molecular weight (Table 4.7).

Complex	Activity [a]	M_w (PDI)[b]	$T_{el,\,max}$[c]	AF %[d]
Pn*ZrCp(Cl)	206	19 (12.7)	110.4	21.0
Pn*ZrCp^{Me}(Cl)	1533	13 (9.3)	107.5	18.1
Pn*ZrCp^{nBu}(Cl)	2869	11 (6.9)	109.8	11.5

Table 4.7. *Slurry phase ethylene/H_2 polymerisation activities and polymer properties for sMAO-activated catalysts. a) kg_{PE}/mol·h·bar; b) kDa, determined by GPC c) Elution temperature maximum of the polymer, determined by CEF d) % amorphous fraction determined by CEF.*

Furthermore, if coordination-insertion was occurring following loss of the Cp ring then observed activities would be similar to Pn*ZrX_2 catalysts given the identical propagating species in both cases. Given the rate of gas uptake does not converge, the catalysts produce large variations in the polymer properties, and the activities are approximately fifty times greater than Pn*ZrX_2 pre-catalysts, this demonstrates the effect of Cp-ring substitution not just during initiation, but throughout the polymerisation.

Retention of the Cp-ring can be further illustrated by hydrolysing the catalyst during polymerisation. A chlorobenzene solution of [Pn*ZrCp][B(3,5–$C_6H_3(CF_3)_2)_4$] was exposed to 2 bar ethylene for 90 seconds before H_2O was added to quench the reaction. Filtration of the supernatant and distillation of a volatile fraction (25 °C, 1 mbar) allows for the observation of cyclopentadiene by GC-MS. Given aqueous treatment of alkyl-cyclopentadienes hypothetically formed during coordination-insertion would not produce cyclopentadiene, this demonstrates the persistence of the Zr–Cp fragment during polymerisation.

Alternatively, spent catalyst can be studied by solid-state NMR spectroscopy. Exposure of solid polymethylaluminoxane-activated Pn*ZrCp(Cl) to 1 bar ethylene in the absence of solvent leads to a large exotherm and over 90 seconds the mass of the catalyst more than triples. ^{13}C CP-MAS ssNMR spectroscopy of the resultant solid indicates the formation of large quantities of polyethylene (31 ppm), and resonances corresponding to solid polymethylaluminoxane (–8, 122-133 and 177 ppm). Importantly, the complete retention of Pn*−Me and Cp resonances is observed at 12 and 110 ppm respectively (Figure 4.10).

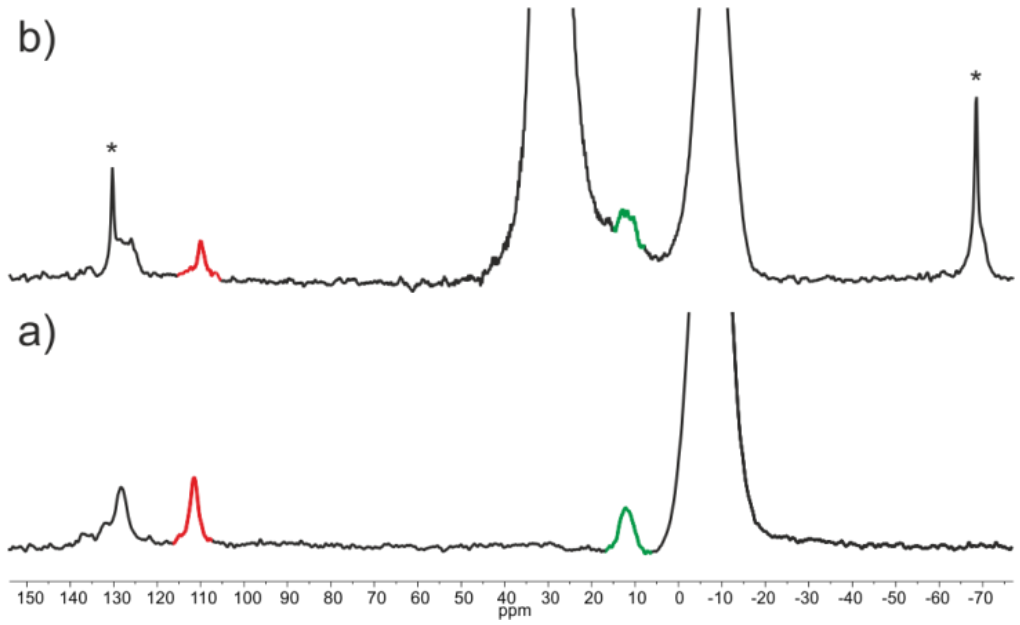
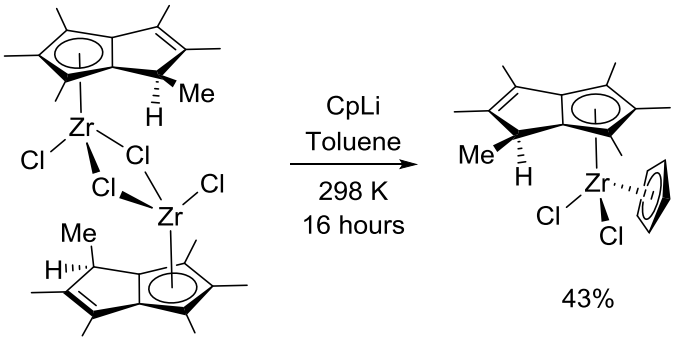


Figure 4.10. *^{13}C CPMAS ssNMR spectrum of a) polymethylaluminoxane supported Pn*ZrCp(Cl) [Zr]:[sMAO] = 1:100. b) catalyst a) following exposure to 1 bar ethylene. * = spinning side bands. –8 ppm (sMAO Al–**Me**), 12 ppm (Pn*–**Me**), 31 ppm (PE -**C**H$_2$-), 110 ppm (**Cp**), 122-133 ppm (**sMAO**). Cp and Pn*–Me resonances highlighted in red and green respectively.*

4.7 Synthesis and characterisation of Pn*(H)ZrCpCl$_2$

In general, the most common decomposition pathway for Pn* complexes involves proton transfer to the carbocycle to form Pn*(H) derivatives. In this case [Pn*(H)ZrCp(R)]$^+$ appears structurally related to coordination-insertion catalysts, [Cp$^{R}_2$ZrMe]$^+$, making it a strong candidate for the active species. The hydropermethypentalene complex can be synthesised from [Pn*(H)ZrCl$_3$]$_2$ and CpLi in toluene overnight. Trituration of a concentrated toluene solution with pentane allows for the isolation of pure Pn*(H)ZrCpCl$_2$ in 43% yield as a green-yellow powder (Scheme 4.12). Single crystals were obtained from a saturated pentane solution at –80 °C (Figure 4.11).



Scheme 4.12. *Synthesis of Pn*(H)ZrCpCl$_2$.*

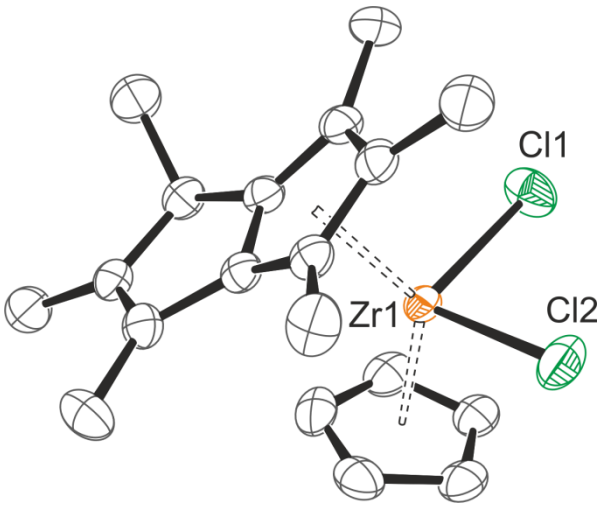


Figure 4.11. *Thermal displacement ellipsoid plot of Pn*(H)ZrCpCl$_2$. H atoms omitted for clarity, ellipsoids shown at 50% probability.*

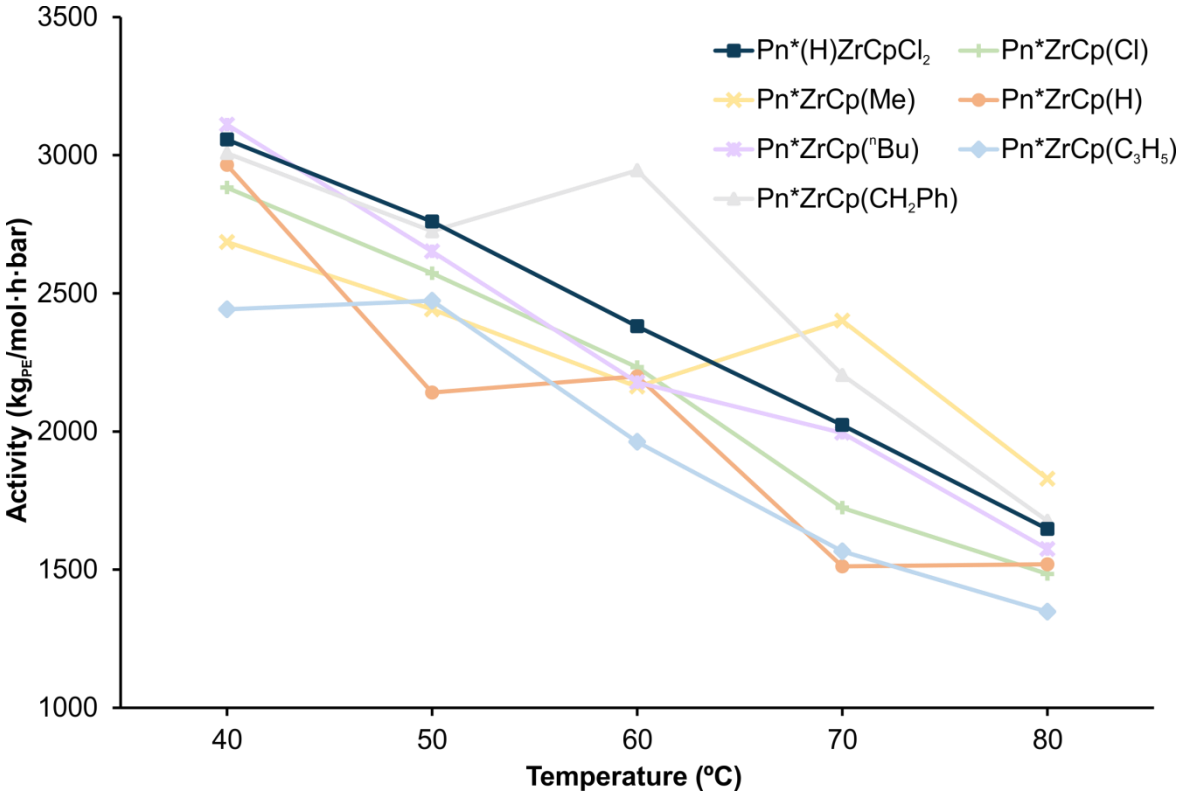


Figure 4.12. *Slurry phase ethylene polymerisation activity of Pn*(H)ZrCpCl$_{2\ sMAO}$ compared to Pn*ZrCp(X) derivatives. Conditions: [Zr]:[sMAO] = 1:200; 2 bar ethylene; 10 mg catalyst loading;50 mL hexane; 150 mg TiBA; 30 minutes.*

This complex was indeed found to be a very active ethylene polymerisation catalyst when immobilised on polymethylaluminoxane (Figure 4.12). However, the temperature profile appears almost identical to other Pn*ZrCp(X) derivatives and so the activation of this complex was studied further.

Following the normal immobilisation procedure described in Chapter 3, Pn*(H)ZrCpCl$_2$ was supported on sMAO at a ratio of 1:200 [Zr]:[sMAO]. The solid was characterised by ^{13}C CPMAS ssNMR spectroscopy, which surprisingly did not indicate the formation of a supported Pn*(H) complex. Related Pn*(H) derivatives typically display 6 distinct Pn*–*Me* environments, and 8 Pn*–C$_{ring}$ environments, one of which is characteristically deshielded, resonating at 40 – 60 ppm (1–Pn*(H)). In the ^{13}C CPMAS ssNMR spectrum of a dry mixture of Pn*(H)ZrCpCl$_2$ and sMAO ([Zr]:[Al] = 1:200), an intense resonance at 43.9 ppm can clearly be observed corresponding to 1–Pn*(H), alongside more extensively split Pn*–*Me* and Pn*–C$_{ring}$ environments (10 – 15 ppm and 120 – 145 ppm respectively, Figure 4.13, a). After immobilisation and activation of the zirconium complex by sMAO in

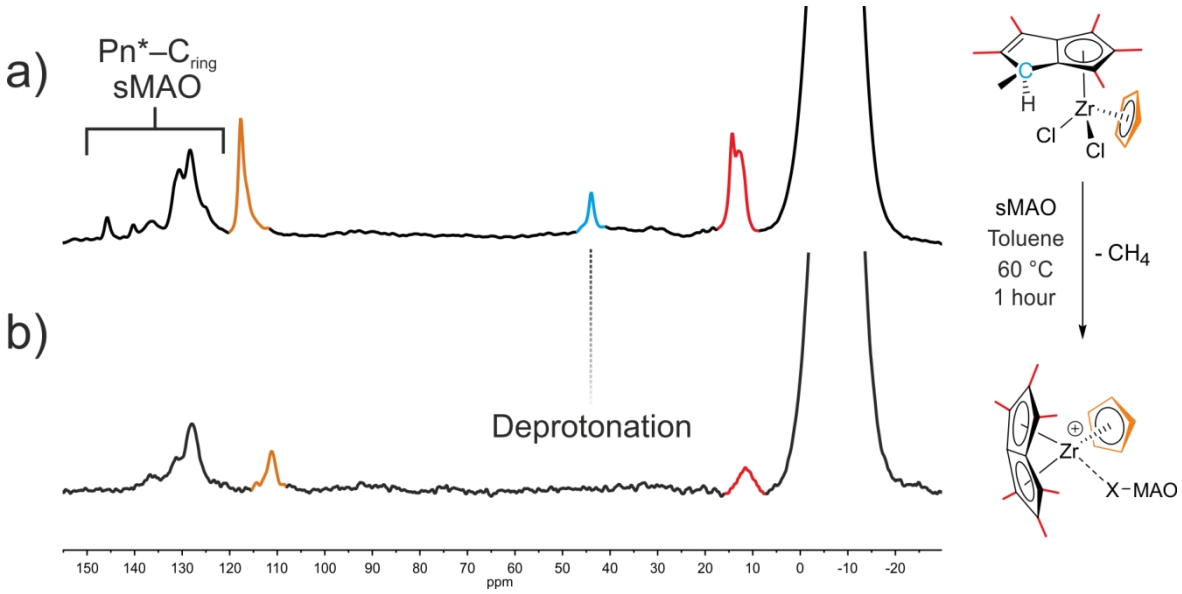


Figure 4.13. *^{13}C CPMAS NMR spectra (10 KHz spinning speed) of a) dry mixture of Pn*(H)ZrCpCl$_2$ and sMAO [Zr]:[sMAO] = 1:200.b) same mixture after pre-catalyst activation in toluene at 60 °C for 1 hour.*

toluene at 60 °C for 1 hour a pale yellow solid is obtained in 83% yield. The resultant ^{13}C CPMAS NMR spectrum indicates complete disappearance of the resonance at 43.9 ppm alongside coalescence of the Pn*–*Me* and Pn*–C$_{ring}$ environments, producing a spectrum that is indistinguishable from Pn*ZrCp(Cl)$_{sMAO}$.

This deprotonation can also be demonstrated in solution. Addition of 50 eq MAO to Pn*(H)ZrCpCl$_2$ in C_6D_6 formed a yellow oil that phase separated from a yellow solution. The supernatant was decanted, and the oil redissolved in C_6D_5Cl as described in section 4.3. Spectroscopic characterisation of the oil by NMR spectroscopy produced resonances indistinguishable from those obtained by activation of Pn*ZrCp(Cl) (Figure 4.14). This activation product is clearly η^8-coordinated; Pn*(H) derivatives display 6 distinct Pn*–*Me* environments in ^{1}H NMR spectra, of which one is characteristically split into a doublet by $^3J_{H\text{-}H}$ coupling to the proton bound at the saturated ring-carbon position. A corresponding quartet can be observed at approximately 3 ppm. The observation of three Pn*–*Me* resonances in the presence of MAO, and the absence of either a quartet or shielded ring-carbon environments demonstrates that MAO is capable of deprotonating the Pn*(H) complex to form η^8 derivatives.

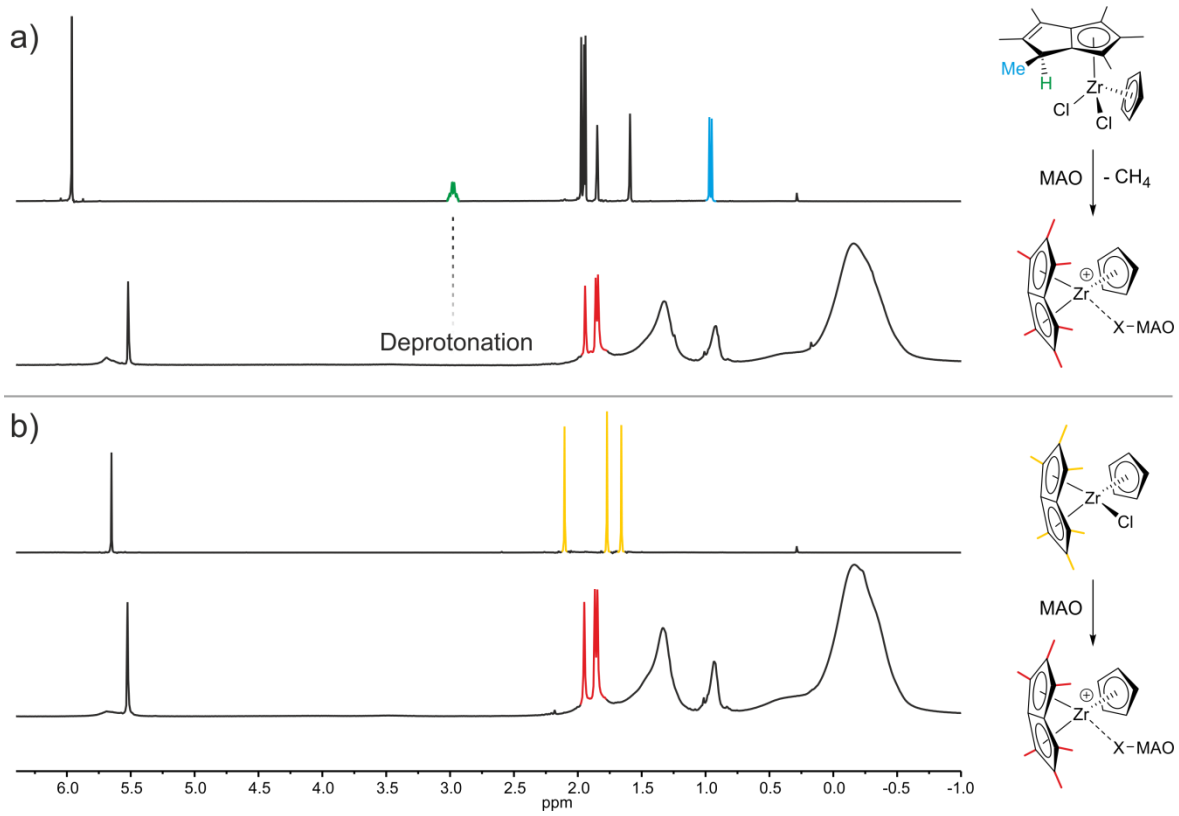


Figure 4.14. *^{1}H NMR spectra (400 Mhz, 298 K) before (C_6D_6) and after MAO activation (C_6D_5Cl) of a) Pn*(H)ZrCpCl$_2$ and b) Pn*ZrCp(Cl).*

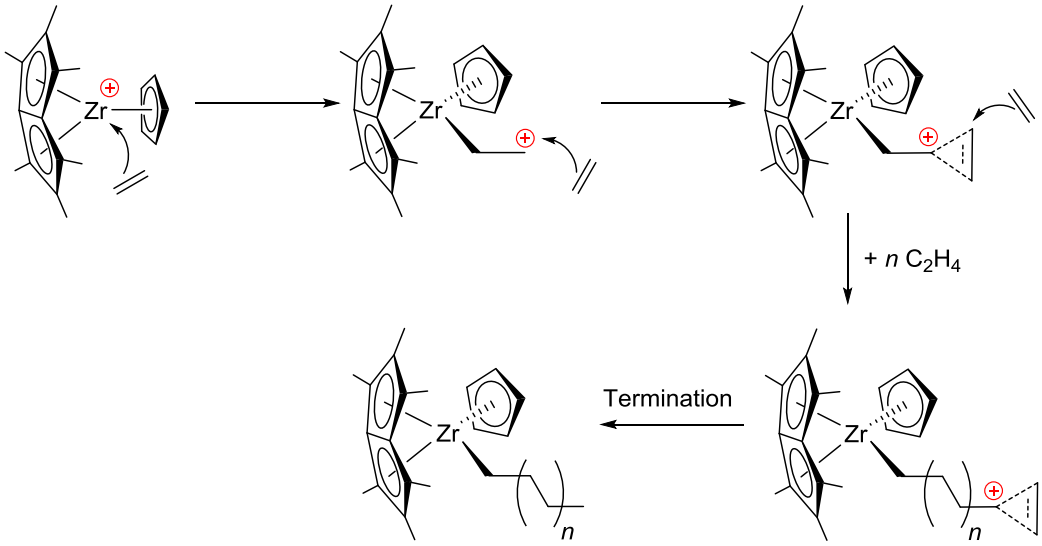
This transformation is particularly remarkable because only two other reagents have previously been observed to deprotonate Pn*(H) metal complexes: MeLi and $AlMe_3$. Under similar conditions, typical strong bases such as ^{n}BuLi/TMEDA, ^{t}BuLi and ^{n}BuLi/KO^{t}Bu, among many others, do not deprotonate Pn*(H).[45] Given the structural similarity of $AlMe_3$ and MAO this parallel reactivity may not be surprising, presumably thermodynamically driven by irreversible methane formation. However, in light of their instability under polymerisation conditions, Pn*(H) derivatives are likely not responsible for the observed ethylene polymerisation activity.

It could be envisaged that the high ethylene polymerisation activities of [Pn*ZrCp][B(Ar^{F})$_4$] in chlorobenzene could result from protonation of the Pn* ring by adventitious moisture to form hydropermethylpentalene derivatives. The role of water in these polymerisations was investigated by using 2,6–di(tert-butyl)pyridine (DtBP), which has previously been employed as a moisture trap in olefin polymerisation catalysis.[46–48] [Pn*ZrCp][B(C_6F_5)$_4$] was exposed to 2 bar ethylene in the presence of excess DtBP (20 equivalents), under conditions otherwise identical to those reported in Table 4.6.

No significant decrease in activity was observed (522 $kg_{PE}/(mol \cdot h \cdot bar)$ *vs.* 547 $kg_{PE}/(mol \cdot h \cdot bar)$ without DtBP), which was accompanied by a slight increase in the polymer molecular weight (M_w = 833 to 872 kDa) and decrease in the polydispersity (M_w/M_n = 4.47 and 2.83 with and without DtBP respectively). ^{1}H NMR spectra of [Pn*ZrCp][$B(C_6F_5)_4$] and DtBP in C_6D_5Cl indicated no coordination of the base to the zirconium centre. Given the increase in polymer molecular weights and decrease in polydispersity in the presence of DtBP, H_2O can be proposed to facilitate chain-transfer, but the insensitivity of polymerisation activity towards DtBP suggests H_2O does not play a role in pre-catalyst activation.

4.8 Cationic initiation by [Pn*ZrCp]$^{+}$

An alternative mechanism could be proposed, distinct from coordination-insertion. Electrophilic activation of the monomer could produce a carbocation that would activate additional monomer and propagate through solution (Scheme 4.13).



Scheme 4.13. *Hypothetical cationic initation of ethylene by [Pn*ZrCp]$^{+}$.*

The key step during cationic propagation is addition of the carbocation across the olefin bond. Just as the ethonium cation $(C_2H_5)^{+}$ adopts a non-classical structure,[49–52] the reaction of propagating RH_2C^{+} with C_2H_4 would also be expected to produce a carbonium ion with non-classical character. Donation of electrons from the ethylene π bond into the vacant p-orbital of the polymer carbenium ion would produce a funtionalised cycloproponium ion

(c-$C_3H_6R^+$). This non-classical motif has previously been proposed across organic and biological chemistry where carbocationic intermediates are implicated.[53–55] Alternatively a primary carbocation would be formed, which is a reactive species prone to rearrange rapidly to secondary and tertiary products.[56–58] By comparison, the parent cycloproponium ion, c-$C_3H_7^+$, is a relatively long-lived carbonium ion that can be formed by the addition of H^+ to cyclopropane.[59,60] Although the secondary carbenium ion, $CH_3CH^+CH_3$, is the thermodynamically most stable isomer,[61,62] in the presence of weak nucleophiles only the 1° functionalised product is observed, which is formed by direct nucleophilic attack at *c*-$C_3H_7^+$.[56,60,63] Even in the presence of very weak nucleophiles such as *p*-xylene, alkylation by c-$C_3H_7^+$ produces near exclusive *n*-propyl substitution of the aromatic (*n*-:*iso*-propyl = 92:8), demonstrating its relatively long-lived nature.[63]

There appears to be a strong inverse correlation between chain length of the α-olefin and the degree of polymerisation achieved under cationic polymerisation conditions. Propylene has been reported to form high molecular weight polymer in the presence of $AlCl_3$,[64–67] while 1-decene produces only oligomers.[54,68,69] Ethylene, the least hindered olefin, might therefore also be expected to produce high molecular weight material in the presence of a suitable initiator, however, only oligomers have been reported previously. This has two main causes: all previous attempts at cationic ethylene polymerisation have employed proton-based initiators, but ethylene is not readily protonated relative to other α-olefins (proton affinity of ethylene = 680.5 kJ/mol, propene = 751.4 kJ/mol).[70] Secondly, the lowest energy isomer of protonated ethylene is the C_{2v} symmetric ethonium cation,[49–52] which displays predominant Brøsted acid, not Lewis acid character.[71–75] It is therefore proposed that [Pn*ZrCp]$^+$ provides an aprotic route to ethylene activation, generating a Lewis acidic carbocation that provides an alternative entry point to the cationic polymerisation of ethylene. With a suitable activation strategy, the degree of polymerisation extrapolated from previous studies on cationic α-olefin polymerisation might therefore be realised for ethylene.

If the propagating species is indeed a carbocation, it should be possible to observe this electrophilic intermediate indirectly by chemically trapping it with a suitable nucleophile. $(CF_3)_3COH$ displays both Brønsted acid and Lewis basic functionalities and is decorated with a large number of 100% natural abundance, spin ½, ^{19}F nuclei to aid spectroscopic

detection. In both coordination-insertion and cationic initiation the carbon atom adjacent to the metal centre is carbanionic in character, and in the presence of a proton source such as an alcohol, will be protonated to form methyl-terminated polymer chains. If a carbocation is in solution, nucleophilic quenching by the alcoholic oxygen will also occur, leading to the formation of nonafluoro-ether terminated polymer chains, which should be observable by NMR spectroscopy (Figure 4.15). The alcoholic quenching of cationic polymer chains has previously been described as a useful tool to demonstrate cationic polymerisation with vinyl ethers,[76] which is elaborated on here by inclusion of an additional ^{19}F NMR spectroscopy handle.

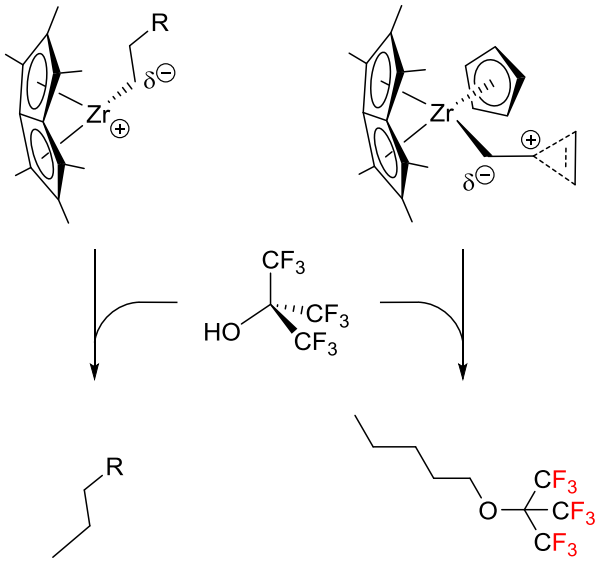


Figure 4.15. *Illustration of fluorine tagging strategy for the indirect observation of transient carbocation.*

Polymerisations were carried out using [Pn*ZrCp][B(C_6F_5)$_4$] and quenched after 90 seconds with $(CF_3)_3COH$. The polymer was worked up by precipitation in cold pentane followed by filtration and washing with $HCl_{(aq)}$, H_2O, acetone and pentane to remove metal residues. ^{19}F DPMAS solid-state NMR spectroscopy revealed weak resonances in the range –120 to –170 ppm assigned to borate decomposition products, and an intense resonance at –66 ppm, corresponding to polymer-O-C$(CF_3)_3$ (Figure 4.16). The ^{1}H NMR spectrum, collected at 24 kHz, displays an intense, broad resonance at 1.3 ppm corresponding to the polyethylene backbone. Spinning side bands are observed indicating restricted motion of the polymer chains, which is unsurprising considering the macromolecular distortions that would be required for the attainment of narrow line-widths.

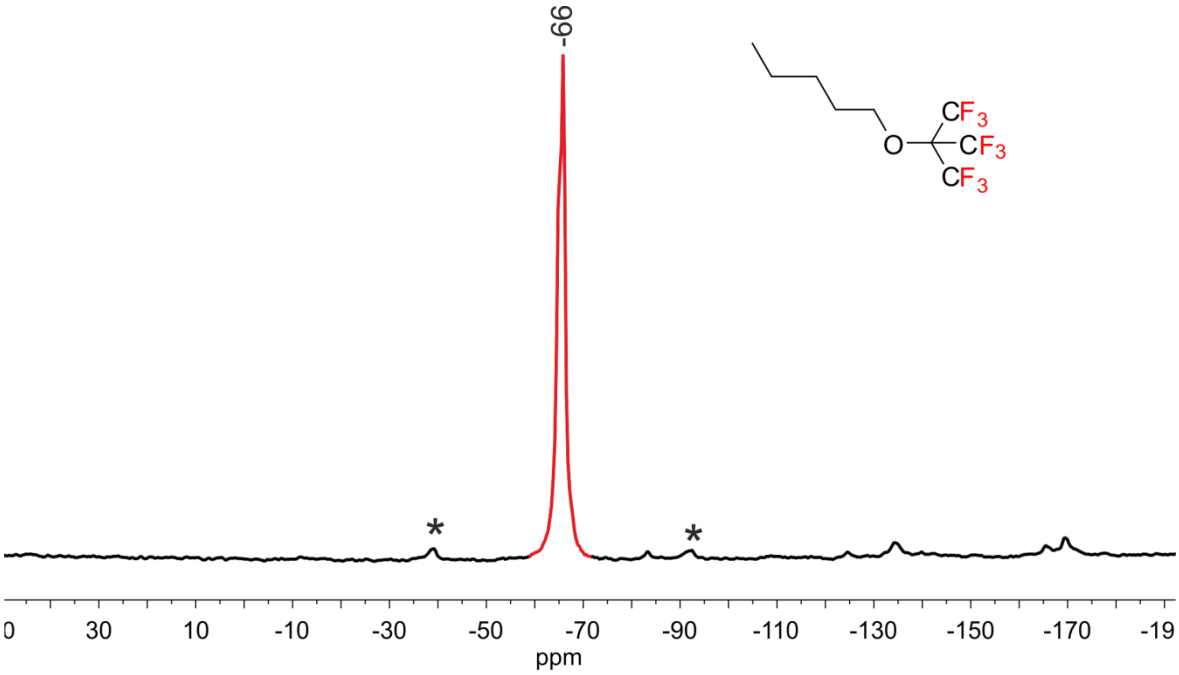


Figure 4.16. *^{19}F DPMAS solid-state NMR spectrum (10 kHz spinning speed) of polymer–O–C(CF$_3$)$_3$ (-66 ppm) isolated from a quenched polymerisation mixture of [Pn*ZrCp][B(C$_6$F$_5$)$_4$], 20 mL C$_6$H$_5$Cl, 2 bar ethylene, 1 mL (CF$_3$)$_3$COH, 90 second reaction time. Spinning side bands highlighted with *.*

A small sharp resonance is also observed at 4.4 ppm, which is tentatively assigned to polymer–C*H*$_2$–O–. Facile molecular motion for the end group is implied by the narrow line widths, as is also observed in the ^{19}F DPMAS spectrum, while the deshielded position of this resonance suggests bonding to an electronegative heteroatom.

The same procedure was also carried out with [Pn*ZrCp][B(3,5–C$_6$H$_3$(CF$_3$)$_2$)$_4$]. In this case the presence of CF$_3$ substituents on the borate leads to the observation of two ^{19}F resonances in close proximity. As before, the resonance at –66 ppm is assigned to polymer-O-C(CF$_3$)$_3$. The second resonance at –63 ppm is assigned to borate hydrolysis products, which was verified by repeating the reaction using MeOH as the quenching agent. The persistence of this resonance at –63 ppm confirms its derivation from the borate anion.

In order to confirm the provenance of this resonance Pn*ZrCp(H), Pn*ZrCp(Me) and [Pn*ZrCp]$^{+}$ were reacted with (CF$_3$)$_3$COH, air and HCl$_{(aq)}$ and the products characterised by NMR spectroscopy.

In the case of Pn*ZrCp(Me) and Pn*ZrCp(H), initial addition of $(CF_3)_3COH$ leads to formation of the metal alkoxide complex Pn*ZrCp($OC(CF_3)_3$) (^{19}F NMR (C_6D_6) δ = 72.6 ppm) with concomitant liberation of CH_4 and H_2 respectively, while $[Pn*ZrCp]^+$ does not react with $(CF_3)_3COH$. Addition of HCl and air to these reactions leads to significant decomposition as judged by broad, complex ^1H NMR spectra along with a number of new species in the ^{19}F NMR spectra, which do not resonate in the region of interest. The most shielded resonance is a triplet observed at –70.21 ppm, with the major hydrolysis product observed at –72.31 ppm (Figure 4.17).

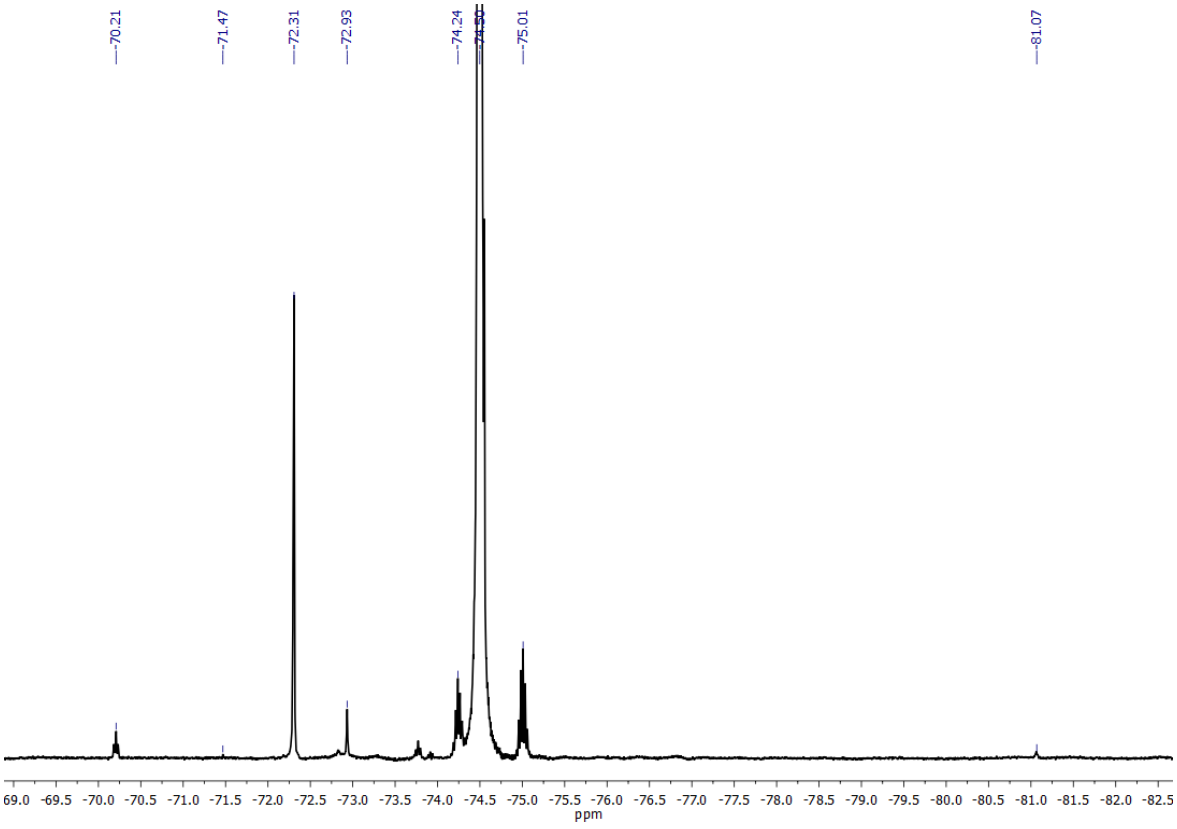


Figure 4.17. *^{19}F NMR spectrum of Pn*ZrCp($OC(CF_3)_3$) following addition of 0.1 mL 1M $HCl_{(aq)}$ (376 MHz, C_6D_5Cl, 298 K). Resonance at –74.50 corresponds to $HOC(CF_3)_3$ (20 eq.). Major resonance following complex hydrolysis observed at –72.31 ppm.*

4.10 Reactivity with 2-butyne

Further insight into cationic olefin activation can be obtained by the use of alkynes as model hydrocarbons, which can be added stoichiometrically, and are generally more reactive than alkenes. Addition of the terminal alkynes Ph–C≡CH and ^{i}Pr–C≡CH to [Pn*ZrCp][B(C_6F_5)$_4$] leads to an initial colour change to deep red, before becoming brown generally within seconds for ^{i}Pr–C≡CH and minutes for Ph–C≡CH. Characterising these solutions by NMR spectroscopy indicated significant decomposition, perhaps initiated by the acidic terminal alkyne proton; a large number of unassignable signals occur in the region 1–3 ppm arising from unidentified Pn* derivatives.

By contrast, the internal alkyne, 2-butyne, does not lead to such rapid decomposition. Addition of 3 eq. 2-butyne to [Pn*ZrCp][B(C_6F_5)$_4$] leads to the formation of a very unusual alkyne-dimerisation product with accompanying ligand functionalisation (Figure 4.18).

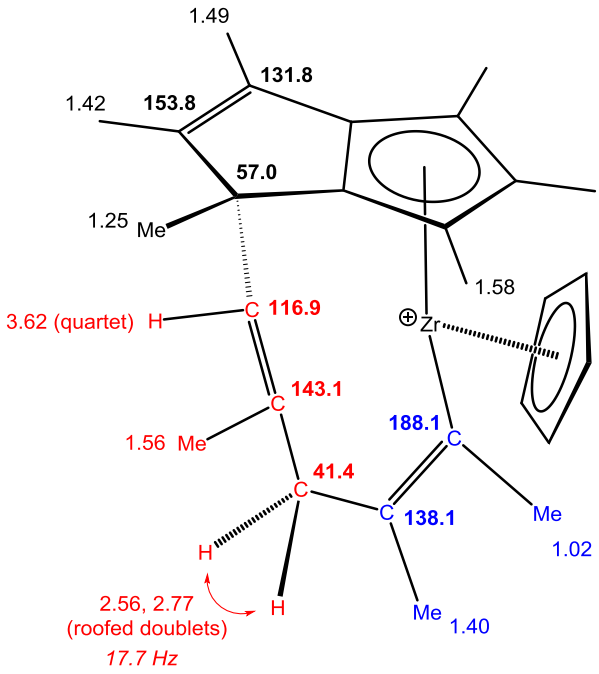


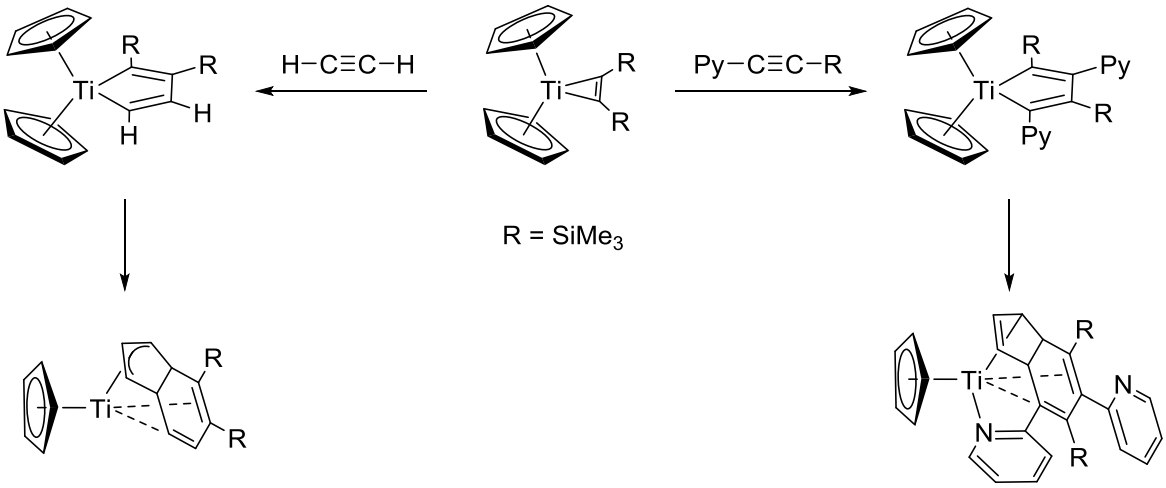
Figure 4.18. *Alkyne dimerisation product formed by reaction of 2-butyne and [Pn*ZrCp][B(C_6F_5)$_4$]. Anion omitted for clarity. Key NMR spectroscopic details shown with ^{13}C NMR shifts highlighted in bold.*

In the ^{1}H NMR spectrum a quartet is observed at 3.62 ppm, corresponding to the vinyl proton adjacent to the Pn* ring and two roofed diastereotopic doublets are found at 2.77

and 2.56 ppm. ^{1}H–^{13}C HSQC NMR spectra confirmed that these latter two doublets correlate to a single carbon environment resonating at 41.1 ppm, suggesting conformational rigidity of a bridging methylene group. A series of singlets are also resolved between 2.02 and 1.02 ppm, which are assigned to the methyl groups found across the complex (excess 2-butyne is also observed at 1.58 ppm). The ^{13}C NMR spectrum shows a shielded resonance at 57.0 ppm characteristic of a saturated Pn*–ring position, which correlates to singlets in the ^{1}H NMR spectrum at 1.42 and 1.25 ppm. A high field resonance is observed at 188.1 ppm by ^{13}C NMR spectroscopy, characteristic of a metal-vinyl carbon environment, which couples to three proton environments at 1.02, 1.40 and 1.58 ppm. This latter coupling is another example of spin-active nuclei adjacent to metal centre coupling to proximal Pn*–*Me* environments as observed for Pn*MCp(X) (M = Ti, Zr; X = H, alkyl).

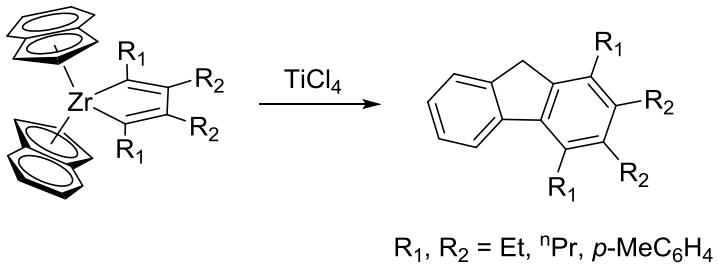
Similar examples of cationic alkyne dimerisation are rare in the literature. Clearly the alkyne-derived fragment highlighted in red has undergone significant rearrangement, where this C_4H_6 fragment can be related to 2-butyne by hydride and methyl shifts, chemistry characteristic of carbocations. Indeed, it is difficult to suggest a plausible mechanism to rationalise the formation of this complex using traditional coordination-insertion type chemistry. Typically alkynes will react with metals by insertion[77–80] or σ-bond metathesis[81] if a suitable σ-bound ligand is present. Indeed, double insertion of 2-butyne is known to form pentadienyl complexes with $[Cp_2ZrMe]^{+}$.[82] Alternatively, if an insertion pathway is not accessible, then alkyne trimerisation to benzene derivatives is commonly encountered.[83,84] However, it is difficult to postulate a mechanism for the formation of the observed product without alkyne isomerisations inaccessible to these reaction pathways.

The reaction of unsaturated hydrocarbons and Cp–Ti bonds has previously been reported by Rosenthal and coworkers.[85] Addition of alkynes (HC≡CH, PyC≡C($SiMe_3$)) to the metallacyclopropene complex, $Cp_2Ti[(SiMe_3)C{=}C(SiMe_3)]$ was observed to functionalise one Cp ring, forming dihydroindenyl Ti(II) derivatives *via* an intermediate metallocyclopentadiene (Scheme 4.14).[86,87]



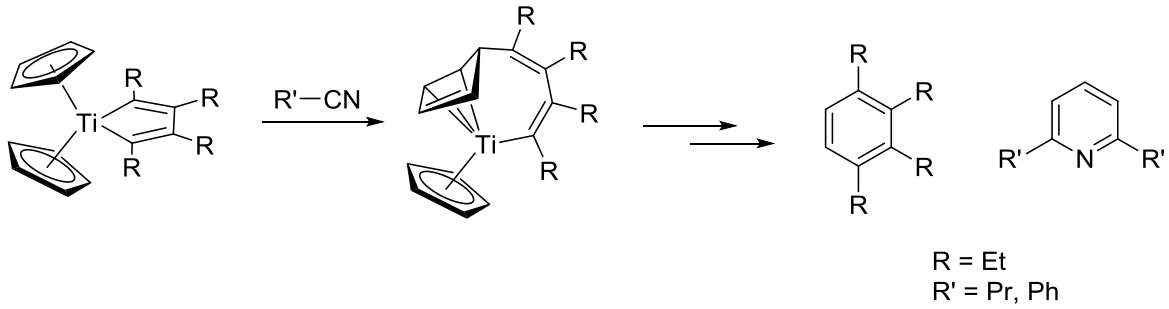
Scheme 4.14. *Cyclopentadienyl ring functionalisation by titanacyclopentadiene complexes.*

Subsequently, zirconacyclopentadiene complexes have been observed to undergo similar transformations in the presence of $TiCl_4$, which was further elaborated upon by employing indenyl-substituted zirconocenes, allowing for the formation of the corresponding fluorene derivatives (Scheme 4.15).[88,89]



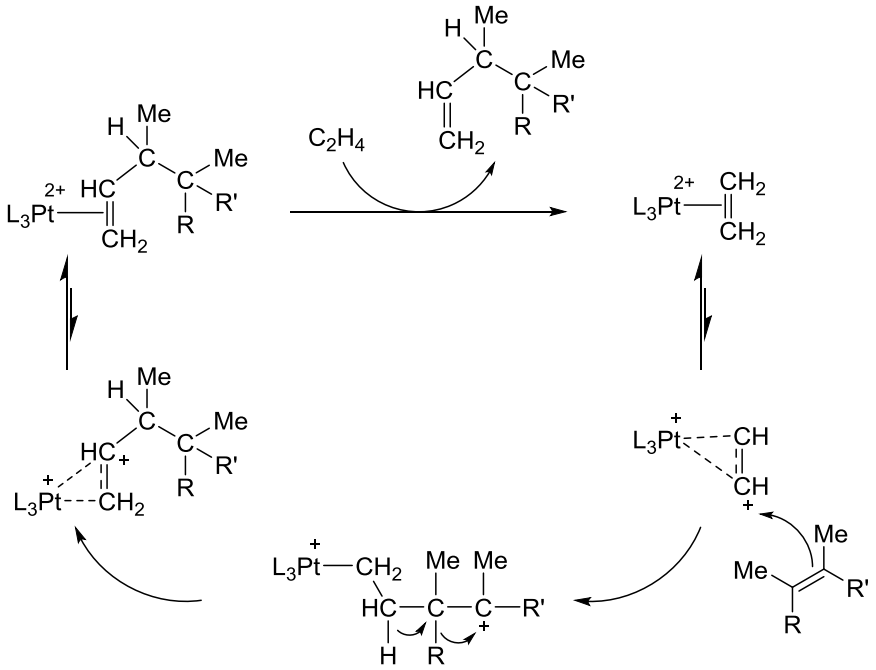
Scheme 4.15. *Indenyl ring functionalisation by zirconacyclopentadiene complexes.*

Computational investigations by Suresh and Koga[90] on the Cp-ring functionalisation of $Cp_2Ti(C_4Et_4)$[91] have suggested that the reaction proceeds *via* initial nucleophilic attack of the Cp ring at the terminal vinyl carbon, forming an intermediate that qualitatively resembles the alkyne dimerisation product shown in Figure 4.18, although this was not experimentally observed. (Scheme 4.16).



Scheme 4.16. *Calculated intermediate in the cyclopentadienyl ring functionalisation of a titanacyclopentadiene complex.*

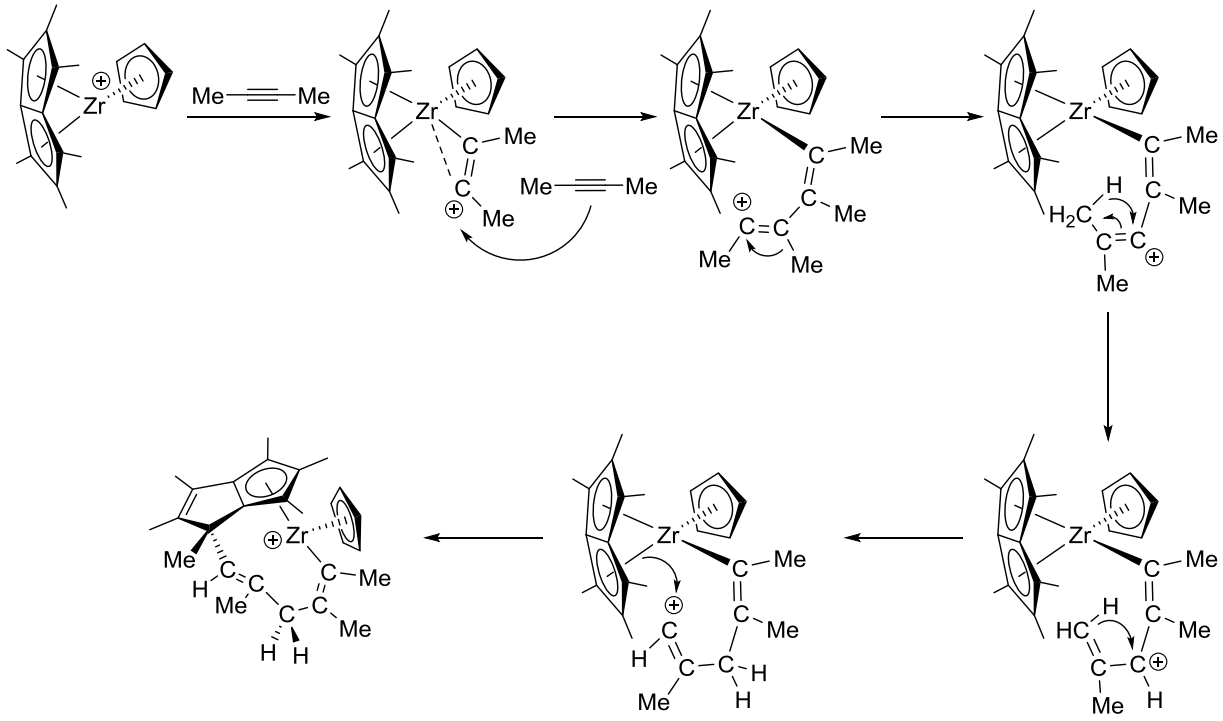
Hahn *et al.* reported the cationic dimerisation of olefins mediated by $[PNP–Pt–(\eta^2–C_2H_4)]^{2+}$ (PNP = 2,6–bis(diphenylphosphinomethyl)pyridine) in which C–C bond formation was accompanied by isomerisation of the olefin fragment, suggesting the participation of hydride/alkyl shifts during catalysis. The authors proposed initial desymmetrisation of the bound ethylene ligand, generating a partial positive charge at the distal position. Concatenation with the added olefin, followed by alkyl and hydride shifts accounted for the isomerised end product, although the postulated carbocationic intermediate could not be observed spectroscopically (Scheme 4.17).



Scheme 4.17. *Proposed mechanism for the catalytic dimerisation of olefins with L_3Pt^{2+} (L_3 = 2,6–bis(diphenylphosphinomethyl)pyridine).*

On the basis of these previous observations a tentative mechanism could be proposed to rationalise the alkyne dimerisation observed with [Pn*ZrCp][B(C_6F_5)$_4$] and 2-butyne (Scheme 4.18). Initial binding of the alkyne at the electrophilic zirconium centre is followed by nucleophilic addition to the distal carbon forming a new C–C bond. A series of hydride and methyl shifts could be postulated to account for the rearranged alkyne-derived fragment. The Pn* ligand then reacts with the carbocation, forming a second new C–C bond and regenerating the cationic zirconium centre.

Surprisingly, exposing a chlorobenzene solution of this alkyne activation complex to 2 bar ethylene leads to no polymerisation, despite its structural similarity to traditional coordination-insertion catalysts. Even in the presence of 1000 eq. MAO, activities of only 32 kg_{PE}/(mol·h·bar) were recorded, which further alludes to the catalytic inefficiency of ring-functionalised Pn* derivatives. Regardless, the ability of [Pn*ZrCp][B(C_6F_5)$_4$] to mediate the concatenation of two alkynes, alongside the hallmark isomerisations of carbocation chemistry, allude to the viability of a cationic olefin polymerisation mechanism.

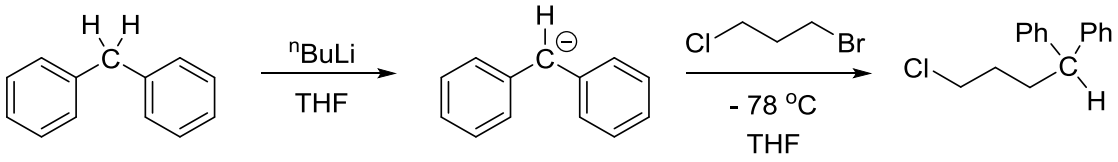


Scheme 4.18. *Proposed mechanism for the formation of alkyne dimerisation product.*

4.11 Attempted synthesis of stable metal-carbocation complexes

It was desireable to synthesise stable carbocations that could demonstrate the viability of cationic initiation by entering the catalytic cycle with a pre-formed carbocation. Phenyl rings are known to stabilise carbocations electronically, by donation of electrons from the π-system of the aromatic rings, and sterically, by inhibiting approach of nucleophiles. The archetypal example, $[CPh_3]^+$ is stable for months when stored under anhydrous conditions, which contrasts with the relatively short lifetimes of aliphatic carbocations, even at cryogenic temperatures.[56,57] Following the successful synthesis of Pn*ZrCp(R) complexes (R = *n*-alkyl) discussed in Chapter 2, the synthesis of di-isophenyl metal alkyl complexes, Pn*ZrCp(R–$CHPh_2$), was targeted, as it was envisaged that the distal methine proton could be selectively abstracted to generate a long-lived carbocation for use in ethylene polymerisation.

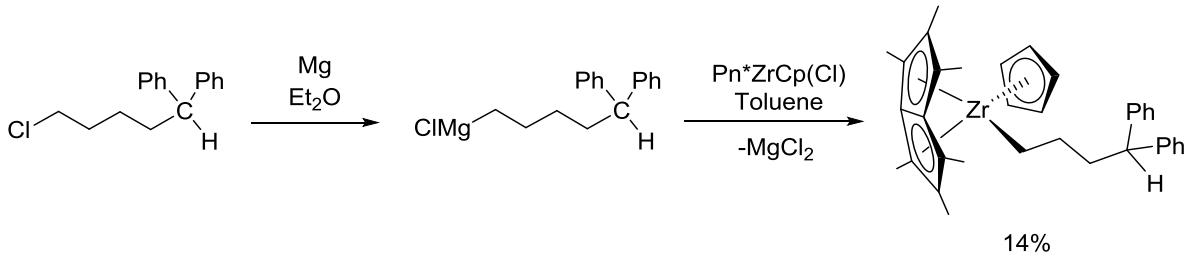
1–chloro,4,4–diphenylbutane has previously been reported, synthesised in a one-pot procedure from *in-situ* generated diphenylmethyl lithium and 1-bromo,3-chloro-propane (Scheme 4.19).[92] Substitution occurs preferentially at the weaker C–Br bond, although the chlorobutane requires purification by fractional distillation to separate it from the double substitution product and unreacted starting material.



Scheme 4.19. *Synthetic route to 1–chloro,4,4–diphenylbutane.*

In Chapter 2 it was noted that salt metathesis with alkyl-lithium reagents gave improved yields relative to Grignard reagents. However, it has previously been observed that rapid isomerisation of primary alkyl-lithium reagents occurs in cases where phenyl-stabilised tertiary anions can be accessed, as is the case here.[93,94] The di-isophenyl alkyl-Grignard was therefore prepared in Et_2O at 30 °C over 2 h, and the required concentration determined by titrating with Pn*ZrCp(Cl) in C_6D_6. Pn*ZrCp(C_4H_7–Ph_2) was synthesised in toluene overnight from Pn*ZrCp(Cl) and ClMg(C_4H_7–Ph_2) and isolated in 14 % yield as a yellow microcrystalline solid (Scheme 4.20). The ^{1}H NMR spectrum displays the

expected 3 Pn*–*Me* environments, alongside 4 discrete environments for each position along the butyl chain. The isophenyl-methine environment is significantly deshielded, resolved at 4.20 ppm and 65.6 ppm in ^{1}H and ^{13}C NMR spectra respectively. Single crystals suitable for X-ray diffraction were grown from slow evaporation of a benzene solution, with the molecular structure shown in Figure 4.19.



Scheme 4.20. *Synthesis of Pn*ZrCp(C$_4$H$_7$–Ph$_2$).*

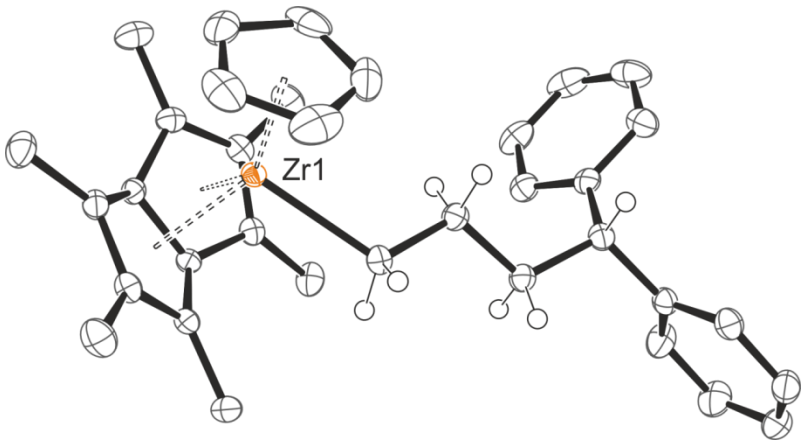


Figure 4.19. *Thermal displacement ellipsoid plot of Pn*ZrCp(C$_4$H$_7$–Ph$_2$). H atoms omitted for clarity, ellipsoids shown at 50% probability.*

Addition of [CPh$_3$][(B(3,5–C$_6$H$_3$(CF$_3$)$_2$)$_4$] to a solution of Pn*ZrCp(C$_4$H$_7$–Ph$_2$) in C$_6$D$_5$Cl led to the observation of [Pn*ZrCp][B(3,5–C$_6$H$_3$(CF$_3$)$_2$)$_4$] as the major species as judged by ^{1}H NMR spectroscopy. Interestingly, HCPh$_3$ was also observed, indicating the successful abstraction of the *iso*-phenyl hydrogen, presumably forming an insoluble product that could not be observed by NMR spectroscopy in C$_6$D$_5$Cl. However, given the high activities reported for [Pn*ZrCp]$^{+}$, competitive alkyl-abstraction would prevent meaningful insights being obtained regarding cationic initiation. Formation of [Pn*ZrCp]$^{+}$ could perhaps be disfavoured further by inclusion of alkyl substituents at the α-position.

However, given the involved synthesis and low isolated yields, these investigations were not pursued further.

4.12 Catalytic cationic initiation

Cationic initiation is structurally different from coordination-insertion catalysis, most importantly in that the metal functions as an initiator and not truly as a catalyst. This is proposed to account for lower observed polymerisation activities of [Pn*ZrCp]$^{+}$ compared with Pn*ZrCp(Cl)/MAO. Catalytic turnover can be realised by addition of MAO to [Pn*ZrCp]$^{+}$ leading to a 122% increase in activity (Table 4.6). Following chain-termination a neutral metal alkyl complex, Pn*ZrCp(Polymeryl) results. This is directly analogous to the metal *n*-alkyl complex, Pn*ZrCp(^{n}Bu), which does not polymerise ethylene in the absence of co-catalyst, verifying that chain termination leads to the formation of an inactive metal site. This contrasts with common chain alterations steps in coordination-insertion catalysis: β–H elimination, chain-transfer to monomer and chain-transfer to aluminium all lead to the reformation of cationic metal alkyl or hydride complexes that can re-enter the catalytic cycle. In this case we can demonstrate the capacity of MAO to regenerate dead initiator by the exposure of a Pn*ZrCp(^{n}Bu)/MAO mixture (1:1000) to ethylene, which leads to activities of 5121 kg_{PE}/(mol·h·bar).

The observation of low branch densities (0.5 – 1 Me/1000CH_2) seems counterintuitive given the commonplace occurrence of hydride shifts in many chemical and biological systems. Branch density is a function of the relative rates of propagation and branching events.[95] Two reasons are therefore proposed for this observed low branch content. First, it is known that the less stabilised the product carbocation, the greater the rate of cationic propagation. For example, isopropyl vinyl ether, mesomerically stabilised by the oxygen lone pair, demonstrates cationic propagation rate constants over 4 orders of magnitude smaller than those found for isobutylene, stabilised only by hyperconjugation.[95] Similarly we would expect reactive ethylenic carbocations to demonstrate even greater rate constants. Secondly, the propagating species is kinetically stabilised as a cycloproponium ion, which is known to be relatively long-lived species. The branch content may therefore be attenuated by increased rates of propagation, and decreased rates of hydride-shifts.

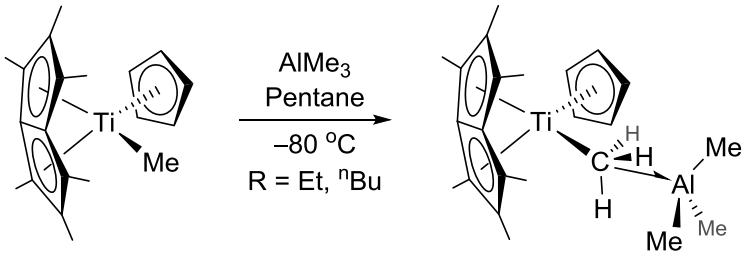
Given the inactivity of [Pn*TiCp]$^+$ towards ethylene polymerisation it may be inferred that the same mechanism does not occur in the titanium system. The inability of [Pn*TiCp]$^+$ to act as a cationic initiator is ascribed to its reduced electrophilicity compared to [Pn*ZrCp]$^+$, a trend commonly observed with group 4 metallocenes. Acknowledging the predisposition of Pn*TiCp(alkyl) complex to decompose *via* homolytic pathways, a radical pathway may be responsible for the observed activities. However detailed investigations to this effect were not undertaken.

4.13 Chain-transfer to aluminium: reactivity of Pn*MCp(Me) and $AlMe_3$

Chain-transfer to aluminium has traditionally been a difficult area of olefin polymerisation to study given the complex equilibria and short lifetimes of these intermediates. Nonetheless, elegant studies have previously been described for group 4 catalysts using mass spectrometry[96,97] or quantitative kinetic analysis.[16,98] However, no structurally characterised chain-transfer intermediates have been reported to date.

In order to better understand the interactions of polymer chain and co-catalyst, metal alkyl complexes were employed to model chain growth: Pn*ZrCp(X) (X = Me, Et, ^{n}Bu). In the case of Pn*ZrCp(Me) addition of 1 eq. $AlMe_3$ leads to the observation of a new C_s symmetric complex with two distinct metal-methyl environments (–0.79 and –0.35 relative integration 3:9). This is assigned to the addition product, Pn*ZrCp(μ–Me)$AlMe_3$. Coalescence of these resonances is not observed up to 360 K in C_7D_8 indicating any exchange is slow relative to the NMR timescale. This contrasts with the reactivity of Pn*TiCp(Me) and $AlMe_3$ where a single metal-methyl resonance is resolved in the ^{1}H NMR spectrum at –0.37 ppm, alongside a C_{2v} symmetric Pn* fragment. Analogous to the fluxional behaviour of [(Pn*TiCp)$_2$(μ–Cl)][(B(3,5–$C_6H_3(CF_3)_2)_4$] discussed in section 4.4, this is proposed to result from rapid reversible coordination of [$AlMe_4$]$^-$ at the metal centre. Single crystals were obtained for this latter complex by reacting Pn*TiCp(Me) and $AlMe_3$ in pentane for 15 minutes before cooling the solution to –80 °C. The product is isolated as the $AlMe_3$ adduct, Pn*TiCp(μ–Me)$AlMe_3$, which corresponds to the structure resolved at low temperature (< 218 K) by ^{1}H NMR spectroscopy in C_7D_8 (Scheme 4.21, Figure 4.20). Satisfactory elemental analysis could not be obtained due to the volatility of the $AlMe_3$ fragment. The bonding observed in the solid state can be rationalised as a 3-centre 2-electron bond between Ti−Me and Al. The Ti−Me bond length is similar to that

observed for Pn*TiCp(Me) (2.2666(14) Å *vs.* 2.2915(18) Å for Pn*TiCp(Me) and Pn*TiCp(μ–Me)AlMe$_3$ respectively), while the Al–C20 bond length is significantly elongated relative to Al–C21/22/23 (2.3305(18) *vs.* an average of 1.972(2) Å). The aluminum fragment displays a slight tetrahedral distortion, which can be measured by taking the distance from aluminium to the mean plane of the adjacent terminal methyl carbon atoms. A value of 0.4207(16) Å is observed for Pn*TiCp(μ–Me)AlMe$_3$, compared to 0.4326(12) for Pn*TiCp(μ–Cl)AlMe$_3$.



Scheme 4.21. *Synthesis of Pn*TiCp(μ–Me)AlMe$_3$.*

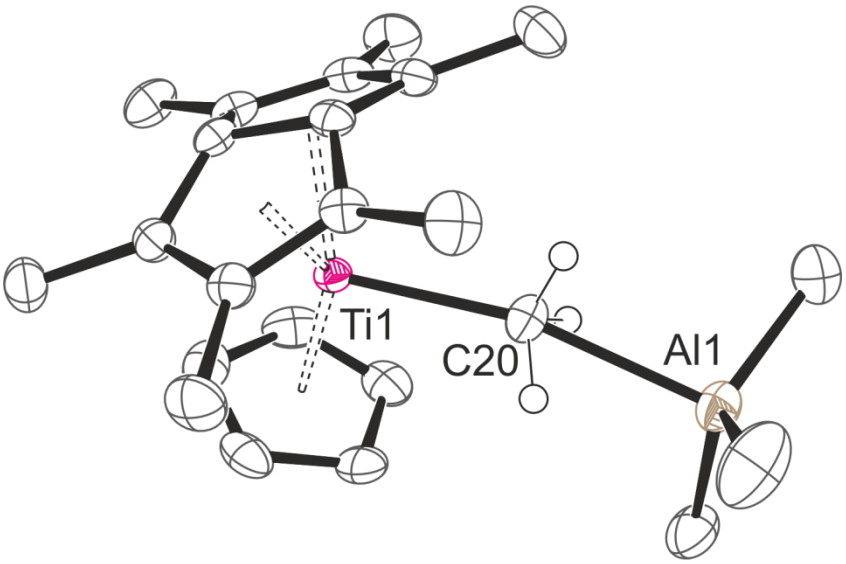
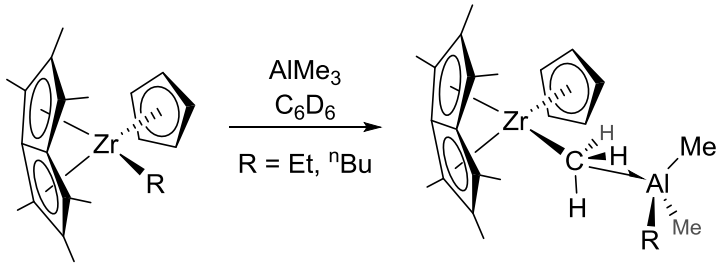


Figure 4.20. *Thermal displacement ellipsoid plot of Pn*TiCp(μ–Me)AlMe$_3$. Ellipsoids shown at 50% probability, H atoms omitted for clarity with the exception of C20a, b, c.*

4.14 Reactivity of Pn*ZrCp(R) (R = Et, ^{n}Bu) and AlMe$_3$

Reacting Pn*ZrCp(R) (R = Et, ^{n}Bu) with 1 eq. AlMe$_3$ a new product is formed of C_S symmetry, in slow equilibrium with the starting materials. This new complex is Pn*ZrCp(μ–Me)AlMe$_2$R (R = Et, ^{n}Bu), which can be considered an intermediate along the

pathway of chain-transfer before abstraction of the polymeryl chain regenerates the cationic active species (Scheme 4.22).



Scheme 4.22. *Synthesis of Pn*ZrCp(μ–Me)AlMe$_2$R (R = Et, ^{n}Bu).*

A through-space coupling can be observed by ^{1}H–^{13}C HMBC NMR spectroscopy between the bridging methyl moiety and one set of NWT Pn*–Me resonances, analogous to the coupling observed for Pn*MCp(R) (R = H, alkyl). Accurate elemental analysis could not be obtained for either complex due to the volatility of the alkyl-aluminium fragment. Under dynamic vacuum a mixture of Pn*ZrCp(Me), Pn*ZrCp(R) (R = Et, ^{n}Bu) and Pn*ZrCp(μ–Me)AlMe$_2$R (R = Et, ^{n}Bu) is obtained. However, single crystals suitable for X-ray diffraction were obtained by cooling a pentane solution to – 80 °C for no more than 48 h. The solid-state structures are shown in Figure 4.21, with key bond metrics given in Table 4.8.

Slight elongation of the Zr–C20 bond length is observed relative to Pn*ZrCp(Me), reflecting the weaker bond resulting from the formation a 3-centre 2-electron bond. More significant variation is observed for bridging and terminal Al–C bonds (1.985(3) and 2.308(2) Å), which alludes to a weak C20–Al interaction. Pyramidalisation about the aluminium, measured by taking the distance from aluminium to the mean plane of the terminal carbon atoms, is more extensive for both zirconium complexes relative to Pn*TiCp(μ–Me)AlMe$_3$ (c.f. 0.4207(16) Å). Hydrogen atoms were placed as an idealised methyl group riding on the bridging carbon atom, with the torsion angle determined by the electron density. Any planar distortion of the bridging methyl groups therefore cannot be accurately determined from the data. However, the orientation of this CH_3 moiety, where the apex of the tetrahedron points towards zirconium is determined by the experimental electron density.

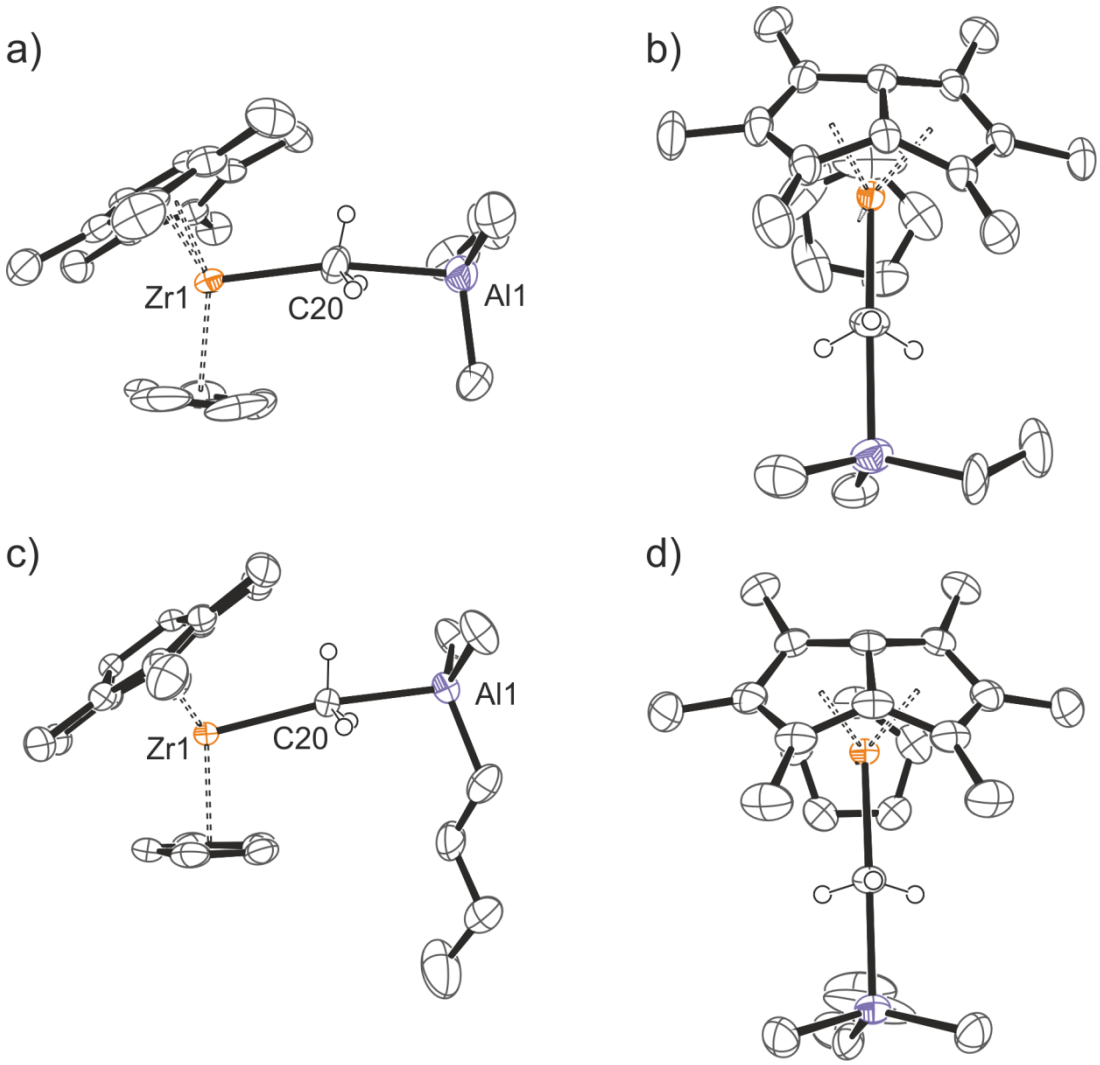


Figure 4.21. *Thermal displacement ellipsoid plot (50% probability) of a) Pn*ZrCp(μ–Me)AlMe$_2$Et side-on, b) top down, c) Pn*ZrCp(μ–Me)AlMe$_2$^{n}Bu side-on, d) top-down. H atoms omitted for clarity with the exception of C20a, b and c.*

Complex	Zr–C20	Al–C20	Al-C$_{3\text{-plane}}$
Pn*ZrCp(Me)	2.3735(18)	-	-
Pn*ZrCp(Et)	2.3634(18)	-	-
Pn*ZrCp(^{n}Bu)	2.3461(16)	-	-
Pn*ZrCp(μ–Me)AlMe$_2$Et	2.392(2)	2.308(2)	0.428(2)
Pn*ZrCp(μ–Me)AlMe$_2$^{n}Bu	2.410(2)	2.309(3)	0.489(2)

Table 4.8. *Summary of key bond metrics for Pn*ZrCp(R)(R = Et, ^{n}Bu) and Pn*ZrCp(μ–Me)AlMe$_2$R (R = Et, ^{n}Bu). Lengths given in Å. C20–H$_{3\text{-plane}}$ is the distance between C20 and the mean plane of H20a/b/c. Al-C$_{3\text{-plane}}$ is the distance between Al and the mean plane of the adjacent terminal carbon atoms.*

Due to their Lewis acidity, alkyl aluminium complexes generally adopt structures with two bridging ligands e.g. Al_2Me_6. However, electronic saturation of the titanium and zirconium complexes under discussion favours a single bridging methyl interaction. In this case three limiting linear conformations can be adopted, shown in Figure 4.22.[99]

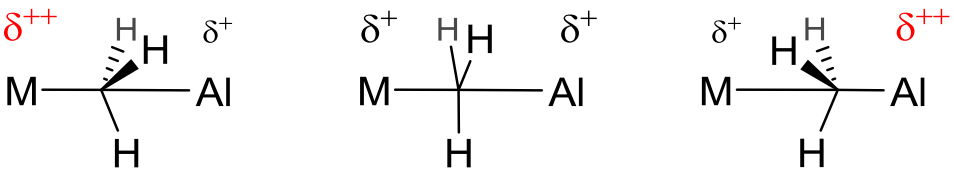


Figure 4.22. *Linear bonding modes of (μ–2) bridging methyl groups in bimetallic complexes.*

The apex of the tetrahedron formed by the bridging methyl group can either point towards aluminium, the transition metal (titanium or zirconium in this case), or it can adopt a planar geometry. The most common conformation has the apex pointed towards aluminium,[100–103] while methyl-bridged homobimetallic complexes generally display a planar geometry.[104,105] Unusually, the methyl-apices of all the heterobimetallic complexes discussed in this chapter point towards the transition metal and not aluminium as is typically observed. Although over 300 similar methyl-bridged bimetallic structures have been deposited in the CCDC (M–Me–Al where M is any metal), only a single complex was found to display the same conformation, $Cp^{Me4}{}_2ZrMe(\mu\text{–}Me)Al(C_6F_5)_4$.[106] Substituting boron for aluminium, the same directionality of the methyl-apex is observed and no structures with an inverted conformation were found. Even highly electrophilic alkali earth metal complexes such as $[(Me_5C_5)Ca(\mu\text{–}Me_3Al.THF)]_2$ and $[((THF)_4Ca\{(\mu_2\text{–}Me)AlMe_2(N(SiPh_3)(SiH_2Ph))\}_2]$ do not display this inverted methyl conformation.[107,108]

The significance of this inverted methyl conformation can be understood by considering a simplified bonding model for these complexes. Pyramidalisation of the bridging methyl group exposes an sp^3 hybridised orbital where the anionic charge primarily resides. The most Lewis-acidic fragment will induce pyramidalisation such that the apex points in this direction to quench its electron deficiency. It is therefore striking given the diversity of deposited structures that these 18-electron complexes should be bound preferentially to the methyl-apex, which alludes to the significant electrophilicity of these metal centres. This

electrophilicity is presumably advantageous in the context of cationic ethylene polymerisation.

Density functional theory calculations were carried out at the B3LYP level of theory on Pn*ZrCp(μ–Me)AlMe$_2$Et in order to understand the nature of the bonding in more detail. The molecular orbital primarily responsible for the C20–Al bonding interaction is shown in Figure 4.23. A carbon-based orbital of sp^3 character with the major lobe pointing towards zirconium overlaps with an aluminium orbital of s-character. However, as expected, this is a weak interaction with a fractional bond order of 0.259. This helps to rationalise the long C20–Al bond length observed experimentally (2.308(2) Å), and illustrates electronically the effect of this inverted methyl conformation.

By contrast, an agostic description seems poorly suited to the bonding situation, with no positive bond orders greater than 0.1 observed between nearby protons and aluminium. Indeed $^1J_{C\text{-}H}$ recorded experimentally is 115 Hz, which is identical to previously reported coupling constants for Al_2Me_6, where values less than 100 Hz would be expected for an agostic interaction.[109]

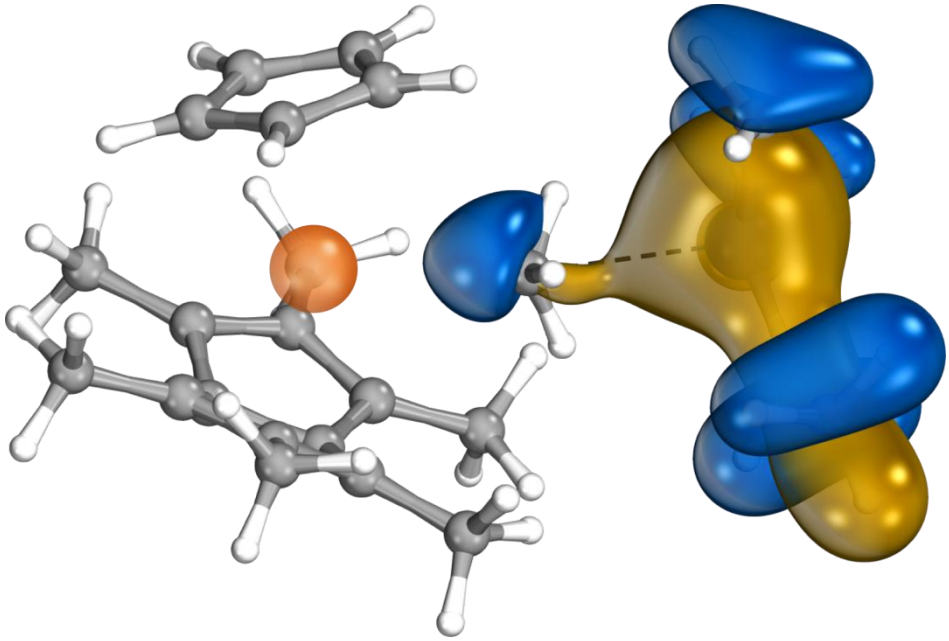


Figure 4.23. *Molecular orbital primarily responsible for C20–Al bonding interaction (HOMO –10) displaying overlap of C20 sp^3-orbital and Al s-orbital.*

Selective NOE experiments indicate that following substitution of the higher alkane it does not appreciably reinsert into the bridging position on the NMR timescale. The three proton

resonances adjacent to aluminium were independently irradiated and, after a brief mixing time (0.02 s), a ^{1}H NMR spectrum was recorded. An in-phase resonance of non-zero intensity indicates magnetisation transfer, which in this case would correspond to chemical exchange. For example, in the case of Pn*ZrCp(μ–Me)AlMe$_2$Et, after selectively irradiating the terminal methyl position (−0.236 ppm) a large in-phase resonance is observed at −0.738 ppm corresponding to the bridging methyl resonance (Figure 4.24). This indicates exchange of these proton environments. However, irradiation of the ethyl or butyl environments adjacent to aluminium does not produce intensity in the bridging position. Nonetheless an equilibrium is clearly established given the persistence of resonances corresponding to Pn*ZrCp(R) (R = Et, ^{n}Bu) with 2 eq. AlMe$_3$, suggesting this reversible process is slow relative to the NMR timescale.

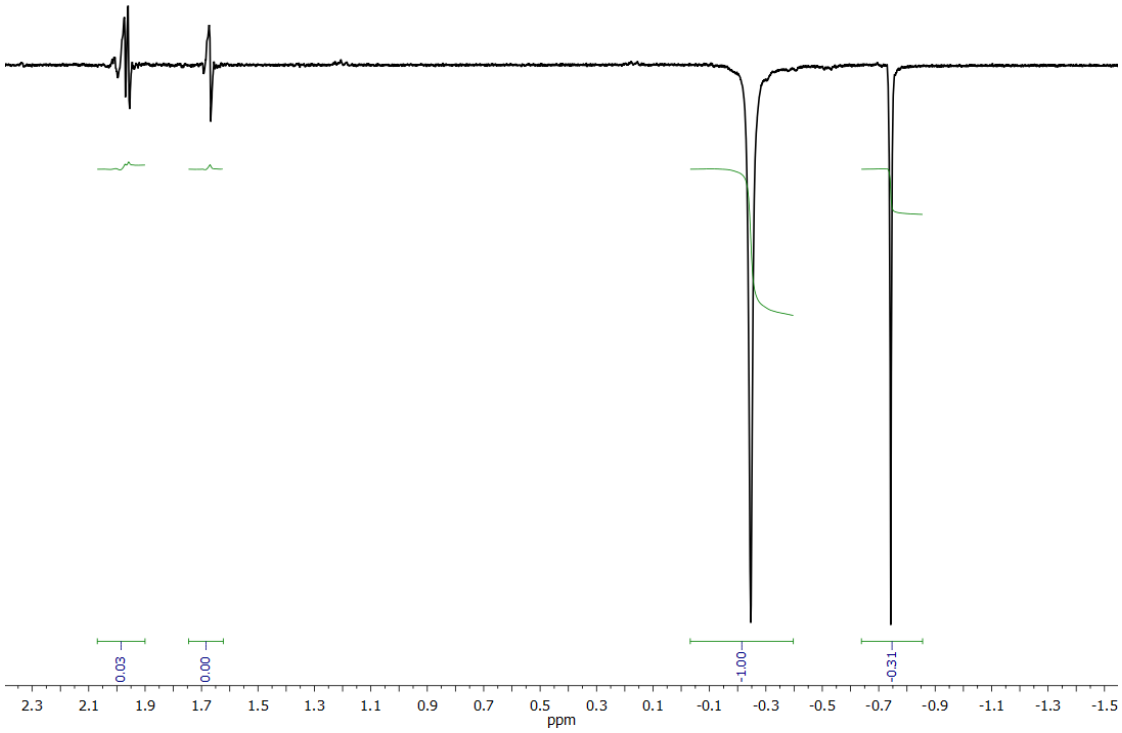
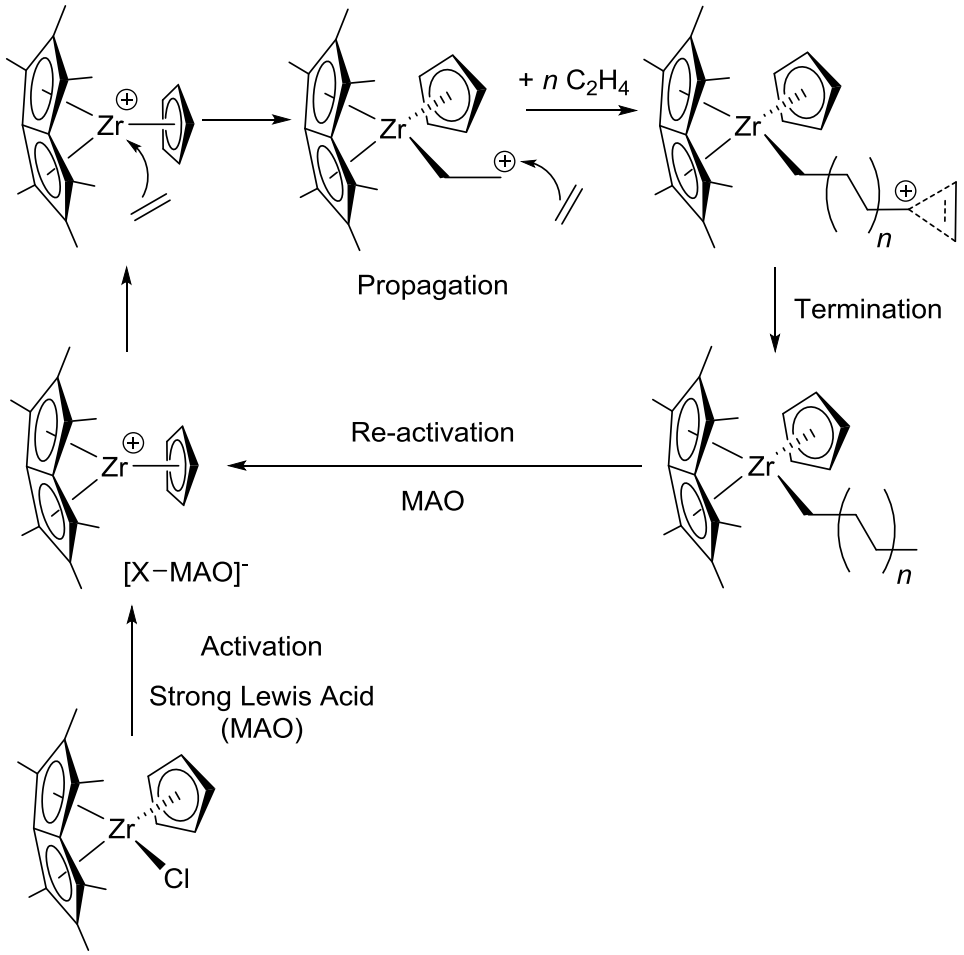


Figure 4.24. *1D selective gradient NOSEY of Pn*ZrCp(μ–Me)AlMe$_2$Et (t_1 = 5.1 seconds,d1 = 35 seconds, frequency = −0.236 ppm). Large intensity negative resonance at −0.738 indicates exchange of terminal and bridging methyl groups.*

The absolute frequency with which this chain-transfer to aluminium takes places during polymerisation has not been determined and will require a more detailed kinetic analysis. However it is interesting to note that hypothetically, if abstraction of the polymeryl chain

occurs before chain termination, not only is a catalytically active [Pn*ZrCp]$^+$ initatior regenerated, but also an aluminium-bound carbocation would propagate through solution.

A proposed mechanism to rationalise the activity of Pn*ZrCp^R(X) catalysts is shown in Scheme 4.23, summarising the findings of this study.



Scheme 4.23. *Proposed mechanism of ethylene polymerisation by Pn*ZrCp(Cl)/MAO system*

4.15 Conclusions

Pn*ZrCp^{R}(X) complexes display ethylene polymerisation activities two orders of magnitude greater than Pn*ZrX$_2$ complexes, which alludes to an unusual mechanism of polymerisation for these coordinatively saturated 18-electron complexes. The activation of these complexes was studied using MAO and AlMe$_3$, implicating the formation cationic derivatives, [Pn*ZrCp]$^{+}$. Rational synthesis of the target cationic zirconocenes was achieved by alkyl/hydride abstraction to form borate stabilised ion pairs. [Pn*ZrCp]$^{+}$ is very reactive and although it could not be crystallographically characterised as a base-free complex, the structure was confirmed by synthesising the pyridine adduct. A decomposition product, [(Pn*ZrCp)$_2$(μ–Cl)][(B(C$_6$F$_5$)$_4$], was also structurally characterised, resulting from the reaction of [Pn*ZrCp][(B(C$_6$F$_5$)$_4$] with chlorobenzene solvent. Remarkably [Pn*ZrCp][B(Ar^{F})$_4$] is an active ethylene polymerisation catalyst despite the absence of alkyl bond into which the monomer can insert.

A number of possible mechanisms were investigated to rationalise this activity. Bimetallic mechanisms, intermediate fulvene/tuck-in complex formation, labile Cp-rings and intermediacy of hydro-permethylpentalene complexes were all tested and found to describe the observed activity poorly on the basis of reactivity studies, *in-situ* gas uptake measurements, and studies of spent catalyst.

An alternative mechanism of cationic ethylene polymerisation is proposed, where the polymer chain propagates as a cycloproponium cation. The intermediate carbocation was trapped with a richly fluorinated tag, (CF$_3$)$_3$COH, allowing for its observation by ^{19}F NMR spectroscopy. Insight into this cationic polymerisation was obtained by reacting the initiator complex, [Pn*ZrCp][B(Ar^{F})$_4$], with 2-butyne, which led to alkyne dimerisation by a proposed cationic mechanism, with evidence of hydride and methyl shifts observed in the final product. Nonetheless this ring-functionalised Pn* derivative was found to be an poor ethylene polymerisation catalyst, despite its structural similarity to traditional coordination-insertion catalysts.

The reactivity of metal alkyl complexes with AlMe$_3$ was studied in order to better understand the role of the co-catalyst in these polymerisations. Crystallographically characterised examples display an unusual inverted methyl conformation, which

qualitatively indicates the significant electrophilicty of the group 4 metal in these complexes. In the case of longer alkyl derivatives, Pn*ZrCp(Et) and Pn*ZrCp(^{n}Bu), transfer of Et/^{n}Bu chains to aluminium was observed crystallographically; the first structurally characterised examples of chain-transfer to aluminium intermediates in any olefin polymerisation system.

As always in catalysis, there remains the possibility that an as-yet unidentified component in the reaction mixture may be responsible for the activity of [Pn*ZrCp]$^{+}$. However, in light of these results, it is hoped that the *a priori* design criteria of ethylene polymerisation catalysts can be updated, and that insight into the polymerisation mechanism of this family of catalysts may be obtained through the investigation of other non-classical catalyst motifs.

4.16 References

(1) Kilpatrick, A. F. R.; Buffet, J.-C.; Nørby, P.; Rees, N. H.; Funnell, N. P.; Sripothongnak, S.; O'Hare, D. *Chem. Mater.* **2016**, *28* (20), 7444–7450.

(2) Buffet, J.-C.; Arnold, T. A. Q.; Khamnaen, T.; O'Hare, D. Symmetrical permethylindenyl catalysts on solid MAO for slurry ethylene polymerisation. GB 1420215.4, 2014.

(3) Wright, C. M. R.; Turner, Z. R.; Buffet, J.-C.; O'Hare, D. *Chem. Commun.* **2016**, *52* (13), 2850–2853.

(4) Kaji, E.; Yoshioka, E. Solid polymethylaluminoxane composition and process for producing same. WO2010055652, May 20, 2010.

(5) Jonas, K.; Kolb, P.; Kollbach, G. Mononuclear and polynuclear transition metal complexes with pentalene ligands bound to single metal atoms. US 5959132 A, 1999.

(6) Cloke, F. G. N.; Parry, J. S. Novel transition metal complexes. WO 1999007716 A1, 1998.

(7) Cloke, F. G. N. Polymerization catalysts. EP0672676 A2, 1995.

(8) Cooper, R. T.; Chadwick, F. M.; Ashley, A. E.; O'Hare, D. *Organometallics* **2013**, *32* (7), 2228–2233.

(9) Chadwick, F. M.; Cooper, R. T.; O'Hare, D. *Organometallics* **2016**, *35* (12), 2092–2100.

(10) Chadwick, F. M. D.Phil Thesis, University of Oxford, 2013.

(11) Theurkauff, G.; Bader, M.; Marquet, N.; Bondon, A.; Roisnel, T.; Guegan, J.-P.; Amar, A.; Boucekkine, A.; Carpentier, J.-F.; Kirillov, E. *Organometallics* **2016**, *35* (2), 258–276.

(12) Bryliakov, K. P.; Semikolenova, N. V.; Yudaev, D. V.; Zakharov, V. A.; Brintzinger, H. H.; Ystenes, M.; Rytter, E.; Talsi, E. P. *J. Organomet. Chem.* **2003**, *683* (1), 92–102.

(13) Bryliakov, K. P.; Semikolenova, N. V.; Yudaev, D. V.; Ystenes, M.; Rytter, E.; Zakharov, V. A.; Talsi, E. P. *Macromol. Chem. Phys.* **2003**, *204* (8), 1110–1117.

(14) Wieser, U.; Schaper, F.; Brintzinger, H.-H. *Macromol. Symp.* **2006**, *236* (1), 63–68.
(15) Babushkin, D. E.; Naundorf, C.; Brintzinger, H. H.; Royo, P.; Serrano, R.; Talsi, E. P.; Macchioni, A.; Bochmann, M. *Dalton Trans.* **2006**, *95* (38), 4539–4544.
(16) Camara, J. M.; Petros, R. A.; Norton, J. R. *J. Am. Chem. Soc.* **2011**, *133* (14), 5263–5273.
(17) Theurkauff, G.; Bondon, A.; Dorcet, V.; Carpentier, J.-F.; Kirillov, E. *Angew. Chem. Int. Ed.* **2015**, *54* (21), 6343–6346.
(18) Shannon, R. D. *Acta Crystallogr. Sect. A* **1976**, *32* (5), 751–767.
(19) Gómez, R.; Green, M. L. H.; Haggitt, J. L. *J. Chem. Soc., Dalton Trans.* **1996**, *0* (6), 939–946.
(20) Vollmerhaus, R.; Rahim, M.; Tomaszewski, R.; Xin, S.; Taylor, N. J.; Collins, S. *Organometallics* **2000**, *19* (11), 2161–2169.
(21) Harney, M. B.; Keaton, R. J.; Fettinger, J. C.; Sita, L. R. *J. Am. Chem. Soc.* **2006**, *128* (10), 3420–3432.
(22) Luo, Y.; Hou, Z. *Organometallics* **2006**, *25* (26), 6162–6165.
(23) Luo, G.; Luo, Y.; Hou, Z.; Qu, J. *Organometallics* **2016**, *35* (5), 778–784.
(24) Ghorbani, N.; Mahdizadeh Ghohe, N.; Torabi, S.; Yates, B. F.; Ariafard, A. *Organometallics* **2013**, *32* (6), 1687–1693.
(25) Talarico, G.; Budzelaar, P. H. M. *Organometallics* **2002**, *21* (1), 34–38.
(26) Talarico, G.; Budzelaar, P. H. M. *Organometallics* **2000**, *19* (26), 5691–5695.
(27) Coles, M. P.; Jordan, R. F. *J. Am. Chem. Soc.* **1997**, *119* (34), 8125–8126.
(28) Korolev, A. V.; Ihara, E.; Guzei, I. A.; Young, V. G.; Jordan, R. F. *J. Am. Chem. Soc.* **2001**, *123* (34), 8291–8309.
(29) Bruce, M.; Gibson, V. C.; Redshaw, C.; Solan, G. A.; White, A. J. P.; Williams, D. J. *Chem. Commun.* **1998**, *0* (22), 2523–2524.
(30) Cameron, P. A.; Gibson, V. C.; Redshaw, C.; Segal, J. A.; Bruce, M. D.; White, A. J. P.; Williams, D. J. *Chem. Commun.* **1999**, *0* (18), 1883–1884.
(31) Kim, J. S.; Wojcinski, L. M.; Liu, S.; Sworen, J. C.; Sen, A. *J. Am. Chem. Soc.* **2000**, *122* (23), 5668–5669.
(32) Ashley, A. E.; Cowley, A. R.; O'Hare, D. *Eur. J. Org. Chem.* **2007**, *2007* (14), 2239–2242.
(33) Ashley, A. E.; Cowley, A. R.; O'Hare, D. *Chem. Commun.* **2007**, No. 15, 1512–1514.
(34) Sun, Y.; Spence, R. E. v. H.; Piers, W. E.; Parvez, M.; Yap, G. P. A. *J. Am. Chem. Soc.* **1997**, *119* (22), 5132–5143.
(35) Àrias, Ò.; Petrov, A. R.; Bannenberg, T.; Altenburger, K.; Arndt, P.; Jones, P. G.; Rosenthal, U.; Tamm, M. *Organometallics* **2014**, *33* (7), 1774–1786.
(36) Brintzinger, H.; Bercaw, J. E. *J. Am. Chem. Soc.* **1971**, *93* (8), 2045–2046.
(37) Bercaw, J. E. *J. Am. Chem. Soc.* **1974**, *96* (16), 5087–5095.
(38) Ebert, H.; Timmermann, V.; Oswald, T.; Saak, W.; Schmidtmann, M.; Friedemann, M.; Haase, D.; Beckhaus, R. *Organometallics* **2014**, *33* (6), 1440–1452.
(39) Bercaw, J. E.; Marvich, R. H.; Bell, L. G.; Brintzinger, H. H. *J. Am. Chem. Soc.* **1972**, *94* (4), 1219–1238.
(40) Bercaw, J. E. *J. Am. Chem. Soc.* **1974**, *96* (16), 5087–5095.
(41) Guo, Z. Y.; Bradley, P. K.; Jordan, R. F. *Organometallics* **1992**, *11* (7), 2690–2693.
(42) Evans, W. J.; Forrestal, K. J.; Ziller, J. W. *Angew. Chem. Int. Ed.* **1997**, *36* (7), 774–776.
(43) Evans, W. J.; Forrestal, K. J.; Ziller, J. W. *J. Am. Chem. Soc.* **1998**, *120* (36), 9273–

9282.
(44) Bistoni, G.; Rampino, S.; Scafuri, N.; Ciancaleoni, G.; Zuccaccia, D.; Belpassi, L.; Tarantelli, F. *Chem. Sci.* **2016**, *7* (2), 1174–1184.
(45) Turner, Z. R. *Unpublished Results*.
(46) Shaffer, T. D.; Ashbaugh, J. R. *J. Polym. Sci. Part A Polym. Chem.* **1997**, *35* (2), 329–344.
(47) Klis, T.; Powell, D. R.; Wojtas, L.; Wehmschulte, R. J. *Organometallics* **2011**, *30* (9), 2563–2570.
(48) Balogh, L.; Faust, R. *Polym. Bull.* **1992**, *28* (4), 367–374.
(49) Andrei, H.-S.; Solcà, N.; Dopfer, O. *Angew. Chem. Int. Ed.* **2008**, *47* (2), 395–397.
(50) Lischka, H.; Koehler, H. J. *J. Am. Chem. Soc.* **1978**, *100* (17), 5297–5305.
(51) Ricks, A. M.; Douberly, G. E.; Schleyer, P. v. R.; Duncan, M. A. *Chem. Phys. Lett.* **2009**, *480* (1–3), 17–20.
(52) Perera, S. A.; Bartlett, R. J.; Schleyer, P. von R. *J. Am. Chem. Soc.* **1995**, *117* (32), 8476–8477.
(53) Thulasiram, H. V.; Erickson, H. K.; Poulter, C. D. *J. Am. Chem. Soc.* **2008**, *130* (6), 1966–1971.
(54) Gee, J. C.; Small, B. L.; Hope, K. D. *J. Phys. Org. Chem.* **2012**, *25* (12), 1409–1417.
(55) Laube, T. *J. Am. Chem. Soc.* **1989**, *111* (26), 9224–9232.
(56) Olah, G. A. *J. Am. Chem. Soc.* **1972**, *94* (3), 808–820.
(57) Olah, G. A. *J. Org. Chem.* **2001**, *66* (18), 5943–5957.
(58) Fărcaşiu, D.; Norton, S. H. *J. Org. Chem.* **1997**, *62* (16), 5374–5379.
(59) Baird, R. L.; Aboderin, A. *Tetrahedron Lett.* **1963**, *4* (4), 235–237.
(60) Baird, R. L.; Aboderin, A. A. *J. Am. Chem. Soc.* **1964**, *86* (2), 252–255.
(61) Radom, L.; Pople, J. A.; Schleyer, P. v. R. *J. Am. Chem. Soc.* **1972**, *94* (17), 5935–5945.
(62) Koch, W.; Liu, B.; Schleyer, P. v. R. *J. Am. Chem. Soc.* **1989**, *111* (9), 3479–3480.
(63) Deno, N. C.; LaVietes, D.; Mockus, J.; Scholl, P. *J. Am. Chem. Soc.* **1968**, *90* (23), 6457–6460.
(64) Fontana, C. M.; Kidder, G. A. *J. Am. Chem. Soc.* **1948**, *70* (11), 3745–3751.
(65) Fontana, C. M.; Kidder, G. A.; Herold, R. J. *Ind. Eng. Chem.* **1952**, *44* (7), 1688–1695.
(66) Fontana, C. M.; Herold, R. J.; Kinney, E. J.; Miller, R. C. *Ind. Eng. Chem.* **1952**, *44* (12), 2955–2962.
(67) Fontana, C. M. *J. Phys. Chem.* **1959**, *63* (7), 1167–1174.
(68) Shubkin, R. L.; Baylerian, M. S.; Maler, A. R. *Ind. Eng. Chem. Prod. Res. Dev.* **1980**, *19* (1), 15–19.
(69) Onopchenko, A.; Cupples, B. L.; Kresge, A. N. *Ind. Eng. Chem. Prod. Res. Dev.* **1983**, *22* (2), 182–191.
(70) Hunter, E. P. L.; Lias, S. G. *J. Phys. Chem. Ref. Data* **1998**, *27* (3), 413–656.
(71) Chiavarino, B.; Crestoni, M. E.; Di Rienzo, B.; Fornarini, S. *J. Am. Chem. Soc.* **1998**, *120* (42), 10856–10862.
(72) Cerichelli, G.; Crestoni, M. E.; Fornarini, S. *J. Am. Chem. Soc.* **1992**, *114* (6), 2002–2009.
(73) Angelini, G.; Bucci, R.; Laguzzi, G.; Siciliano, C.; Segre, A. L. *J. Phys. Chem. A* **1998**, *102* (32), 6464–6469.
(74) Fornarini, S.; Crestoni, M. E. *Acc. Chem. Res.* **1998**, *31* (12), 827–834.

(75) Chiavarino, B.; Crestoni, M. E.; Fornarini, S. *J. Am. Chem. Soc.* **1999**, *121* (11), 2619–2620.
(76) Wang, Q.; Baird, M. C. *Macromolecules* **1995**, *28* (24), 8021–8027.
(77) Jordan, R. F.; LaPointe, R. E.; Bradley, P. K.; Baenziger, N. *Organometallics* **1989**, *8* (12), 2892–2903.
(78) Guram, A. S.; Jordan, R. F.; Taylor, D. F. *J. Am. Chem. Soc.* **1991**, *113* (5), 1833–1835.
(79) Eisch, J. J.; Piotrowski, A. M.; Brownstein, S. K.; Gabe, E. J.; Lee, F. L. *J. Am. Chem. Soc.* **1985**, *107* (24), 7219–7221.
(80) Burger, B. J.; Thompson, M. E.; Cotter, W. D.; Bercaw, J. E. *J. Am. Chem. Soc.* **1990**, *112* (4), 1566–1577.
(81) Thompson, M. E.; Baxter, S. M.; Bulls, A. R.; Burger, B. J.; Nolan, M. C.; Santarsiero, B. D.; Schaefer, W. P.; Bercaw, J. E. *J. Am. Chem. Soc.* **1987**, *109* (1), 203–219.
(82) Horton, A. D.; Orpen, A. G. *Organometallics* **1992**, *11* (1), 8–10.
(83) Ozerov, O. V.; Ladipo, F. T.; Patrick, B. O. *J. Am. Chem. Soc.* **1999**, *121* (34), 7941–7942.
(84) Galan, B. R.; Rovis, T. *Angew. Chem. Int. Ed.* **2009**, *48* (16), 2830–2834.
(85) Rosenthal, U.; Burlakov, V. V.; Arndt, P.; Baumann, W.; Spannenberg, A. *Organometallics* **2003**, *22* (5), 884–900.
(86) Rosenthal, U.; Lefeber, C.; Arndt, P.; Tillack, A.; Baumann, W.; Kempe, R.; Burlakov, V. V. *J. Organomet. Chem.* **1995**, *503* (2), 221–223.
(87) Thomas, D.; Peulecke, N.; Burlakov, V. V.; Heller, B.; Baumann, W.; Spannenberg, A.; Kempe, R.; Rosenthal, U.; Beckhaus, R. *Zeitschrift für Anorg. und Allg. Chemie* **1998**, *624* (5), 919–924.
(88) Ren, S.; Igarashi, E.; Nakajima, K.; Kanno, K.; Takahashi, T. *J. Am. Chem. Soc.* **2009**, *131* (22), 7492–7493.
(89) Liu, R.; Zhou, X. *Chem. Commun.* **2013**, *49* (31), 3171.
(90) Suresh, C. H.; Koga, N. *Organometallics* **2006**, *25* (8), 1924–1931.
(91) Xi, Z.; Sato, K.; Gao, Y.; Lu, J.; Takahashi, T. *J. Am. Chem. Soc.* **2003**, *125* (32), 9568–9569.
(92) Bunce, R. A.; Sullivan, J. P. *Synth. Commun.* **1990**, *20* (6), 865–868.
(93) Maercker, A.; Passlack, M. *Chem. Ber.* **1982**, *115* (2), 540–577.
(94) Maercker, A.; Passlack, M. *Chem. Ber.* **1983**, *116* (2), 710–723.
(95) Odian, G. G. *Principles of polymerization*, 4th ed.; John Wiley & Sons, Inc.: Hoboken, New Jersey, 2004.
(96) di Lena, F.; Quintanilla, E.; Chen, P.; Rosaaen, K. A.; Landis, C. R. *Chem. Commun.* **2005**, *169* (46), 5757.
(97) Quintanilla, E.; di Lena, F.; Chen, P. *Chem. Commun.* **2006**, *100* (41), 4309.
(98) Petros, R. A.; Norton, J. R. *Organometallics* **2004**, *23* (22), 5105–5107.
(99) Campos, J.; López-Serrano, J.; Peloso, R.; Carmona, E. *Chem. Eur. J.* **2016**, *22* (19), 6432–6457.
(100) Stahl, N. G.; Salata, M. R.; Marks, T. J. *J. Am. Chem. Soc.* **2005**, *127* (31), 10898–10909.
(101) Zimmermann, M.; Törnroos, K. W.; Anwander, R. *Angew. Chem. Int. Ed.* **2007**, *46* (17), 3126–3130.
(102) Bojer, D.; Venugopal, A.; Neumann, B.; Stammler, H.-G.; Mitzel, N. W. *Angew. Chem. Int. Ed.* **2010**, *49* (14), 2611–2614.

(103) Dietrich, H. M.; Ziller, J. W.; Anwander, R.; Evans, W. J. *Organometallics* **2009**, *28* (4), 1173–1179.
(104) Chen, E. Y.-X.; Abboud, K. A. *Organometallics* **2000**, *19* (26), 5541–5543.
(105) Ihara, E.; Young, V. G.; Jordan, R. F. *J. Am. Chem. Soc.* **1998**, *120* (32), 8277–8278.
(106) Liu, Z.; Somsook, E.; Landis, C. R. *J. Am. Chem. Soc.* **2001**, *123* (12), 2915–2916.
(107) Wolf, B. M.; Maichle-Mössmer, C.; Anwander, R. *Angew. Chem. Int. Ed.* **2016**, *55* (44), 13893–13897.
(108) Tanner, P. S.; Williams, R. A.; Hanusa, T. P. *Inorg. Chem.* **1993**, *32* (11), 2234–2235.
(109) Yamamoto, O. *J. Chem. Phys.* **1975**, *63* (7), 2988.

Chapter 5: Synthesis of Metal-Hydride Complexes

5.1 Introduction

The addition of hydrogen to unsaturated substrates is one of the most common chemical transformations employed in the production of commodity and fine chemicals alike.[1–4] The ability of metal-hydrides to overcome kinetic barriers to hydrogen transfer has encouraged widespread investigation into their organometallic chemistry.[5–7] However, despite the intensity with which they have been studied, the reactivity of metal-hydrides remains often unexpected.

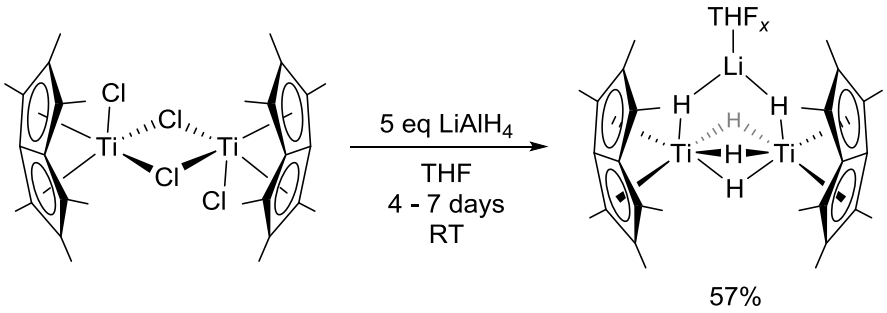
There are a number of synthetic strategies used to access metal-hydride complexes. With reduced metal complexes, oxidative addition of H_2 provides an atom economical route to install hydride ligands,[8–10] or alternatively alkyl, benzyl or aryl derivatives can undergo σ-bond metathesis, which proceeds with loss of protonated ligand.[11–13] With metal-halide complexes hydride transfer reagents can be employed,[14–17] which provide a useful lever to control the reaction outcome by tuning the hydride donor capacity of the H^- source.[18] Less commonly, reaction of metal-halide complexes with alkylating agents bearing β-hydrogens can allow for the synthesis of metal-hydride complexes following elimination.

In this chapter, two new metal-hydride complexes are synthesised by the reaction of hydride transfer reagents and Pn* metal-chloride precursors. The chemistry of $Pn^*_3Ti_3(\mu_2–H)_3(\mu_3–H)$, previously investigated within the group, is studied in further detail, and the reactivity of $(Pn^*TiCl)_2(\mu–Cl)_2$ and ^{n}BuLi is explored in pursuit of novel metal-hydride complexes.

5.2 Synthesis of $Pn^*_2Ti_2(\mu_2–H)_5Li.THF_x$

The reactivity of $(Pn^*TiCl)_2(\mu–Cl)_2$ with a variety of hydride transfer reagents was investigated. LiH, KH and $NaBH_4$ all displayed no reactivity in polar and non-polar solvents at both ambient and elevated temperatures. By contrast $LiAlH_4$ in THF was observed to successfully form hydride derivatives, consuming starting material and forming a number of new hydridic resonances in ^{1}H NMR spectra < 0 ppm. Despite repeated attempts, variation of the reaction conditions did not allow for the clean isolation of these intermediate-hydride species. However, allowing the reaction to proceed for 7

days with 5 eq. $LiAlH_4$ the eventual formation of a single product is observed spectroscopically, $Pn^*_2Ti_2(\mu_2–H)_5Li.THF_x$ (Scheme 5.1). Bulk synthesis was achieved by the reaction of $(Pn^*TiCl)_2(\mu–Cl)_2$ and 5 eq. $LiAlH_4$ in THF over 4 to 7 days. Extraction into benzene and filtration through celite was found essential to remove salts and unreacted $LiAlH_4$. Subsequent crystallisation from THF afforded yellow crystals of $Pn^*_2Ti_2(\mu_2–H)_5Li.THF_x$ in 57% yield, determined pure by elemental analysis.



Scheme 5.1. *Synthesis of $Pn^*_2Ti_2(\mu_2–H)_5Li.THF_x$*

The ^1H NMR spectrum in C_4D_8O displays 3 Pn*–*Me* resonances of relative integration 12:12:12 indicating the presence of a time-averaged mirror plane parallel to the Pn* bridgehead bond. The quantity of coordinated C_4H_8O in solution can be measured by integration of ^1H NMR spectra with values of $x = 0.8 – 1.1$ typically observed. The THF resonances display no significant deviation from their expected chemical shifts, indicating exchange of the donor ligand is fast on the NMR timescale. Three discrete hydride environments are observed of relative integration 2:2:1, (−1.09, −2.14 and −4.60 ppm) where the second of these resonances is well resolved as a quartet (J = 11.7 Hz). Confident assignment of these resonances and their coupling pathways was not possible. Selective NOE experiments were carried out in C_6D_6 with a drop of THF (*vide infra*), irradiating each hydride environment individually to examine any chemical exchange. No magnetisation transfer was observed indicating that the hydride ligands do not readily exchange, and that the structure in solution is rather static.

Single crystals of $Pn^*_2Ti_2(\mu_2–H)_5Li.THF_2$ suitable for X-ray diffraction were grown by slow-evaporation of a THF solution (Figure 5.1). Key bond metrics are discussed in more detail in section 5.5.

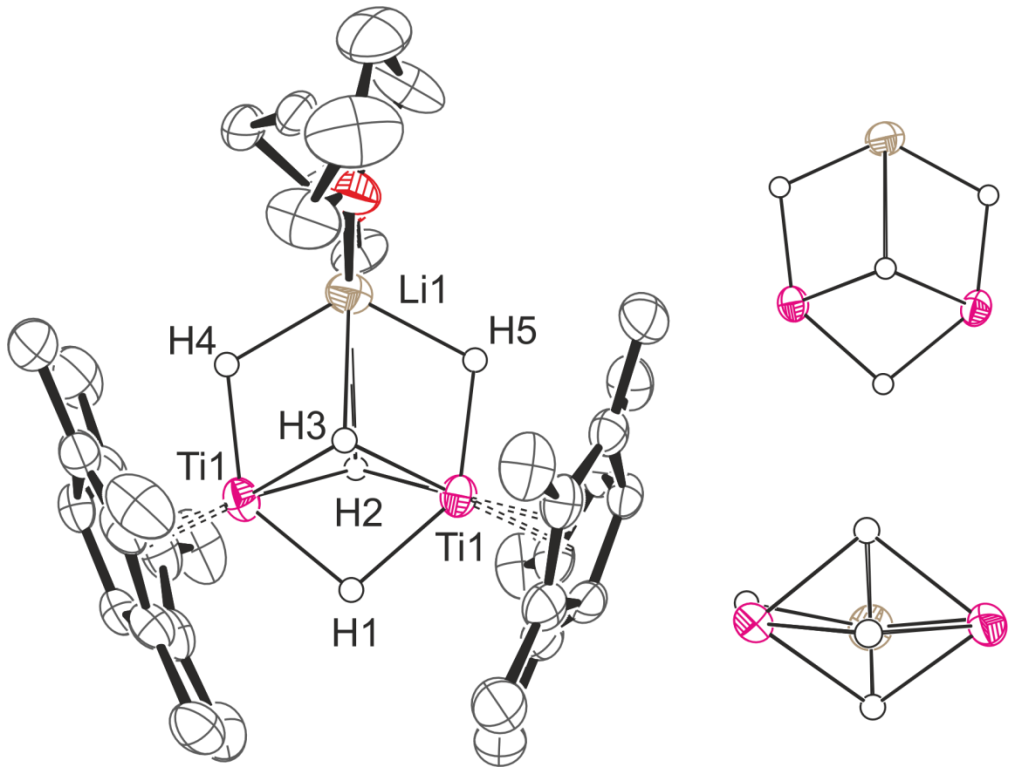


Figure 5.1. *Left: Thermal displacement ellipsoid plot (50% probability) of $Pn^*_2Ti_2(\mu_2–H)_5Li.THF_2$. Pn* and THF hydrogen atoms omitted for clarity. Right: Illustration of hexagonal bipyramidal geometry formed by the metal-hydride core.*

The structure is analogous to the zirconium (IV) complex, $Pn^*_2Zr_2(\mu_2–Cl)_5Li.THF_x$, and can be similarly rationalised in terms of its Lewis structure as two Ti(IV) centres with intercalated LiH. The central metal-hydride core forms a distorted hexagonal bipyramid, illustrated at the right of Figure 5.1, which appears to be a favoured structural motif of group 4 Pn* complexes. The exposed lithium ion at the cluster's apex is weakly bound to donor solvent, and the complex was serendipitously crystallised as a mono-THF solvate and a mixed THF-benzene solvate. Under prolonged dynamic vacuum additional THF can be removed, although it was not possible to completely desolvate the material. The lability of this coordinated solvent can complicate spectroscopic characterisation, so reactivity was generally studied in C_6D_6 with a drop of added C_4D_8O, or else in neat C_4D_8O. Alternatively, 1,4–dioxane was found to coordinate more strongly, producing similar spectroscopic features to the bis(THF) solvate. Single crystals of the dioxane complex were obtained from slow evaporation of a benzene solution, with the structure shown in Figure 5.2.

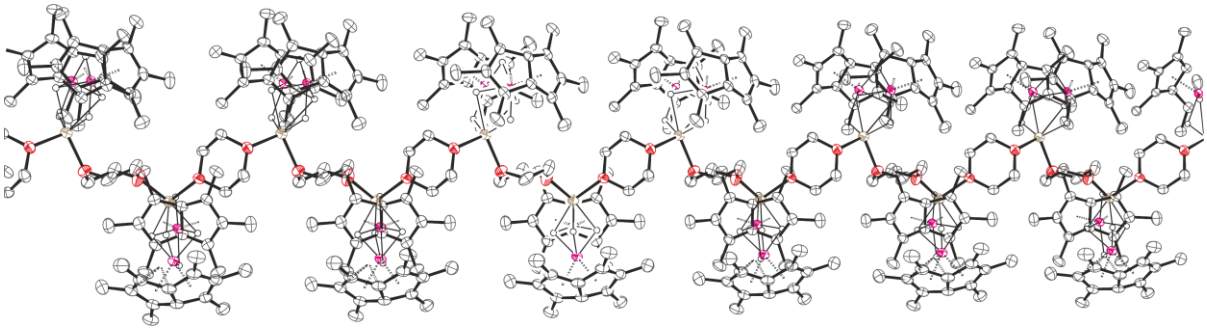


Figure 5.2. *Thermal displacement ellipsoid plot (50% probability) of* $[Pn^*_2Ti_2H_5Li.dioxane]_n$. *Pn* and dioxane H atoms omitted for clarity.*

The bidentate donor bridges across two neighbouring lithium ions forming a 1D polymer composed of metal-hydride clusters and dioxane linker units. Beyond the polymeric nature of this material, the key bond lengths and angles are similar to the bis(THF) complex, and are provided in appendix A.

The observation of hexagonal bipyramidal geometry contrasts with the preference of early transition metal Cp_2M fragments to adopt the more familiar bent metallocene structure found for Cp_2ZrCl_2.[19–22] Indeed Cp_2M fragments with vacant coordination sites display a preference for planar co-ligand bonding, as is observed for Cp_2TaH_3,[23,24] rather than the four-fold co-ligand coordination that permits formation of this trimetallic bipyramid. This is a result of differences in the frontier orbitals of Cp_2Ti *vs* Pn*Ti fragments.

DFT calculations were carried out on $Pn^*_2Ti_2(\mu_2–H)_5Li.THF_2$ at the B3LYP[25–27] level of theory, with Ahlrich's triple-ζ basis set employed for heavy elements and hydride ligands.[28–30] Geometry optimisations reproduced the experimental data well, although some variation was observed in the orientation of coordinated THF. In the following discussion the molecular symmetry is approximated as C_{2v}, which is valid in the absence of coordinated THF and assumes this coordinated solvent has negligible effect on the frontier molecular orbitals. The hexagonal plane is primarily supported by two orbitals of the Pn*Ti fragment: one of a_1 symmetry with $d_{x^2-y^2}$ and d_{z^2} character, projecting electron density above and below the plane bisecting the Pn*–bridgehead bond, bonding to the whole hydride system, and a second of b_1 symmetry, predominantly d_{yz} in character. Unlike analogous Cp_2Ti fragments, an orthogonal b_1 symmetric orbital is also accessible, which supports Ti−H2/H3 bonding, securing the hydride caps of the hexagonal bipyramid

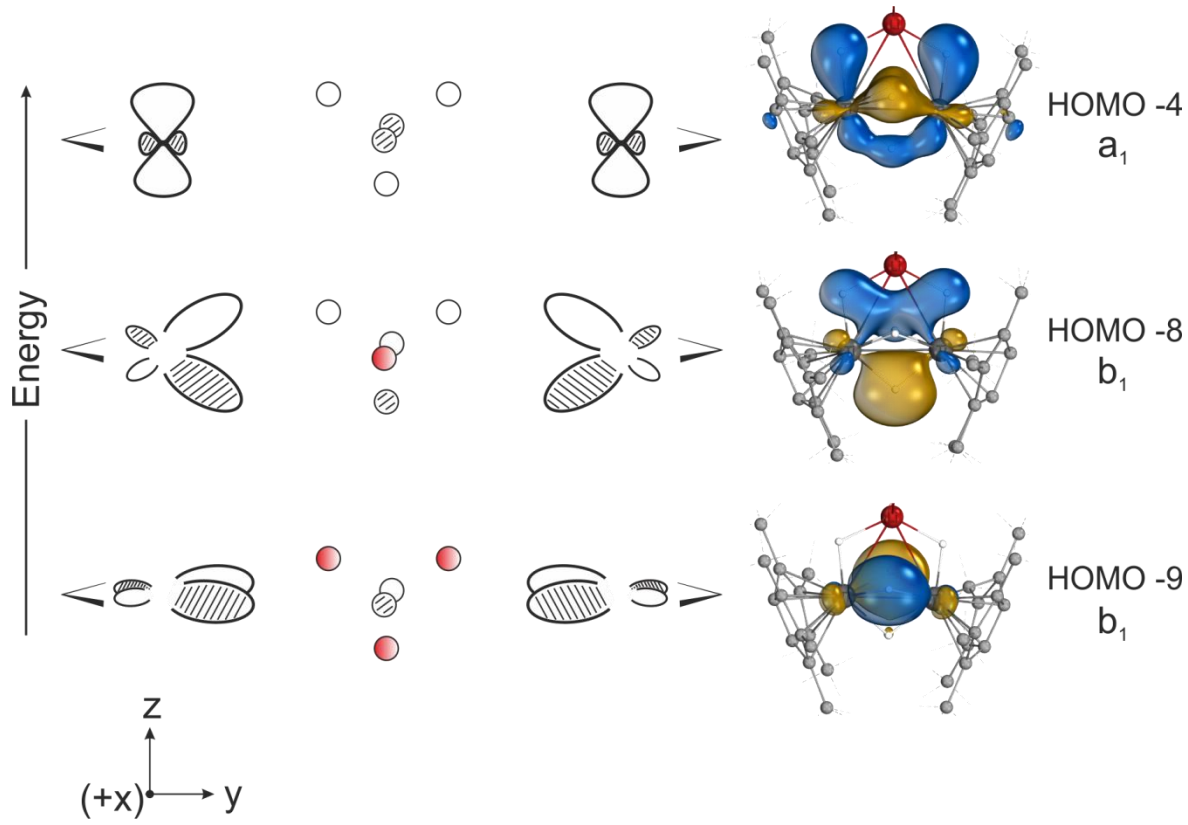


Figure 5.3. *Primary Ti–H bonding orbitals calculated for $Pn^*_2Ti_2(\mu_2–H)_5Li.THF_2$, illustrating the projection of electron density in two orthogonal planes: zy (HOMO -4, HOMO -8) and xy (HOMO -9). Red circles represent hydrogen atoms uninvolved in bonding for each MO.*

(Figure 5.3). This geometry, rarely encountered for Cp_2Ti, is therefore a consequence of electron density projected in two orthogonal planes. Interestingly, the calculations also predict a metal-metal bonding interaction between the titanium centres, with a calculated Mayer bond order of 0.616.[31,32] Indeed, the distance between the two titanium ions of 2.79 Å (2.82 Å calculated) is well below the sum of the Van der Waals radii (4.30 Å for titanium). No molecular orbitals were found to uniquely describe a metal-metal bonding interaction, with this orbital overlap clearly mediated by bridging hydride ligands.

The observed formation of a stable Ti(IV)-hydride is rather unusual, particularly given its synthesis from $LiAlH_4$. Often Ti(IV)-hydrides decompose *via* loss of H_2 to give reduced titanium products as is observed for $Cp^*_2TiH_2$, which although stable as a solid, decomposes in pentane solutions to form Cp^*_2Ti.[10,33–35] Moreover $LiAlH_4$ is generally observed to form reduced titanium-hydride complexes. For example $Cp^*_2TiH(Cl)$ reacts with $LiAlH_4$ to give the Ti(III) derivative, $Cp^*_2Ti(\mu–H_2)AlH_2.Et_2O$,[36–38] while under more

forcing conditions $Cp^{Me4}{}_2TiCl_2$ reacts with $LiAlH_4$ to form the allyl-diene complex shown in Figure 5.4.[39,40] Indeed, $LiAlH_4$ is certainly a viable reducing agent for $[Pn^*TiCl(\mu–Cl)]_2$, which is discussed further in Chapter 6. It may be that this hexagonal bipyramidal motif offers a degree of kinetic stabilisation with respect to H_2 loss and reduction of the metal centres; the Pn* is less sterically demanding than a corresponding bis(Cp) fragment, and contributes two fewer electrons. Steric protection by intercalation of LiH, and alleviation of electron deficiency by formation of 4 (μ–H) bonds may favour formation of the Ti(IV)–Ti(IV) dimer over any reduced alternative.

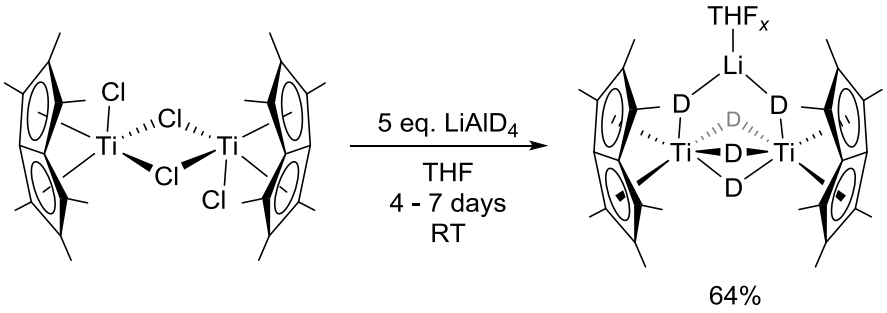


Figure 5.4. *Illustration of reduced titanium-hydride complexes formed by reaction of Cp*TiHCl and Cp*TiCl₂ with LiAlH₄.*

5.3 Reactivity of $Pn^*{}_2Ti_2(\mu_2–H)_5Li.THF_x$

The complex is surprisingly inert towards many small molecules. When exposed to stoichiometric or excess 2-butyne in C_6D_6/THF, no reaction was observed up to 60 °C by ^1H NMR spectroscopy. Similarly, the complex was found to be inert towards alkenes: *cis*–1,2–diphenylethylene, cyclohexene and ethylene did not react. Under 1 bar D_2 trace amounts of HD can be observed by ^1H NMR spectroscopy (4.51 ppm, t, $^1J_{H\text{-}D}$ = 43 Hz) characteristic of exchange. However, after heating to 60 °C for 4 days the extent of deuterium incorporation was still insufficient to be resolved by ^2D NMR spectroscopy. The sluggish reactivity of $Pn^*{}_2Ti_2(\mu_2–H)_5Li.THF_x$ may be a result of the crowded coordination environment around the titanium centres preventing approach of these small molecules.

Although the deuteride complex could not be formed by H–D exchange, its synthesis was achieved by the reaction of $LiAlD_4$ in THF over 4 – 7 days. Following extraction into benzene and subsequent crystallisation from THF, $Pn^*{}_2Ti_2(\mu_2–D)_5Li.THF_x$ was obtained as a crystalline yellow solid in 64% yield, determined pure by elemental analysis (Scheme 5.2).



Scheme 5.2. *Synthesis of Pn*$_2$Ti$_2$(μ$_2$–D)$_5$Li.THF$_x$.*

The ^{1}H NMR spectrum displays the same Pn*–*Me* resonances unshifted relative to the hydride analogue, with no peaks corresponding the complex observed below 2.02 ppm. *x* was found to be 0.96 by integration against Pn*–*Me* resonances, with no significant deviation in the THF chemical shift observed (Figure 5.5). The deuteride resonances were observed by ^{2}D NMR spectroscopy at −1.06, −2.12 and −4.49 ppm (c.f. −1.09, −2.14 and −4.60 ppm for the corresponding hydride resonances), demonstrating the successful synthesis of the isotopically labelled complex.

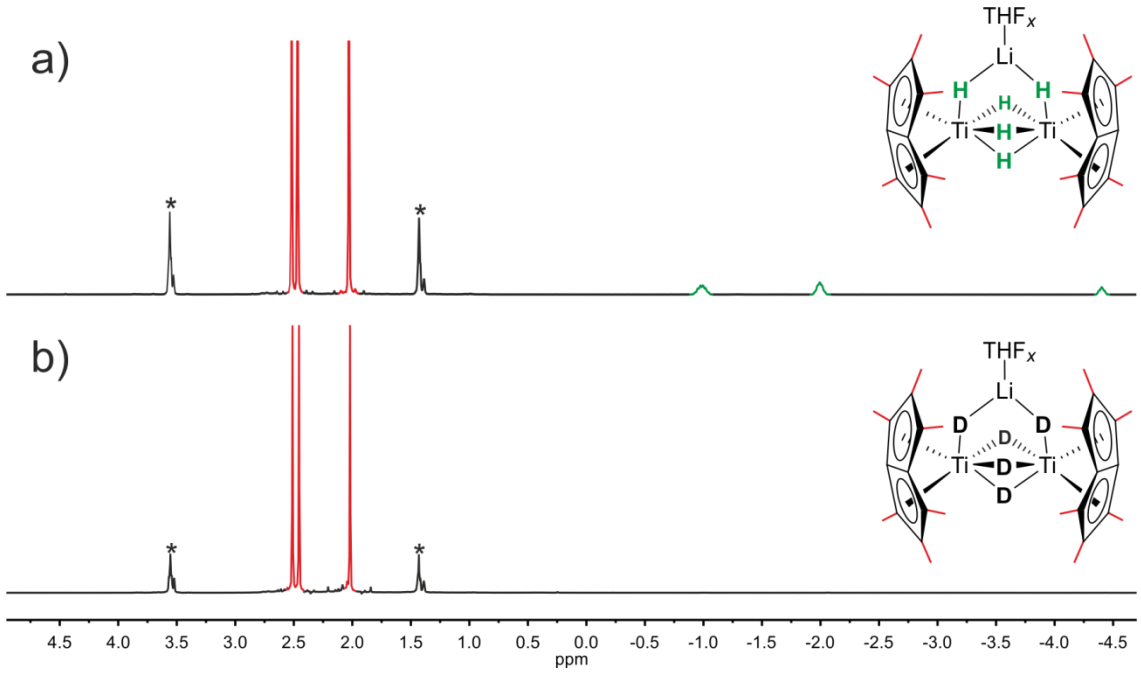


Figure 5.5. *^{1}H NMR spectra (400 MHz, 298 K, C$_6$D$_6$/C$_4$D$_8$O 9:1) of a) Pn*$_2$Ti$_2$(μ$_2$–H)$_5$Li.THF$_x$.b) Pn*$_2$Ti$_2$(μ$_2$–D)$_5$Li.THF$_x$. * = THF residual from synthesis.*

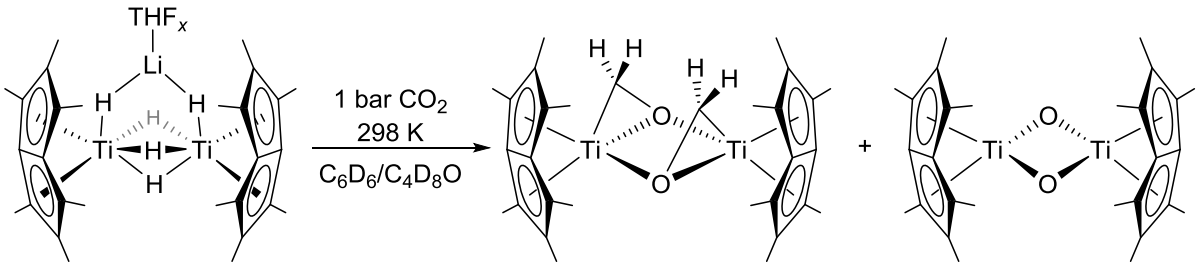
Comparison of FTIR spectra of Pn*$_2$Ti$_2$(μ$_2$–H)$_5$Li.THF$_x$ and Pn*$_2$Ti$_2$(μ$_2$–D)$_5$Li.THF$_x$ allows for the definitive assignment of Ti–H/D stretching frequencies. An intense peak at

1507 cm^{-1} is observed for the hydride complex, which is shifted to 1099 cm^{-1} on perdeuteration, which is in good agreement with the value calculated using the reduced mass formula (1077 cm^{-1}). A second hydride-stretch observed at 1291 cm^{-1} is red-shifted to 941 cm^{-1}, in close agreement with the predicted value of 922 cm^{-1}.

$Pn^*_2Ti_2(\mu_2–H)_5Li.THF_x$ was found to be more reactive towards oxygen-containing substrates. Addition of CO leads to rapid consumption of the starting material and a colour change from brown to red. However, ^1H NMR spectroscopy of the product indicates decomposition, with the formation of a broad featureless resonance at approximately 1.8 ppm, presumably resulting from indiscriminate oxide formation.

Addition of CO_2 to $Pn^*_2Ti_2(\mu_2–H)_5Li.THF_x$ leads to consumption of the starting material and colour change from brown to red. 6 Pn*–*Me* resonances are observed between 1.55 and 2.10 ppm, however HMBC NMR spectra indicate the presence of two discrete η^8–Pn* rings in a 1:1 ratio contributing 3 Pn*–*Me* resonances each. Alongside this, two new deshielded multiplets are resolved at 4.55 and 5.45 ppm. These were confirmed as C*H*$_2$ environments by gradient selective HSQC experiments, with both protons coupling to a single carbon environment at 90.3 ppm, as well as mutually coupling in COSY NMR spectra. On the basis of relative integrations, it can be proposed that the products are dimeric, and therefore the environments at 4.55 and 5.45 ppm correspond to two protons each. Addition of CO_2 to $Pn^*_2Ti_2(\mu_2–D)_5Li.THF_x$ leads only to the observation of 6 new Pn*–*Me* resonances in ^1H NMR spectra, with no deshielded resonances resolved, confirming their derivation from Ti–*H* transfer.

These data are consistent with the formation of a dimeric titanaoxirane, in which both methylene groups are bound to the same face of the Ti–O plane (Scheme 5.3). The predicted C_2 axis perpendicular to the Ti–O plane would account for 3 Pn*–*Me* resonances observed spectroscopically, which in combination with the conformational rigidity of the oxirane moiety provides a rationalisation for observation of two diasteropic proton environments. It can then be inferred that the remaining 3 Pn*–*Me* resonances arise from the concomitant formation of $[Pn^*Ti(\mu–O)]_2$.



Scheme 5.3. *Reactivity of Pn*$_2$Ti$_2$(μ_2–H)$_5$Li.THF$_x$ with CO$_2$.*

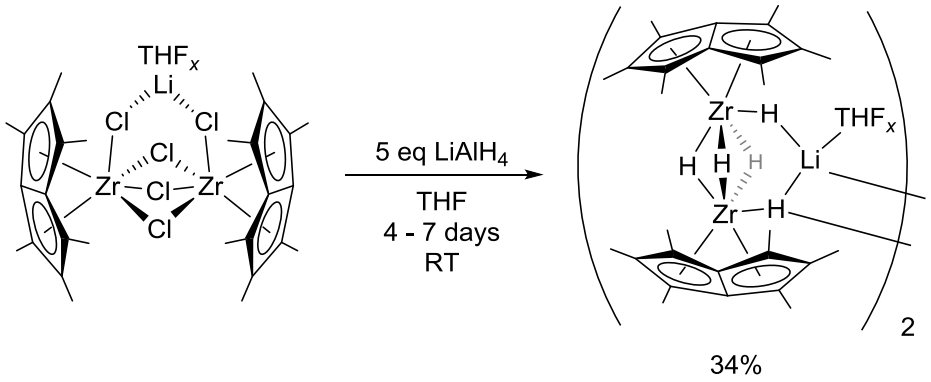
Similar oxirane products have previously been observed in the reaction of zirconium aryl complexes with CO, although fewer titanium examples are described in the literature. One of the few crystallographically characterised titanaoxiranes was obtained from reaction of the butadiene complex, Cp*Ti(2,3–dimethyl–1,3–butadiene)Cl, and CO to form [Cp*Ti{μ–OCCH$_2$C(Me)=C(Me)CH$_2$}Cl]$_2$, in contrast to the zirconium and hafnium analogues, which form [Cp*M(O)Cl]$_n$.[41] Cp$_2$ZrPh$_2$ similarly reacts with CO to form diphenyl substituted zirconaoxiranes,[42] while COTZr(mes)$_2$ displays analogous CO insertion chemistry with the bulkier mesityl ligand.[43] More recently, work in this laboratory has described the reactivity of Pn*TiMe$_2$ and CO, which was observed to proceed with formation of the titanaoxirane complex, [Pn*Ti(μ–η^1(O):η^2–OC(Me)$_2$)]$_2$, among other unidentified byproducts.[44]

It is very unusual, however, to observe metalaoxirane formation from CO$_2$. An analogy can perhaps be found in the studies of Kilpatrick *et al*. on the reductive deoxygenation of CO$_2$ with (μ:η^5,η^5–Pn†)$_2$Ti$_2$. Formation of the di(carbonyl) complex, (μ:η^5,η^5–Pn†)$_2$Ti$_2$(CO)$_2$, was accompanied by formation of the oxo-bridged dimer, [η^8–Pn†Ti(μ–O)]$_2$.[45,46] Unfortunately, attempts to crystallise either Pn* complex from benzene and THF were unsuccessful, potentially due in part to the presence of two components in solution.

5.4 Synthesis of Pn*$_2$Zr$_2$(μ_2–H)$_5$Li.THF$_x$

Reacting the zirconium halide precursor, Pn*$_2$Zr$_2$(μ_2–Cl)$_5$Li.THF$_x$, with LiH, KH, and NaBH$_4$ in polar and non-polar solvents at both ambient and elevated temperatures did not allow for the synthesis of metal-hydride derivatives. As observed for titanium, 5 eq. LiAlH$_4$ in THF over 7 days forms a single product by NMR spectroscopy, during which

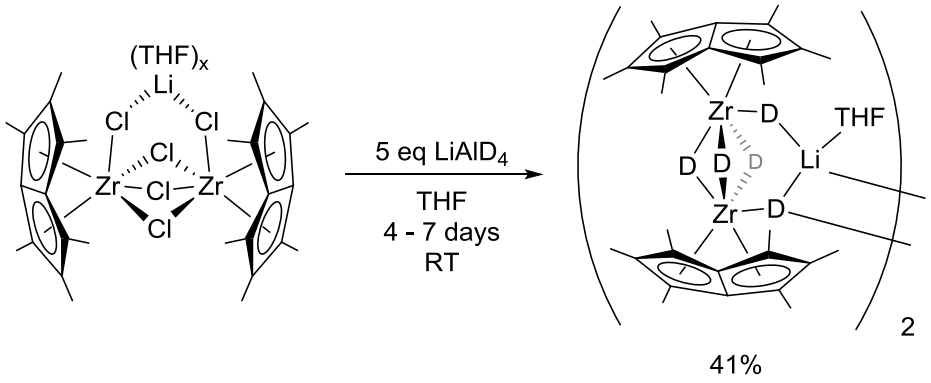
time a number of unidentified hydride intermediates could be observed. Attempts to isolate these intermediates were unsuccessful. Following an analogous procedure as described for $Pn^*_2Ti_2(\mu_2–H)_5Li.THF_x$, $[Pn^*_2Zr_2(\mu_2–H)_4(\mu_3–H)Li.THF_x]_2$ could be isolated in 34% yield as a pale yellow powder (Scheme 5.4).



Scheme 5.4. *Synthesis of* $[Pn^*_2Zr_2(\mu_2–H)_4(\mu_3–H)Li.THF_x]_2$

The NMR spectrum qualitatively resembles the titanium congener, with 3 Pn*–*Me* resonances observed indicating the presence of a time-averaged mirror plane parallel to the Pn*–bridgehead bond. The hydride resonances are somewhat shielded relative to the titanium analogue, resonating at 1.83, 1.67 and −0.36 ppm of relative integrations 2:2:1 (c.f. −1.09, −2.14 and −4.60 ppm for $Pn^*_2Ti_2(\mu_2–H)_5Li.THF_x$). The implied C_{2v} symmetry indicates the formation of a dimeric species in solution, as observed for $Pn^*_2Ti_2(\mu_2–H)_5Li.THF_x$. Values for *x* were determined by integration of C_4H_8O and Pn*–*Me* resonances, and were found to vary between 0.5 and 0.8. Minimal deviation from the expected chemical shift of THF is observed suggesting facile exchange of the coordinated donor on the NMR timescale. Selective NOE experiments at identical mixing times employed in section 5.2 indicate facile exchange between the two hydride environments at 1.83 and -0.36 ppm, while magnetisation transfer to the third was not observed. This corresponds to exchange between H2/H3 and H4/H5 (Figure 5.6), while coordination of H1 remains static on the NMR timescale. This observation is slightly unexpected given the stronger metal-ligand bonds expected for zirconium relative to titanium, but may result from strain associated with the radially expanded zirconium d-orbitals accommodating a hexagonal bipyramidal geometry.

In light of this chemical exchange, it is perhaps unsurprising to note comparatively facile D_2 incorporation, with complete disappearance of hydride resonances observed after 4 days under 1 bar D_2 at room temperature. This is accompanied by HD formation, which can be clearly resolved by ^{1}H NMR spectroscopy. The deuteride complex was synthesised on a preparative scale by the reaction of $Pn^*_2Zr_2Cl_5Li.THF_x$ and $LiAlD_4$ in THF. Extraction into benzene and crystallisation from THF allowed for the isolation of $[Pn^*_2Zr_2(\mu_2–D)_4(\mu_3–D)Li.THF_x]_2$ in 41% yield as a yellow powder (Scheme 5.5).



Scheme 5.5. *Synthesis of $[Pn^*_2Zr_2(\mu_2–D)_4(\mu_3–D)Li.THF_x]_2$.*

The ^{1}H NMR spectrum of $Pn^*_2Zr_2(\mu_2–D)_5Li.THF_x$ closely resembles that of the hydridic analogue, with three Pn*–*Me* resonances observed at 2.44, 2.42 and 2.05 ppm, (c.f. 2.49, 2.46 and 2.08 for $Pn^*_2Zr_2(\mu_2–H)_5Li.THF_x$). The THF content, *x*, was calculated as 0.79, and no significant perturbation of its chemical shift was observed. Two deuteride resonances can be observed by ^{2}D NMR spectroscopy at 1.75 and −0.43 ppm, with a third peak at approximately 1.58 ppm partially obscured by solvent. FTIR spectra of $[Pn^*_2Zr_2(\mu_2–H)_5Li.THF_x]_2$ display a peak at 1258 cm^{-1}, with a corresponding peak at 895 cm^{-1} found for $[Pn^*_2Zr_2(\mu_2–D)_5Li.THF_x]_2$, in good agreement with the value predicted by the reduced mass formula of 910 cm^{-1}.

Single crystals suitable for X-ray diffraction were grown by slow evaporation of a THF solution, which identified the product as $[Pn^*_2Zr_2(\mu_2–H)_4(\mu_3–H)Li.THF]_2$ (Figure 5.6). The solid-state structure is C_1 symmetric, bridging through two apical Li–H fragments, each stabilised by a single THF molecule. The basic structure of the metal-hydride core consists of edge-fused distorted hexagonal bipyramids, similar to those found in $Pn^*_2Ti_2(\mu_2–H)_5Li.THF_2$, albeit with more extensive puckering observed, which may be a

consequence of dimerisation. A comparison of key bond lengths and angles are provided in Table 5.1 for $Pn^*_2Ti_2(\mu_2–H)_4(\mu_3–H)Li.THF_2$ and $[Pn^*_2Zr_2(\mu_2–H)_4(\mu_3–H)Li.THF]_2$, along with $Pn^*_2Zr_2(\mu_2–Cl)_5Li.THF_2$,[47] which also displays this hexagonal bipyramid motif.

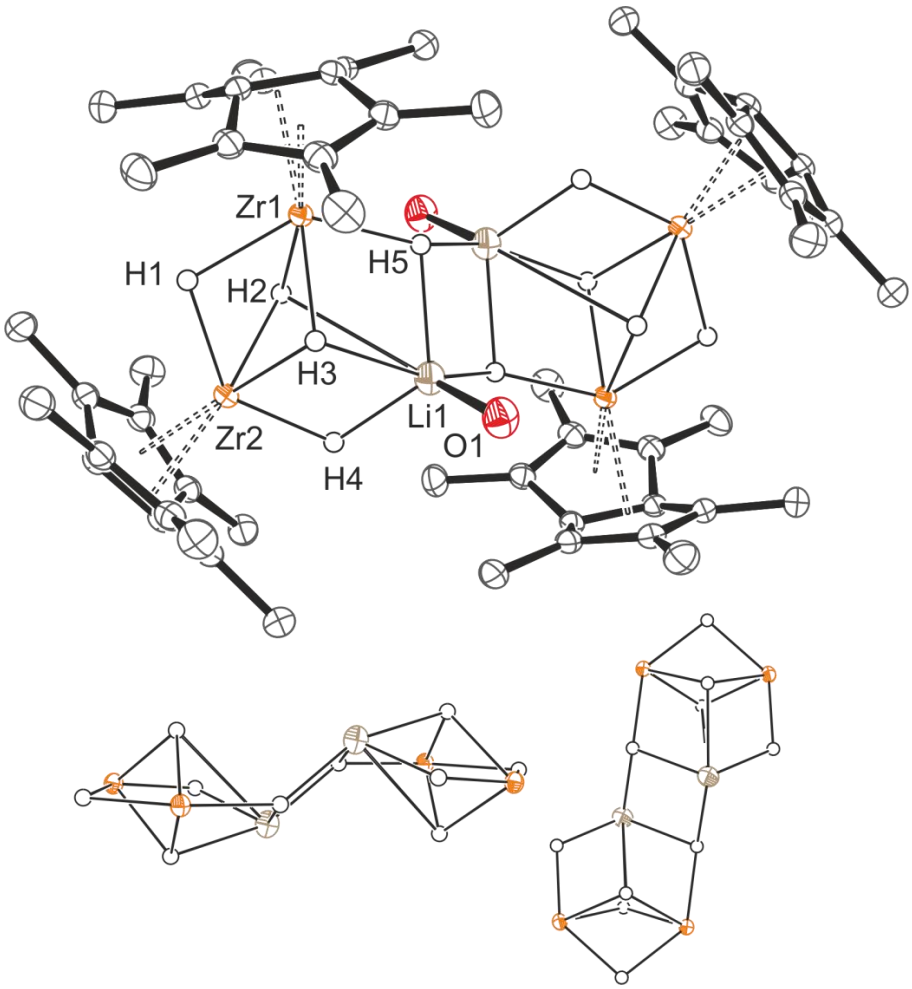


Figure 5.6. *Top: Thermal displacement ellipsoid plot (50% probability) of $[Pn^*_2Zr_2(\mu_2–H)_4(\mu_3–H)Li.THF]_2$. THF carbon atoms, Pn* and THF hydrogen atoms omitted for clarity. Bottom: Illustrations of edge-fused hexagonal bypramidal geometry adopted by the metal hydride core.*

5.5 Comparison of solid-state structures, $Pn^*_2Ti_2(\mu_2–H)_5Li.THF_2$ and $[Pn^*_2Zr_2(\mu_2–H)_4(\mu_3–H)Li.THF]_2$

	$Pn^*_2Ti_2(\mu_2–H)_5$ $Li.THF_2$	$[Pn^*_2Zr_2(\mu_2–H)_4$ $(\mu_3–H)Li.THF]_2$	$Pn^*_2Zr_2(\mu_2–Cl)_5$ $Li.THF_2$[47]
Fold Angle	35.52(10)	32.13(8)	30.0(3)
	34.17(12)	31.25(7)	30.0(3)
M–Pn^*_{cent}	1.9442(10)	2.0965(7)	2.1095(3)
M–H1 or Cl1	1.83(2)	2.01(2)	2.6431(14)
M–H2/3 or Cl2/3	1.86(3)	2.06(2)	2.6524(13)
M–H4 or Cl4	1.79(3)	1.90(2)	2.5916(12)
M–H5 or Cl5	1.86(3)	2.00(2)	2.5701(13)
H/Cl2–$Plane_{H1/4/5}$	1.08(3)	1.28(3)	1.8103(14)
H/Cl3–$Plane_{H1/4/5}$	1.10(3)	1.17(3)	1.8378(15)
Puckering: $\Sigma\lvert\phi\rvert^a$	72.7991(14)	113.3(16)	143.78(4)
Circumference[b]	10.88	11.9	15.16
M–M[c]	2.7874(5)	3.0816(4)	3.6549(9)

Table 5.1. *Comparison of selected bond lengths (Å), angles (°) and other pertinent structural metrics. a) Puckering, given in degrees, is the sum of the magnitude of the dihedral angles around the perimeter of the metal-hydride/chloride core. For a planar structure this value is 0°. b) The circumference refers to the sum of the bond lengths around the perimeter of the metal-hydride core. c) M–M refers to Ti–Ti or Zr–Zr distance.*

Contraction of ionic radii from zirconium to titanium leads to a large increase in the fold angle measured for $Pn^*_2Ti_2(\mu_2–H)_5Li.THF_2$, along with a decrease in M–Pn^*_{cent} and M–H bond lengths. This leads to compression of the hexagonal bipyramid, which can be straightforwardly visualised by considering both the decreased circumference of the metal-hydride core, as well as the decreased H2/3–$Plane_{H1/4/5}$ bond lengths corresponding to narrowing of the pyramidal apices. Puckering of the hexagonal plane can be measured by summing the dihedral angles around the central metal-hydride/chloride core, where a value of zero corresponds to a planar structure. As would be expected based on a qualitative examination of the structure, more extensive puckering is observed for $[Pn^*_2Zr_2(\mu_2–H)_4(\mu_3–H)Li.THF]_2$, although given the further increase observed for $Pn^*_2Zr_2(\mu_2–Cl_5)Li.THF_2$, this is probably not simply a consequence of the former's greater nuclearity.

The zirconium III/IV redox couple is less accessible than for titanium (first ionisation energies: Ti = 4175, Zr = 3313 kJ/mol),[48] which leads to the observation of less facile reduction with $LiAlH_4$. $Cp^*_2ZrCl_2$ and $LiAlH_4$ react to give the Zr(IV) complex, $Cp^*_2ZrH(\mu\text{–}H)_2AlH_2$, which can be further reacted with ^{n}BuLi to form the anionic zirconocene hydride, $[Cp^*_2ZrH_3]^-$.[49] As expected, the three hydride ligands in these complexes are arranged in a co-planar fashion, due to the projection of Cp^R_2Zr frontier orbitals in a single plane, in contrast to those observed for $[Pn^*_2Zr_2(\mu_2\text{–}H)_4(\mu_3\text{–}H)Li.THF]_2$. While the Cp analogue is less stable,[50] its synthesis from Cp_2ZrCl_2 and $LiAlH_4$ can be realised by inclusion of an amine donor to stabilise the complex, forming $Cp_2ZrH(\mu\text{–}H)_2AlH_2(NR_3)$.[51]

Reduced species can be accessed from Cp_2ZrCl_2 by addition of substoichiometric amounts of $CoBr_2$ alongside $LiAlH_4$, which allows for the formation of $[(Cp_2Zr)_2(\mu\text{–}H)](\mu\text{–}H)_2AlCl_2$, in which the Zr-H-Al core displays a hexagonal planar geometry similar to that reported for the Pn* complexes discussed in this chapter, albeit without capping hydride ligands.[52] Interestingly, a hexagonal bipyramidal geometry has been reported in a zirconocene-hydride complex previously. Hydrogenation of the doubly silylene-bridged *ansa*-zirconocene, $[\{(Me_2Si)_2(\eta^5\text{–}C_5H_3)_2\}ZrMe_2]$ forms the structurally characterised trimetallic hydride cluster, $[\{(Me_2Si)_2(\eta^5\text{–}C_5H_3)_2\}Zr]_3(\mu_3\text{–}H)_2(\mu_2\text{–}H)_3$,[53] although use of the hydride transfer reagent, $NaBEt_3H$, produces the more commonly observed zirconium-hydride motif, $[\{(Me_2Si)_2(\eta^5\text{–}C_5H_3)_2\}ZrH]_2(\mu_2\text{–}H)_2$ (Figure 5.7).[54] Unfortunately due its insolubility no further characterising data is reported for $[\{(Me_2Si)_2(\eta^5\text{–}C_5H_3)_2\}Zr]_3(\mu_3\text{–}H)_2(\mu_2\text{–}H)_3$.

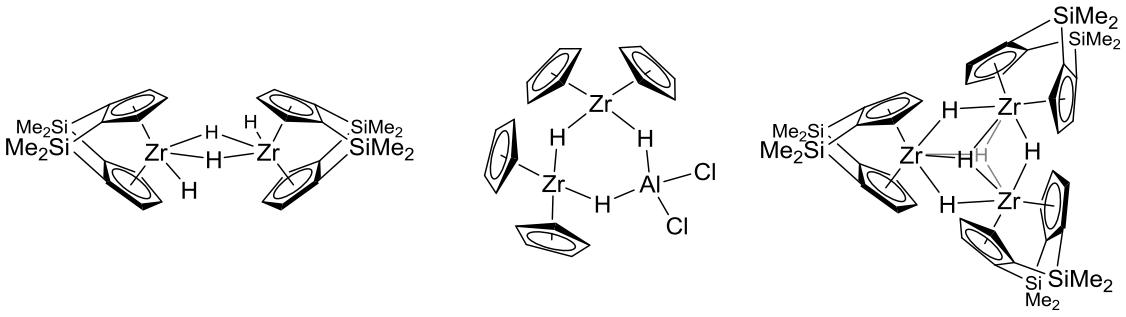


Figure 5.7. *Left: illustration of the more commonly encountered zirconocene-hydride motif. Middle, right: zirconocene-hydride complex displaying hexagonal and hexagonal bipyramidal geometries.*

DFT calculations were carried at the B3LYP level theory using the same basis set as for $Pn^*_2Ti_2(\mu_2–H)_5Li.THF_2$, which reproduced the experimental data adequately. Similar metal-metal bonding interactions are predicted with Zr–Zr bond orders of 0.463 and 0.468, lower than those computed for the titanium analogue. This mirrors an increase in the intermetallic distance to 3.12 Å (3.08 Å observed experimentally *vs.* 2.79 Å for $Pn^*_2Ti_2(\mu_2–H)_5Li.THF_2$), which remains well below the sum of the van der Waals radii for zirconium, 4.60 Å. As before no molecular orbital was calculated to uniquely describe this bonding interaction, with the lower symmetry resulting from dimerisation leading to greater orbital mixing.

5.6 Synthesis and characterisation of $Pn^*_3Ti_3(\mu_2–H)_3(\mu_3–H)$

Previous work carried out by Dr. Robert Cooper on the hydrogenation of $Pn^*Ti(CH_2SiMe_3)_2$ described the formation of a diamagnetic hydride cluster formulated as the mixed-valence complex, $Pn^*_3Ti_3(\mu_2–H)_3(\mu_3–H)$ (Ti(III), Ti(III), Ti(IV)).[44] Single crystal X-ray diffraction data was collected, but was of insufficient quality to locate the hydride atoms, and some ambiguity remained about its formation, reactivity and bonding. Its synthesis was therefore reinvestigated to study the complex in greater detail.

The purple titanium alkyl precursor, $Pn^*Ti(CH_2SiMe_3)_2$, was synthesised by established procedures.[44] On exposing a C_6D_6 solution of $Pn^*Ti(CH_2SiMe_3)_2$ to H_2 the solution turned black-green over the course of 48 hours. ^{1}H NMR spectra indicated the consumption of the starting material and the formation of new diamagnetic and paramagnetic species alongside $SiMe_4$ (Figure 5.8, the complex's paramagnetism is discussed further in section 5.7). Only after drying the sample under dynamic vacuum was a clean, diamagnetic complex obtained, with 2 Pn*–*Me* resonances resolved at 2.31 and 2.16 ppm, alongside a single hydride resonance at −2.91 ppm, in agreement with previously reported data for $Pn^*_3Ti_3(\mu_2–H)_3(\mu_3–H)$ (Figure 5.8).[44]

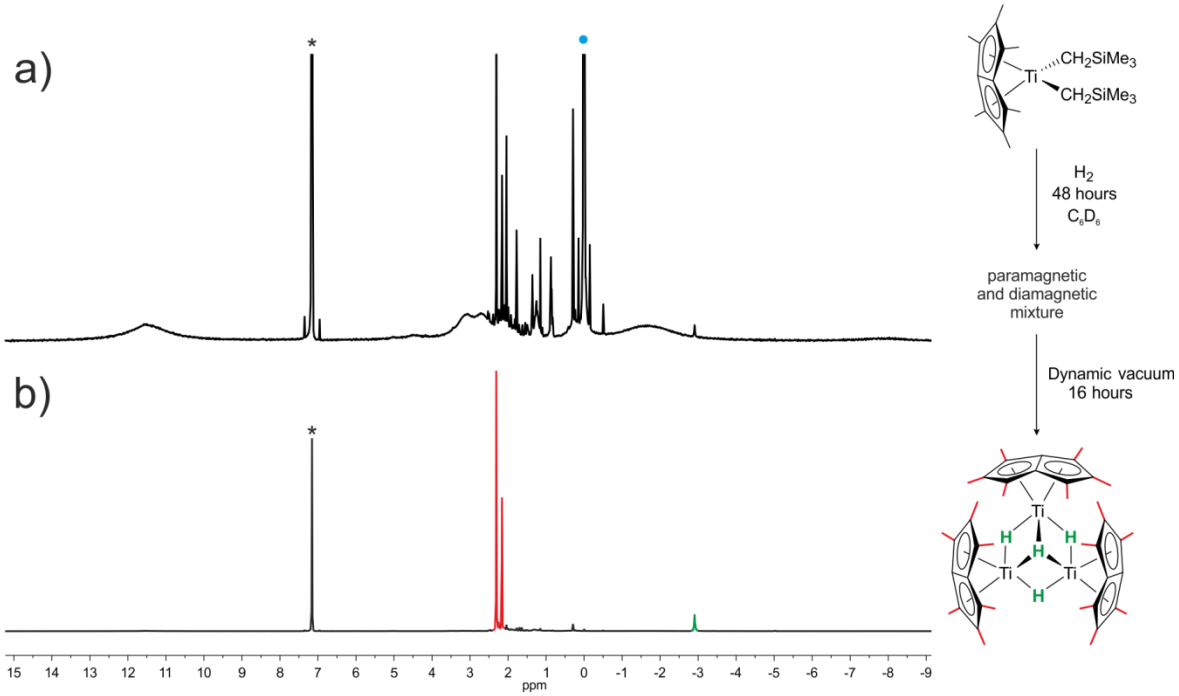
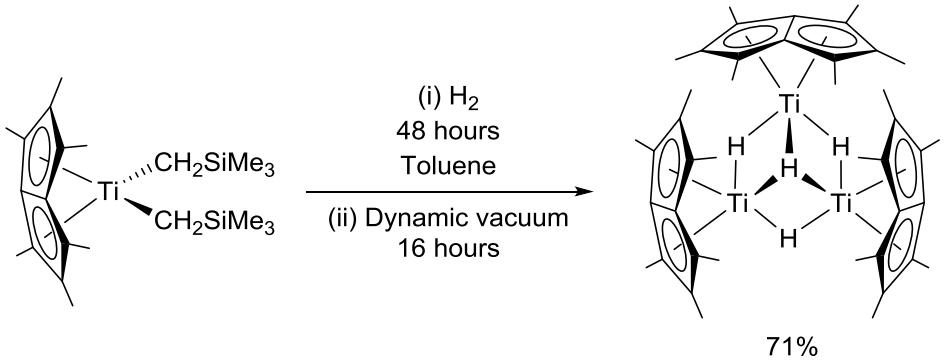


Figure 5.8. *^{1}H NMR spectra (400 MHz, 298 K, C_6D_6) of a) Pn*Ti(CH_2SiMe_3)$_2$ under 1 bar H_2, b) the same sample after exposure to dynamic vacuum for 16 hours. * = C_6D_6 solvent residual signals, blue circle = $SiMe_4$.*

This transformation is reversible; readmission of H_2 produces identical ^{1}H NMR spectra, which following exposure to dynamic vacuum and redissolution in C_6D_6 reproduces the diamagnetic hydride complex unchanged. Attempts to decoalesce the diamagnetic hydride resonances and gain insight into fluxional hydride-exchange by VT NMR spectroscopy were unsuccessful, with no peak separation observed in the range 193 – 300 K in C_7D_8.

Synthesis at a preparative scale was achieved by hydrogenation of Pn*Ti(CH_2SiMe_3)$_2$ in toluene for 48 hours, before drying under dynamic vacuum overnight. The product was isolated as an air-sensitive, black crystalline solid in 71% yield, with bulk purity confirmed by combustion analysis (Scheme 5.6).



Scheme 5.6. *Synthesis of Pn*$_3$Ti$_3$(μ_2–H)$_3$(μ_3–H).*

Single crystals suitable for an X-ray diffraction study were grown from slow evaporation of a benzene solution with 1 drop of added toluene (Figure 5.9), which confirms the previously proposed structure, Pn*$_3$Ti$_3$(μ_2–H)$_3$(μ_3–H).

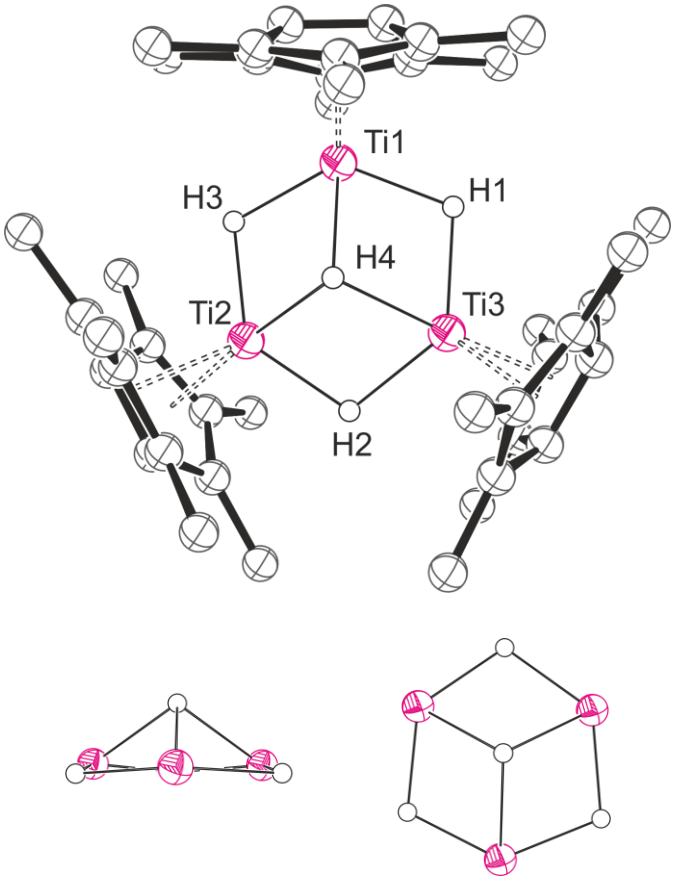


Figure 5.9. *Top: Thermal displacement ellipsoid plot (50% probability) of Pn*$_3$Ti$_3$(μ_2–H)$_3$(μ_3–H) shown with H4 in one of two partially occupied positions. Pn* H atoms omitted for clarity. Bottom: Illustration of the hexagonal pyramidal geometry formed by the metal-hydride core.*

The central metal-hydride core adopts a hexagonal pyramidal geometry with one face uncapped, similar to the complexes discussed previously in this chapter. The hydride atoms were crystallographically located, although H4 was found to be partially disordered across both faces of the hexagon. A comparison of key bond lengths and angles are provided in Table 5.2 alongside $[\{(Me_2Si)_2(\eta^5\text{–}C_5H_3)_2\}Zr]_3H_5$ (Figure 5.7),[53] which is the closest structural analogue found in the literature.

	$Pn^*_3Ti_3(\mu_2\text{–}H)_3(\mu_3\text{–}H)$	**$[\{(Me_2Si)_2(\eta^5\text{–}C_5H_3)_2\}Zr]_3H_5$**[53]
Fold Angle	33.43(10) 32.27(9) 32.27(9)	-
M–Pn^*_{cent}/Cp_{cent}	1.9810(10)	2.2648(10)
M–H1	1.78(3)	1.963(19)
M–H2	1.84(3)	2.16(2)
M–H3	1.84(3)	1.94(2)
M–H4	1.995(16)	1.94(2)
M–H5		2.16(2)
H4–$Plane_{H1/3/4}$	1.17(2)	0.93(2)
H5–$Plane_{H1/3/4}$		0.93(2)
Puckering: $\Sigma\lvert\phi\rvert$ [a]	82(6)	28.4(11)
Circumference[b]	10.91(24)	11.67(12)
M–M[c]	2.9454(9)	3.2939(10)

Table 5.2. *Comparison of selected bond lengths (Å), angles (°) and other pertinent structural metrics. a) Puckering, given in degrees, is the sum of the magnitude of the dihedral angles around the perimeter of the metal-hydride core. For a planar structure this value is 0°. b) The circumference refers to the sum of the bond lengths around the perimeter of the metal-hydride core. c) M–M given as an average of 3 values.*

The fold-angles are more shallow for $Pn^*_3Ti_3(\mu_2\text{–}H)_3(\mu_3\text{–}H)$ than $Pn^*_2Ti_2(\mu_2\text{–}H)_5Li.THF_2$, which is likely a result of formal reduction of two titanium centres to Ti(III). Although it is tempting to postulate the contraction of the third fold angle is a result of localised Ti(IV) character, this variation could also reasonably be due to crystal packing effects or other artefacts; similar discrepancies are found in the fold angles of the previously discussed Pn*–Ti/Zr hydrides. Elongation of the apical hydride–titanium bond is observed, which is

also mirrored in the zirconium complex provided for comparison in Table 5.2. Slightly surprising is the contraction of bipyramid apices for $[\{(Me_2Si)_2(\eta^5\text{–}C_5H_3)_2\}Zr]_3H_5$ relative to $Pn^*_3Ti_3(\mu_2\text{–}H)_3(\mu_3\text{–}H)$, despite an increased ionic radius in the former case. The titanium complex is more puckered than the zirconium analogue, which may be facilitated by the symmetrical displacement of capping hydride ligands in $[\{(Me_2Si)_2(\eta^5\text{–}C_5H_3)_2\}Zr]_3H_5$. Similarly, $Pn^*_2Ti_2(\mu_2\text{–}H)_5Li.THF_2$, with two capping hydride ligands, displays a less puckered structure than $Pn^*_3Ti_3(\mu_2\text{–}H)_3(\mu_3\text{–}H)$, suggesting the structural stabilisation afforded by this symmetrical ligand placement outweighs any distorting effects resulting from hetero-metal incorporation. Despite this, the circumference of $Pn^*_3Ti_3(\mu_2\text{–}H)_3(\mu_3\text{–}H)$ is almost identical to that found for $Pn^*_2Ti_2(\mu_2\text{–}H)_5Li.THF_2$, although a slight increase in average Ti–Ti distance is observed.

5.7 Reactivity of $Pn^*_3Ti_3(\mu_2\text{–}H)_3(\mu_3\text{–}H)$

A solution of $Pn^*_3Ti_3(\mu_2\text{–}H)_3(\mu_3\text{–}H)$ in C_7D_8 was exposed to 1 bar D_2 at 298 K and analysed by NMR spectroscopy after 15 minutes. The ^1H NMR spectrum indicated the presence of paramagnetic products even after this short reaction time, with broad overlapping resonances observed between 5 and 1 ppm, alongside starting material and other unidentified diamagnetic resonances. ^2D NMR spectra displayed a new resonance at −3.1 ppm, resulting from deuterium exchange, although no peaks corresponding to HD could be observed. After 48 hours the ^1H NMR spectrum was somewhat similar to that observed under H_2. However, clear differences can be observed both in the number and position of the paramagnetic and diamagnetic components (Figure 5.10).

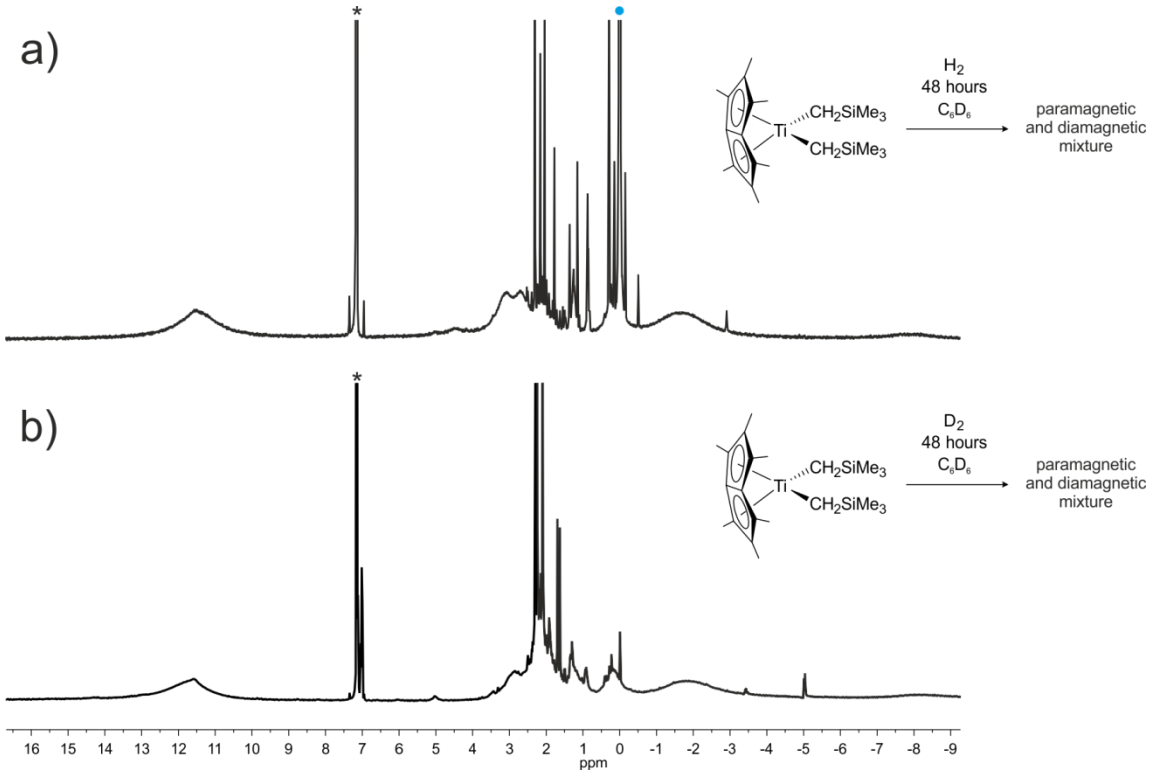
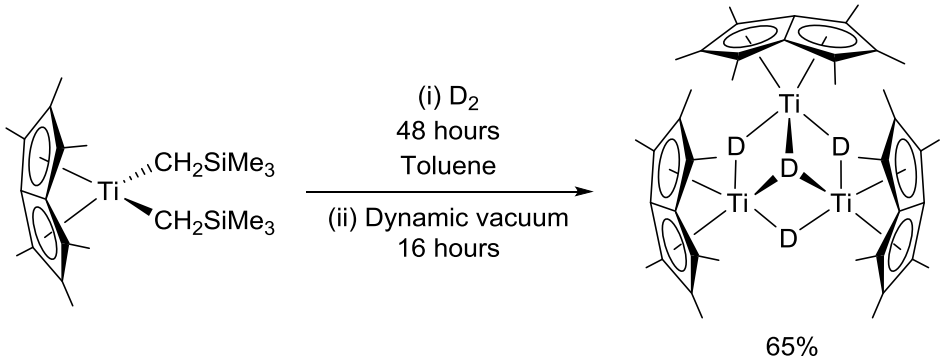


Figure 5.10. *^{1}H NMR spectra (400 MHz, 298 K, C_6D_6) of a) Pn*Ti(CH_2SiMe_3)$_2$ under 1 bar H_2, b) Pn*Ti(CH_2SiMe_3)$_2$ under 1 bar D_2. * = C_6D_6, blue circle = $SiMe_4$.*

The rapid reaction with D_2 contrasts dramatically with the slow exchange observed for Pn*$_2$Ti$_2$(μ_2–H)$_5$Li.THF$_x$, which is presumably a consequence of the vacant coordination site presented by Pn*$_3$Ti$_3$(μ_2–H)$_3$(μ_3–H). After exposing the paramagnetic mixture to dynamic vacuum and redissolving in C_7D_8, the diamagnetic deuterated complex, Pn*$_3$Ti$_3$(μ_2–D)$_3$(μ_3–D) could observed by NMR spectroscopy. Two Pn*–*Me* peaks at 2.30 and 2.15 ppm are the only resonances observed by ^{1}H NMR spectroscopy, with a corresponding deuteride resonance at −3.1 ppm.

Pn*$_3$Ti$_3$(μ_2–D)$_3$(μ_3–D) was synthesised on a preparative scale by an analogous method to Pn*$_3$Ti$_3$(μ_2–H)$_3$(μ_3–H), with D_2 gas instead of H_2. The product was obtained in 65% yield as a black crystalline solid, whose bulk purity was confirmed by elemental analysis (Scheme 5.7).



Scheme 5.7. *Synthesis of Pn*$_3$Ti$_3$(μ$_2$–D)$_3$(μ$_3$–D).*

FTIR Spectroscopy of the hydride and deuteride complexes display stretches at 1310 and 936 cm^{-1} respectively, which is in close agreement with values predicted by the reduced mass formula (1310 and 944 cm^{-1}). A new peak at 1043 cm^{-1} in the spectrum of Pn*Ti$_3$D$_4$ could not be related by its reduced mass to a corresponding peak in the spectrum of Pn*$_3$Ti$_3$(μ$_2$–H)$_3$(μ$_3$–H) (expected value 1457 cm^{-1}) due to overlap with an intense broad peak at 1444 cm^{-1} assigned to Pn* C=C bond stretching.

Given the observation of paramagnetism under H$_2$/D$_2$, Pn*$_3$Ti$_3$(μ$_2$–H)$_3$(μ$_3$–H) was studied by X-band EPR spectroscopy in the presence of these gases. A toluene solution of Pn*$_3$Ti$_3$(μ$_2$– H)$_3$(μ$_3$–H) was pressurised with 1 bar H$_2$ in a J-Youngs Quartz EPR tube and spectra collected after 30 minutes, 6 hours and 48 hours (Figure 5.11). Complicated speciation was inferred from the observation of a number of paramagnetic components between g = 1.96 and 1.98. Due to the overlap and weak intensity of these resonances, it is not possible to confidently assign the number of minor components. The major component at g = 1.993 is clearly resolved 30 minutes after gas addition, and is observed to increase in relative intensity over the course of 48 hours, with intermediate conversion observed at 6 hours. That the additional components are the result of speciation and not decomposition was confirmed by repeating the reaction at a fivefold increase in concentration (25 mM *vs.* 5 mM), which produced these minor components to the same extent. Indeed the presence of both paramagnetic and diamagnetic components by ^{1}H NMR spectroscopy under H$_2$ pressure further alludes to the formation of multiple products and it could be envisaged that variation in nuclearity and hydride/deuteride content under H$_2$/D$_2$ may lead to the observed speciation. Unfortunately, no hyperfine coupling to the hydride ligands was observed, which limits additional insight into the nature of these complexes.

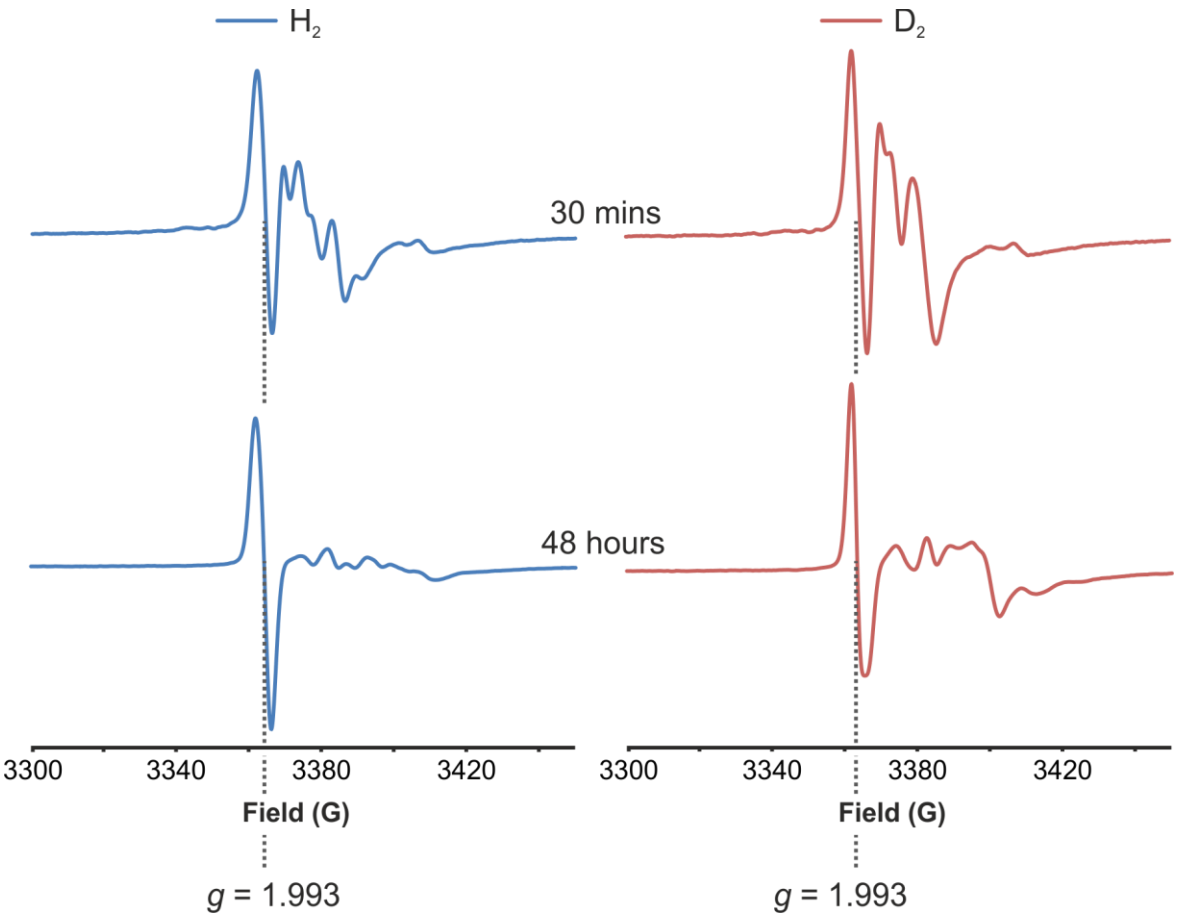


Figure 5.11. *X-band EPR spectra (5 mM toluene solution, 298 K) of Pn*$_3$Ti$_3$(μ$_2$–H)$_3$(μ$_3$–H) and Pn*$_3$Ti$_3$(μ$_2$–D)$_3$(μ$_3$–D) under H$_2$ and D$_2$ gas (1 bar overpressure).*

Repeating the reaction with D_2 similar, reactivity was observed. The same resonance at $g = 1.993$ is observed, formed within 30 minutes and increasing in intensity over the course of 48 hours. However, the distribution of minor components is altered relative to H_2, with a more intense resonance at $g = 1.972$ resolved under D_2 after 48 hours. No additional splitting of peaks is observed (D, S = 1; H, S = ½), confirming the absence of hyperfine coupling at the experimental resolution.

Attempts to crystallise the major product from saturated toluene solutions of Pn*$_3$Ti$_3$(μ$_2$–H)$_3$(μ$_3$–H) under H_2 pressure were unsuccessful, preventing the conclusive identification of these paramagnetic complexes. The challenge of its crystallisation may be due in part to the equilibria that appear to be operative under gas pressure. Under these conditions more hydrogen-dense products will be favoured. Some plausible structures for

this major paramagnetic component could be therefore be proposed. $Pn^*_3Ti_3(\mu_2–H)_3(\mu_3–H)_2$, related to the diamagnetic starting complex by incorporation of an additional hydride ligand across the open face of the hexagonal bipyramid, would be expected to paramagnetic. Alternatively, it could be envisaged that variation in the nuclearity of the metal-hydride product could occur, forming complexes such as the mixed valence hydride dimer, $(Pn^*Ti)_2(\mu–H)_3$, displaying a Ti:H ratio of 1:1.5, (1:1.33 for the diamagnetic starting complex). Additional experiments would be required to provide a more definitive assignment and gain deeper understanding of these equilibria.

An interesting comparison can be drawn between $Pn^*_3Ti_3(\mu_2–H)_3(\mu_3–H)$ and the titanium half-sandwich hydride, $[(Cp'Ti)_3(\mu_3–H)(\mu_2–H)_6]$ ($Cp' = C_5Me_4SiMe_3$), formed by hydrogenation of $Cp'Ti(CH_2SiMe_3)_3$ (Figure 5.12).[55] The structure can be considered analogous to that of in $Pn^*_3Ti_3(\mu_2–H)_3(\mu_3–H)$, only with six hydride ligands bracing the hexagonal plane to account for the substitution of Pn* for a monoanionic carbocycle, Cp′. This contrasts with the tetrametallic clusters observed following hydrogenation of $Cp'M(CH_2SiMe_3)_3$ (M = Zr, Hf), where all four metal centres are in the +3 oxidation state.[56]

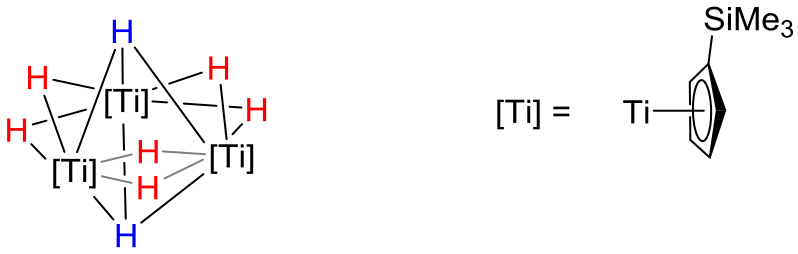


Figure 5.12. *Related titanium-hydride cluster, $[(Cp'Ti)_3(\mu_3–H)(\mu_2–H)_6]$. $Cp' = Cp(SiMe_3)$.*[55,57]

$[(Cp'Ti)_3(\mu_3–H)(\mu_2–H)_6]$ displays remarkable reactivity, cleaving the dinitrogen triple bond to form two bridging $[NH]^{2-}$ ligands in 90% yield,[55] as well as activating benzene to form methylcyclopentenyl derivatives.[57,58] Unfortunately, despite their structural similarity, comparable transformations were not observed with in $Pn^*_3Ti_3(\mu_2–H)_3(\mu_3–H)$. The complex is stable in benzene, and does not react with 4 bar N_2. With CO, decomposition is observed, similar to the reported reactivity with $Pn^*_2Ti_2(\mu_2–H)_5Li.THF_x$, while with CO_2 no evidence for hydride transfer is observed although a number of new hydride resonances could be resolved by NMR spectroscopy, perhaps resulting from the

formation of titanium–oxide–hydride derivatives. The complex is unreactive towards 2-butyne, although reactivity is observed with ethylene. Following the reaction by ^{1}H NMR spectroscopy, slow consumption of the starting material was observed alongside the formation of a large number of Pn*–*Me* and the appearance of 8 new hydride environments in the region –0.49 to –6.54 ppm. This divergent reactivity of complexes that appear electronically and structurally so related highlights the importance of ancilliary ligand set in directing the chemistry of metal-hydrides. Although clean reaction with small-molecules could not be realised, it is interesting to contrast the reactivity of $Pn^*_3Ti_3(\mu_2–H)_3(\mu_3–H)$ to the stability $Pn^*_2Ti_2(\mu_2–H)_5Li.THF_x$ under similar conditions, which may be driven by the presence of a suitable vacancy in the coordination sphere of the metal centres in $Pn^*_3Ti_3(\mu_2–H)_3(\mu_3–H)$.

5.8 Density Functional Theory analysis of $Pn^*_3Ti_3(\mu_2–H)_3(\mu_3–H)$

$Pn^*_3Ti_3(\mu_2–H)_3(\mu_3–H)$ is a mixed-valence hydride cluster with d-electron count d^0-d^1-d^1, which might be expected to behave as a paramagnet. However, spectroscopic evidence indicates that it is diamagnetic. Density Functional Theory calculations were therefore carried out by Professor Jennifer Green to probe the origins of this diamagnetism, gain insight into the nature of bonding in the complex, and investigate energetically accessible derivatives that may aid in the rationalisation of the EPR data.

Density functional calculations were carried using the Amsterdam Density Functional package[59] and triple-ζ quality basis sets augmented with a one polarisation function (ADF basis TZP). The local density approximation (LDA) of Vosko, Wilk and Nusair (VWN)[60] was used together with the exchange correlation corrections of Becke and Perdew (BP86).[61,62] The geometries of both $Ti_3Pn_3(\mu_2–H)_3(\mu_3–H)$ and $Ti_3Pn^*_3(\mu_2–H)_3(\mu_3–H)$ were successfully optimised with C_{3v} symmetry found for the Pn complex and the Ti_3H_4 core of the Pn* analogue. For simplicity, a bonding analysis was carried out on $Ti_3Pn_3(\mu_2–H)_3(\mu_3–H)$, which is shown in Figure 5.13.

The HOMO, $18a_1$, is a cluster-based bonding orbital composed primarily of metal d_{z^2} orbitals, projecting onto the vacant face of the hexagonal pyramid. The diamagnetism of the complex can be understood to result from the overlap of these d_{z^2} orbitals, which accommodates the two otherwise unpaired electrons. The next six lower energy orbitals

describe titanium-pentalene bonding interactions, which are followed by a set of obritals, some of which have Ti–H bonding characteristics ($23e_1$ and $16a_1$) that describe the Ti–H–Ti 3c-2e bonds in a localised bonding model. The apical hydride bonding interaction is primarily exhibited lower in the manifold in orbitals $14a_1$ and $13a_1$, with the edge-bridging hydrides contributing to lesser extent.

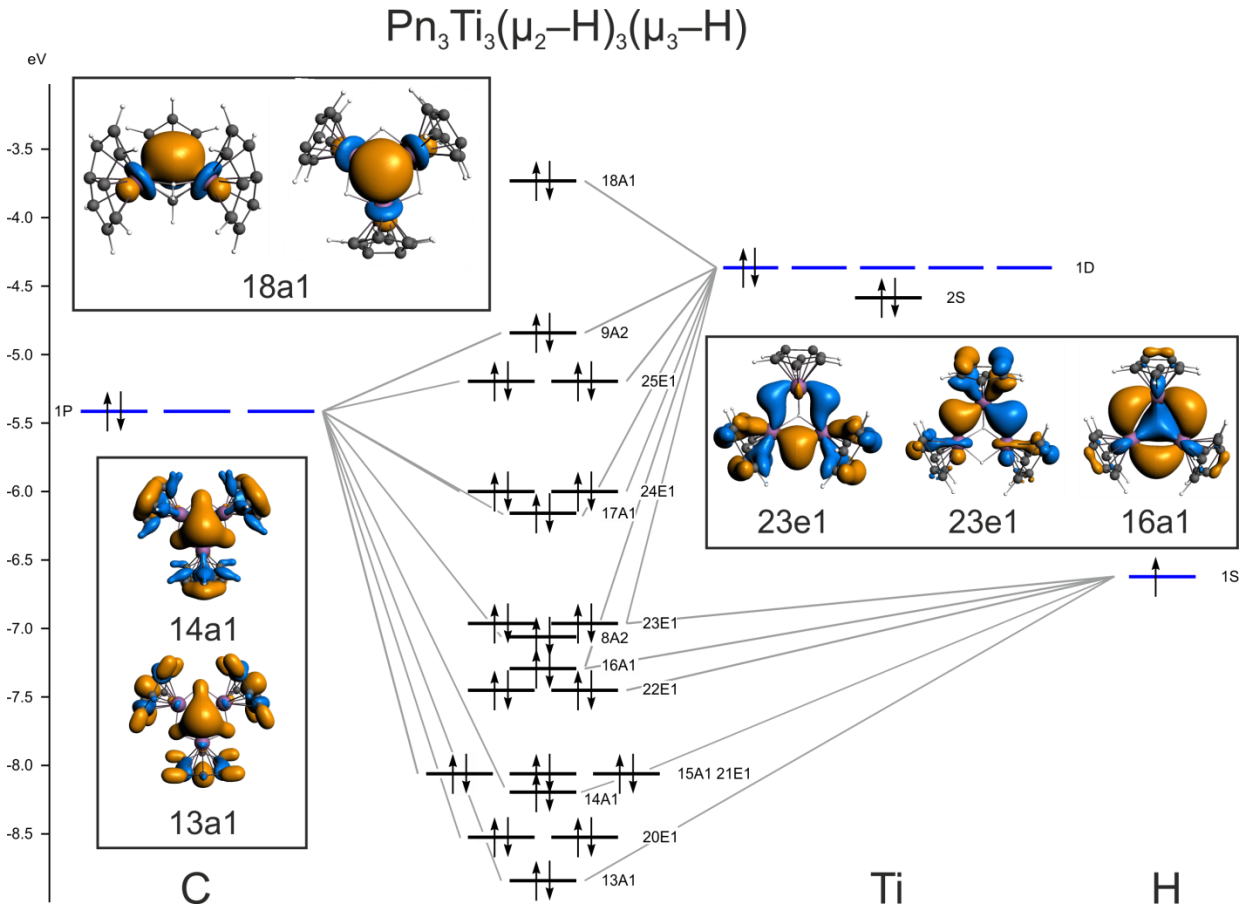


Figure 5.13. *Molecular orbital diagram for $Ti_3Pn^*_3(\mu_2–H)_3(\mu_3–H)$, with key Ti–Ti and Ti–H bonding interactions highlighted.*

Calculations were also performed on $Ti_3Pn^*_3(\mu_2–H)_3(\mu_3–H)_2$, a paramagnetic species, and $Ti_3Pn_3(\mu_2–H)_3(\mu_3–H)_2$. Various starting structures were attempted, the lowest energy of which was a D_{3h} symmetric structure with the additional hydride atom localised on the exposed face of the hexagonal pyramid. The extra electron occupies a SOMO, $26e_1$, localised on the three titianium atoms, shown in Figure 5.14 for the Pn analogue. Jahn-Teller distortion from pure D_{3h} symmetry is therefore predicted, but given the weak bonding/anti-bonding characteristics of the $26e_1$ orbital such a distortion might not be static. As discussed in relation to $Pn^*_2Ti_2(\mu_2–H)_5Li.THF_2$, this hexagonal bipyramidal

metal-hydride core can be understood to result from the orthogonal disposition of the PnTi frontier molecular orbitals.

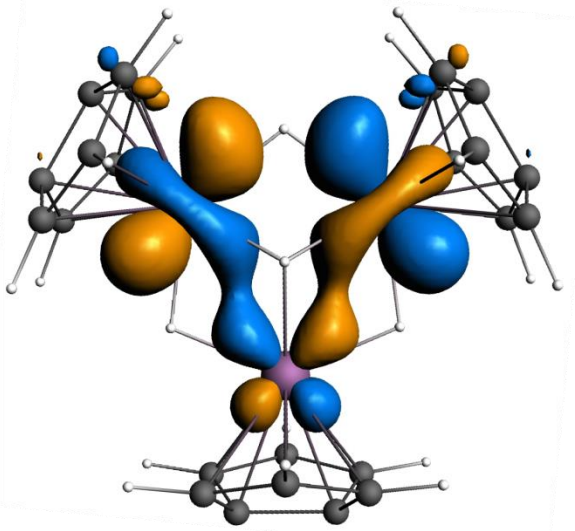


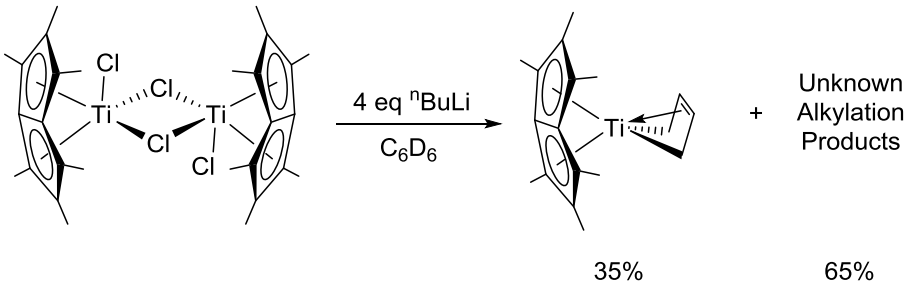
Figure 5.14. *SOMO calculated for paramagnetic hydride complex, $Ti_3Pn_3(\mu_2–H)_3(\mu_3–H)_2$.*

5.9 Attempted synthesis of titanium hydrides *via* β–hydride elimination

Attempts were made to exploit the tendency of metal-alkyl complexes bearing β-hydrogens to eliminate alkenes in pursuit of metal–hydride derivatives. Addition of 4 eq. ^{n}BuLi (1.6 M in hexanes) to $(Pn^*TiCl)_2(\mu–Cl)_2$ leads to complete consumption of the starting material and a colour change from red-brown to purple. No obvious effervescence was observed, and no H_2 or butene could be observed by ^{1}H NMR spectroscopy. Due to the presence of hexanes it was not possible to identify whether butane is formed, although a precipitate of LiCl could be observed. After removing the volatiles and redissolving in C_6D_6 two new components can be observed by NMR spectroscopy, which surprisingly provide no evidence for Ti–H bond formation (Scheme 5.8).

The minor component (approximately 35%) displays a low-symmetry Pn* fragment, with six Pn*–*Me* environments observed between 1.75 and 2.15 ppm (relative integration 3:3:3:3:3:3). Three additional multiplets can be resolved by ^{1}H NMR spectroscopy (5.39, 2.38 and 0.01 ppm) of relative integration 2:2:2, which couple to two corresponding ^{13}C environments (55.8 and 111.6 ppm), as well as mutually coupling to one another in COSY NMR spectra. These data would be consistent with formation of a butadiene complex, $Pn^*Ti(C_4H_6)$. A second component, which also appears to be a butylated Pn*Ti complex

could not be confidently assigned. A summary of the NMR spectroscopic features are given in Figure 5.15. In particular, the observation of a shielded resonance at 18.6 ppm in the ^{13}C NMR spectrum (^{1}H = 7.55 ppm, 1H, dt, 9.7 Hz, 1.1 Hz), which was confirmed to correspond to a CH/CH_3 environment by gradient selective HSQC experiments, is difficult to reconcile with the otherwise deshielded carbon environments (136.1, 101.2, 68.6 ppm).



Scheme 5.8. *Synthesis of Pn*Ti(C_4H_6) via alkylation of [Pn*TiCl(μ–Cl)]$_2$.*

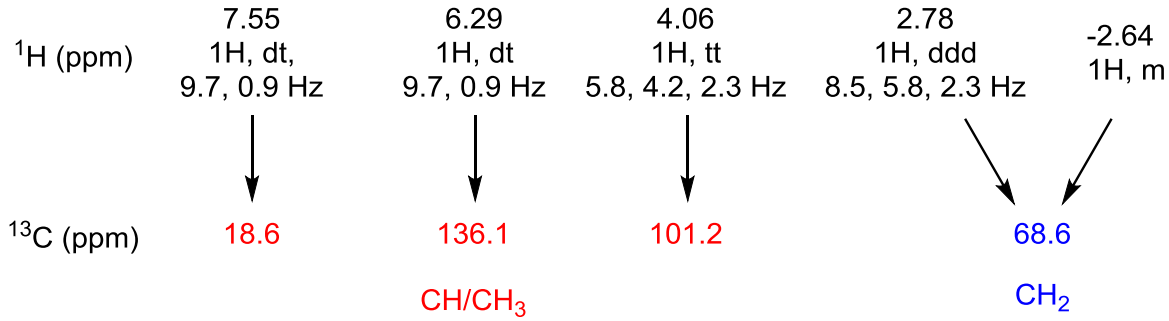


Figure 5.15. *Illustration of key NMR spectroscopic features of unidentified alkylation byproduct from reaction of (Pn*TiCl)$_2$(μ–Cl)$_2$ and ^{n}BuLi.*

The reaction was repeated at a preparative scale in toluene. Crystallisation of the crude product from pentane at –80 °C produced crystalline material suitable for an X-ray diffraction study. The data is of poor quality, due in part to the air-sensitivity of product, which rapidly decomposed to an unidentified yellow solid while attempts were made to mount a crystal. However, the structure shown in Figure 5.16, demonstrates the formation of a butadiene complex, and is therefore proposed to correspond to the minor component observed spectroscopically.

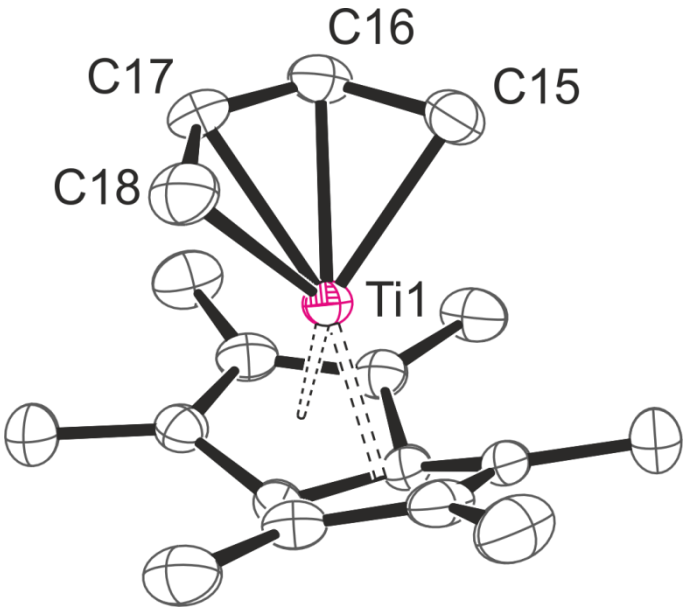


Figure 5.16. *Thermal displacement ellipsoid plot (50% probability) of Pn*Ti(C_4H_6). H atoms omitted for clarity.*

The butadiene ligand can adopt a number of different bonding modes,[63] the most relevant of which are illustrated in Figure 5.17.

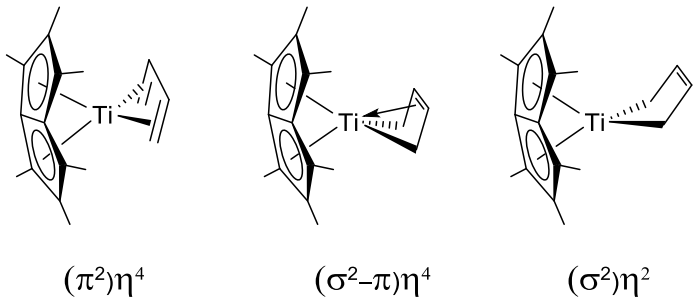


Figure 5.17. *Illustration of some key bonding modes of the butadiene ligand.*

Formal diene coordination, $(\pi^2)\eta^4$, is characterised structurally by small differences in metal-carbon bond lengths to both terminal and internal diene-carbon bonds (Δd generally < 0.1 Å). Additionally, the dihedral angle, $\phi_{dihedral}$, made between the mean plane of the butadiene carbon atoms and the mean plane of the metal and terminal carbons atoms should increase commensurately with enhanced metallocyclopentene character, where values < 100° would generally indicate a π-bonding component (Figure 5.18).[63] For example, $Ti(C_4H_6)_2$(dmpe) displays minimal bond length variation (+0.016 Å) and relatively contracted dihedral angles (91.9°) that would convincingly point towards η^4-coordination.[64] However, more often the structural data are ambiguous, as in

Cp*TiCl(C_4H_6), where values of -0.101 Å and 105.0° are reported for Δd and $\phi_{dihedral}$ respectively, requiring additional spectroscopic characterisation to differentiate between η^4-isomers.[65] The value of $^1J_{H\text{-}C}$ for the terminal butadiene environment can be used as in indication of hybridisation, where values greater than 150 Hz would indicate sp^2 and therefore butadiene character, while values less than 140 Hz would suggest sp^3 hybridisation and a σ^2-type interaction.

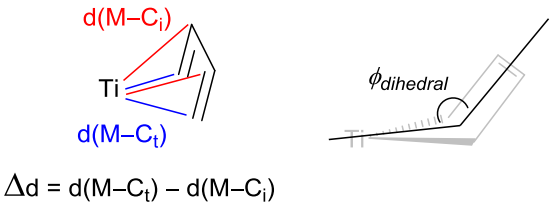


Figure 5.18. *Illustration of some key bond metrics employed for the characterisation of metal-butadiene complexes.*

	Pn*Ti(C_4H_6)
Fold Angle	35.3
Ti–Pn*$_{cent}$	1.910(3)
	1.933(3)
Δd[a]	-0.038
$\varphi_{dihedral}$[b]	97.2
C15–C16	1.427(11)
C16–C17	1.377(11)
C17–C18	1.453(12)

Table 5.3. *Comparison of selected bond lengths (Å), angles (°) and other pertinent structural metrics. a) average difference between Ti–$C_{terminal}$ and Ti–$C_{internal}$. b) angle between the mean planes of Ti/C18/C15 and C15/16/17/18.*

In Pn*Ti(C_4H_6) there is little variation in the Ti–C bond lengths (–0.038 Å), and $\varphi_{dihedral}$ is calculated as 97.2°, which suggests η^4-coordination (Table 5.3). However, on the basis of C–C bond length alternation, the mono-unsaturated metallocyclopentene structure provides the best fit of the data.[66] Indeed the magnitude of the fold angle is greater than those reported for other Pn*Ti($X)_2$ complexes (X = CH_2SiMe_3, ^{t}Bu, Bn), which typically fall in the range 32.9 – 33.1°, consistent with the formulation of Pn*Ti(C_4H_6) as Ti(IV).[44,67]

$^1J_{C\text{-}H}$ for the terminal diene position was found to be 138 Hz, which indicates sp^3 character. In light of these data, the $(\sigma^2\text{–}\pi)\eta^4$ bonding mode is proposed, as illustrated in Scheme 5.8.

The formation of butadiene complexes *via* decomposition of metal alkyl intermediates is rather unusual. Typically, they are accessed by salt-metathesis with dienemagnesium[66,68–70] or pentadienyl reagents,[71] or alternatively by reduction in the presence of a suitable diene.[72–74] The chemistry of group 4 metal *n*-alkyl complexes, particularly mixtures of Cp_2ZrCl_2 and ^{n}BuLi, have been widely studied in the context of the Zr(II) "Negishi reagent, $Cp_2Zr(\eta^2\text{–butene})$.[75–77] However, the transiently formed $Cp_2M(^nBu)_2$ typically undergoes intramolecular deprotonation at the β–position. By contrast, the formation $Pn^*Ti(C_4H_6)$ implies deprotonation of the δ–position followed by double β–hydride elimination (Figure 5.19), analogous to the chemistry observed for tantalum metallacyclopentene complexes reported by Schrock and coworkers.[78–80] The reasons for this divergent reactivity remains unclear and would certainly be an interesting area for future investigation.

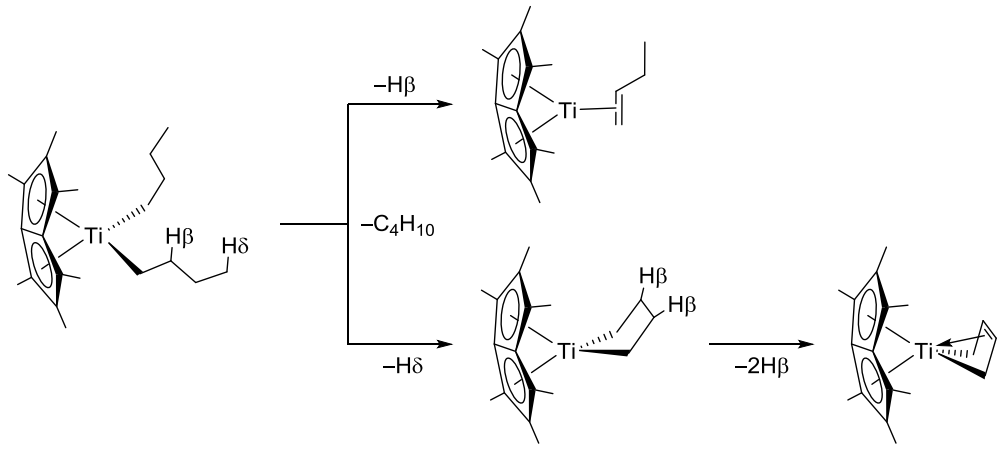


Figure 5.19. *Top: Illustration of Negishi-type chemistry expected to result from β–H deprotonation. Bottom: Proposed δ–H deprotonation to form unobserved metallocyclopentane intermediate.*

5.10 Conclusion

In this chapter, the preparation of two new Pn* metal-hydride complexes is described, $Pn^*_2Ti_2(\mu_2\text{–}H)_5Li.THF_x$ and $[Pn^*_2Zr_2(\mu_2\text{–}H)_5Li.THF_x]_2$, which can both be accessed from the corresponding M(IV) chloride precursor and $LiAlH_4$ in THF. Although a number of intermediate hydride species were observed spectroscopically they were not successfully isolated. The titanium-hydride complex is not fluxional on the NMR timescale, and does

not readily exchange with D_2, while the zirconium congener undergoes chemical exchange between two of the three observed hydride environments. As expected given its fluxional solution-phase behaviour, the zirconium complex also readily exchanged with D_2 gas in a C_6D_6/THF solution. The deuteride complexes, $Pn^*_2Ti_2(\mu_2–D)_5Li.THF_x$ and $[Pn^*_2Zr_2(\mu_2–D)_5Li.THF_x]_2$, were successfully synthesised using $LiAlD_4$, and characterised by NMR and FTIR spectroscopy. Both complexes were structurally characterised with a variety of solvents coordinated to the apical lithium atom, and demonstrate an unusual hexagonal bipyramidal geometry. In the case of $[Pn^*_2Zr_2(\mu_2–H)_4(\mu_3–H)Li.THF]_2$, edge-fused bipyramids are observed in the solid state, forming a more puckered hydride cluster. This geometry has only rarely been encountered previously, and can be rationalised by Density Functional Theory calculations as the result of frontier orbital electron density projected in two orthogonal planes, in contrast with the co-planar orientation found for Cp_2M complexes.

The diamagnetic mixed-valence titanium hydride cluster, in $Pn^*_3Ti_3(\mu_2–H)_3(\mu_3–H)$, was also reinvestigated in detail. Surprisingly, under H_2, the complex reversibly forms a large number of unidentified paramagnetic components, which are all converted to $Pn^*_3Ti_3(\mu_2–H)_3(\mu_3–H)$ under dynamic vacuum overnight. The proposed structure was crystallographically confirmed, and further corroborated by DFT calculations, which illustrated the formation of a metal-cluster bonding orbital responsible for the diamagnetism of the complex.

Finally, attempts to synthesise metal-hydride complexes *via* transient metal *n*-alkyl intermediates allowed for the unexpected isolation of a butadiene complex, $Pn^*Ti(C_4H_6)$. On the basis of structural and spectroscopic data, a $(\sigma^2–\pi)\eta^4$ bonding mode is suggested, which is tentatively proposed to occur by a rather unusual intramolecular δ–deprotonation of $Pn^*Ti(^nBu)_2$.

5.11 References

(1) Ager, D. J.; de Vries, A. H. M.; de Vries, J. G. *Chem. Soc. Rev.* **2012**, *41* (8), 3340–3380.
(2) Johnson, N. B.; Lennon, I. C.; Moran, P. H.; Ramsden, J. A. *Acc. Chem. Res.* **2007**, *40* (12), 1291–1299.
(3) Shultz, C. S.; Krska, S. W. *Acc. Chem. Res.* **2007**, *40* (12), 1320–1326.
(4) Blaser, H.-U.; Pugin, B.; Spindler, F.; Thommen, M. *Acc. Chem. Res.* **2007**, *40* (12), 1240–1250.
(5) Bauer, I.; Knölker, H.-J. *Chem. Rev.* **2015**, *115* (9), 3170–3387.
(6) Chirik, P. J. *Acc. Chem. Res.* **2015**, *48* (6), 1687–1695.
(7) Li, Y.-N.; Ma, R.; He, L.-N.; Diao, Z.-F. *Catal. Sci. Technol.* **2014**, *4* (6), 1498–1512.
(8) Manriquez, J. M.; McAlister, D. R.; Sanner, R. D.; Bercaw, J. E. *J. Am. Chem. Soc.* **1978**, *100* (9), 2716–2724.
(9) Wolczanski, P. T.; Bercaw, J. E. *Acc. Chem. Res.* **1980**, *13* (4), 121–127.
(10) Bercaw, J. E.; Marvich, R. H.; Bell, L. G.; Brintzinger, H. H. *J. Am. Chem. Soc.* **1972**, *94* (4), 1219–1238.
(11) Curtis, C. J.; Haltiwanger, R. C. *Organometallics* **1991**, *10* (9), 3220–3226.
(12) Chirik, P. J.; Day, M. W.; Bercaw, J. E. *Organometallics* **1999**, *18* (10), 1873–1881.
(13) Guo, Z. Y.; Bradley, P. K.; Jordan, R. F. *Organometallics* **1992**, *11* (7), 2690–2693.
(14) Jones, S. B.; Petersen, J. L. *Inorg. Chem.* **1981**, *20* (9), 2889–2894.
(15) Grossman, R. B.; Doyle, R. A.; Buchwald, S. L. *Organometallics* **1991**, *10* (5), 1501–1505.
(16) Larsonneur, A. M.; Choukroun, R.; Jaud, J. *Organometallics* **1993**, *12* (8), 3216–3224.
(17) Wielstra, Y.; Gambarotta, S.; Spek, A. L. *Organometallics* **1990**, *9* (3), 572–577.
(18) Heiden, Z. M.; Lathem, A. P. *Organometallics* **2015**, *34* (10), 1818–1827.
(19) Green, J. C.; Green, M. L. H.; Prout, C. K. *J. Chem. Soc., Chem. Commun.* **1972**, *0* (7), 421–422.
(20) Petersen, J. L.; Dahl, L. F. *J. Am. Chem. Soc.* **1975**, *97* (22), 6422–6433.
(21) Long, N. J. *Metallocenes : an introduction to sandwich complexes*; Blackwell Science, 1998.
(22) Green, J. C. *Chem. Soc. Rev.* **1998**, *27* (4), 263–271.
(23) Green, J. C.; Jackson, S. E.; Higginson, B. *J. Chem. Soc., Dalton Trans.* **1975**, *0* (5), 403–409.
(24) Wailes, P. C. *J. Organomet. Chem.* **1976**, *119*, 243–259.
(25) Becke, A. D. *J. Chem. Phys.* **1986**, *84* (8), 4524–4529.
(26) Lee, C.; Yang, W.; Parr, R. G. *Phys. Rev. B* **1988**, *37* (2), 785–789.
(27) Becke, A. D. *J. Chem. Phys.* **1993**, *98* (7), 5648–5652.
(28) Schäfer, A.; Horn, H.; Ahlrichs, R. *J. Chem. Phys.* **1992**, *97* (4), 2571–2577.
(29) Schäfer, A.; Huber, C.; Ahlrichs, R. *J. Chem. Phys.* **1994**, *100* (8), 5829–5835.
(30) Weigend, F.; Ahlrichs, R. *Phys. Chem. Chem. Phys.* **2005**, *7* (18), 3297–3305.
(31) Mayer, I. *J. Comput. Chem.* **2007**, *28* (1), 204–221.
(32) Bridgeman, A. J.; Cavigliasso, G.; Ireland, L. R.; Rothery, J. *J. Chem. Soc., Dalton Trans.* **2001**, *0* (14), 2095–2108.
(33) Bercaw, J. E. *J. Am. Chem. Soc.* **1974**, *96* (16), 5087–5095.
(34) Brintzinger, H.; Bercaw, J. E. *J. Am. Chem. Soc.* **1971**, *93* (8), 2045–2046.

(35) Pinkas, J.; Gyepes, R.; Císařová, I.; Kubišta, J.; Horáček, M.; Mach, K. *Dalton Trans.* **2017**, *46* (25), 8229–8244.
(36) Sizov, A. I.; Zvukova, T. M.; Bel'sky, V. K.; Bulychev, B. M. *Russ. Chem. Bull.* **1998**, *47* (6), 1186–1192.
(37) Bulichev, B. M.; Evdokimova, E. V.; Sizov, A. I.; Soloveichik, G. L. *J. Organomet. Chem.* **1982**, *239* (2), 313–320.
(38) Bel'sky, V. K.; Sizov, A. I.; Bulychev, B. M.; Soloveichik, G. L. *J. Organomet. Chem.* **1985**, *280* (1), 67–80.
(39) Mach, K.; Varga, V.; Hanuš, V. *J. Organomet. Chem.* **1991**, *415* (1), 87–95.
(40) Troyanov, S. I.; Mach, K.; Varga, V. *Organometallics* **1993**, *12* (9), 3387–3389.
(41) Hessen, B.; Blenkers, J.; Teuben, J. H.; Helgesson, G.; Jagner, S. *Organometallics* **1989**, *8* (12), 2809–2812.
(42) Erker, G.; Dorf, U.; Czisch, P.; Peterson, J. L. *Organometallics* **1986**, *5* (4), 668–676.
(43) Berno, P.; Stella, S.; Floriani, C.; Chiesi-Villa, A.; Guastini, C. *J. Chem. Soc., Dalton Trans.* **1990**, No. 9, 2669–2677.
(44) Cooper, R. T. D.Phil Thesis, University of Oxford, 2012.
(45) Kilpatrick, A. F. R.; Cloke, F. G. N. *Chem. Commun.* **2014**, *50* (21), 2769.
(46) Kilpatrick, A. F. R.; Green, J. C.; Cloke, F. G. N. *Organometallics* **2015**, *34* (20), 4816–4829.
(47) Cooper, R. T.; Chadwick, F. M.; Ashley, A. E.; O'Hare, D. *Organometallics* **2013**, *32* (7), 2228–2233.
(48) Emsley, J. *The Elements*; Oxford University Press, 1998.
(49) Etkin, N.; Hoskin, A. J.; Stephan, D. W. *J. Am. Chem. Soc.* **1997**, *119* (47), 11420–11424.
(50) Wailes, P. C.; Weigold, H. *J. Organomet. Chem.* **1970**, *24* (2), 405–411.
(51) Khan, K.; Raston, C. L.; McGrady, J. E.; Skelton, B. W.; White, A. H. *Organometallics* **1997**, *16* (15), 3252–3254.
(52) Sizov, A. I.; Zvukova, T. M.; Khvostov, A. V.; Belsky, V. K.; Stash, A. I.; Bulychev, B. M. *J. Organomet. Chem.* **2003**, *681* (1–2), 167–173.
(53) Chirik, P. J.; Henling, L. M.; Bercaw, J. E. *Organometallics* **2001**, *20* (3), 534–544.
(54) Cuenca, T.; Galakhov, M.; Royo, E.; Royo, P. *J. Organomet. Chem.* **1996**, *515* (1–2), 33–36.
(55) Shima, T.; Hu, S.; Luo, G.; Kang, X.; Luo, Y.; Hou, Z. *Science* **2013**, *340* (6140), 1549–1552.
(56) Hu, S.; Shima, T.; Luo, Y.; Hou, Z. *Organometallics* **2013**, *32* (7), 2145–2151.
(57) Hu, S.; Shima, T.; Hou, Z. *Nature* **2014**, *512* (7515), 413–415.
(58) Kang, X.; Luo, G.; Luo, L.; Hu, S.; Luo, Y.; Hou, Z. *J. Am. Chem. Soc.* **2016**, *138* (36), 11550–11559.
(59) Vrije Universiteit: Amsterdam, The Netherlands 2016.
(60) Vosko, S. H.; Wilk, L.; Nusair, M. *Can. J. Phys.* **1980**, *58* (8), 1200–1211.
(61) Becke, A. D. *Phys. Rev. A* **1988**, *38* (6), 3098–3100.
(62) Perdew, J. P. *Phys. Rev. B* **1986**, *33* (12), 8822–8824.
(63) Yasuda, H.; Nakamura, A. *Angew. Chem. Int. Ed.* **1987**, *26* (8), 723–742.
(64) Spencer, M. D.; Wilson, S. R.; Girolami, G. S. *Organometallics* **1997**, *16* (13), 3055–3067.
(65) Yamamoto, H.; Yasuda, H.; Tatsumi, K.; Lee, K.; Nakamura, A.; Chen, J.; Kai, Y.; Kasai, N. *Organometallics* **1989**, *8* (1), 105–119.

(66) Yasuda, H.; Tatsumi, K.; Okamoto, T.; Mashima, K.; Lee, K.; Nakamura, A.; Kai, Y.; Kanehisa, N.; Kasai, N. *J. Am. Chem. Soc.* **1985**, *107* (8), 2410–2422.
(67) Cooper, R. T.; Chadwick, F. M.; Ashley, A. E.; O'Hare, D. *Chem. Commun.* **2015**, *51* (59), 11856–11859.
(68) Yasuda, H.; Tatsumi, K.; Nakamura, A. *Acc. Chem. Res.* **1985**, *18* (4), 120–126.
(69) Yasuda, H.; Kajihara, Y.; Mashima, K.; Nagasuna, K.; Lee, K.; Nakamura, A. *Organometallics* **1982**, *1* (2), 388–396.
(70) Kai, Y.; Kanehisa, N.; Miki, K.; Kasai, N.; Mashima, K.; Nagasuna, K.; Yasuda, H.; Nakamura, A. *J. Chem. Soc., Chem. Commun.* **1982**, *0* (3), 191–192.
(71) Yasuda, H.; Nagasuna, K.; Akita, M.; Lee, K.; Nakamura, A. *Organometallics* **1984**, *3* (10), 1470–1478.
(72) Beatty, R. P.; Datta, S.; Wreford, S. S. *Inorg. Chem.* **1979**, *18* (11), 3139–3145.
(73) Datta, S.; Wreford, S. S.; Beatty, R. P.; McNeese, T. J. *J. Am. Chem. Soc.* **1979**, *101* (4), 1053–1054.
(74) Erker, G.; Wicher, J.; Engel, K.; Rosenfeldt, F.; Dietrich, W.; Krueger, C. *J. Am. Chem. Soc.* **1980**, *102* (20), 6344–6346.
(75) Negishi, E.-I.; Takahashi, T. *Acc. Chem. Res.* **1994**, *27* (5), 124–130.
(76) Keaton, R. J.; Koterwas, L. A.; Fettinger, J. C.; Sita, L. R. *J. Am. Chem. Soc.* **2002**, *124* (21), 5932–5933.
(77) Fischer, R.; Walther, D.; Gebhardt, P.; Görls, H. *Organometallics* **2000**, *19* (13), 2532–2540.
(78) Fellmann, J. D.; Rupprecht, G. A.; Schrock, R. R. *J. Am. Chem. Soc.* **1979**, *101* (17), 5099–5101.
(79) McLain, S. J.; Wood, C. D.; Schrock, R. R. *J. Am. Chem. Soc.* **1977**, *99* (10), 3519–3520.
(80) McLain, S. J.; Wood, C. D.; Schrock, R. R. *J. Am. Chem. Soc.* **1979**, *101* (16), 4558–4570.

Chapter 6: Synthesis of Reduced Titanium Permethylpentalene Complexes

6.1 Introduction

The reduction chemistry of η^8-pentalene metal complexes is under-explored by comparison to the growing literature concerning d^0 organometallic derivatives.[1,2] Recent reports from Kilpatrick *et al.* have described the unusual reactivity of the double-sandwich complex, $(\mu\text{–}\eta^5\text{:}\eta^5\text{–}Pn^\dagger)_2Ti_2$ ($Pn^\dagger = [C_8H_4\{Si^iPr_3\text{−}1,4\}_2]^{2-}$), formed by reduction of the η^8-pentalene complex, $(Pn^\dagger Ti)(\mu\text{–}Cl)_3$.[3–7] $(\mu\text{–}\eta^5\text{:}\eta^5\text{–}Pn^\dagger)_2Ti_2$ was observed to reductively deoxygenate CO_2, as well as forming a "tuck-in" complex in the presence of an *N*-heterocyclic carbene, with concomitant formation of a bridging hydride moiety.[8] The first reports on the reduction of zirconium η^8–pentalene complexes demonstrated the ability of the Pn*Zr(II) fragment to activate arenes, although the oxidation state of these inverted sandwich compounds could not be confidently assigned.[9]

The rich chemistry of reduced $Cp^R{}_2M$ fragments provides the impetus for this preliminary investigation. $Cp^*{}_2Ti$ has been reported to weakly activate N_2, forming either monomeric $Cp^*{}_2Ti(\eta^1\text{–}N_2)$ or dimeric $(Cp^*{}_2Ti)_2(\mu\text{–}\eta^1\text{:}\eta^1\text{–}N_2)$, while in the absence of N_2, C–H activation of the Cp* ring periphery was observed.[10–12] Reaction products are sensitive to the ancilliary ligand set, which can be illustrated by considering the formal 2-electron of N_2 observed for $(1,2,4\text{–}Me_3\text{–}Cp)_2Ti_2(\mu\text{–}\eta^2\text{:}\eta^2\text{–}N_2)$. Beyond dinitrogen activation, reduced titanocene derivatives have found widespread application in the catalytic functionalisation of epoxide,[13] carbonyl[14–16] and imine[17] functional groups, among many others.[18,19]

In this chapter, the reduction chemistry of $[(Pn^*TiCl(\mu\text{–}Cl)]_2$ is explored with $LiAlH_4$, KC_8, $Li_2[Pn^*]$, and Mg, which are observed to induce chlorine atom abstraction, ligand scrambling and dinitrogen activation. The products are characterised spectroscopically, crystallographically, and computationally, providing an outline for the reactivity of reduced η^8-permethylpentalene titanium complexes.

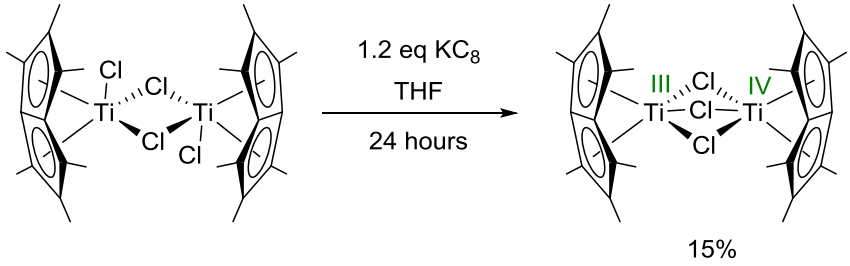
6.2 Synthesis and Characterisation of $(Pn^*Ti)_2(\mu–Cl)_3$

The synthesis of $(Pn^*Ti)_2(\mu–Cl)_3$ was previously been reported by West *et al*. in 2008.[20] Reaction of $[(Pn^*TiCl(\mu–Cl)]_2$ and 1.2 eq KC_8 in THF for 24 hours allowed for the isolation and crystallographic characterisation of a mixed-valence paramagnetic halide complex, $(Pn^*Ti)_2(\mu–Cl)_3$. However, bulk purity was not confirmed and accurate EPR data was not obtained.

While investigating the reactivity of the titanium(IV) chloride dimer, $[(Pn^*TiCl(\mu–Cl)]_2$, $(Pn^*Ti)_2(\mu–Cl)_3$ was observed as the first reduction product under a variety of conditions. In the previous chapter, the reaction of $[(Pn^*TiCl(\mu–Cl)]_2$ and $LiAlH_4$ in THF was observed to produce $Pn^*_2Ti_2H_5Li.THF_x$. However, in benzene, $(Pn^*Ti)_2(\mu–Cl)_3$ is first formed. $[(Pn^*TiCl(\mu–Cl)]_2$ and 4 eq. $LiAlH_4$ were combined in C_6D_6 and monitored over the course of 1 week by ^{1}H NMR spectroscopy, during which time consumption of the starting material was accompanied by a colour change from red-brown to green. The ^{1}H NMR spectrum displayed 3 very weak resonances at 2.27, 1.96 and 1.76 ppm. Slow evaporation of this mixture allowed for the isolation of single-crystals of $(Pn^*Ti)_2(\mu–Cl)_3$.

Pn^*Li_2 was also observed to form this mixed-valence halide when added in an appropriate stoichiometry. 0.5 eq. $Li_2[Pn^*]$ and $[(Pn^*TiCl(\mu–Cl)]_2$ were dissolved in C_6D_6 and monitored by ^{1}H NMR spectroscopy over 1 week. The starting material was slowly consumed, as the colour changed from brown-red to green, with a large number of weak resonances observed between 2.70 and 0.78 ppm. Slow evaporation of this reaction mixture again produced single-crystals of $(Pn^*Ti)_2(\mu–Cl)_3$.

However, neither route is well-suited to the preparative synthesis of $(Pn^*Ti)_2(\mu–Cl)_3$ due to the concomitant formation of diamagnetic Pn*-containing impurities. In the absence of an improved synthesis, $(Pn^*Ti)_2(\mu–Cl)_3$ was obtained according to the procedure of West, by KC_8 reduction of $[(Pn^*TiCl(\mu–Cl)]_2$ in THF in 15% yield as a pure green solid following crystallisation from pentane at –78 °C (Scheme 6.1).[20]



Scheme 6.1. *Synthesis of (Pn*Ti)$_2$(μ–Cl)$_3$.*

Solutions of (Pn*Ti)$_2$(μ–Cl)$_3$ are intensely green and paramagnetic, with no NMR spectroscopic features resolved in the region 20 to –60 ppm. The product is extremely air-sensitive with pentane solutions partially decolourising to form red-brown unidentified decomposition products in a glove-box atmosphere over 1-2 hours. This severe oxygen/moisture sensitivity is proposed to account for the decreased isolated yields. The complex is EPR-active displaying an isotropic resonance at g_{iso} = 1.9909, with hyperfine coupling resolved to spin active titanium nuclei, Ti^{47} and Ti^{49}, which was successfully modelled for A = 2.3 G for both nuclei (Figure 6.1). No half field signal was observed, which is consistent with an S = ½ ground state for the bimetallic complex.

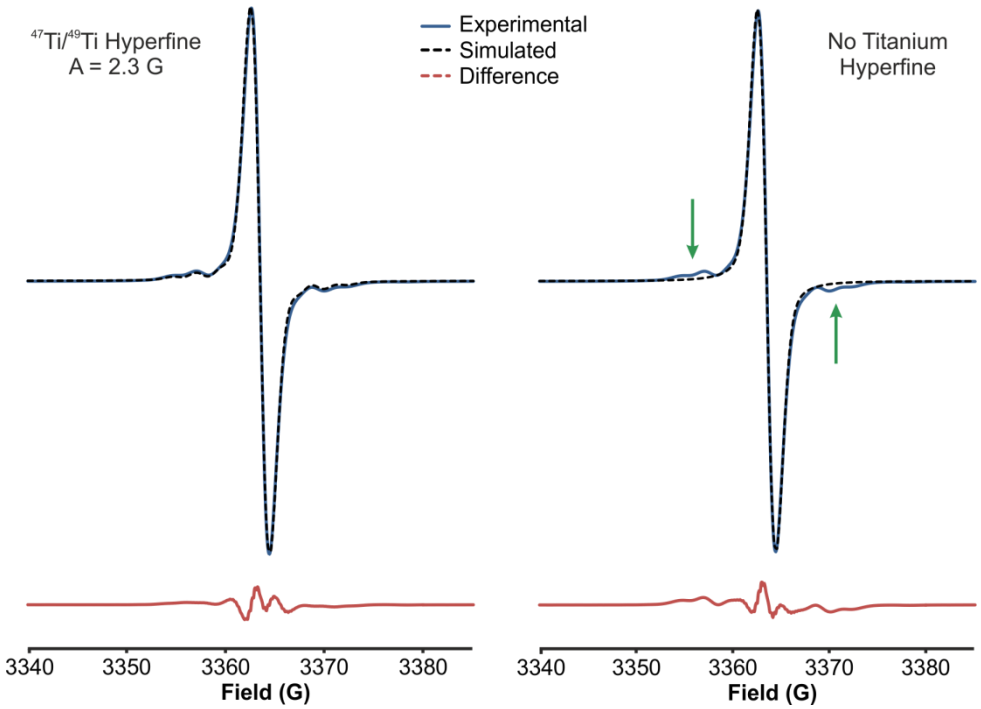


Figure 6.1. *X-band EPR spectrum of (Pn*Ti)$_2$(μ–Cl)$_3$ simulated with titanium hyperfine coupling (left) and without (right). Toluene solution, 298K.*

The related silylated complex. $Pn^{\dagger}{}_2Ti_2(\mu\text{–}Cl_3)$, has previously been synthesised by reaction of $TiCl_3(THF)_3$ and $[K]_2Pn^{\dagger}$.[3,21] It is similarly paramagnetic, and was found to be temperature sensitive, decomposing to an unidentified orange product over 12 hours at room temperature. Its EPR spectrum was recorded, displaying a principle signal at g = 1.985, indicating a greater degree of spin-orbit coupling relative to the Pn* derivative. Similarly, the isoelectronic complex, $[(\eta^8\text{–}COT')Ti]_2(\mu\text{–}Cl)_3$ (COT′ = $[C_8H_6\{Si^iPr_3\text{−}1,4\}_2]^{2-}$), displays an isotropic g value of 1.988 in a toluene glass at 133 K.[22]

Unrestricted Hartee-Fock DFT calculations were carried out on $(Pn^*Ti)_2(\mu\text{–}Cl)_3$ with eclipsed Pn* ligands at the B3LYP level of theory.[23–25] The bond metrics are compared to the previously reported structural data in Table 6.1.

	Staggered	Eclipsed	Eclipsed Calculated
Fold Angle (Ti1/3)	32.21(13)	32.93(11)	29.68
Fold Angle (Ti2/4)	33.16(13)	33.11(11)	32.88
Ti1/3–Pn^*_{cent}	1.9458(12)	1.9484(11)	1.9898
	1.9507(12)	1.9481(11)	1.9839
Ti2/4–Pn^*_{cent}	1.9578(12)	1.9574(10)	1.9705
	1.9518(12)	1.9443(10)	1.9581
Ti1/3–Cl	2.5004(7)	2.4552(6)	2.4612
	2.4916(7)	2.5094(8)	2.4435
	2.5430(8)	2.4911(7)	2.4706
Ti2/4–Cl	2.4465(7)	2.4975(7)	2.6529
	2.4262(7)	2.4439(7)	2.6534
	2.4923(8)	2.5057(8)	2.6180

Table 6.1. *Comparison of experimental and calculated bond lengths (Å) and angles (°) of $(Pn^*Ti)_2(\mu\text{–}Cl)_3$.*

The calculations predict localisation of the unpaired electron on a single titanium centre with the SOMO highlighted in Figure 6.2, composed primarily of d_{xz} (46%) and $d_{x^2\text{-}y^2}$ (41%) obritals. No Ti–Ti bonding interaction was predicted, although weaker Ti–Cl bonds to the Ti(III) centre are demonstrated by reduction in the Mayer bond orders

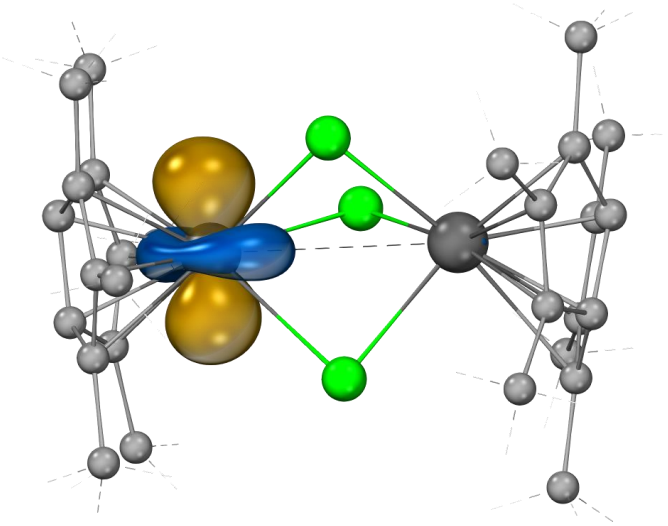
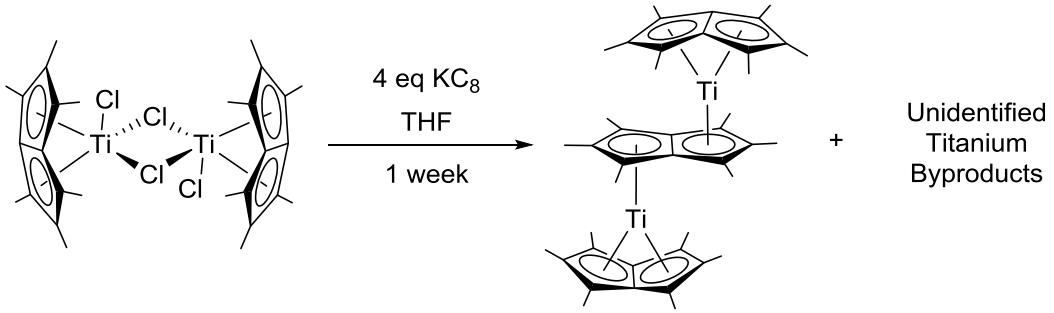


Figure 6.2. *Calculated SOMO of (Pn*Ti)$_2$(μ–Cl)$_3$.*

(average of Ti(III)–Cl and Ti(IV)–Cl = 0.357 *vs* 0.657 respectively). This localised description predicts a much larger variation in the bond metrics for each titanium centre than observed experimentally. For example, the difference in the average Ti–Cl bond lengths is calculated as 0.183 Å, where the experimentally observed difference is 0.003 Å. This may indicate the inadequacy of a localised bonding model or alternatively may reflect spin-disorder in the single-crystalline sample.

6.3 Synthesis and characterisation of (η^8–Pn*)Ti(μ–η^5;η^5–Pn*)Ti(η^8–Pn*)

Although reduction of [(Pn*TiCl(μ–Cl)]$_2$ to (Pn*Ti)$_2$(μ–Cl)$_3$ is facile with KC_8, subsequent reduction occurs less rapidly. Reacting [(Pn*TiCl(μ–Cl)]$_2$ with 3 eq KC_8 for 1 hour, the only species resolved by EPR spectroscopy is (Pn*Ti)$_2$(μ–Cl)$_3$. However, further reduction occurs over longer time periods; reaction with 4 eq. KC_8 over 1 week in THF produces a complex ^{1}H NMR spectrum that could not be assigned, containing a mixture of diamagnetic and paramagnetic components. Slow evaporation of a THF solution allowed for the isolation of X-ray quality single crystals of (η^8–Pn*)Ti(μ–η^5;η^5–Pn*)Ti(η^8–Pn*), the first homoleptic triple-decker metallocene of pentalene reported to date (Scheme 6.2, Figure 6.3). It can be seen, on mass balance, that abstraction of a Pn* ligand must have occurred, presumably by disproportionation forming unknown titanium by-products.



Scheme 6.2. *Synthesis of (η^8–Pn*)Ti(μ–η^5;η^5–Pn*)Ti(η^8–Pn*) by KC_8 reduction.*

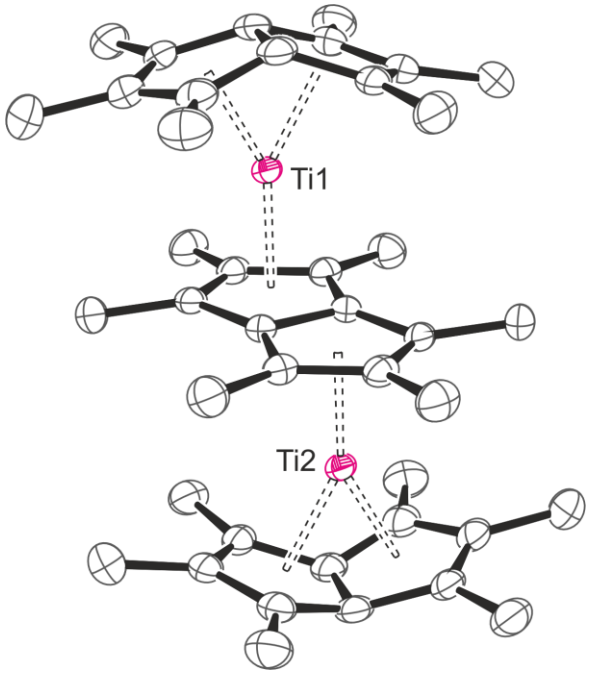


Figure 6.3. *Thermal displacement ellipsoid plot (50% probability) of (η^8–Pn*)Ti(μ–η^5;η^5–Pn*)Ti(η^8–Pn*). Disordered molecule and H atoms omitted for clarity.*

A number of similar *trans*–μ–η^5:η^5–Pn^R complexes have previously been reported. *Trans*-$(Cp^*Fe)_2Pn^R$ (Pn^R = $Pn^\dagger$, Pn*) can be synthesised by the reaction of $M_2[Pn^R]$ (M = K, Li; Pn^R = $Pn^\dagger$, Pn*) and 2 equivalents of Cp*FeCl(TMEDA), producing triple-decker analogues to ferrocene.[26,27] The cobaltacene analogues can similarly be synthesised by the addition of $M_2[Pn^R]$ to Cp*Co(acac) (acac = acetylacetonate).[27,28] Manriquez *et al.* reported a series of neutral, mono- and di-cationic complexes, $[Cp^*M(Pn)M'Cp^*]^{n+}$ (M, M′ = Fe, Fe; Co, Co; Ni, Ni; Ru, Ru; Fe, Ru; Fe, Co; *n* = 0, 1, 2). Significant electronic interactions between the metal centres were proposed on the basis of electrochemical, UV/Vis and magnetic susceptibility studies.[29] The rare earth elements

have also been observed to adopt this bonding mode in *trans*-$(Cp^*Ln)_2Pn^\dagger$ (Ln = Eu, Yb, Sm) and *trans*-$[Cp^*Ln(THF)_2]_2Pn^\dagger$ (Ln = Eu, Yb).[21,30,31] However, this geometry has not previously been observed with group 4 metals.

Two molecules are found in the asymmetric unit, one of which contains one η^8–Pn* ligand disordered over two positions. Bond metrics are given for the molecule displaying no disorder (Table 6.2). No significant canting of the Pn* ligand is observed, in contrast to previously discussed η^8–Pn* complexes, and the titanium atoms are bound rather symmetrically to the bridging Pn* moiety. This can be measured by taking the difference between the average Ti–C(bridgehead) distances and the remaining Ti–C(wingtip) bond lengths, Δ, illustrated in Figure 6.4. The observed value of 0.0517 Å convincingly indicates η^5–coordination, rather than the allyl-like η^3–coordination as reported for *trans*-$(Cp^*Ni)_2Pn^*$ (Δ = 0.2652 Å).[27] The observed fold angles of 34.21(16)° and 33.87(15)° are significantly contracted relative to Pn*TiCp (29.19(7)°), which likely reflects the improved donor capacity of Cp^- when compared to $[\eta^5$–Pn*$]^-$.

$(\eta^8$–Pn*$)$Ti$(\mu$–η^5:η^5–Pn*$)$Ti$(\eta^8$–Pn*$)$	
Fold Angle	34.21(16)
	33.87(15)
Ti– η^8–Pn*$_{cent}$	1.9492(14)
Ti– η^5–Pn*$_{cent}$	2.0096(13)
Δ	0.0517

Table 6.2. *Comparison of selected bond lengths (Å) and angles (°) for $(\eta^8$–Pn*$)$Ti$(\mu$–η^5;η^5–Pn*$)$Ti$(\eta^8$–Pn*$)$. Obtained from the molecule in the asymmetric unit displaying no disorder.*

These structural data are consistent with the formation of two 17 valence electron d^1 titanium centres, and can be represented according to the CBC formalism as shown in Figure 6.4.

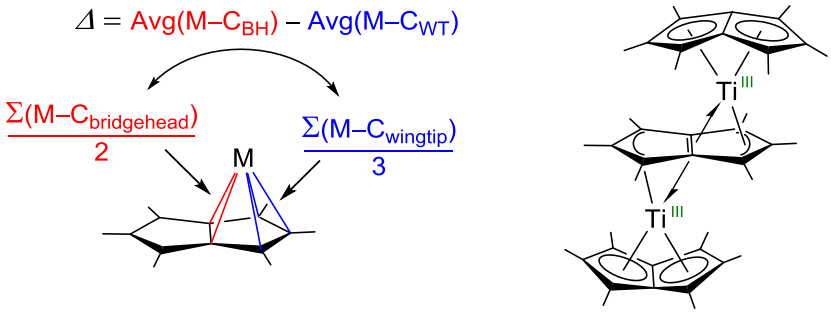
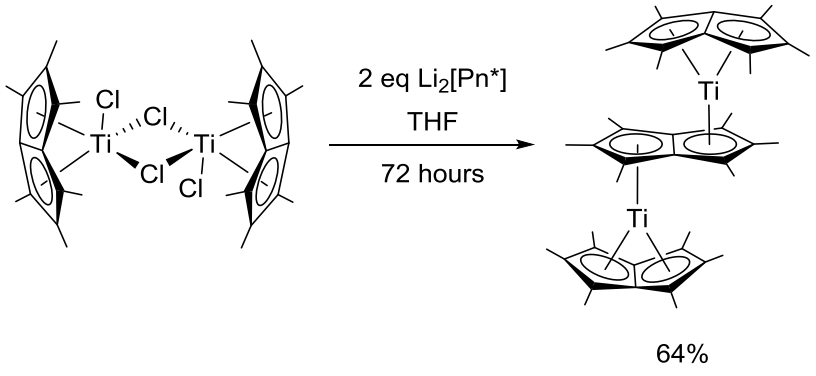


Figure 6.4. *Left: Illustration of the structural parameter, Δ. Right: Representation of (η^8–Pn*)Ti(μ–η^5;η^5–Pn*)Ti(η^8–Pn*) according to CBC formalism.*

Given the ligand scrambling required to form this complex by KC_8 reduction, a rational synthetic route was desireable. Reaction of [(Pn*TiCl(μ–Cl)]$_2$ with 2 eq Li_2[Pn*] in THF over 72 hours deposited brown single crystals, which were confirmed as (η^8–Pn*)Ti(μ–η^5;η^5–Pn*)Ti(η^8–Pn*) by X-ray diffraction. The bimetallic complex is sparingly soluble in THF, which allows for its straightforward purification by washing with THF, giving (η^8–Pn*)Ti(μ–η^5;η^5–Pn*)Ti(η^8–Pn*) in 64% isolated yield, with analytical purity confirmed by elemental analysis (Scheme 6.3). Given the observation that Li_2[Pn*] will reduce [(Pn*TiCl(μ–Cl)]$_2$ to (Pn*Ti)$_2$(μ–Cl)$_3$, it is postulated that the first equivalent of Li_2[Pn*] reduces the Ti(IV) halide, before a second equivalent undergoes salt-metathesis to form the bimetallic product.



Scheme 6.3. *Synthesis of (η^8–Pn*)Ti(μ–η^5;η^5–Pn*)Ti(η^8–Pn*) by reaction with Li_2[Pn*].*

Weak paramagnetic resonances were resolved in the ^{1}H NMR spectrum of (η^8–Pn*)Ti(μ–η^5;η^5–Pn*)Ti(η^8–Pn*) in C_4D_8O at 24.6, 13.6 and 8.7 ppm, and the complete removal of LiCl can be confirmed by ^{7}Li NMR spectroscopy. X-band EPR spectroscopy of a THF solution at 298 K displays a single sharp peak at g_{iso} = 1.9918, which is slightly

shifted for a powdered crystalline sample to g_{iso} = 1.9925 alongside significant line broadening ($\upsilon_{1/2}$ =18.3 G *vs*. 2.6 G for THF solution). This is slightly shifted relative to Pn*TiCp (g_{iso} = 1.9946), although the latter solution EPR spectrum was measured in in toluene rather than THF. No half-field signal was observed, which suggests poor intermetallic communication and demonstrates the formation of a discrete diradical. Although direct metal-metal interaction would be expected to be weak given the large Ti–Ti distance (4.5389(7) Å), the pentalene ligand has previously been observed to facilitate strong exchange interactions. For example, Cp^*_2Co and Cp^*_2Ni are both paramagnetic, while the bimetallic pentalene analogues, $(Cp^*Co)_2Pn$ and $(Pn^*Ni)_2Pn$, are diamagnetic, with electronic exchange mediated by the delocalised pentalene ligand.[32–34]

The temperature dependent magnetic behaviour was characterised by SQUID magnetometry on powdered crystalline material whose bulk purity was confirmed by elemental analysis. The magnetic susceptibility can be related to temperature by the Curie-Weiss law, where χ is magnetic susceptibility, C is the Curie constant, T is the temperature in Kelvin, and θ is the Curie temperature.

$$\chi = \frac{C}{T - \theta}$$

The sign and magnitude of θ indicates the presence or absence of ferromagnetic or anti-ferromagnetic behaviour when θ is positive and negative respectively. If the Curie-Weiss Law is obeyed, a plot of χ^{-1} *vs* T should produce a straight line of gradient 1/C.[35] After applying a diamagnetic correction[36,37] and accounting for temperature independent paramagnetism[35] a linear plot of $1/\chi$ *vs* T was obtained indicating Curie-Weiss behaviour in the temperature range 10 – 300 K. From this plot, the values of C = 0.3557 K^{-1} mol^{-1} and θ = 0.0487 K^{-1} were calculated, suggesting the absence of magnetic exchange interactions. However, the calculated effective magnetic moment, μ_{eff}, is significantly lower than expected; 1.69 μ_B per complex, and 1.20 μ_B per metal, where values of 2.45 and 1.73 μ_B would be predicted on the basis of the spin only formula (Figure 6.5).

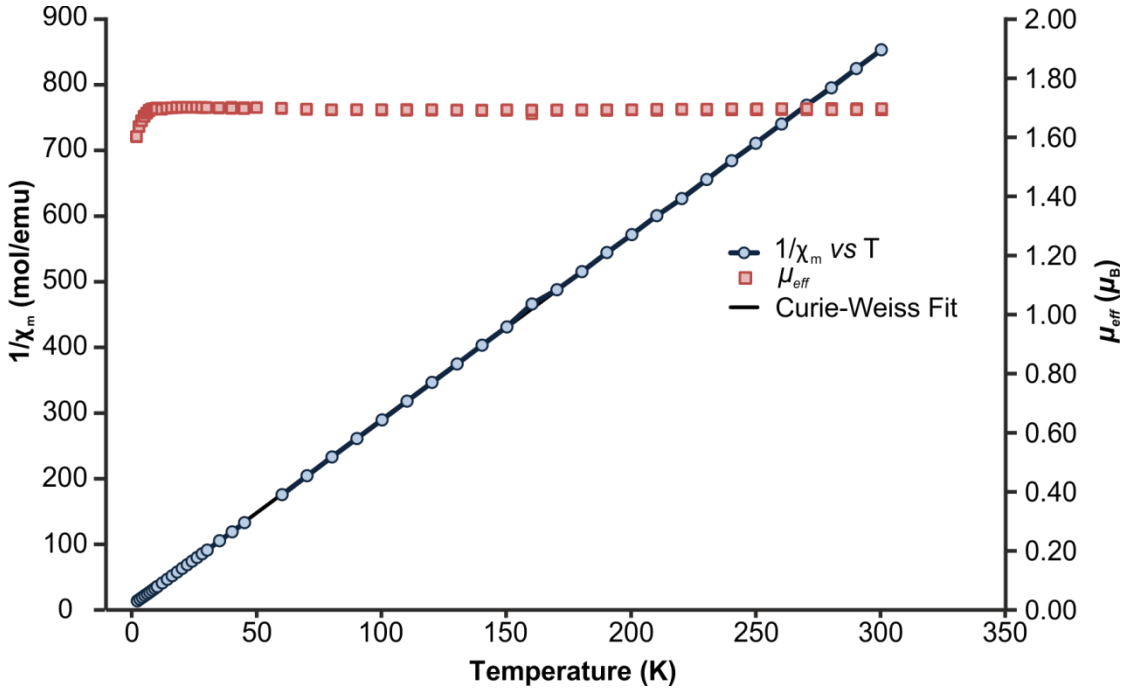


Figure 6.5. *Temperature dependence of the solid state μ_{eff} and $1/\chi_m$ for (η^8–Pn*)Ti(μ–η^5;η^5–Pn*)Ti(η^8–Pn*) at 1000 Oe.*

Spin-orbit coupling (SOC) would be expected to reduce the observed magnetic moment for d^1 metal centres, although the experimental value is significantly decreased. If SOC was responsible, the EPR spectrum should similarly display a large decrease in the observed *g* value. However, (η^8–Pn*)Ti(μ–η^5;η^5–Pn*)Ti(η^8–Pn*) displays an EPR resonance at g_{iso} = 1.9918, a value relatively close to that of the free electron. Alternatively, decomposition of the paramagnetic complex during loading into the SQUID magnetometer may have occurred, leading to partial oxidation of the sample.

Unrestricted Hartree-Fock calculations were carried out on the eclipsed isomer at the B3LYP level of theory. Two SOMOs were identified, separated by 23 kJ/mol, which are shown in Figure 6.6. Spin density is localised on the two titanium atoms (> 99%), in a mixed orbital of of d_{z^2}, d_{xz} and d_{yz} character (48%, 25%, 17% respectively), with the two calculated SOMOs corresponding to an in-phase and out-of-phase combination of these orbitals.

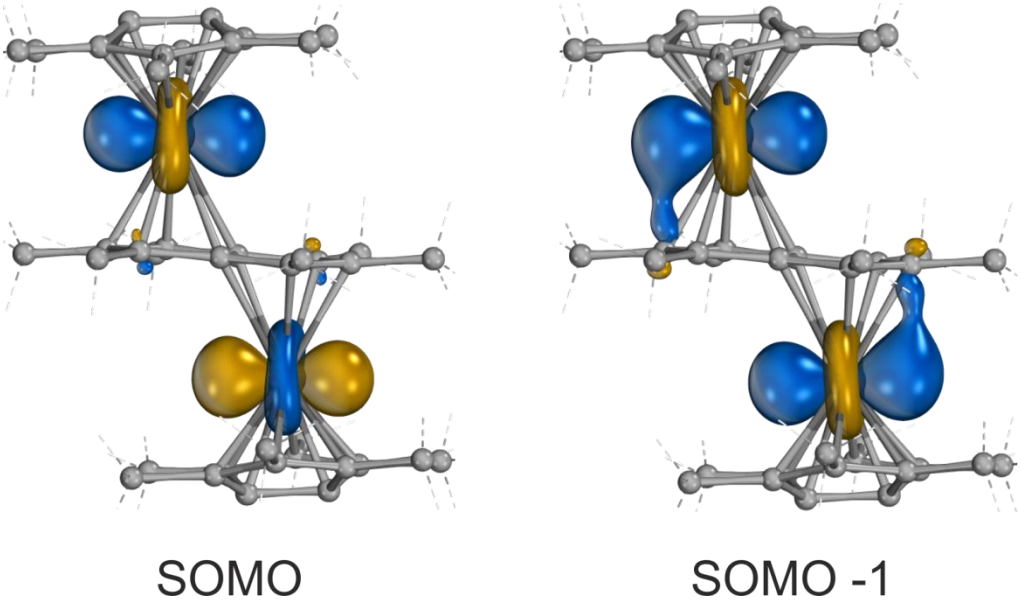
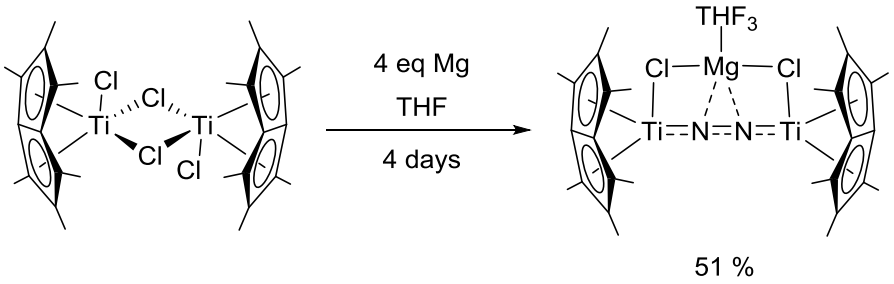


Figure 6.6. *Calculated SOMOs of (η^8–Pn*)Ti(μ–η^5;η^5–Pn*)Ti(η^8–Pn*).*

It has previously been reported by Jonas *et al.* that oxidation of PnTiCp could be achieved using 1,2-dichloroethane or 1,2-dibromoethane.[38] Unfortunately attempts to replicate this oxidation with (η^8–Pn*)Ti(μ–η^5;η^5–Pn*)Ti(η^8–Pn*) were unsuccessful in C_4H_8O at 80 °C over 1 week, perhaps due to the very low solubility of the bimetallic complex in THF.

6.4 Synthesis and Characterisation of Pn*Ti(μ–N_2)TiPn*.$MgCl_2$.3THF

In pursuit of more selective reducing agents than KC_8, Zn and Mg were reacted with [(Pn*TiCl(μ–Cl)]$_2$ in THF. In the case of Zn no reaction was observed after heating to 80 °C for 4 days. However, in the presence of Mg a deep emerald green colour was observed after 1-2 hours, suggesting formation of (Pn*Ti)$_2$(μ–Cl)$_3$. Leaving the reaction for 4 days with periodic agitation, but no stirring, brown crystalline material was deposited, which could be further crystallised from THF at –80 °C, giving Pn*Ti(μ–N_2)TiPn*.$MgCl_2$.3THF in 51% yield (Scheme 6.4).



Scheme 6.4. *Synthesis of Pn*Ti(μ–N_2)TiPn*.$MgCl_2$.3THF.*

Single crystals suitable for an X-ray diffraction study were deposited from the magnesium reduction of $(Pn^*TiCl)_2(\mu–Cl)_2$ in THF in an NMR tube (Figure 6.7, Table 6.3). The Ti–N_2–Ti moiety is braced by a near linear $MgCl_2$ fragment (172.02(2)°), stabilised by 3 molecules of THF. The N_2 ligand is bound end-on ($\mu–\eta^1:\eta^1–N_2$), as opposed to side on ($\mu–\eta^2:\eta^2–N_2$), which is often encountered for group 4 dinitrogen complexes.[39] A number of Lewis structures could be considered to represent the complex, from formal extremes of $(Ti^{2+})_2 – (N_2)^0$ to $(Ti^{4+})_2 – (N_2)^{4–}$ (Figure 6.8). The observed N–N bond length of 1.289(2) Å is consistent with two-electron reduction of dinitrogen to $(N_2)^{2–}$ (PhN=NPh = 1.255 Å, free N_2 = 1.0975 Å, $H_2N–NH_2$ = 1.460 Å).[40] However, the fold angles are relatively large at 34.19(9)° and 34.25(9)°, which are typical of a more oxidised titanium (IV) centre.

Pn*Ti(μ–N_2)TiPn*.$MgCl_2$.3THF	
Fold Angle	34.19(9)
	34.25(9)
Ti–Pn^*_{cent} [a]	1.9775(9)
Ti–N	1.8061(5)
	1.8101(5)
N–N	1.289(2)
Ti–Cl	2.4633(5)
	2.4388(5)
Mg–Cl	2.6816(7)
	2.6144(7)

Table 6.3. *Comparison of selected bond lengths (Å) and angles (°) for Pn*Ti(μ–N_2)TiPn*.$MgCl_2$.3THF. a) average of 4 values.*

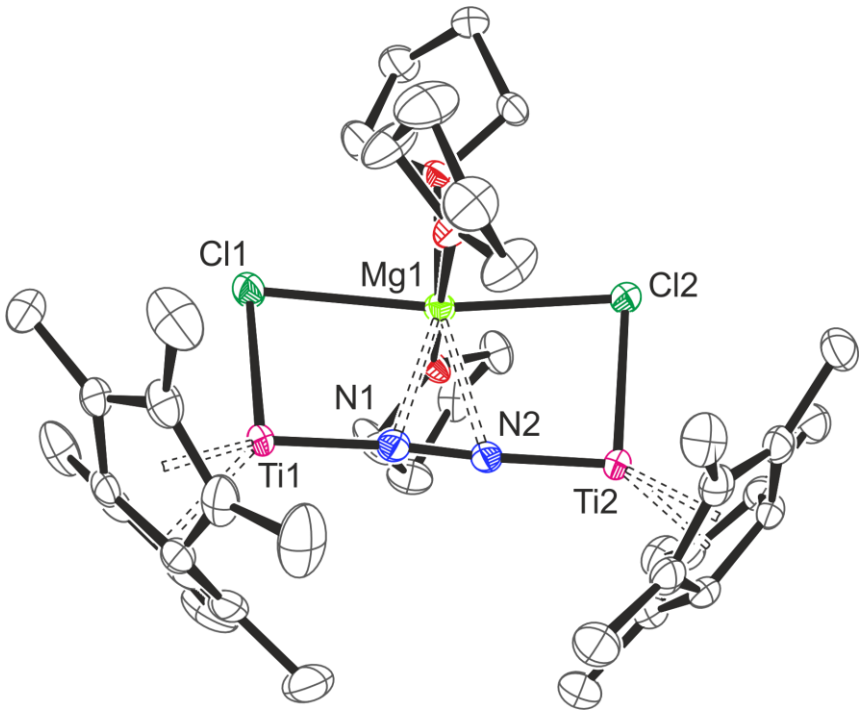


Figure 6.7. *Thermal displacement ellipsoid plot (50% probability) of Pn*Ti(μ–N_2)TiPn*.$MgCl_2$.3THF.*

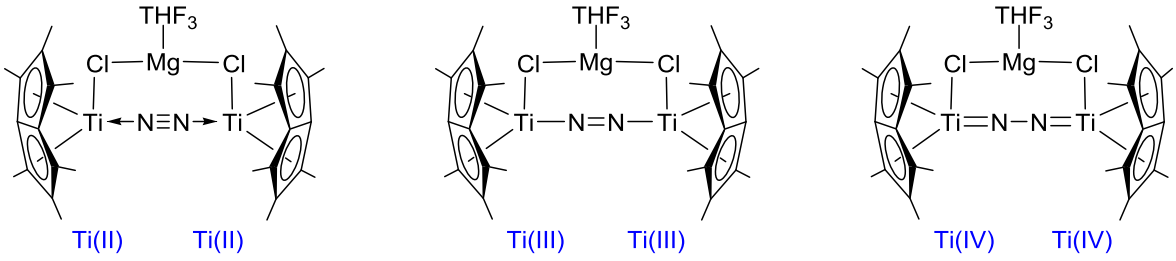


Figure 6.8. *Illustration of possible Lewis structures and titanium oxidation states for Pn*Ti(μ–N_2)TiPn*.$MgCl_2$.3THF.*

Insight into the oxidation state of the titanium centres, and therefore the extent of N_2 activation, could be obtained by EPR spectroscopy, so to that end the crude crystalline material deposited in the reaction vessel was dissolved in THF and the EPR spectrum collected. This did not indicate the formation of any new paramagnetic species, although small amounts of (η^8–Pn*)Ti(μ–η^5;η^5–Pn*)Ti(η^8–Pn*) could be observed, indicating parallel reactivity for both Mg and KC_8 reductants.

Pn*Ti(μ–N_2)TiPn*.$MgCl_2$.3THF is diamagnetic in C_4D_8O solution, displaying three Pn*–*Me* resonances in ^{1}H NMR spectra at 2.29, 1.90 and 1.88 ppm. No IR-active N_2

stretching frequency could be observed, however, an N–N stretch was observed by Raman spectroscopy at 1286 cm^{-1}, significantly red-shfited relative to free N_2 (2331 cm^{-1}).[41] The observed stretching frequency is between that expected for $(N_2)^{2-}$ and $(N_2)^{4-}$, the former of which generally displays stretches in the region 1700 – 1400 cm^{-1}. For example $\{[N_3N]Mo–N=N\}_2Mg(THF)_2$ (N_3N = $[(Me_3SiNCH_2CH_2)_3N]^{3-}$) displays an IR stretch as 1718 cm^{-1},[42] while $[(1,2,4–^tBu–Cp)_2Nd]_2(\mu–\eta^2:\eta^2–N_2)$[43] and $[\{Me_3Si)_2N\}_2Y(THF)]_2(\mu–\eta^2:\eta^2–N_2)$[44] demonstrate N–N stretching frequencies of 1622 and 1425 cm^{-1} respectively. By contrast an $(N_2)^{4-}$ ligand would be expected to resonate below 1000 cm^{-1}, as found for $\{[(^iPr_2PCH_2SiMe_2)_2N]Zr(O–2,6–Me_2C_6H_3)\}_2(\mu–\eta^2:\eta^2–N_2)$ (751 cm^{-1}).[45]

These data appear difficult to accommodate into a coherent picture of bonding. On the basis of N–N bond lengths, an $(N_2)^{2-}$ formulation would be proposed, however the Raman stretching frequency is between the expected values of $(N_2)^{2-}$ and $(N_2)^{4-}$. On the basis of the complex's diamagnetism, $(N_2)^{4-}$ appears most likely, which is corroborated by the sharp fold angles (> 34°).

Density functional theory calculations were carried out at the B3LYP level of theory on $Pn^*Ti(\mu–N_2)TiPn^*.MgCl_2.3THF$, in order to gain a better understanding into the nature of the bonding in this complex and to resolve some of these conflicting pieces of data. The calculations were found to reproduce the experimental data well, with the computed N–N bond length of 1.2968 Å in close agreement with the crystallographically determined bond length of 1.289(2) Å. The major Ti–N bonding orbitals are displayed in Figure 6.9. The HOMO and HOMO –1 illustrate overlap of two orthogonal nitrogen-based p-orbitals with two Ti-based frontier orbitals of suitable symmetry. These are highly covalent interactions with the HOMO composed of 55% Ti, 45% N_2, while the HOMO –1 is 52% Ti, 48% N_2. Unusually, HOMO –2 and HOMO –3 show overlap of these p-orbitals with a Pn*–Ti bonding orbital that is generally uninvolved in co-ligand bonding, and normally exclusively describes metal-carbocycle bonding. Tellingly, all these high-lying orbitals are anti-bonding with respect to the N–N bond, illustrating how electron donation from metal to the bound N_2 weakens this bond. Indeed, the predicted N–N bond order is only 1.113,

while Ti–N bond orders of 1.580 and 1.591 are calculated. Weak Mg–N interactions (bond orders of 0.172 and 0.186) and Ti–Ti bonds (0.289) are also predicted.

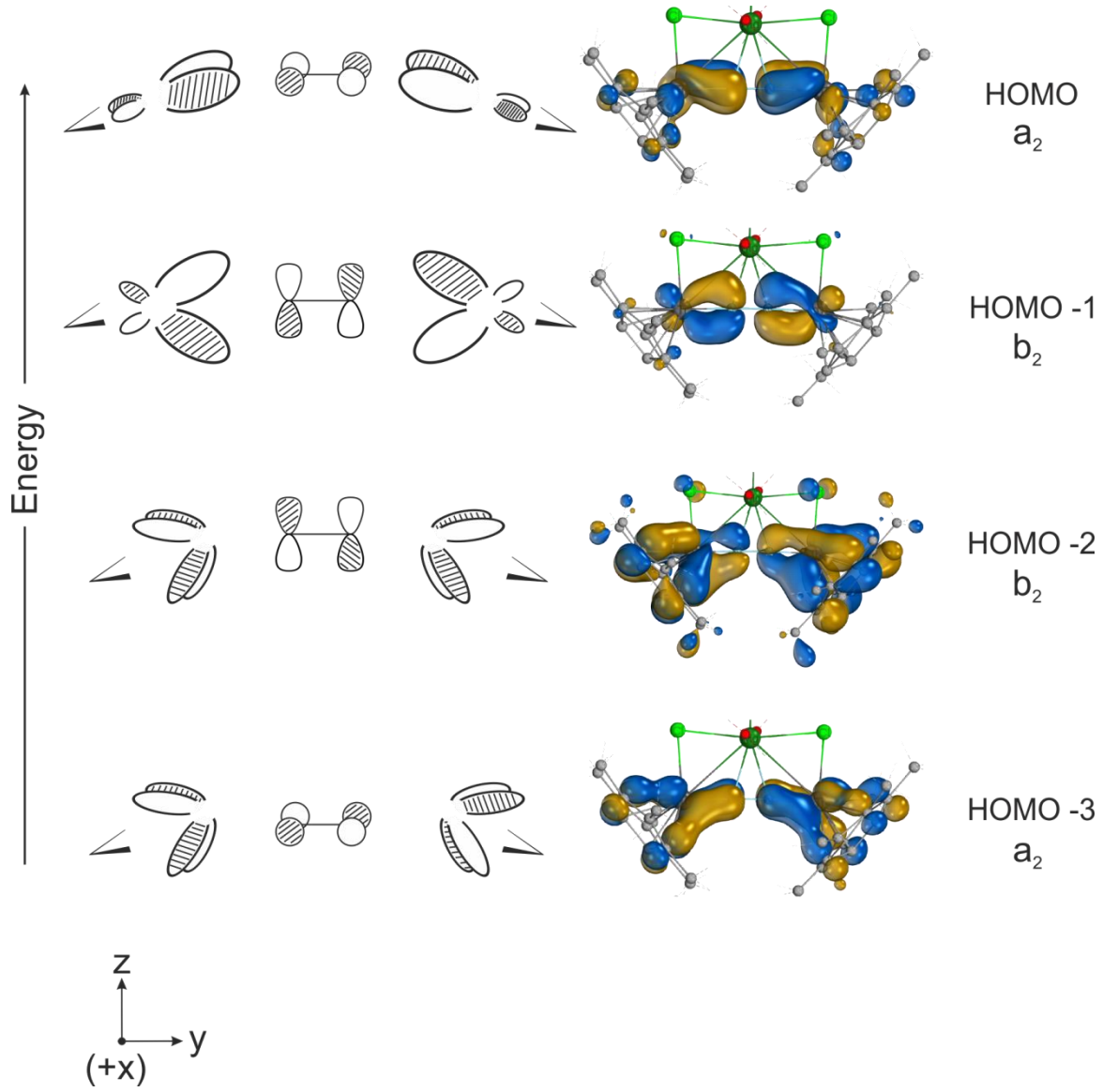


Figure 6.9. *Illustration of frontier molecular orbitals of Pn*Ti(μ–N_2)TiPn*.$MgCl_2$.3THF.*

An interesting comparison can be made to {[$(Me_3Si)_2$N]TiCl(TMEDA)}$_2$(μ–η^1:η^1–N_2), which displays very similar structural and spectroscopic features to Pn*Ti(μ–η^1:η^1–N_2)TiPn*.$MgCl_2$.THF_3.[46–48] The compound is diamagnetic, with an N–N bond length of 1.289(9), while a Raman active stretch was observed at 1284 cm^{-1} (c.f. 1.289(2) and 1286 cm^{-1} in this work). Similarly each Ti(II) fragment, [$(Me_3Si)_2$N]TiCl(TMEDA), could be envisaged to donate between 0 and 2 electrons. Computational studies by Studt *et al.* attempted to rationalise the bonding in terms of its molecular orbitals and charge distributions. They note the formal transfer of 4 electrons from both titanium centres to produce a notionally $(N_2)^{4-}$ ligand. The molecular orbitals that describe this interaction are

the HOMO and HOMO –1, which are highly covalent (46% and 44% Ti, N; 49% 44% Ti, N; HOMO and HOMO –1 respectively), similar to the HOMO and HOMO –1 calculated for Pn*Ti(μ–η^1:η^1–N_2)TiPn*.$MgCl_2$.THF_3. Given this covalency, the authors suggest the effective charge transfer to the N_2 ligand is in fact approximately half; the complex is Ti(IV), Ti(IV) and $(N_2)^{2-}$ simultaneously. A similar description would account well for the experimental data presented for Pn*Ti(μ–η^1:η^1–N_2)TiPn*.$MgCl_2$.THF_3.

6.5 Synthesis of Pn*$_2$Ti$_2$HK.THF

$(Pn^*Ti)_2(\mu–Cl)_3$ was prepared from $(Pn^*TiCl)_2(\mu–Cl)_3$ and $LiAlH_4$ in benzene. The product obtained was slightly impure; a weak diamagnetic component was resolved with three Pn*–Me resonances at 2.28, 2.27 and 2.04 ppm. This product was heated to 75 °C in C_4D_8O with 4 eq KH for 4 days during which time 8 new singlets were observed by ^{1}H NMR spectroscopy alongside the formation of two new paramagnetic resonances at 8.7 and 13.7 ppm. Slow evaporation of this crude mixture allowed for the serendipitous isolation of single crystals of Pn*$_2$Ti$_2$HK.THF (Figure 6.10).

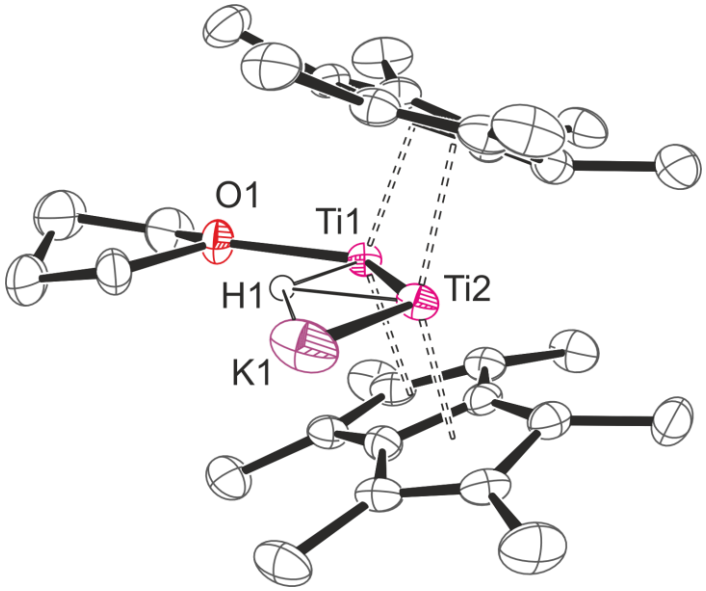


Figure 6.10. *Thermal displacement ellipsoid plot (50% probability) of Pn*$_2$Ti$_2$HK.THF. H atoms omitted for clarity.*

The structure is similar to the double sandwich complex, $(Pn^{\dagger}Ti)_2(NHC)(\mu_2–H)(\mu_1–H)$ (NHC = 1,3,4,5-tetramethylimidazol-2-ylidene) recent reported by Cloke and coworkers.[8] However, considering the structure of Pn*$_2$Ti$_2$HK.THF as a potassium "-ate" complex

would lead to the proposition of a Ti(II) oxidation state. Unfortunately, time limitations prevented a more detailed study on this complex that might shed light on its bonding and reactivity.

6.6 Conclusions

The previously reported mixed-valence halide dimer, $(Pn^*Ti)_2(\mu–Cl)_3$, was observed in the reduction of $[Pn^*TiCl(\mu–Cl)]_2$ with $LiAlH_4$ and $Li_2[Pn^*]$ in benzene, however, the presence of diamagnetic impurities limited the synthetic usefulness of these routes. $(Pn^*Ti)_2(\mu–Cl)_3$ was characterised by EPR spectroscopy, which demonstrated coupling of the unpaired spin to Ti^{47}/Ti^{49} nuclei. Attempts to reproduce previously reported structural data by DFT calculations were unsuccessful, predicting unobserved bond length variation in a spin-localised bonding description.

The first homoleptic bimetallic pentalene complex, $(\eta^8–Pn^*)Ti(\mu–\eta^5;\eta^5–Pn^*)Ti(\eta^8–Pn^*)$, was synthesised initially by reduction of $[Pn^*TiCl(\mu–Cl)]_2$ with 4 eq. KC_8. A rational route was developed, employing $Li_2[Pn^*]$ as both the reducing agent and Pn* transfer reagent. The product was characterised by EPR spectroscopy, however, accurate magnetic susceptibility data could not be obtained.

A dinitrogen activation complex, $Pn^*Ti(\mu–\eta^1:\eta^1–N_2)TiPn^*.MgCl_2.THF_3$, was obtained from the magnesium reduction of $[Pn^*TiCl(\mu–Cl)]_2$. The structural and spectroscopic data provide conflicting indications as to the extent of dinitrogen activation and the oxidation state of the titanium centres. However, by comparison to the similar data previously reported for $[(Me_3Si)_2N]TiCl(TMEDA)$, the structure is formulated as two Ti(IV) centres bound to an $N_2^{2–}$ ligand.

6.7 References

(1) Summerscales, O. T.; Cloke, F. G. N. *Coord. Chem. Rev.* **2006**, *250* (9–10), 1122–1140.
(2) Cloke, F. G. N.; Green, J. C.; Kilpatrick, A. F. R.; O'Hare, D. *Coord. Chem. Rev.* **2017**, *344*, 238–262.
(3) Kilpatrick, A. F. R.; Green, J. C.; Cloke, F. G. N.; Tsoureas, N. *Chem. Commun.* **2013**, *49* (82), 9434.
(4) Kilpatrick, A. F. R.; Cloke, F. G. N. *Chem. Commun.* **2014**, *50* (21), 2769.
(5) Kilpatrick, A. F. R.; Green, J. C.; Cloke, F. G. N. *Organometallics* **2015**, *34* (20), 4816–4829.
(6) Kilpatrick, A. F. R.; Green, J. C.; Cloke, F. G. N. *Organometallics* **2017**, *36* (2), 352–362.
(7) Kilpatrick, A. F. R.; Green, J. C.; Cloke, F. G. N. *Organometallics* **2015**, *34* (20), 4830–4843.
(8) Tsoureas, N.; Green, J. C.; Cloke, F. G. N. *Chem. Commun.* **2017**, *53* (98), 13117–13120.
(9) Kilpatrick, A. F. R.; Green, J. C.; Turner, Z. R.; Buffet, J.-C.; O'Hare, D. *Chem. Commun.* **2017**, *53* (88), 12048–12051.
(10) Brintzinger, H.; Bercaw, J. E. *J. Am. Chem. Soc.* **1971**, *93* (8), 2045–2046.
(11) Bercaw, J. E. *J. Am. Chem. Soc.* **1974**, *96* (16), 5087–5095.
(12) Manriquez, J. M.; Bercaw, J. E. *J. Am. Chem. Soc.* **1974**, *96* (19), 6229–6230.
(13) Gansäuer, A.; Hildebrandt, S.; Michelmann, A.; Dahmen, T.; von Laufenberg, D.; Kube, C.; Fianu, G. D.; Flowers, R. A. *Angew. Chem. Int. Ed.* **2015**, *54* (24), 7003–7006.
(14) Fleury, L. M.; Ashfeld, B. L. *Org. Lett.* **2009**, *11* (24), 5670–5673.
(15) Streuff, J.; Feurer, M.; Frey, G.; Steffani, A.; Kacprzak, S.; Weweler, J.; Leijendekker, L. H.; Kratzert, D.; Plattner, D. A. *J. Am. Chem. Soc.* **2015**, *137* (45), 14396–14405.
(16) Barrero, A. F.; Rosales, A.; Cuerva, J. M.; Gansäuer, A.; Oltra, J. E. *Tetrahedron Lett.* **2003**, *44* (5), 1079–1082.
(17) Gruber-Woelfler, H.; Khinast, J. G.; Flock, M.; Fischer, R. C.; Sassmannshausen, J.; Stanoeva, T.; Gescheidt, G. *Organometallics* **2009**, *28* (8), 2546–2553.
(18) Harrod, J. F. *Coord. Chem. Rev.* **2000**, *206–207*, 493–531.
(19) Clark, T. J.; Russell, C. A.; Manners, I. *J. Am. Chem. Soc.* **2006**, *128* (30), 9582–9583.
(20) West, R. M.Chem. Thesis, University of Oxford, 2008.
(21) Kilpatrick, A. F. R. Ph.D Thesis, University of Sussex, 2014.
(22) Horáček, M.; Kupfer, V.; Thewalt, U.; Polášek, M.; Mach, K. *J. Organomet. Chem.* **1999**, *579* (1–2), 126–132.
(23) Becke, A. D. *J. Chem. Phys.* **1986**, *84* (8), 4524–4529.
(24) Lee, C.; Yang, W.; Parr, R. G. *Phys. Rev. B* **1988**, *37* (2), 785–789.
(25) Becke, A. D. *J. Chem. Phys.* **1993**, *98* (7), 5648–5652.
(26) Kilpatrick, A. F. R.; Johnston, D. R.; Green, J. C.; Tsoureas, N.; Coles, M. P.; Cloke, F. G. N. *Polyhedron* **2016**, *116*, 26–37.
(27) Binding, S. C. D.Phil Thesis, University of Oxford, 2015.
(28) Bunel, E. E.; Valle, L.; Jones, N. L.; Carroll, P. J.; Barra, C.; Gonzalez, M.; Munoz, N.; Visconti, G.; Aizman, A.; Manriquez, J. M. *J. Am. Chem. Soc.* **1988**, *110* (19),

6596–6598.
(29) Manriquez, J. M.; Ward, M. D.; Reiff, W. M.; Calabrese, J. C.; Jones, N. L.; Carroll, P. J.; Bunel, E. E.; Miller, J. S. *J. Am. Chem. Soc.* **1995**, *117* (23), 6182–6193.
(30) Kilpatrick, A. F. R.; Cloke, F. G. N. *Dalton Trans.* **2017**, *46* (17), 5587–5597.
(31) Summerscales, O. T.; Jones, S. C.; Cloke, F. G. N.; Hitchcock, P. B. *Organometallics* **2009**, *28* (20), 5896–5908.
(32) Bunel, E. E.; Valle, L.; Jones, N. L.; Carroll, P. J.; Barra, C.; Gonzalez, M.; Munoz, N.; Visconti, G.; Aizman, A.; Manriquez, J. M. *J. Am. Chem. Soc.* **1988**, *110* (19), 6596–6598.
(33) Kölle, U.; Khouzami, F.; Lueken, H. *Chem. Ber.* **1982**, *115* (3), 1178–1196.
(34) Long, N. J. *Metallocenes : an introduction to sandwich complexes*; Blackwell Science, 1998.
(35) Carlin, R. L. *Magnetochemistry*; Springer Berlin Heidelberg: Berlin, Heidelberg, 1986.
(36) Bain, G. A.; Berry, J. F. *J. Chem. Educ.* **2008**, *85* (4), 532.
(37) Baker, W. A.; Janus, A. R. *J. Inorg. Nucl. Chem.* **1964**, *26* (12), 2087–2097.
(38) Jonas, K.; Kolb, P.; Kollbach, G.; Gabor, B.; Mynott, R.; Angermund, K.; Heinemann, O.; Krüger, C. *Angew. Chem. Int. Ed.* **1997**, *36* (16), 1714–1718.
(39) MacLachlan, E. A.; Fryzuk, M. D. *Organometallics* **2006**, *25* (7), 1530–1543.
(40) Fryzuk, M. D.; Johnson, S. A. *Coord. Chem. Rev.* **2000**, *200–202*, 379–409.
(41) Walter, M. D. In *Advances in Organometallic Chemistry*; Academic Press, 2016; Vol. 65, pp 261–377.
(42) O'Donoghue, M. B.; Davis, W. M.; Schrock, R. R. *Inorg. Chem.* **1998**, *37* (20), 5149–5158.
(43) Jaroschik, F.; Momin, A.; Nief, F.; Le Goff, X.-F.; Deacon, G. B.; Junk, P. C. *Angew. Chem. Int. Ed.* **2009**, *48* (6), 1117–1121.
(44) Evans, W. J.; Lee, D. S.; Rego, D. B.; Perotti, J. M.; Kozimor, S. A.; Moore, E. K.; Ziller, J. W. *J. Am. Chem. Soc.* **2004**, *126* (44), 14574–14582.
(45) Cohen, J. D.; Fryzuk, M. D.; Loehr, T. M.; Mylvaganam, M.; Rettig, S. J. *Inorg. Chem.* **1998**, *37* (1), 112–119.
(46) Studt, F.; Tuczek, F. *J. Comput. Chem.* **2006**, *27* (12), 1278–1291.
(47) Studt, F.; Lehnert, N.; Wiesler, B. E.; Scherer, A.; Beckhaus, R.; Tuczek, F. *Eur. J. Inorg. Chem.* **2006**, *2006* (2), 291–297.
(48) Duchateau, R.; Gambarotta, S.; Beydoun, N.; Bensimon, C. *J. Am. Chem. Soc.* **1991**, *113* (23), 8986–8988.

Appendix A: Polymerisation data tables

Complex	Mol_{Ti}	PE yield (g)	Activity (kg_{PE}/mol·h·bar)	Average Activity	Standard Deviation
$[Pn^*TiCl(\mu–Cl)]_2$	8.19E-07	0.038	23.2	24.4	1.7
	8.19E-07	0.042	25.6		
$Pn^*TiCp(Cl)$	1.49E-06	0.042	28.1	30.1	2.8
	1.49E-06	0.048	32.1		
$Pn^*TiCp^{Me}(Cl)$	1.43E-06	0.034	23.7	25.1	2.0
	1.43E-06	0.038	26.5		
$Pn^*TiCp^{tBu}(Cl)$	1.28E-06	0.057	44.6	35.2	13.3
	1.28E-06	0.033	25.8		
$Pn^*TiInd(Cl)$	1.43E-06	0.0565	39.5	34.5	7.2
	1.43E-06	0.042	29.4		
$Pn^*TiCp(H)$	1.58E-06	0.037	23.4	24.0	0.9
	1.58E-06	0.039	24.7		

Table 1: *Solution phase ethylene polymerisation activity of Pn*Ti complexes. Conditions: 250 eq. MAO, 30 minutes, 50 mL toluene, 2 bar* C_2H_4.

Complex	Mol_{Zr}	PE yield (g)	Activity (kg_{PE}/mol·h·bar)	Average Activity	Standard Deviation	M_W (kDa)	PDI
Pn*ZrCp(Cl)	1.52088E-06	0.603	2378.9	2280.3	139.5	630.9	2.75
	1.52088E-06	0.553	2181.6				
Pn*ZrCp^{Me}(Cl)	1.40274E-06	0.812	3473.2	3353.4	113.1	443.1	2.55
	1.1987E-06	0.649	3248.5				
	1.1987E-06	0.667	3338.6				
Pn*ZrCp^{tBu}(Cl)	1.1516E-06	0.131	682.5	789.3	151.0	188.4	6.55
	1.1516E-06	0.172	896.1				
Pn*ZrCp^{nBu}(Cl)	1.03644E-06	0.568	3288.2	3299.8	16.4		
	1.03644E-06	0.572	3311.3				
Pn*ZrCp^{Me3}(Cl)	1.42806E-06	0.739	3104.9	2773.0	469.4	222.8	2.5
	1.42806E-06	0.581	2441.1				
Pn*ZrInd(Cl)	1.05108E-06	0.612	3493.5	3584.9	129.2	369.0	7.1
	1.05108E-06	0.644	3676.2				
Pn*ZrCp^{Me}(Cl)	1.34524E-06	0.800	3568.1	3307.2	260.9		
	1.34524E-06	0.683	3046.3				
Pn*ZrCp(^{n}Bu)	1.25084E-06	0.532	2551.9	2484.7	95.0	670.5	6.25
	1.25084E-06	0.504	2417.6				

Table 2: *Solution phase ethylene polymerisation with Pn*ZrCp^{R}(X) complexes. Conditions: 250 eq. MAO, 60 °C, 5 minutes, 50 mL toluene, 2 bar C_2H_4.*

Complex	Time (minutes)	Mol_{Zr}	PE yield (g)	Activity (kg_{PE}/mol·h·bar)	Average Activity	Standard Deviation	M_W (kDa)	PDI
Pn*ZrCp(Cl)	5	9.3711E-07	2.428	2590.9	2605.3	20.3	885.25	2.9
	5	9.28743E-07	2.433	2619.7				
	15	8.45072E-07	2.345	2774.9	2832.6	81.6	446.8	2.45
	15	9.12009E-07	2.636	2890.3				
	30	9.45477E-07	3.255	3442.7	3624.1	256.5	388.8	2.6
	30	9.95679E-07	3.789	3805.4				
	60	8.53439E-07	2.604	3051.2	3055.7	6.4	292.75	2.5
	60	8.70173E-07	2.663	3060.3				

Table 3: *Slurry phase ethylene polymerisation of Pn*ZrCp(Cl)$_{sMAO}$. Conditions: [Zr]:[sMAO] = 1:200, 60 °C, 50 mL toluene, 2 bar C_2H_4, 150 mg TiBA.*

Complex	Temperature (°C)	Mol_{Zr}	PE yield (g)	Activity (kg_{PE}/mol·h·bar)	Average Activity	Standard Deviation	M_W (kDa)	PDI
Pn*ZrCp(Cl)	40	9.3711E-07	2.428	2590.9	2605.3	20.3	885.3	2.9
	40	9.2874E-07	2.433	2619.7				
	50	8.4507E-07	2.345	2774.9	2832.6	81.6	446.8	2.45
	50	9.1201E-07	2.636	2890.3				
	60	9.4548E-07	3.255	3442.7	3624.1	256.5	388.8	2.6
	60	9.9568E-07	3.789	3805.4				
	70	8.5344E-07	2.604	3051.2	3055.7	6.4	292.8	2.5
	70	8.7017E-07	2.663	3060.3				
	80	8.7854E-07	2.104	2394.9	2443.0	68.1	248.6	2.7
	80	8.0324E-07	2.001	2491.2				
Pn*ZrCp^{Me}(Cl)	40	8.9714E-07	2.365	2636.2	2563.2	103.2	819.9	3.25
	40	8.7221E-07	2.172	2490.2				
	50	9.0544E-07	2.645	2921.2	2987.9	94.3	523.4	3.1
	50	8.8883E-07	2.715	3054.6				
	60	9.3036E-07	3.964	4260.7	4209.2	72.9	308.5	2.55
	60	8.9714E-07	3.730	4157.7				

Table 4: *Slurry phase ethylene polymerisation of Pn*ZrCp^{R}(X)$_{sMAO}$ complexes. Conditions: [Zr]:[sMAO] = 1:200, 30 minutes, 50 mL toluene, 2 bar C_2H_4, 150 mg TiBA.*

Complex	Temperature (°C)	Mol_{Zr}	PE yield (g)	Activity (kg_{PE}/mol·h·bar)	Average Activity	Standard Deviation	M_W (kDa)	PDI
Pn*ZrCp^{Me}(Cl)	70	8.3899E-07	2.923	3484.0	3367.8	164.3	281.4	3.2
	70	8.2237E-07	2.674	3251.6				
	80	8.8052E-07	2.463	2797.2	2840.7	61.5	308.6	3.05
	80	7.9745E-07	2.3	2884.2				
Pn*ZrCp^{tBu}(Cl)	60	8.2891E-07	0.193	232.8	293.9	86.4	329.9	7.75
	60	8.6207E-07	0.306	354.9				
Pn*ZrCp^{nBu}(Cl)	40	7.9576E-07	3.721	4676.1	4786.0	155.5	556.7	2.85
	40	7.9576E-07	3.896	4896.0				
	50	9.1180E-07	4.719	5175.5	5024.9	213.0	406.4	2.75
	50	9.0351E-07	4.404	4874.3				
	60	9.0351E-07	3.655	4045.3	4096.1	71.8	302.5	2.8
	60	8.2062E-07	3.403	4146.8				
	70	9.6983E-07	3.208	3307.8	3445.6	194.8	212.9	2.8
	70	1.0030E-06	3.594	3583.3				
	80	8.7865E-07	3.039	3458.7	3502.4	61.8	192.7	3.05
	80	9.0351E-07	3.204	3546.2				

Table 4 cont'd: *Slurry phase ethylene polymerisation of Pn*ZrCp^{R}(X)$_{sMAO}$ complexes. Conditions: [Zr]:[sMAO] = 1:200, 30 minutes, 50 mL toluene, 2 bar C_2H_4, 150 mg TiBA.*

Complex	Temperature (°C)	Mol_{Zr}	PE yield (g)	Activity (kg_{PE}/mol·h·bar)	Average Activity	Standard Deviation	M_W (kDa)	PDI
Pn*ZrCp^{Me3}(Cl)	40	8.533E-07	1.439	1686.5	1605.5	114.5	658.8	3.4
	40	9.111E-07	1.389	1524.5				
	50	7.882E-07	1.495	1896.8	1910.9	20.0	609.6	3.35
	50	6.363E-07	1.225	1925.1				
	60	7.303E-07	1.107	1515.7	1567.3	72.9	367.8	3.85
	60	7.376E-07	1.194	1618.8				
	70	8.099E-07	1.388	1713.8	1618.2	135.2	339.2	3.95
	70	6.870E-07	1.046	1522.7				
	80	8.316E-07	1.59	1912.0	1831.9	113.4	280.8	4.25
	80	6.725E-07	1.178	1751.7				
Pn*ZrInd(Cl)	40	7.243E-07	1.578	2178.8	2299.4	170.6	592.5	3.2
	40	7.822E-07	1.893	2420.1				
	50	7.822E-07	1.675	2141.4	2327.2	262.7	524.1	3.35
	50	6.880E-07	1.729	2512.9				
	60	8.329E-07	2.391	2870.7	2840.1	43.3	347.8	3.6
	60	8.112E-07	2.279	2809.5				

Table 4 cont'd: *Slurry phase ethylene polymerisation of Pn*ZrCp^{R}(X)$_{sMAO}$ complexes. Conditions: [Zr]:[sMAO] = 1:200, 30 minutes, 50 mL toluene, 2 bar C_2H_4, 150 mg TiBA.*

Complex	Temperature (°C)	Mol_{Zr}	PE yield (g)	Activity (kg_{PE}/mol·h·bar)	Average Activity	Standard Deviation	M_W (kDa)	PDI
Pn*ZrInd(Cl)	70	6.156E-07	2.028	3294.2	3144.4	211.9	291.1	3.75
	70	7.677E-07	2.299	2994.6				
	80	6.953E-07	2.038	2931.2	2883.0	68.2	232.9	3.95
	80	8.184E-07	2.32	2834.8				
Pn*ZrCp(CH_2Ph)	40	5.8685E-07	1.064	1813.1	1669.2	203.5	957.2	2.85
	40	5.8086E-07	0.886	1525.3				
	50	6.2877E-07	0.956	1520.4	1611.4	128.6	643.2	3.2
	50	6.1679E-07	1.05	1702.4				
	60	5.6290E-07	1.405	2496.0	2429.2	94.4	551.6	3.2
	60	6.1080E-07	1.443	2362.5				
	70	5.6888E-07	1.978	3477.0	3058.9	591.3	335.9	2.85
	70	7.0661E-07	1.866	2640.8				
	80	6.7667E-07	1.966	2905.4	3204.8	423.4	197.1	2.8
	80	7.3057E-07	2.56	3504.1				
Pn*ZrCp(H)	40	7.2622E-07	2.391	1668.9	1711.8	60.7	1034.8	2.95
	40	7.6937E-07	2.279	1754.7				

Table 4 cont'd: *Slurry phase ethylene polymerisation of Pn*ZrCp^R(X)$_{sMAO}$ complexes. Conditions: [Zr]:[sMAO] = 1:200, 30 minutes, 50 mL toluene, 2 bar C_2H_4, 150 mg TiBA.*

Complex	Temperature (°C)	Mol_{Zr}	PE yield (g)	Activity (kg_{PE}/mol·h·bar)	Average Activity	Standard Deviation	M_W (kDa)	PDI
Pn*ZrCp(H)	50	7.6937E-07	1.692	2199.2	2057.8	200.0	730.4	2.9
	50	7.4779E-07	1.433	1916.3				
	60	7.9813E-07	1.839	2304.1	2278.3	36.5	500.3	3
	60	8.0532E-07	1.814	2252.5				
	70	6.9746E-07	1.782	2555.0	2798.8	344.8	386.2	2.65
	70	7.0465E-07	2.144	3042.6				
	80	9.2755E-07	2.347	2530.3	2510.2	28.4	220.8	3
	80	9.0598E-07	2.256	2490.1				
Pn*ZrCp(C_3H_5)	40	8.5644E-07	1.365	1593.8	1658.0	90.8	874.3	3
	40	7.9838E-07	1.375	1722.2				
	50	8.4193E-07	1.571	1866.0	1913.5	67.2	670.3	3.05
	50	7.4757E-07	1.466	1961.0				
	60	6.9677E-07	1.257	1804.0	1751.2	74.8	473.4	3.45
	60	6.8951E-07	1.171	1698.3				
	70	7.1854E-07	1.683	2342.2	2375.6	47.2	303.3	2.85
	70	7.1854E-07	1.731	2409.0				

Table 4 cont'd: *Slurry phase ethylene polymerisation of Pn*ZrCp^R(X)$_{sMAO}$ complexes. Conditions: [Zr]:[sMAO] = 1:200, 30 minutes, 50 mL toluene, 2 bar C_2H_4, 150 mg TiBA.*

Complex	Temperature (°C)	Mol_{Zr}	PE yield (g)	Activity (kg_{PE}/mol·h·bar)	Average Activity	Standard Deviation	M_W (kDa)	PDI
Pn*ZrCp(C_3H_5)	80	6.6048E-07	1.703	2578.4	2482.4	135.8	223.0	3.2
	80	7.4757E-07	1.784	2386.4				
Pn*ZrCp(^{n}Bu)	40	7.882E-07	1.495	1986.7	1890.0	136.7	609.6	3
	40	6.363E-07	1.225	1793.3				
	50	7.303E-07	1.107	2081.5	1931.7	211.8	367.8	2.85
	50	7.376E-07	1.194	1781.9				
	60	8.099E-07	1.388	2324.8	2253.7	100.5	339.2	2.85
	60	6.870E-07	1.046	2182.6				
	70	8.316E-07	1.59	2419.6	2471.0	72.6	280.8	3.05
	70	6.725E-07	1.178	2522.3				
	80	7.243E-07	1.578	2706.4	2650.0	79.7	592.5	2.9
	80	7.822E-07	1.893	2593.7				
Pn*ZrCp(Me)	40	7.3892E-07	1.254	1697.1	1688.3	12.3	793.5	2.9
	40	7.2457E-07	1.217	1679.6				
	50	7.4609E-07	1.411	1891.2	1869.3	31.0	526.4	3
	50	6.2413E-07	1.153	1847.4				

Table 4 cont'd: *Slurry phase ethylene polymerisation of Pn*ZrCp^R(X)$_{sMAO}$ complexes. Conditions: [Zr]:[sMAO] = 1:200, 30 minutes, 50 mL toluene, 2 bar C_2H_4, 150 mg TiBA.*

Complex	Temperature (°C)	Mol_{Zr}	PE yield (g)	Activity (kg_{PE}/mol·h·bar)	Average Activity	Standard Deviation	M_W (kDa)	PDI
Pn*ZrCp(Me)	60	8.9675E-07	2.492	2778.9	2717.2	87.4	389.4	4.3
	60	7.2457E-07	1.924	2655.4				
	70	7.6044E-07	3.12	4102.9	3745.8	505.0	275.6	2.7
	70	7.3892E-07	2.504	3388.7				
	80	6.3131E-07	2.034	3221.9	3373.9	215.1	230.1	2.95
	80	6.3131E-07	2.226	3526.0				
Pn*ZrCp^{Me}(Me)	40	7.5083E-07	1.934	2575.8	2639.0	89.3	595.6	2.9
	40	7.8420E-07	2.119	2702.1				
	50	8.9266E-07	4.194	4698.3	4735.2	52.2	387.9	2.7
	50	8.4260E-07	4.021	4772.1				
	60	7.6752E-07	3.087	4022.1	4025.2	4.5	306.6	2.7
	60	8.9266E-07	3.596	4028.4				
	70	9.8443E-07	2.999	3046.4	2778.2	379.3	209.2	2.95
	70	9.6774E-07	2.429	2510.0				
	80	8.5094E-07	2.365	2779.3	2662.8	164.7	182.5	3.4
	80	9.5940E-07	2.443	1781.9				

Table 4 cont'd: *Slurry phase ethylene polymerisation of Pn*ZrCp^{R}(X)$_{sMAO}$ complexes. Conditions: [Zr]:[sMAO] = 1:200, 30 minutes, 50 mL toluene, 2 bar C_2H_4, 150 mg TiBA.*

Complex	Temperature (°C)	Mol_{Zr}	PE yield (g)	Activity (kg_{PE}/mol·h·bar)	Average Activity	Standard Deviation
Pn*ZrCp^{Me}(Cl)	40	3.0524E-07	0.163	534.0	503.6	43.0
	40	2.7472E-07	0.13	473.2		
	50	2.4975E-07	0.139	556.6	563.4	9.7
	50	2.5252E-07	0.144	570.3		
	60	2.6362E-07	0.109	413.5	457.9	62.8
	60	2.7472E-07	0.138	502.3		
	70	3.0247E-07	0.27	892.7	849.6	60.9
	70	2.9137E-07	0.235	806.5		
	80	2.6085E-07	0.228	874.1	942.7	97.0
	80	2.7195E-07	0.275	1011.2		

Table 5: *Slurry phase ethylene polymerisation of SSMAO immobilised Pn*ZrCp^{Me}(Cl). Conditions: [Zr]:[Al] = 1:200, 30 minutes, 50 mL toluene, 2 bar C_2H_4, 150 mg TiBA.*

Complex	Temperature (°C)	Mol_{Zr}	PE yield (g)	Activity (kg_{PE}/mol·h·bar)	Average Activity	Standard Deviation
Pn*ZrCp^{Me}(Cl)	40	2.5042E-07	0.271	1082.2	1116.1	48.0
	40	2.5302E-07	0.291	1150.1		
	50	2.5042E-07	0.309	1233.9	1206.0	39.5
	50	2.5042E-07	0.295	1178.0		
	60	2.7389E-07	0.417	1522.5	1501.4	29.9
	60	2.8172E-07	0.417	1480.2		
	70	2.7128E-07	0.438	1614.5	1521.7	131.3
	70	2.8693E-07	0.41	1428.9		
	80	2.7128E-07	0.399	1470.8	1612.2	200.0
	80	2.4520E-07	0.43	1753.7		

Table 6: *Slurry phase ethylene polymerisation of LDH-MAO immobilised Pn*ZrCp^{Me}(Cl). Conditions: [Zr]:[Al] = 1:200, 30 minutes, 50 mL toluene, 2 bar C_2H_4, 150 mg TiBA.*

Complex	Temperature (°C)	Mol_{Zr}	PE yield (g)	Activity (kg_{PE}/mol·h·bar)	Average Activity	Standard Deviation	M_W (kDa)	PDI
Pn*ZrCp(Cl)	40	6.0516E-07	1.814	2997.5	2882.6	162.6	750.4	2.8
	40	7.0602E-07	1.954	2767.6				
	50	6.4839E-07	1.74	2683.6	2572.5	157.1	558.9	2.9
	50	7.2764E-07	1.791	2461.4				
	60	6.9161E-07	1.573	2274.4	2232.5	59.3	404.9	3
	60	6.9161E-07	1.515	2190.5				
	70	7.6366E-07	1.301	1703.6	1723.6	28.2	231.8	3
	70	7.7086E-07	1.344	1743.5				
	80	6.7000E-07	0.977	1458.2	1484.1	36.7	156.5	2.95
	80	6.5559E-07	0.99	1510.1				
Pn*ZrCp(CH_2Ph)	40	6.168E-07	2.004	3249.1	3007.1	342.3	907.0	2.9
	40	6.228E-07	1.722	2765.0				
	50	5.749E-07	1.657	2882.4	2724.7	222.9	618.5	3.05
	50	5.629E-07	1.445	2567.1				
	60	5.928E-07	1.719	2899.6	2945.5	64.9	523.4	3.15
	60	6.228E-07	1.863	2991.4				

Table 7: *Slurry phase ethylene polymerisation of Pn*ZrCp^R(X)$_{sMAO}$ complexes. Conditions: [Zr]:[sMAO] = 1:200, 30 minutes, 50 mL hexane, 2 bar C_2H_4, 150 mg TiBA.*

Complex	Temperature (°C)	Mol_{Zr}	PE yield (g)	Activity (kg_{PE}/mol·h·bar)	Average Activity	Standard Deviation	M_W (kDa)	PDI
Pn*ZrCp(CH_2Ph)	70	4.671E-07	1.043	2233.0	2204.5	40.3	271.5	3.45
	70	5.868E-07	1.277	2176.0				
	80	6.946E-07	1.241	1786.5	1676.1	156.3	158.9	2.85
	80	6.228E-07	0.975	1565.6				
Pn*ZrCp(H)	40	7.3341E-07	2.268	3092.4	2964.6	180.7	762.5	2.85
	40	7.4060E-07	2.101	2836.9				
	50	7.4779E-07	1.616	2161.0	2141.0	28.4	538.6	3
	50	7.7656E-07	1.647	2120.9				
	60	7.5498E-07	1.649	2184.2	2199.3	21.4	376.3	3.1
	60	7.4060E-07	1.64	2214.4				
	70	7.8375E-07	1.114	1421.4	1511.4	127.4	228.8	3.1
	70	6.9746E-07	1.117	1601.5				
	80	6.9027E-07	1.156	1674.7	1519.2	219.9	131.5	2.95
	80	7.4060E-07	1.01	1363.8				
Pn*ZrCp(C_3H_5)	40	7.6209E-07	1.935	2539.1	2441.8	137.5	807.7	3
	40	8.4193E-07	1.974	2344.6				

Table 7 cont'd: *Slurry phase ethylene polymerisation of Pn*ZrCp^R(X)$_{sMAO}$ complexes. Conditions: [Zr]:[sMAO] = 1:200, 30 minutes, 50 mL hexane, 2 bar C_2H_4, 150 mg TiBA.*

Complex	Temperature (°C)	Mol_{Zr}	PE yield (g)	Activity (kg_{PE}/mol·h·bar)	Average Activity	Standard Deviation	M_W (kDa)	PDI
Pn*ZrCp(C_3H_5)	50	6.5322E-07	1.611	2466.2	2473.1	9.7	644.3	3
	50	6.3145E-07	1.566	2480.0				
	60	6.5322E-07	1.308	2002.4	1962.2	56.8	373.9	3.1
	60	7.3306E-07	1.409	1922.1				
	70	6.8225E-07	1.011	1481.9	1566.1	119.1	265.0	3.2
	70	6.6774E-07	1.102	1650.4				
	80	7.6209E-07	1.058	1388.3	1347.0	58.3	174.1	3.4
	80	6.3870E-07	0.834	1305.8				
Pn*ZrCp(Me)	40	6.3131E-07	1.694	2683.3	2685.6	3.2	760.1	2.9
	40	6.6000E-07	1.774	2687.9				
	50	7.0305E-07	1.667	2371.1	2442.1	100.4	511.5	3
	50	7.3892E-07	1.857	2513.1				
	60	5.5957E-07	1.237	2210.6	2162.2	68.5	321.1	3.25
	60	7.8914E-07	1.668	2113.7				
	70	6.0979E-07	1.441	2363.1	2400.9	53.5	275.7	3.15
	70	7.6761E-07	1.872	2438.7				

Table 7 cont'd: *Slurry phase ethylene polymerisation of Pn*ZrCp^R(X)$_{sMAO}$ complexes. Conditions: [Zr]:[sMAO] = 1:200, 30 minutes, 50 mL hexane, 2 bar C_2H_4, 150 mg TiBA.*

Complex	Temperature (°C)	Mol_{Zr}	PE yield (g)	Activity (kg_{PE}/mol·h·bar)	Average Activity	Standard Deviation	M_W (kDa)	PDI
Pn*ZrCp(Me)	80	6.7435E-07	1.212	1797.3	1828.1	43.7	179.5	3.6
	80	7.4609E-07	1.387	1859.0				
Pn*ZrCp(^{n}Bu)	40	5.8459E-07	1.825	3121.8	3110.4	16.2		
	40	6.1311E-07	1.9	3099.0				
	50	6.9866E-07	1.867	2672.3	2651.5	29.4		
	50	6.9866E-07	1.838	2630.8				
	60	6.9153E-07	1.428	2065.0	2178.0	159.9		
	60	6.6301E-07	1.519	2291.1				
	70	7.5569E-07	1.476	1953.2	1994.8	58.9		
	70	7.8421E-07	1.597	2036.4				
	80	6.6301E-07	1.071	1615.4	1573.9	58.7		
	80	6.6301E-07	1.016	1532.4				
Pn*(H)ZrCpCl$_2$	40	7.9853E-07	2.409	3016.8	3056.6	56.4	789.5	2.95
	40	7.5537E-07	2.339	3096.5				
	50	8.2011E-07	2.206	2689.9	2759.5	98.4	570.1	3
	50	7.5537E-07	2.137	2829.1				

Table 7 cont'd: *Slurry phase ethylene polymerisation of Pn*ZrCp^R(X)$_{sMAO}$ complexes. Conditions: [Zr]:[sMAO] = 1:200, 30 minutes, 50 mL hexane, 2 bar C_2H_4, 150 mg TiBA.*

Complex	Temperature (°C)	Mol_{Zr}	PE yield (g)	Activity (kg_{PE}/mol·h·bar)	Average Activity	Standard Deviation	M_W (kDa)	PDI
$Pn^*(H)ZrCpCl_2$	60	7.3379E-07	1.789	2438.0	2380.5	81.3	395.1	3.1
	60	7.9853E-07	1.855	2323.0				
	70	7.1940E-07	1.45	2015.6	2023.3	10.9	248.6	3.25
	70	7.7695E-07	1.578	2031.0				
	80	6.9782E-07	1.132	1622.2	1646.7	34.6	167.6	3
	80	6.4746E-07	1.082	1671.1				

Table 7 cont'd: *Slurry phase ethylene polymerisation of $Pn^*ZrCp^R(X)_{sMAO}$ complexes. Conditions: [Zr]:[sMAO] = 1:200, 30 minutes, 50 mL hexane, 2 bar C_2H_4, 150 mg TiBA.*

Complex	Mol_{Zr}	Time (seconds)	PE yield (g)	Activity (kg_{PE}/mol·h·bar)	Average Activity	Standard Deviation	M_W (kDa)	PDI
Pn*ZrCp(Cl)	3.3468E-08	2459	0.159	840.6	640.6	282.9	368.5	2.85
	3.3468E-08	3600	0.122	440.6				
Pn*ZrCp^{Me}(Cl)	1.6614E-08	2814	0.156	1451.9	1035.1	589.5	404.0	3.2
	1.6614E-08	3601	0.085	618.2				
Pn*ZrCp^{nBu}(Cl)	1.6578E-08	1584	0.160	2651.1	2663.5	17.5	367.0	3.3
	1.6578E-08	1589	0.162	2675.8				
Pn*ZrCp(^{n}Bu)	1.0694E-08	2263	0.159	2858.8	2918.7	84.7	292.5	2.45
	1.0694E-08	2172	0.159	2978.6				
Pn*ZrCp(H)	1.7976E-08	3600	0.151	1015.3	1140.8	177.5	323.5	2.7
	1.0785E-08	3600	0.113	1266.3				
Pn*ZrCp(CH_2Ph)	1.4442E-08	1232	0.162	3961.7	4228.9	377.8	338.0	3.2
	1.4442E-08	1099	0.164	4496.0				
Pn*ZrCp(Me)	1.4348E-08	1044	0.164	4763.8	4799.2	50.0	325.5	3.6
	1.4348E-08	1035	0.165	4834.6				

Table 8: *Slurry phase ethylene polymerisation of Pn*ZrCp^{R}(X)$_{sMAO}$ complexes. Conditions: [Zr]:[sMAO] = 1:200, 5 mL heptane, 120 psi C_2H_4, 150 µM TiBA, 80 °C.*

Complex	Mol_{Zr}	Time (seconds)	PE yield (g)	Activity (kg_{PE}/mol·h·bar)	Average Activity	Standard Deviation	M_W (kDa)	PDI
Pn*ZrCp(Cl)	3.3468E-08	2796	0.148	688.2	660.6	39.0	62.5	17.4
	3.3468E-08	2896	0.141	633.0				
Pn*ZrCp^{Me}(Cl)	3.3227E-08	709	0.157	2899.8	1901.9	1411.2	35	9.05
	2.4920E-08	2839	0.147	904.1				
Pn*ZrCp^{nBu}(Cl)	1.6578E-08	993	0.155	4096.8	4057.4	55.7	17	5.65
	1.6578E-08	1019	0.156	4018.0				
Pn*ZrCp(^{n}Bu)	1.0694E-08	3600	0.130	1469.3	2012.5	768.2	27.5	7.95
	1.0694E-08	2404	0.151	2555.7				
Pn*ZrCp(H)	1.7976E-08	3600	0.076	511.0	630.9	169.6	16	7.95
	1.0785E-08	3600	0.067	750.8				
Pn*ZrCp(CH_2Ph)	1.4442E-08	3024	0.152	1514.4	1250.7	372.9	23	8.5
	1.4442E-08	3602	0.118	987.0				
Pn*ZrCp(Me)	1.4348E-08	1418	0.161	3443.2	2385.6	1495.6	26	7.75
	1.4348E-08	3448	0.151	1328.1				

Table 9: *Slurry phase ethylene polymerisation of Pn*ZrCp^{R}(X)$_{sMAO}$ complexes. Conditions: [Zr]:[sMAO] = 1:200, 5 mL heptane, 120 psi C_2H_4, 150 µM TiBA, 80 °C, 0.8% H_2.*

Complex	Mol_{Zr}	Time (seconds)	PE yield (g)	Activity (kg_{PE}/mol·h·bar)	Average Activity	Standard Deviation	M_W (kDa)	PDI
Pn*ZrCp(Cl)	3.3468E-08	3600	0.057	205.8	162.5	61.3	17	12.6
	3.3468E-08	3600	0.033	119.2				
Pn*ZrCp^{Me}(Cl)	3.3227E-08	1247	0.146	1533.2	960.6	809.8	11.5	9.2
	2.4920E-08	3600	0.08	388.0				
Pn*ZrCp^{nBu}(Cl)	1.6578E-08	1509	0.151	2626.3	2869.5	343.8	13	6.7
	1.6578E-08	1307	0.155	3112.6				
Pn*ZrCp(^{n}Bu)	1.0694E-08	3600	0.048	542.5	446.4	135.9	7.05	11.3
	1.0694E-08	3600	0.031	350.4				
Pn*ZrCp(H)	1.7976E-08	3600	0.041	275.7	262.2	19.0	6.25	9.45
	1.7976E-08	3600	0.037	248.8				
Pn*ZrCp(CH_2Ph)	1.4442E-08	1326	0.153	3476.4	3476.4		12	6.1
Pn*ZrCp(Me)	1.4348E-08	1294	0.155	3632.5	3632.5		12	5.6

Table 10: *Slurry phase ethylene polymerisation of Pn*ZrCp^{R}(X)$_{sMAO}$ complexes. Conditions: [Zr]:[sMAO] = 1:200, 5 mL heptane, 120 psi C_2H_4, 150 µM TiBA, 80 °C, 1.6% H_2.*

Complex	Mol_{Zr}	Time (seconds)	PE yield (g)	Activity (kg_{PE}/mol·h·bar)	Average Activity	Standard Deviation	M_W (kDa)	PDI
Pn*ZrCp(Cl)	3.3468E-08	1796	0.124	897.6	805.4	130.4	267	2.85
	3.3468E-08	2078	0.114	713.2				
Pn*ZrCp^{Me}(Cl)	1.6614E-08	3388	0.109	842.6	748.7	132.8	231.5	2.95
	1.6614E-08	3600	0.09	654.8				
Pn*ZrCp^{nBu}(Cl)	1.6578E-08	1516	0.104	1800.5	1866.9	93.8	207	2.55
	1.6578E-08	1507	0.111	1933.2				
Pn*ZrCp(^{n}Bu)	1.7823E-08	997	0.109	2669.0	2588.9	113.4	225	2.25
	1.7823E-08	1051	0.108	2508.7				
Pn*ZrCp(H)	2.8761E-08	1540	0.106	1041.3	1008.2	46.8	229	2.25
	2.8761E-08	1629	0.105	975.1				
Pn*ZrCp(CH_2Ph)	1.0831E-08	902	0.113	5032.6	4478.3	783.9	141	2.6
	1.4442E-08	906	0.118	3924.1				
Pn*ZrCp(Me)	1.0761E-08	880	0.11	5054.3	4639.6	586.5	147	2.55
	1.4348E-08	847	0.118	4224.9				

Table 11: *Slurry phase ethylene polymerisation of Pn*ZrCp^{R}(X)$_{sMAO}$ complexes. Conditions: [Zr]:[sMAO] = 1:200, 5 mL heptane, 120 psi C_2H_4, 150 µM TiBA, 80 °C, 125 µL hexene.*

Complex	Mol_{Zr}	Time (seconds)	PE yield (g)	Activity (kg_{PE}/mol·h·bar)	Average Activity	Standard Deviation	M_W (kDa)	PDI
Pn*ZrCp(Cl)	3.3468E-08	2094	0.110	682.9	698.1	21.4	243.5	3.7
	3.3468E-08	2005	0.110	713.3				
Pn*ZrCp^{Me}(Cl)	1.6614E-08	3600	0.104	756.6	676.6	113.2	167.5	3.05
	1.6614E-08	3600	0.082	596.6				
Pn*ZrCp^{nBu}(Cl)	1.6578E-08	1702	0.112	1727.1	1714.1	18.5	161	2.5
	1.6578E-08	1759	0.114	1701.0				
Pn*ZrCp(^{n}Bu)	1.7823E-08	1028	0.112	2659.8	2520.8	196.6	188.5	2.3
	1.7823E-08	1107	0.108	2381.8				
Pn*ZrCp(H)	2.8761E-08	1601	0.111	1048.9	978.5	99.6	179.5	2.4
	2.8761E-08	1816	0.109	908.0				
Pn*ZrCp(CH_2Ph)	1.4442E-08	1077	0.115	3217.1	3217.1	160.5	156.5	2.65
	1.4442E-08	1006	0.115	3444.1				
Pn*ZrCp(Me)	1.4348E-08	935	0.115	3729.9	3729.9	131.0	165.5	2.75
	1.4348E-08	914	0.118	3915.2				

Table 12: *Slurry phase ethylene polymerisation of Pn*ZrCp^{R}(X)$_{sMAO}$ complexes. Conditions: [Zr]:[sMAO] = 1:200, 5 mL heptane, 120 psi C_2H_4, 150 µM TiBA, 80 °C, 250 µL hexene.*

Complex	Mol_{Zr}	Hexene Amount (µL)	H_2 (%)	Time (seconds)	PE yield (g)	Activity (kg_{PE}/mol·h·bar)	M_W (kDa)	PDI
Pn*ZrCp(CH_2Ph)	1.44418E-08	125	1	326	0.119	10997.9	10	3.3
	1.44418E-08	250	1	301	0.12	12011.5	9	2.9
	1.44418E-08	125	2	2316	0.096	1248.9	7.7	6
Pn*ZrCp(Me)	1.43479E-08	125	1	326	0.122	11349.0	10	3
	1.43479E-08	250	1	268	0.125	14144.5	11	2.6
	1.43479E-08	125	2	1752	0.099	1713.6	9.4	6.7

Table 13: *Slurry phase ethylene polymerisation of Pn*ZrCp^R(X)$_{sMAO}$ complexes. Conditions: [Zr]:[sMAO] = 1:200, 5 mL heptane, 120 psi C_2H_4, 150 µM TiBA, 80 °C.*

Complex	Mol_{Zr}	Hexene Amount (mL)	H_2 (%)	Temperature (°C)	Time (minutes)	PE yield (g)	Activity (kg_{PE}/mol·h·bar)	M_W (kDa)	PDI
Pn*ZrCp^{nBu}(Cl)	1.7823E-06	0	0	70	60	32.22	2259.7	470.5	5.7
	3.5646E-06	0	0.38	70	60	77.65	2723.0	390.1	4.2
	5.1330E-06	0	0.74	70	60	56.75	1382.0	101.5	19.9
	1.7823E-06	10	0	60	60	19.52	1369.0	363.8	3.9
	4.9904E-06	10	0.36	60	55	71.6	1793.4	76.7	7.8
	4.9904E-06	10	0.87	60	60	77.83	1949.5		
Pn*ZrCp(^{nBu})	1.7823E-06	0	0	70	60	38.45	2696.7	417.8	4.5
	4.9904E-06	0	0.41	70	60	95.82	2400.1	46.4	4.5
	4.9904E-06	0	0.76	70	60	84	2104.0	36.9	7.7
	2.8517E-06	10	0	60	60	51.39	2252.6	293.1	4.1
	4.9904E-06	10	0.76	60	60	87.4	2189.2	57.0	12.0

Table 14: *Slurry phase ethylene polymerisation activity of Pn*ZrCp^{R}(X)$_{sMAO}$ complexes. Conditions: [Zr]:[sMAO] = 1:200; 8 bar ethylene; 850 mL hexane; 2.5 mL $AlEt_3$.*

Complex	Mol_{Zr}	Co-catalyst	PE yield (g)	Activity (kg_{PE}/mol·h·bar)	Average Activity	Standard Deviation	M_W (kDa)	PDI
Pn*ZrCp(Cl)	1.19026E-06	250 eq.	0.212	1068.7	1106.5	53.5		
	1.19026E-06	MAO	0.227	1144.3				
[Pn*ZrCp][$B(Ar^F)_4$]	4.36529E-06		0.261	358.7	345.0	19.4	259.4	6.3
	4.36529E-06		0.241	331.2				
[Pn*ZrCp][$B(Ar^F)_4$]	1.4551E-06	250 eq.	0.183	754.2	767.2	18.4	1055.6	38.8
	1.4551E-06	MAO	0.189	780.2				
[Pn*ZrCp][$B(C_6F_5)_4$]	4.36529E-06		0.405	556.7	546.4	14.6	871.5	2.83
	4.36529E-06		0.390	536.0				
[$(Pn*ZrCp)_2(\mu–Me)$]	8.94729E-06		0.114	76.4	71.1	7.6		
[$B(C_6F_5)_4$]	8.94729E-06		0.098	65.7				
[Pn*ZrCp(Py)][$B(Ar^F)_4$]	3.11548E-06		0.176	339.0	349.5	15.0		
	3.11548E-06		0.187	360.1				
[Pn*ZrCp][$B(C_6F_5)_4$]	4.36529E-06	20 eq. DtBP	0.388	533.3	522.3	15.6		
	4.36529E-06		0.372	511.3				

Table 15: *Solution phase ethylene polymerisation with $[Pn*ZrCp]^+$ complexes. Conditions: 25 °C, 5 minutes, 50 mL C_6H_5Cl, 2 bar C_2H_4. Ar^F = 3,5–$C_6H_3(CF_3)_2$.*